AN ABSTRACT OF THE DISSERTATION OF

<u>Nicole E. Moore</u> for the degree of <u>Doctor of Philosophy</u> in Geology presented on <u>June 12, 2018.</u>

Title: <u>Petrogenesis of the Steens Basalt: Variation in Source Contributions and Effects of Crustal Passage During the Onset of Columbia River Flood Basalt Volcanism</u>

Abstract approved:

_____

Anita L. Grunder

Continental flood basalts represent short-lived but immense blasts of mafic magma to the continental crust. The youngest and smallest continental flood basalt worldwide, the Columbia River Basalt, initiated with the eruption of the most mafic member, the Steens Basalt (~16.9 Ma). The Steens Basalt is exposed in southeast Oregon, southwest Idaho and northern Nevada. The flows were fed by dikes near Steens Mountain, with eruptions spanning no more than a few 100,000 years. The Steens Basalt has been informally subdivided into lower and upper units based on compositional distinctions. The lower flows are most mafic, tholeiitic and incompatible trace element poor, whereas the upper flows are less magnesian, mildly alkalic, and generally more enriched in incompatible trace elements. These chemostratigraphic excursions signal variations in petrogenetic processes occurred in time over the life of the flood basalt event.

The work presented here is motivated by questions evoked from the observed compositional changes with stratigraphic position in the Steens Basalt. The driving questions are how a flood basalt system evolves in response to changing mass and energy flux from the mantle, how the balance of recharge, fractional crystallization and assimilation processes impart geochemical patterns to the lavas, and how crustal architecture is modified by the influx of magma during a continental flood basalt event. In order to fully characterize the relative contributions of recharge,

assimilation, and fractional crystallization (RAFC) processes to generation of the Steens Basalt, a comprehensive petrologic and geochemical data set is presented, including detailed petrography, whole-rock and mineral chemistry, and isotopic data. All of these data are utilized to interpret geochemical patterns, constrain intensive parameters (i.e., temperature, pressure, initial H_2O content, and oxygen fugacity), and model RAFC processes using the Magma Chamber Simulator (MCS) and other modeling tools, with the goal of understanding, describing, and quantifying the full range of open system processes that combined to generate the Steens Basalt.

The volcanological and chemostratigraphic characteristics of the Steens Basalt record a three-stage history: the lower A, lower B, and upper Steens Basalt stages. The lower A stage is represented by a newly discovered and minimally exposed section at Steens Mountain that is characterized by initially heterogeneous flows that become increasing homogeneous upsection. During this stage, cooling and crystal fractionation of the magmas outpaces recharge. The lower B stage contains the most primitive compositions, is volumetrically dominant, and represents waxing of the basaltic pulse. The increasingly magnesian compositions upsection during this stage signal an interval of recharge dominance and high eruptive frequency. In the waning upper Steens Basalt stage, recharge is subordinate to fractionation and assimilation becomes an important contributor. These temporal petrogenetic changes are analogous to chemostratigraphic excursions in the Imnaha and Grande Ronde Basalts of the Columbia River Basalt Group, other continental flood basalts such as the Deccan and Siberian Traps, and to phase and cryptic layering present in layered mafic intrusions. Compositional changes in time in these other systems record a change in RAFC processes and suggest large mafic systems share similar evolutionary histories.

Two component isotopic mixing models of 5% partial mantle melts suggest that a combination of depleted upper mantle, and a more enriched mantle endmember contribute roughly equal proportions to magma generation up through the waxing stage of the Steens Basalt. Additionally, these mixing models indicate the contribution by the depleted mantle component increases during the onset of waning magmatism and that crustal contamination by partial melts from mafic accreted terranes contributes to magma generation during the upper Steens Basalt stage. High

Os concentrations in the lower B Steens Basalt indicate consumption of phase in which Os is compatible, either sulfides in the mantle source or previously fractionated from Steens Basalt magmas in the crust. Cryptic deep fractionation of abundant clinopyroxene is suggested by enrichment of $\delta^{18}O$ in some flows.

MCS modeling aids in the interpretation of the processes that dominate during the lower B Steens Basalt stage and elucidate additional processes at play during the waxing stage of magmatic input. Two trends in the lower B Steens Basalt, one at high and one at low MgO, initially increase in magnesian character upsection and have distinct evolutionary histories. Best fit models for the high MgO trend suggest that these compositions are staged in the mid to upper crust and are generated by increasingly voluminous recharge events with minor amounts of intervening crystallization. Where a decrease in MgO occurs upsection in the high MgO trend, lavas are modified by a combination of fractionation, cumulate entrainment, and magma mixing. The sparsely phyric flows of the low MgO trend result from fractionation of a primitive high MgO parent at shallower crustal levels, whereas low MgO giant plagioclase basalts are formed by cumulate entrainment into fractionated melts. The shallower low MgO reservoirs are pulsed by magmas from the recharge dominated high MgO trend, such that both high and low MgO trend lavas increase in MgO over the interval during which recharge is dominant. A preliminary integrated mass balance calculation for the lower B Steens Basalt stage suggests possible intrusive to extrusive ratios of ~8:1 to 14:1 and cumulate addition to the crust of 5-28 km. This initial attempt at an upsection integrated mass balance suggests that significant gabbroic underplating occurs over the life of the flood basalt event, indicating thickening of the crust and perhaps requiring foundering and delamination of deep crustal roots into the overlying mantle.

This research provides a framework for comparative studies of chemostratigraphic changes in other continental flood basalts. It also provides a strategy for modeling compositional changes with stratigraphy in large mafic systems using the relatively new Magma Chamber Simulator, and the first attempt to quantify and integrate the mass balance of RAFC contributions through a section of a continental flood basalt.

Petrogenesis of the Steens Basalt: Variation in Source Contributions and Effects of
Crustal Passage During the Onset of Columbia River Flood Basalt Volcanism

by
Nicole E. Moore

A DISSERTATION

submitted to

Oregon State University

in partial fulfillment of
the requirements for the
degree of

Doctor of Philosophy

Presented June 12, 2018
Commencement June 2019

Doctor of Philosophy dissertation of Nicole E. Moore presented on June 12, 2018

APPROVED:

_____
Major Professor, representing Geology

_____
Dean of the College of Earth, Ocean and Atmospheric Sciences

_____
Dean of the Graduate School

I understand that my dissertation will become part of the permanent collection of Oregon State University libraries. My signature below authorizes release of my dissertation to any reader upon request.

_____
Nicole E. Moore, Author

ACKNOWLEDGEMENTS

wonderful teacher and advisor, and who was always willing to offer help and advice no matter the request. Your constant interest in and excitement about all the research going on in our group is inspiring. Frank Tepley offered support and comic relief during my many hours in the probe lab and has also offered much appreciated advice and support in terms of my research and career. I made it through my first few years of life as PhD student because of my incoming VIPER cohort, Brad Pitcher, Richard Bradshaw, Ado Mucek, and Henri Sanville. Thanks for being my cheerleaders and sounding boards! I was privileged to have two amazing office mates with whom to share my fabulous campus space in Dawes House, Federico Cernuschi and Susan Schnur. Fede, thanks for loving the same music as I and for allowing me to sing out loud to you all day every day. Your constant hard work and dedication to your family and friends inspired me. Susan, you provided comic relief whenever I started to take things too seriously ("get to da choppa!"), and it always seemed like comfort food in the form of your wonderful baked treats and/or chocolate showed up at the perfect moments. I would not be the Adobe Illustrator proficient I am today without you.

My time in and around Steens Mountain was filled with wonderful encounters. I had fantastic field assistants with whom I was lucky enough to share the beauty of Steens Mountain; I am ever grateful to Henri Sanville, Julie Klath, and Ben Murphy for braving the insanely steep terrane and brutal temperatures of the high desert in southeast Oregon. I like to think the amazing beauty of the area made it well worth it for you all. Thank you to Rick Wells, geologist at the Burns District BLM Office for helping facilitate field work in the Steens Mountain Wilderness. Both Joe (and his never to be forgotten parrot companion, Herman) and Rose, caretakers at the Alvord Hot Springs, showed a constant curiosity for my work that helped me recognize there is a scientist in all of us, and made visiting the area feel like coming home. George and Renée Stroemple, owners of the Wildhorse Ranch, were kind enough to allow me access to their private land for sampling and overnight camping stays.

I never would have made it through these last years without the constant love and support of my best friend and hetero life partner, Nicole Rocco. I'm still mostly sane, happy, excited and healthy because you were there through it all to remind me

that I love what I do, that I need a work-life balance, and that it is ok to not have all the answers. Not only was Henri Sanville part of my VIPER cohort and a dedicated field assistant, but a wonderful friend and constant source of support. Without you both behind me, telling me that I actually am a good scientist, mother, and friend, I really would have given up many times over. You have both told me I inspire you, which is more than an honor, but you have both inspired me with your hard work, dedication, and willingness to always put up with my many ups and downs.

Another true inspiration is my son, Kaylen. I returned to college when he was a baby, as an example to him and with the hope that his life would be all the better if his mother could follow her dreams and love what she does. I truly hope this was the case. The support of his father, Jeremy, through these past two decades, is the reason I was able to simultaneously follow my dreams and raise our son together. My family, particularly my mother Patty, my father Verne, and my sisters Heather and Christina, have always been proud of my accomplishments and supported my decisions, no matter that they took me thousands of miles away. I will never forget that growing up, my parents constantly reminded me that I could do anything I set my mind to in life. The proof is in the pudding, and that pudding is this dissertation and my doctoral degree.

CONTRIBUTION OF AUTHORS

Chapter 2: Significant contributions to the writing of the Chapter 2 manuscript were made by Anita L. Grunder and Wendy A. Bohrson. Minor contributions to the writing were made by Geosphere manuscript reviewers Victor E. Camp and John A. Wolff.

Chapter 3: Contributions to the writing of the Analytical Methods section of Chapter 3 were made by Richard W. Carlson and David W. Graham.

TABLE OF CONTENTS

TABLE OF CONTENTS (Continued)

TABLE OF CONTENTS (Continued)

TABLE OF CONTENTS (Continued)

LIST OF FIGURES

LIST OF FIGURES (Continued)

LIST OF TABLES

LIST OF SUPPLEMENTAL FILES

These files are attached separately in the Oregon State University Scholars Archive.

<u>Supplement</u>

1 Ar- Ar Age Protocol and Results Summary

2 Lower Steens Basalt Mineral Compositions

3 Steens Basalt Whole Rock and Location Data

4 Steens Basalt Bootstrapping Data and Results

5 Plots to Demonstrate Lack of Cryptic Alteration in the Steens Basalt

6 Sr, Nd, Pb and Hf Uncertainty and Interference Ratios from DTM

7 Steens Basalt Re-Homogenized Melt Inclusion Data

8 Mass Balance Calculations for Integrated Volumes in the Lower B Steens Basalt

CHAPTER 1

Introduction

1.1 RESEARCH PURPOSE AND OVERVIEW

The purpose of the research presented herein is to understand how a flood basalt magmatic system evolves in response to changing mass and energy flux from the mantle, how the balance of recharge and differentiation in the crust imparts geochemical patterns to erupted lavas, and how crustal architecture is modified by this influx and processing of magma. A rich rock and mineral record of open system processes (magma recharge/mixing, assimilation, fractional crystallization - RAFC) is stored in the hundreds of stacked flows of the Steens Basalt in SE Oregon. A stratigraphically controlled petrologic and geochemical data set is used to decipher the contributions of RAFC processes that generated lavas erupted at various stages of Steens Basalt magmatism. Qualitative and quantitative interpretations are used to present a comprehensive picture of magma system evolution, including use of an array of computational petrologic tools, from geothermobarometry to simple mixing models to state-of-the art energy-balanced models of RAFC using the Magma Chamber Simulator (MCS). The overall goal is to interpret the magmatic history of the entire Steens Basalt, from mantle generation of magmas, to crustal staging, eruption, and emplacement of magma residua in the crust.

1.2 LARGE IGNEOUS PROVINCES AND CONTINENTAL FLOOD BASALTS

Large igneous provinces (LIP) are massive volumes of dominantly mafic magmas emplaced intrusively and extrusively in the crust. The formation mechanisms for these large volumes of magma over relatively short periods of time are contentious, but models include an anomalous heat contribution to the mantle from upwelling hotspot plumes (e.g. Richards et al. 1989), continental breakup (e.g. McKenzie, 1984), delamination of dense eclogitic lithospheric roots (e.g. Anderson, 2005; Elkins-Tanton, 2005), and meteorite impacts (e.g. Ingle and Coffin, 2004). Given their overall mafic character and lack of associations with tectonic boundaries, lavas from these provinces provide a geochemical view of the mantle away from plate boundaries (Coffin and Eldholm, 1994). Though similarities exist in the spatial, temporal, and geochemical evolution among these provinces (Coffin and Eldholm, 1994; Coffin et al. 2006), there are distinctions between LIP erupted through relatively thin oceanic crust (oceanic LIP) and those erupted through

thicker continental crust (continental flood basalts).

The large igneous provinces expressed as continental flood basalts (CFB) signal short-lived, catastrophic events with far-reaching consequences from lava inundation of fossil landscapes to potential climatic effects and mass extinctions (e.g., Hofmann et al. 1997; Self et al. 2006; Whiteside et al. 2010). Many decades of work on CFB have set the stage for wrestling with the questions of how mantle-derived flood basalt magmas impact the crust through which they pass and how melts in equilibrium with mantle peridotite or pyroxenite are related to compositions typical of continental flood basalts. Most CFB provinces have sparse high-Mg primitive lavas, but on the whole, CFB have compositions consistent with crustal differentiation from high-Mg melts (e.g., Cox, 1980; Thompson et al. 1983; Garfunkel, 2008; viz., high Fe/Mg, low MgO, low Mg#, and low Ni). As a counterpoint, some workers propose that melt of substantially metasomatized mantle sources (e.g., Turner et al. 1996; Hawkesworth et al. 1999) or of eclogite account for dominant CFB compositions (e.g., Luttinen et al. 2010; Takahahshi et al. 1998; Camp and Hanan, 2008). Sparse high Fo olivines (91-93.6) in some CFB are interpreted as relicts of a mantle differentiation history from melts with estimated MgO range of 18-27 wt.% (e.g., Larsen and Pederson, 2000; Thompson et al. 2001; Herzberg and O'Hara 2002), depending on inferred depth of separation and degree of melting. A key observation is that most CFB lavas arrive at the surface significantly modified from their mantle parentage.

1.3 WHY STUDY THE STEENS BASALT

The Steens Basalt (~16.7 Ma) is the oldest member of the Columbia River Flood Basalt event, which reached peak eruption rate between 16.3 and 15.8 Ma (Baksi, 2013). The Steens Basalt is a superb natural laboratory for the following reasons:

1. An exceptional, over 1 km thick exposure of Steens Basalt at Steens Mountain preserves a spectacular record of flood basalt volcanism. At least 200 flows and flows lobes, stacked without intervening sediments or significant soils, erupted in less than ~300,000 years, and many in as little as 50,000 years (Mankinen et al. 1987; Johnson et al. 1998; Jarboe et al. 2008; 2010; Camp et al. 2013).

2. The Steens Basalt has a lower, more mafic section that includes the most magnesian tholeiitic basalt lavas of the Columbia River CFB, an upper more evolved section that includes mildly alkalic basalt, and is capped by trachy-basaltic andesite compositions, indicating systematic changes in magmatism over a relatively short period (Camp et al. 2013).

3. The Steens Basalt is part of the youngest CFB on Earth, and the rocks are reasonably fresh.

4. Isotopic characterization has identified important mantle and crustal components (Carlson et al. 1981; Carlson, 1984; Carlson and Hart, 1987; Brandon et al. 1993; Dodson et al. 1997; Chesley and Ruiz, 1998; Hooper and Hawkesworth, 1993; Wolff et al. 2008; Wolf and Ramos, 2013; Ramos et al. 2005; 2013).

Systematic stratigraphic variations in the composition of Steens Basalt have resulted in an informal designation between lower and upper flows (Camp et al. 2013). Compositional data suggest that the lower, more mafic section represents a recharge-dominated time of crustal staging, coupled with crystal fractionation, during early penetration of basalt from the mantle. This idea is based on high and variable Mg (and Ni) and low and less variable La (Johnson et al. 1998). In this sense, an analogy can be drawn to cumulate zones in layered mafic intrusions, where zig-zag cryptic layering (e.g., Ni, Cr, MgO) signals a fractionation-recharge history (i.e., Jackson, 1970; Lee and Ripley, 1996; Cawthorn and Walraven, 1998). The upper, generally more differentiated Steens Basalt section is characterized by lower Ni, higher La and SiO_2 and generally higher $^{87}Sr/^{86}Sr$ (Camp et al. 2013, Ramos et al. 2013), suggesting a magmatic history more influenced by fractionation (Gunn and Watkins, 1970) and crustal assimilation, similar to the interpretation of the rest of the main phase formations of the CRBG, the Deccan Traps (Kumar et al. 2010), the Skye Igneous Centre of the British Tertiary Volcanic Province (Fowler et al. 2004), and the Karoo CFB (Heinonen et al. 2010; 2013). These observations evoke questions about temporal changes in depth of differentiation, mass and thermal flux from the mantle, and involvement of crustal-derived components. In turn, magma passage and differentiation must change the thermal, mass and compositional profile of the crust.

My interest is to quantify how the balance of petrologic processes (RAFC) changes in time during initiation of a flood basalt pulse, as a gauge of the evolving balance between mantle flux and crustal contributions. The questions evoked by existing data can be answered by interpreting an expanded, stratigraphically controlled data set of whole-rock, mineral, and isotopic compositions coupled with qualitative petrologic and computational modeling. Comprehensive models for the Steens Basalt magmatic system can in turn be used to compare stratigraphic changes upsection in other CFB to decipher source and process changes and look for similarities in the evolution of these large mafic systems. Using layered mafic intrusions as an analog for cumulate residue of long term fractionation within the crust provides a connection to the mass, thermal and compositional changes made to the crust by a blast of mafic magmatism.

1.4 GEOLOGIC SETTING AND PETROLOGY OF THE STEENS BASALT

The Steens Basalt of SE Oregon and NW Nevada covers about 53,000 km^2 (Mankinen et al. 1987; Camp et al. 2013). The volcanic field is ~100 km in diameter, and has reported ages ranging from 16.8 to 16.1 Ma (Brueseke et al. 2007; Camp et al. 2013 and references therein), making this eruptive phase roughly coeval with the Imnaha flows of the Columbia River Basalt Group (CRBG, Hooper et al. 2002). In detail, Steens lavas erupted within no more than 300,000 years of the 16.73 Ma Steens magnetic reversal (Jarboe et al. 2008; 2010; recently revised to 16.5 Ma by Mahood and Benson, 2018). To the south, "Steens-like" basaltic andesite to andesite lavas are as young as 15.1 Ma (Brueseke et al. 2007). The Steens Basalt crops out in a spectacular, km-thick sequence of as many as 200 thin (generally <10 m) compound flow lobes and single lava flows that were fed by NNE-striking dikes exposed along the Steens Mountain escarpment (Minor et al. 1987a, b; Jarboe et al. 2010; Camp et al., 2013). The prevalent interpretation is that the Steens Basalt is the remnant of a shield volcano (Mankinen et al. 1987; Rytuba, 1988), although Bondre and Hart (2008) attribute the shield-like morphology to Basin and Range block uplift, modest tilting, and erosion. Regardless, Steens Mountain is an important volcanic locus because there the Steens Basalt section is thickest, the age span is the longest, the compositional range is widest, and dikes are common.

The crust of eastern Oregon is made of accreted Paleozoic to Mesozoic terranes stitched with Mesozoic plutons (Walker et al. 1991). Under Steens Mountain, the crust is 32-35 km thick, thins to 30 km under the adjacent High Lava Plains and northern Basin and Range, and thickens to 42 km to the east, coincident with the $^{87}Sr/^{86}Sr_i$ 0.706 line at edge of the North America craton. Steens Mountain lies just east of the $^{87}Sr/^{86}Sr_i$ 0.704 line (Eagar et al. 2010). The lower crust is inferred to be mafic and dense with a thin, still denser root, implying substantial intra- and underplating of the crust by mafic magma (Cox and Keller, 2010; Eagar et al. 2010; Wagner et al. 2010), thickening from ~28 km in the eastern High Lava Plains to ~32 km at Steens Mountain (Eagar et al. 2011). Carlson and Hart (1987) argue that substantial crustal genesis in the region is through gabbroic intraplating, analogous to Shervais et al. (2006) who petrologically correlate sills and lavas on the Snake River Plain.

The Steens Basalt has a footprint comparable to the combined subaerial footprint of Mauna Loa and Kilauea, but at ~32,000 km^3, it is only a small portion of the estimated 210,000 km^3 for the Columbia CFB (Reidel et al. 2013; Camp et al. 2013). The Steens Basalt includes the most primitive lavas of the CRBG and falls within the SiO_2-MgO range defined by global CFB (GEOROC compilation; Moore et al. 2018, in press). The Steens Basalt thus links global CFB provinces and the anomalously silicic bulk composition of the Columbia River Basalt represented by the most voluminous Grande Ronde Basalt (53-58 wt.% SiO_2; Hooper, 2000). Isotopic data suggest that the source of the Steens Basalt is a combination of an enriched, OIB type mantle (Imnaha) component and a depleted mantle component (Carlson, 1984; Camp and Hanan, 2008; Wolff et al. 2008, Wolff and Ramos, 2013). While there is general agreement that a high-$^3He/^4He$ plume source and crustal contamination played a role in the generation of the CRBG, not all workers agree to a plume source (e.g., Carlson, 1984; Brandon et al. 1993; Hooper and Hawkesworth, 1993; Durand and Sen, 2004; Ramos et al. 2005; Hooper et al. 2007; Graham et al. 2009); other models include melting of delaminated mafic crust plus depleted mantle plus significant portions of the crust, complex mantle flow that mixes multiple mantle components, and crustal extension (Carlson and Hart, 1987; Camp and Hanan, 2008; Camp, 2013).

The Steens Basalt is divided into upper and lower sections based on chemostratigraphic distinctions (Camp et al. 2013). These compositional variations, first recognized by a detailed set of whole-rock data from a transect of samples by Gunn and Watson (1970), who suggested this variation reflects changes in magma differentiation processes through time as the Steens Basalt evolved. The lower Steens Basalt is most widely distributed and covers the full areal extent of the Steens Basalt. In contrast, the upper Steens Basalt is centered on Steens Mountain. The lower flows are more mafic and tholeiitic, whereas the upper flows are less magnesian and mildly alkalic. The upper Steens Basalt is generally more enriched in incompatible trace elements, taken to reflect crustal influence (Johnson et al. 1998; Camp et al. 2013). Pilot $\delta^{18}O$ analyses of plagioclase are up to 6.6 ‰ (Colón et al. 2015). On the other hand, radiogenic isotopes suggest an overall shift to a more enriched, Imnaha-like mantle source from a depleted Pacific MORB-like source. A general correlation between age and declining MgO (or increasing Fe/Mg) is also observed between the Imnaha and Grande Ronde flows of the CRB (Wolff and Ramos, 2013) and invites comparison to the compositional change from ultramafic to banded zones common in many layered mafic intrusions (LMI) worldwide (e.g. Naslund, 1984; Raedeke and McCallum, 1984). Chemical distinctions between lower and upper Steens Basalt imply a change in the petrologic evolution of the magma system up section through time.

1.5 DISSERTATION SCOPE AND ORGANIZATION

At the heart of quantifying changes in mantle and crustal mass and thermal flux is the collection of complete and consistent mineral and whole-rock data on a set of stratigraphically controlled samples. Petrologic modeling of these data, including determination of magmatic conditions from geothermobarometers germane to basalts as well as modeling liquid lines of descent for an open system present important evidence for crustal staging depths and the extent to which differentiation processes operated throughout the life of the flood basalt. Modeling with the Magma Chamber Simulator (MCS), a thermodynamic, energy and mass constrained tool calculates how composition, mass, and thermal constraints in a crustal magmatic system vary in response to recharge

(i.e., mixing), assimilation, and crystallization (Bohrson et al. 2014). The goal of this work is to quantify the temporal evolution of depth of differentiation, relative importance of magmatic processes, variations in mass and energy contributions from the mantle, and the response of the crust as recorded in the Steens Basalt, but with application for understanding the Steens Basalt/CRBG as a whole and continental flood basalt magmatism in general by comparison.

Following this introductory chapter, this dissertation is organized into three main chapters (2-4) that present a comprehensive, stratigraphically controlled data set on the Steens Basalt. These main chapters are generally formatted as stand-alone manuscripts for submission to scientific peer reviewed journals; chapter 2 is accepted and in press with the journal *Geosphere*. As such, repetitions occur among chapters in various sections such as geologic setting and references, as well as some figures. In chapter 2, we use whole-rock major and trace element and mineral compositional data to define a three-stage history for the evolution of the Steens Basalt magmatic system corresponding to temporal changes in dominant differentiation processes. The petrochemical evolution includes an earliest stage represented by flows that have been previously unsampled, and we provide a new age of onset for Steens magmatism from the base flow of this earliest stage. Also in this chapter, we compare the temporal evolution of the Steens Basalt to other CFB (Deccan and Siberian Traps) and to layered mafic intrusions. In chapter 3, we use isotopic compositions to describe the mantle source and crustal contamination components responsible for magma generation in time throughout the three-stage history of the Steens Basalt. Other processes that result from crustal passage of the magmas evident in isotope and whole-rock major and trace element compositions are also described. Lastly in chapter 4 we present computational modeling using the Magma Chamber simulator that explains the compositional variation and change in dominant processes up section for the recharge dominated waxing stage, the lower B Steens Basalt.

1.6 REFERENCES CITED

Anderson, D.L., 2005, Large igneous provinces, delamination, and fertile mantle: Elements, v.1 p. 271-275.

Baksi, A.K., 2013, Timing and duration of volcanism in the Columbia River Basalt Group: A review of existing radiometric data and new constraints on the age of the Steens through Wanapum Basalt extrusion: Geological Society of America Special Papers, v. 497, p. 67-85.

Brandon, A.D., Hooper, P.R., Goles, G.G., and Lambert, R.S.J., 1993, Evaluating crustal contamination in continental basalts: the isotopic composition of the Picture Gorge Basalt of the Columbia River Basalt Group: Contributions to Mineralogy and Petrology, v. 114, no. 4, p. 452-464.

Bohrson, W.A., Spera, F.J., Ghiorso, M.S., Brown, G.A., Creamer, J.B., and Mayfield, A., 2014, Thermodynamic model for energy-constrained open-system evolution of crustal magma bodies undergoing simultaneous recharge, assimilation and crystallization: The magma chamber simulator: Journal of Petrology, v. 55, p. 1685-1717.

Bondre, N.R., and Hart, W.K., 2008, Morphological and textural diversity of the Steens Basalt lava flows, Southeastern Oregon, USA: implications for emplacement style and nature of eruptive episodes: Bulletin of Volcanology, v. 70, no. 8, p. 999-1019.

Brueseke, M.E., Heizler, M.T., Hart, W. K., and Mertzman, S.A., 2007, Distribution and geochronology of Oregon Plateau (USA) flood basalt volcanism: The Steens Basalt revisited: Journal of Volcanology and Geothermal Research, v. 161, p. 187-214.

Camp, V.E., 2013, Origin of Columbia River Basalt: Passive rise of shallow mantle, or active upwelling of a deep-mantle plume: Geological Society of America Special Paper 497, p. 181-199.

Camp, V.E., and Hanan, B.B., 2008, A plume-triggered delamination origin for the Columbia River Basalt Group: Geosphere, v. 4, no. 3, p. 480.

Camp, V.E., Ross, M.E, Duncan, R.A., Jarboe, N.A., Coe, R.S., Hanan, B.B., and Johnson, J.A., 2013, The Steens Basalt: earliest lavas of the Columbia River Basalt Group: Geological Society of America Special Paper 497, p. 87-116.

Carlson, R.W., 1984, Tectonic influence on magma composition of Cenozoic basalts from the Columbia Plateau and Northwestern Great Basin, USA: FR Boyd (panel chairman), Explosive Volcanism: Inception, Evolution, and Hazards. National Research Council, p. 23-33.

Carlson, R.W., and Hart, W.K., 1987, Crustal Genesis on the Oregon Plateau: Journal of Geophysical Research-Solid Earth and Planets, v. 92, no. B7, p. 6191-6206.

Carlson, R.W., Lugmair, G.W., and Macdougall, J.D., 1981, Columbia River volcanism: the question of mantle heterogeneity or crustal contamination: Geochimica et Cosmochimica Acta, v. 45, p. 2483-2499.

Cawthorn, R.G., and Walraven, F., 1998, Emplacement and crystallization time for the Bushveld Complex: Journal of Petrology, v. 39, p. 1669-1687.

Chesley, J.T., and Ruiz, J., 1998, Crust–mantle interaction in large igneous provinces: implications from the Re–Os isotope systematics of the Columbia River flood basalts: Earth and Planetary Science Letters, v. 154, no. 1, p. 1-11.

Coffin, M.F., Duncan, R.A., Eldholm, O., Fitton, J.G., Frey, F.A., Larsen, H.C., Mahoney, J.J, Saunders, A.D., and Wallace, P.J., 2006, Large igneous provinces and scientific ocean drilling: Status quo and a look ahead: Oceanography, v. 19, p. 150-160.

Coffin, M. F., and Eldholm, O., 1994, Large igneous provinces: crustal structure, dimensions, and external consequences. Reviews of Geophysics, v. 32, p. 1-36.

Colón, D.P., Bindeman, I.N., Stern, R.A., and Fisher, C.M., 2015, Isotopically diverse rhyolites coeval with the Columbia River Flood Basalts: evidence for mantle plume interaction with the continental crust: Terra Nova, v. 27, p. 270-276.

Cox, C., and Keller, G., Crustal Structure of the High Lava Plains of the Pacific Northwest-Source Seismic and Gravity Modeling, *in* Proceedings AGU Fall Meeting Abstracts 2010, Volume 1, p. 07.

Cox, K.G., 1980, A Model for flood basalt vulcanism: Journal of Petrology, v. 21, no. 4, p. 629-650.

Dodson, A., Kennedy, B.M., and DePaolo, D.J., 1997, Helium and neon isotopes in the Imnaha Basalt, Columbia River Basalt Group: Evidence for a Yellowstone plume source: Earth and Planetary Science Letters, v. 150, p. 443-451.

Durand, S.R., and Sen, G., 2004, Pre-eruption history of the Grande Ronde Formation lavas, Columbia River Basalt Group, American Northwest: Evidence from phenocrysts: Geology, v. 32, no. 4, p. 293-296.

Eagar, K.C., Fouch, M.J., and James, D.E., 2010, Receiver function imaging of upper mantle complexity beneath the Pacific Northwest, United States: Earth and Planetary Science Letters, v. 297, no. 1, p. 141-153.

Eagar, K.C., Fouch, M.J., James, D.E., and Carlson, R.W., 2011, Crustal structure beneath the High Lava Plains of eastern Oregon and surrounding regions from receiver function analysis: Journal of Geophysical Research: Solid Earth, v. 116 no. B2.

Elkins-Tanton, L.T., 2005, Continental magmatism caused by lithospheric delamination: Geological Society of America Special Papers, v. 388, p. 449-462.

Fowler, S.J., Bohrson, W.A., and Spera, F.J., 2004, Magmatic evolution of the Skye igneous centre, western Scotland: modeling of assimilation, recharge and fractional crystallization: Journal of Petrology, v. 45, p. 2481-2505.

Garfunkel, Z., 2008, Formation of continental flood volcanism - the perspective of setting of melting: Lithos, v. 100, no. 1-4, p. 49-65.

GEOROC Database – Geochemistry of Rocks of the Oceans and Continents, Accessed July, 2016, http://georoc.mpch-mainz.gwdg.de/georoc/.

Graham, D.W., Reid, M.R., Jordan, B.T., Grunder, A.L., Leeman, W.P., and Lupton, J.E., 2009, Mantle source provinces beneath the Northwestern USA delimited by helium isotopes in young basalts: Journal of Volcanology and Geothermal Research, v. 188, no. 1-3, p. 128-140.

Gunn, B.M., and Watkins, N.D., 1970, Geochemistry of the Steens Mountain Basalts, Oregon: Geological Society of America Bulletin, v. 81, p. 1497-1516.

Hawkesworth, C., Kelley, S., Turner, S., le Roex, A., and Storey, B., 1999, Mantle processes during Gondwana break-up and dispersal: Journal of African Earth Sciences, v. 28, no. 1, p. 239-261.

Heinonen, J.S., Carlson, R.W., and Luttinen, A.V., 2010, Isotopic (Sr, Nd, Pb, and Os) composition of highly magnesian dikes of Vestfjella, western Dronning Maud Land, Antarctica: A key to the origins of the Jurassic Karoo large igneous province?: Chemical Geology, v. 277, p. 227-244.

Heinonen, J.S., Luttinen, A.V., Riley, T.R., and Michallik, R.M., 2013, Mixed pyroxenite-peridotite sources for mafic and ultramafic dikes from the Antarctic segment of the Karoo continental flood basalt province: Lithos, v. 177, p. 366-380.

Herzberg, C., and O'Hara, M.J., 2002, Plume-associated ultramafic magmas of phanerozoic age: Journal of Petrology, v. 43, no. 10, p. 1857-1883.

Hofmann, A., 1997, Mantle geochemistry: the message from oceanic volcanism: Nature, v. 385, no. 6613, p. 219-229.

Hooper, P.R., 2000, Chemical discrimination of Columbia River basalt flows: Geochemistry, Geophysics, Geosystems, v. 1, no. 6.

Hooper, P., and Hawkesworth, C., 1993, Isotopic and geochemical constraints on the origin and evolution of the Columbia River Basalt: Journal of Petrology, v. 34, no. 6, p. 1203-1246.

Hooper, P.R., Binger, G.B., and Lees, K.R., 2002, Ages of the Steens and Columbia River flood basalts and their relationship to extension-related calc-alkalic volcanism in eastern Oregon: Geological Society of America Bulletin, v. 114, no. 1, p. 43-50.

Hooper, P.R., Camp, V.E., Reidel, S.P., and Ross, M. E., 2007, The origin of the Columbia River flood basalt province: Plume versus non-plume models: Geological Society of America Special Papers, v. 430, p. 635-668.

Ingle, S., and Coffin, M.F., 2004, Impact origin for the greater Ontong Java Plateau?: Earth and Planetary Science Letters, v. 218, p.123-134.

Jackson, E.D., 1970, The cyclic unit in layered intrusions—a comparison of repetitive stratigraphy in the ultramafic parts of the Stillwater, Muskox, Great Dyke, and Bushveld complexes, in Symposium on the Bushveld Igneous complex and other layered intrusions: Geological Society of South Africa Special Publication 1, p. 391–424.

Jarboe, N.A., Coe, R.S., Renne, P.R., Glen, J.M.G., and Mankinen, E.A., 2008, Quickly erupted volcanic sections of the Steens Basalt, Columbia River Basalt Group: Secular variation, tectonic rotation, and the Steens Mountain reversal: Geochemistry Geophysics Geosystems, v. 9, no. 11.

Jarboe, N.A., Coe, R.S., Renne, P.R., and Glen, J.M.G., 2010, The age of the Steens reversal and the Columbia River Basalt Group: Chemical Geology, v. 274, no. 3-4, p. 158-168.

Johnson, J.A., Hawkesworth, C.J., Hooper, P.R., and Binger, G.B., 1998, Major and trace element analyses of Steens Basalt, southeastern Oregon: U.S. Geological Survey Open File Report 98-482, 26 p.

Kumar, V.K., Chavan, C., Sawant, S., Naga Raju, K., Kanakdande, P., Patode, S., Deshpande, K., Krishnamacharyulu, S.K.G., Vaideswaran, T., and Balaram, V., 2010, Geochemical investigation of a semi-continuous extrusive basaltic section from the Deccan Volcanic Province, India: implications for the mantle and magma chamber processes: Contributions to Mineralogy and Petrology, v. 159, no. 6, p. 839-862.

Larsen, L.M., and Pedersen, A.K., 2000, Processes in high-mg, high-T magmas: Evidence from olivine, chromite and glass in palaeogene picrites from West Greenland: Journal of Petrology, v. 41, no. 7, p. 1071-1098.

Lee, I., and Ripley, E.M., 1996, Mineralogic and Oxygen Isotopic Studies of Open System Magmatic Processes in the South Kawishiwi Intrusion, Spruce Road Area, Duluth Complex, Minnesota: Journal of Petrology, v. 37, p. 1437-1461.

Mahood, G.A., and Benson, T.R., 2017, Using 40 Ar/39 Ar ages of intercalated silicic tuffs to date flood basalts: Precise ages for Steens Basalt Member of the Columbia River Basalt Group: Earth and Planetary Science Letters, v. 459, p. 340-351.

Mankinen, E.A., Larson, E.E., Gromme, C.S., Prevot, M., and Coe, R.S., 1987, The Steens Mountain (Oregon) Geomagnetic Polarity Transition: 3. Its regional significance: Journal of Geophysical Research, v. 92, no. B8, p. 8057.

McKenzie, D., 1984, A possible mechanism for epeirogenic uplift: Nature, v. 307, p. 616-618.

Minor, S.A., Rytuba, J.J., Goeldner, C.A., and Tegtmeyer, K.J., 1987a, Geologic map of the Alvord Hot Springs quadrangle, Harney County, Oregon: U.S. Geological Survey Miscellaneous Field Studies Map MF-1916, scale 1:24,000.

Minor, S.A., Rytuba, J.J., Meulen, D.B., Grubensky, M.J., and Tegtmeyer, K.J., 1987b, Geologic map of the Wildhorse Lake quadrangle, Harney County, Oregon: U.S. Geological Survey Miscellaneous Field studies Map MF-1915, scale 1:24,000.

Moore, N.E., Grunder, A.L. and Bohrson, W.A., in press 2018, The three-stage petrochemical evolution of the Steens Basalt compared to large igneous provinces and layered mafic intrusions: Geosphere.

Naslund, H., 1984, Petrology of the Upper Border Series of the Skaergaard intrusion: Journal of Petrology, v. 25, no. 1, p. 185-212.

Raedeke, L., and McCallum, I., 1984, Investigations in the Stillwater complex: Part II. Petrology and petrogenesis of the ultramafic series: Journal of Petrology, v. 25, no. 2, p. 395-420.

Ramos, F.C., Wolff, J.A., Starkel, W., Eckberg, A., Tollstrup, D.L., and Scott, S., 2013, The changing nature of sources associated with Columbia River flood basalts: Evidence from strontium isotope ratio variations in plagioclase phenocrysts: Geological Society of America Special Paper 497, p. 231-257.

Ramos, F.C., Wolff, J.A., and Tollstrup, D.L., 2005, Sr isotope disequilibrium in Columbia River flood basalts: Evidence for rapid shallow-level open-system processes: Geology, v. 33, no. 6, p. 457-460.

Reidel, S.P., Camp, V.E., Tolan, T.L., and Martin, B.S., 2013, The Columbia River flood basalt province: Stratigraphy, areal extent, volume, and physical volcanology: Geological Society of America Special Papers, v. 497, 1-43.

Richards, M.A., Duncan, R.A., Courtillot, V.E., 1989, Flood basalts and hot-spot tracks: plume heads and tails: Science, v. 246, p.103–107.Rossman, G., 2011, The Chinese feldspar controversy: chronology of research through July 2009: Gems and Gemology, v. 47, no. 1, p. 16-30.

Rytuba, J.J., 1988, Volcanism, extensional tectonics, and epithermal mineralization in the Northern Basin and Range Province, California, Nevada, Oregon, and Idaho: U.S. Geological Survey Circular 1035, p. 59-62.

Self, S., Widdowson, M., Thordarson, T., and Jay, A.E., 2006, Volatile fluxes during flood basalt eruptions and potential effects on the global environment: A Deccan perspective: Earth and Planetary Science Letters, v. 248, no. 1, p. 518-532.

Shervais, J.W., Vetter, S.K., Hanan, B.B., 2006, Mafic layered sill complex beneath the eastern Snake River Plain: evidence from cyclic geochemical variations in basalt: Geology v. 34, no. 5, p. 365-368.

Takahahshi, E., Nakajima, K., and Wright, T.L., 1998, Origin of the Columbia River basalts: melting model of a heterogeneous plume head: Earth and Planetary Science Letters, v. 162, no. 1, p. 63-80.

Thompson, R., Gibson, S., Dickin, A., and Smith, P., 2001, Early Cretaceous basalt and picrite dykes of the southern Etendeka region, NW Namibia: windows into the role of the Tristan mantle plume in Paraná–Etendeka magmatism: Journal of Petrology, v. 42, no. 11, p. 2049-2081.

Thompson, R., Morrison, M., Dickin, A., and Hendry, G., 1983, Continental flood basalts... arachnids rule OK: Continental basalts and mantle xenoliths, p. 158-185.

Turner, S., Hawkesworth, C., Gallagher, K., Stewart, K., Peate, D., and Mantovani, M., 1996, Mantle plumes, flood basalts, and thermal models for melt generation beneath continents: Assessment of a conductive heating model and application to the Parana: Journal of Geophysical Research-Solid Earth, v. 101, no. B5, p. 11503-11518.

Wagner, L., Forsyth, D.W., Fouch, M.J., and James, D.E., 2010, Detailed three-dimensional shear wave velocity structure of the northwestern United States from Rayleigh wave tomography: Earth and Planetary Science Letters, v. 299, no. 3, p. 273-284.

Walker, G.W., MacLeod, N.S., Russell, D., and Earnest, P., 1991, Geologic map of Oregon, Geological Survey.

Whiteside, J.H., Olsen, P.E., Eglinton, T., Brookfield, M.E., and Sambrotto, R.N., 2010, Compound-specific carbon isotopes from Earth's largest flood basalt eruptions directly linked to the end-Triassic mass extinction: Proceedings of the National Academy of Sciences of the United States of America, v. 107, no. 15, p. 6721-6725.

Wolff, J.A., and Ramos, F.C., 2013, Source materials for the main phase of the Columbia River Basalt Group: geochemical evidence and implications for magma storage and transport: Geological Society of America Special Paper 497, p. 273-291.

Wolff, J. A., Ramos, F. C., Hart, G. L., Patterson, J. D., and Brandon, A. D., 2008, Columbia River flood basalts from a centralized crustal magmatic system: Nature Geoscience, v. 1, no. 3, p. 177-180.

CHAPTER 2

The three-stage petrochemical evolution of the Steens Basalt compared to large igneous provinces and layered mafic intrusions

Moore, N.E.[1], Grunder, A.L.[1], and Bohrson, W.A.[2]

[1]College of Earth, Ocean and Atmospheric Sciences, Oregon State University, 104 CEOAS Administration Building, Corvallis, OR 97331

[2]Department of Geological Sciences, 400 E. University Way, Central Washington University, Ellensburg, WA 98926

2.1 ABSTRACT

The Steens Basalt initiated at 17 Ma as the earliest pulse of the Columbia River Flood Basalt. New and existing stratigraphically controlled data reveal temporal changes in lava flow character, and whole-rock and mineral compositions, which we use to evaluate how the balance of magma differentiation processes change in time. Temporal petrochemical variations in the Steens Basalt are analogous to the transition from Imnaha Basalt to Grande Ronde Basalt units of the Columbia River Flood Basalt and have parallels to the temporal evolution of the Deccan and Siberian Traps, as well as to the stratigraphic sequences of the Bushveld and Stillwater layered mafic intrusions. The excellent stratigraphic control from the Steens Basalt provides a detailed record for comparison across this variety of large mafic systems, providing ability to focus on commonalities among differentiation processes in time.

Chemostratigraphic excursions and volcanological characteristics in the Steens Basalt record a three-stage history. A minimally-exposed early stage preserved in the lower A Steens Basalt section is characterized by heterogeneity (3-8 wt.% MgO) collapsing to homogeneity (~5 wt.% MgO), suggesting crystal fractionation outpaces recharge. Sparse weathering horizons indicate some time elapses between eruptions. The second stage, lower B Steens Basalt, is volumetrically dominant and represents waxing of the basaltic pulse. Flows are stacked immediately upon one another without evidence of weathering or intervening sedimentary horizons, indicating high eruptive frequency. Compositions oscillate over a ΔMgO of ~4-5 wt.% between low- and high-MgO basalt, both of which become more magnesian upsection, signaling a period dominated by recharge. This stage closes with declining oscillations to produce homogeneous compositions (6-8 wt.% MgO). The waning stage of eruption is represented by the upper Steens Basalt section, where thin intercalated weathering horizons occur especially high in the section. The upper Steens Basalt is characterized by overall declining MgO and increasing incompatible element concentrations confirming the dominance of crystal fractionation accompanied by crustal assimilation. In detail, the upper Steens Basalt initiates with a small stack of heterogeneous flows (5-8 wt.% MgO), followed by a period of relatively homogeneous flows (~6 wt.% MgO) and closes with highly variable basalts

to trachybasaltic andesites. These compositional characteristics coupled with a change in average flow thickness from lower to upper Steens Basalt of <5 m to 5-10 m illustrate a shift to more silicic compositions and higher viscosity upsection.

The chemical changes upsection in other large igneous provinces record similar variations in differentiation processes through time, suggesting that these large volume systems share similar evolutionary histories: the earliest records suggest the magmatic systems are initially more ephemeral and compositionally variable as magma traverses relatively cool crust. With waxing, a transition to regimes of high thermal and mass input results in a stage where recharge outpaces crystal fractionation. Thermal priming of the crust during these events coupled with waning input yields magmas in which fractionation plus crustal assimilation dominates over recharge late in the system; pulses of later stage felsic magmatism in many large mafic provinces are consistent with this evolution. Using layered mafic intrusions as an analog for intrusive, cumulus-dominated residua of voluminous fractionation, as well as oceanic large igneous provinces as an analog for total magma volumes in continental flood basalt regimes, leads to the suggestion that 50-85% of the total magma volume in a flood basalt remains in the crust, effectively remaking the crust in these regions.

2.2 INTRODUCTION

The large igneous provinces (LIP) expressed as continental flood basalts (CFB) signal geologically short-lived, catastrophic events with far-reaching consequences, from lava inundation of fossil landscapes to potential climatic effects and mass extinctions (e.g., Hofmann, 1997; Self et al. 2006; Whiteside et al. 2010). CFB are generally less voluminous and cover smaller areas than oceanic LIP (Fig. 2.1; Coffin and Eldhom, 1994; Coffin et al. 2006). Unlike their oceanic counterparts, CFB are filtered through several tens of kilometers of continental crust prior to eruption. If the melting anomalies that drive both continental and oceanic LIP are comparable, then a substantial amount of magma is sequestered as intrusions during continental flood basalt magmatism. CFB volumes appear to have been generally consistent in time over the past 350 Ma, with most on the order of 1 to 3×10^6 km^3 (Fig. 2.1; Courtillot and Renne, 2003). The

maximum volume, >3 million km^3, is found in the Triassic Siberian Traps (250 Ma), coinciding with initiation of the breakup of Pangaea. The smallest, with an estimated volume of 210,000 km^3, is the Neogene Columbia River Basalt Group (CRBG; ~16.8 to 6 Ma). On the other hand, it has been proposed that the Siletzia-Crescent Terrane (Fig. 2.1) is the oceanic LIP that represents the initiation of the Yellowstone hotspot, and that the CRBG is the resurgence of that plume after the interference by the subducting slab overriding the plume (Coble and Mahood, 2012; Wells et al. 2014). The volume of the unsubducted portion of the Siletzia-Crescent Terrane is $\sim 2.6 \times 10^6$ km^3, on par with most Phanerozoic CFB but far smaller than the great oceanic LIPs of Kerguelen or Ontong Java.

Many decades of work on CFB have set the stage for wrestling with the questions of how mantle-derived floods of basalt impact the crust through which they pass and how melts in equilibrium with the mantle evolve to compositions typical of continental flood basalts. Most CFB provinces include high-Mg primitive lavas, but on the whole, the bulk of CFB have compositions consistent with crustal differentiation from high-Mg melts as indicated by MgO typically less than 8 wt.% and Ni generally less than 200 ppm (e.g., Cox 1980; Thompson et al. 1983; Garfunkel 2008). As a counterpoint, some workers propose that melt from substantially metasomatized mantle sources (e.g., Turner et al. 1996; Hawkesworth et al. 1999) or of eclogite account for dominant CFB compositions (e.g., Takahahshi et al. 1998; Camp and Hanan 2008; Luttinen et al. 2010).

The Columbia River Basalt Group, the youngest and smallest CFB worldwide, covers 210,000 km^2 of the Pacific Northwest (Reidel et al. 2013; Figs. 2.1 and 2.2A). The main eruptive stage spanned from ~17 to ~15.6 Ma, but the waning stage persisted until ca. 6 Ma (Reidel et al. 1989; Baksi, 2013; Barry et al. 2013). The CRBG lavas are dominantly basaltic andesite; the most voluminous formation, the Grande Ronde Basalt, has an average silica content of 54.3 wt.% SiO_2 (n=230; Hooper, 2000), reflective of differentiation processes that affected the basalts as they passed through the crustal filter. This is in contrast to most CFB, which are largely basaltic in composition (Fig. 2.3). The Steens Basalt is not only the oldest member of the CRBG but is also largely basalt (48.5-

52 wt.% SiO_2, Fig. 2.3), and thus links global CFB provinces and the differentiated bulk composition of the CRBG.

Thick sections of broadly conformable lavas of Steens Basalt record a temporal change from basaltic to basaltic andesite composition. The Steens Basalt is informally divided into a lower, more mafic and tholeiitic section that includes the most primitive basalts of the CRBG, and an upper less magnesian, mildly alkalic section more enriched in select incompatible trace elements and more crustal isotopic character (Camp et al. 2013). We explore how the temporal changes in composition reflect variation in dominant magma differentiation processes within the crust (i.e. recharge, fractional crystallization, assimilation). Our focus is how a large basaltic pulse is affected by crustal staging.

Geochemical changes in time are evident in other CFB (cf. Deccan Traps; Beane et al. 1986) as well as other voluminous mafic magmatic systems such as layered mafic intrusions (Raedeke and McCallum, 1984; Yudovskaya et al. 2013). In this paper, we describe the textural and geochemical changes in time during the Steens Basalt eruptive event with emphasis on the lower and most mafic Steens Basalt and compare these changes to those found in the Imnaha and Grande Ronde Basalt formations of the CRBG. We explore the temporal changes in other voluminous mafic provinces with stratigraphically controlled data, including the Deccan and Siberian Traps (CFB) and layered mafic intrusions, comparing them with the Steens Basalt history to show relationships among the nature and evolution of magmatic processes across these various LIP settings. The detailed stratigraphic data available for the Steens Basalt sequence and interpretation of the distinct phases within serves as a baseline for comparative study to these other large mafic systems.

2.3 GEOLOGIC SETTING

The Steens Basalt covers about 53,000 km^2 of SE Oregon with an average thickness of 600 m (Camp et al. 2013) and has reported ages ranging from 16.8 to 16.1 Ma (Camp et al. 2013 and references therein; Mahood and Benson, 2017; all ages from these references calibrated to Fish Canyon Tuff sanidine standard age of 28.201 ± 0.023

Ma of Kuiper et al. 2008), making them broadly coeval with the Imnaha Basalt flows of
the CRBG (Hooper et al. 2002, Fig. 2.2B). Steens Basalt lavas at Steens Mountain
erupted within no more than 300,000 years of the Steens Mountain magnetic reversal,
estimated at 16.7 Ma (Jarboe et al. 2010) and revised to 16.5 Ma (Mahood and Benson,
2017). To the south and east, "Steens-like" (basaltic andesite to andesite) lavas are as
young as 15.1 Ma (Brueseke et al. 2007). The Steens Basalt crops out in a spectacular,
one km-thick sequence of as many as 200 lava flows, most of which are relatively thin
lobes (<5m) within compound pahoehoe flows (after Walker, 1971) with lesser and
thicker (5-10 m) a'a and pahoehoe single flows particularly high in the section (Bondre
and Hart, 2008; Camp et al. 2013). The section is cut by NNE-striking Steens Basalt
dikes exposed along the Steens Mountain escarpment (Minor et al. 1987a, 1987b; Jarboe
et al. 2010; Camp et al. 2013). The Steens Basalt covers an area comparable to the
combined subaerial footprint of Mauna Loa and Kilauea, but at 31,800 km^3, it is only
15% of the 210,000 km^3 estimated total volume of the CRBG (Hooper et al. 2007; Camp
et al. 2013). A prevalent interpretation is that the Steens Basalt is the remnant of a shield
volcano (Mankinen et al. 1987; Rytuba 1988), but Bondre and Hart (2008) attribute the
shield-like morphology to Basin and Range block uplift, modest tilting, and erosion.
Regardless, Steens Mountain is an important volcanic locus because the basalt section
there is thickest, the age record is longest, the compositional range is widest, and dikes
are common. The lower Steens Basalt covers the full areal extent of Steens Basalt lavas,
while the upper Steens Basalt is less widespread, with a minimum estimated footprint of
~33,000 km^2 (Camp et al. 2013). Where both are exposed at Steens Mountain, the upper
Steens Basalt is ~2/3 of the section, making for an upper Steens Basalt volume of
approximately 13,200 km^3, compared to 18,600 km^3 for the lower Steens Basalt.

The Steens Basalt is inferred to have come from a combination of isotopically
defined mantle sources including a depleted mid-ocean ridge-like source (C1 source of
Carlson, 1984; Pacific MORB of Wolff and Ramos, 2013) and an ocean island basalt
(OIB) type component (Imnaha component of Wolff and Ramos, 2013) or a depleted
mantle component that has been contaminated by subducted oceanic sediments (C2 of
Carlson, 1984). Potential crustal contamination in the upper Steens Basalt is based on

elevated $^{87}Sr/^{86}Sr_i$ and enrichment in incompatible elements (Fig. 2.2; Wolff et al. 2008; Wolff and Ramos, 2013).

Under Steens Mountain, the crust is 32-35 km thick, thins to 30 km west under the adjacent High Lava Plains and northern Basin and Range, and thickens to 42 km to the east, coincident with the $^{87}Sr/^{86}Sr_i$ 0.706 line (Fig. 2.2) taken to be the edge of the North America craton (Eagar et al. 2011). Steens Mountain lies just west of the $^{87}Sr/^{86}Sr_i$ 0.704 line. The crust of eastern Oregon is made of accreted Paleozoic to Mesozoic terranes stitched with Mesozoic plutons (Walker et al. 1991). The lower crust is inferred to be mafic and dense with a thin, still denser root, implying substantial intra- and underplating of the crust by mafic magma (Cox and Keller, 2010; Eagar et al. 2010; Wagner et al. 2010). Carlson and Hart (1987) argued that substantial crustal genesis in the region is through gabbroic intraplating, analogous to Shervais et al. (2006) who suggest abundant fractional crystallization in a series of sills left a seismically imaged 10 km layered mafic intrusion in the crust along the Snake River Plain. The mantle under Steens Mountain today is part of a low-velocity upper mantle anomaly that extends under the High Lava and Snake River Plains (Gao et al. 2011; Wagner et al. 2010; Warren et al. 2008).

2.4 ANALYTICAL METHODS

2.4.1 Sampling

A transect of samples was collected at Steens Mountain by Johnson et al. (1998) and has since been defined as the type section of the Steens Formation, or Steens Basalt (Camp et al. 2013). Samples for this study were taken from individually recognized flows and compound flow lobes of greater than 0.5 m where not pervasively altered. Some flows were sampled multiple times where mineral texture variations were evident. We treat each of these samples as separate chemical proxies of the Steens Basalt magmatic system. Between 2013 and 2016, sampling was conducted to replenish samples that were exhausted from original analysis (Johnson et al. 1998) and reanalysis by Wolff et al. (2008). Johnson et al. (1998) originally measured a composite of two sections summing to 982 m, but they acknowledge that a section of flows at the transition was unsampled.

We have added 115 m to the transition (gap at ~800 m on inset Fig. 2.5), but sampling remains incomplete due to poor accessibility. We also sampled additional sections to document lateral variability and to search for the base of the formation. Samples were collected as far north as Willow Creek, as far south as Miners Creek Road, and to the east of Steens Mountain at Mickey Butte (Fig. 2.4). The Wildhorse Canyon section of the lower Steens Basalt occupies a paleovalley and is approximately 400 m thick; at least 25 compound flow lobes and sparse single flows are exposed, of which we sampled 18 of the least altered massive interiors. The Wildhorse Canyon section exposes flows that stratigraphically underlie the base of the previously recognized lower Steens Basalt flows. These lowest Steens Basalt flows in Wildhorse Canyon overlie a flow that appears texturally similar to the pre-Steens andesites (~19 Ma, Minor et al. 1987b). We refer to this newly identified lower Steens Mountain section from Wildhorse Canyon as the lower A Steens Basalt section, and to the original lower Steens Basalt as lower B Steens Basalt. Wherever we subsequently refer only to "lower" Steens, this includes both the A and B sections.

Each of the stratigraphic sections sampled for this study has been correlated to the original transect (Fig. 2.5) by physical correlation, which is based on elevation and location relative to the original transect, and (or) by comparing the variation in chemical patterns with stratigraphy in the original transect. Detailed flow by flow lithological correlations are not possible. The sections physically correlated include the lower A Steens Basalt (Wildhorse Canyon), Miners Cabin Road, Indian Creek, and Kiger Gorge (Figs. 2.4 and 2.5). Lower A Steens Basalt is on strike with the upper Steens Basalt original transect at the head of Wildhorse Canyon, so the stratigraphy was physically correlated by adjusting for elevation difference in the deeper, lower A section. The base of the Miners Cabin Road section is located approximately 20 m above a contact between Steens Basalt and the underlying Pike Creek Formation. The Indian Creek section is on strike with the highest portions of the lower B original transect, so the stratigraphy was correlated for that section based on elevation comparison with the original transect, as with the lower A section. Kiger Gorge was sampled for the MS thesis of Bendaña (2016) at Central Washington University as a collaborative part of this study. The east rim of

Kiger Gorge is on strike with the upper Steens Basalt portion of the original transect, near the summit of Steens Mountain. We took the difference in elevation of the summit sample from the original transect and the high point of the east rim of the Gorge to find the stratigraphic height that would correlate with the original section on the east rim. We then accounted for a 5° dip of the Steens Basalt flows over the 2 km distance from the Kiger Gorge east rim to the west rim, where the section was sampled. By then assigning that stratigraphic height in the section from the east rim to a given elevation on the west rim, we were able to determine a correlating stratigraphic height to each sample in the Kiger Gorge section. All of these sections were also chemically correlated.

The remainder of the sections were correlated with the original transect by comparing compositional changes up section (Mickey Butte, Tuffy Creek, Willow Creek; Figs. 2.4 and 2.5) as physical correlations are impossible due to various fault interactions. The inset of Figure 2.5 shows changes in MgO wt.% with stratigraphic height, color-coded to match each newly sampled section. The patterns match closely with their original transect counterparts; trends of increasing or decreasing MgO match over a similar range of height. We do not expect a perfect correlation given the nature of the Steens lava flows (dominantly compound pahoehoe) and potential paleotopography; nevertheless, the chemical patterns are well matched. This holds true for the majority of other elements, including most of the major elements, Ni, Cr, Cu, Rb, Ba, Sr, Nb, Zr and the REE (not shown). None of the physical or chemical correlations suggest that the lower A Steens Basalt is exposed in any of the sections other than in Wildhorse Canyon. The gaps in the chemical section (inset Fig. 2.5) reflect unsampled regions, mainly owing to inaccessibility, and thus the exact stratigraphic location of transition between lower A, lower B, and upper Steens Basalt is uncertain.

2.4.2 ^{40}Ar-^{39}Ar Dating

We selected sample NMSB55 for ^{40}Ar-^{39}Ar dating as it represents the basal flow from the lower A section and overlies a pre-Steens andesite flow. As this sample is sparsely phyric (<1% plagioclase and olivine), a microcrystalline groundmass separate was analyzed. Hand selected chips were crushed in a disk mill or mortar and pestle, and

then sieved to 150-212 μm. A non-magnetic groundmass fraction was separated and acid leached following the procedure of Koppers et al. (2011). About 20 mg of the least altered material was handpicked for analysis. The sample was then irradiated and analyzed at the TRIGA nuclear reactor and Argon Geochronology Lab at Oregon State University, according to the protocol of Koppers et al. (2011). Irradiation and analytical protocol, all analytical results including total fusion age, normal and inverse isochrons, MSWD, operating conditions, constant values and other metadata are summarized in Supplement 1.

2.4.3 Mineral Compositions

Compositions of olivine, clinopyroxene, plagioclase, Fe–Ti oxides, and chromium spinel were obtained using a Cameca SX-100 at the Electron Microprobe Laboratory, College of Earth, Ocean, and Atmospheric Sciences, Oregon State University. Accelerating voltage was set to 15 kV, with a beam current of 30 nA. Beam diameter was set at 1 μm for all phases except plagioclase, which was analyzed at 5 μm. Peak count times ranged from 10 to 60 seconds depending on the phase and element of interest. Smithsonian microbeam standards were used to calibrate for each mineral phase and multiple points of each standard were analyzed as unknowns to determine analytical error. Table 2.1 reports representative compositions for all mineral phases, and Supplement 2 contains mineral composition data for all phases analyzed from the lower Steens Basalt, as well as calibration standards and error. Mineral phases analyzed from the upper Steens Basalt are reported in the M.S. thesis of Graubard (2016) from Central Washington University.

2.4.4 Major and Trace Element Compositions

Major and trace element analysis was conducted at the P. R. Hooper GeoAnalytical Laboratory at Washington State University (WSU) using a ThermoARL Advant'XP + sequential XRF spectrometer (XRF) and an Agilent 7700 quadrupole inductively coupled plasma mass spectrometer (ICP-MS). Select rock chips from each sample were ground for 2 minutes in a tungsten carbide SPEX Shatterbox grinding mill.

Powders were fused into beads using a 2:1 mix of dry dilithium tetraborate flux to dry rock powder and placed in graphite crucibles, then heated in a 1,000°C furnace for 10 minutes. Beads were re-ground in tungsten carbide for 1 minute, 1 gram of powder was weighed out for ICP-MS analysis, and the remaining powder was re-fused by the above method to ensure sample homogeneity. The resulting bead was used for XRF analysis, and the 1 g aliquot of powder was dissolved and used for ICP-MS analysis. Reproducibility for XRF analyzed elements is less than analytical error (Kelly et al. 2016). Precision for the ICP-MS method is generally 5% (relative standard deviation) for the rare earth elements (REE) and 10% for the remaining trace elements. Analytical procedure, accuracy and precision are described by Johnson et al. (1999) for XRF and by Knaack et al. (1994) for ICP-MS. Table 2.2 reports representative whole-rock major and trace element compositions for all three stages of the Steens Basalt. All XRF and ICP-MS compositional data for the samples obtained for this study, analytical detection limits, and other precision and accuracy details are in Supplement 3.

2.4.5 Weighted Bootstrap Resampling

In order to verify that chemical distinctions between the lower A, lower B, and upper Steens Basalt are statistically significant, the weighted bootstrapping approach was employed, which is a statistical resampling technique. In this approach, values from a data set are randomly sampled to estimate a particular population parameter. In this case, the mean of each element concentration in the whole-rock data set was cast from random subpopulations. The Steens Basalt data were divided into lower A, lower B, and upper sets, with a total of 16, 55, and 60 samples in each, respectively. Only samples with a full suite of major, trace, and REE data were selected, which includes all samples from this study, and the subset of samples from Johnson et al. 1998 that were reanalyzed by Wolff et al. (2008). Samples from dikes were excluded.

The filtered data sets were then used to determine the mean and standard deviation for each element of interest (51 total elements) in each section. Samples were weighted independently in each set to account for some flows that were sampled multiple times (done so to capture within flow heterogeneity), using the following equation:

$$w = 1 - \left(\frac{n_{analyses}}{n_{total}}\right) / \left(\frac{n_{maximum} + 1}{n_{total}}\right)$$

Where $n_{analyses}$ is the number of samples from a given flow, n_{total} is the total number of samples in the section (lower A, lower B, or upper), and $n_{maximum}$ is the number of samples in the largest location (i.e. the most sampled flow in the section). For each data set, the values of each element were randomly sampled 100 times, with replacement of the values after each sampling, to determine a bootstrapped mean and standard deviation. This approach was repeated 50 times, for a total of 50 bootstrapped mean and standard deviation calculations. The bootstrapped mean values compared to values across the data sets and to the true mean of each set. The selected individual data sets, mean calculations and bootstrap results are reported in Supplement 4.

2.5 RESULTS

2.5.1 Ar-Ar Age from Lower A Steens Basalt Section

The lowest Steens Basalt flow in the lower A section (sample NMSB55) gives a weighted plateau age of 16.97 ± 0.06 Ma (2σ) and establishes ~17 Ma as the onset of CRBG volcanism. The weighted plateau age was calculated from 11 contiguous heating steps that contained ~45% of the total ^{39}Ar released (Fig. 2.6). Age calibration was performed using the Fish Canyon Tuff sanidine standard age of 28.201 ± 0.023 Ma (1σ; Kuiper et al. 2008). The overall plateau is generally well behaved, though it does contain some typical early excess and late depleted steps, and isochron regression is within error of the 295.5 atmospheric ^{40}Ar/^{36}Ar value (Supplement 1). This new date is the oldest reported from samples at Steens Mountain, and the oldest high precision Ar-Ar age of the Steens Basalt (see summary of Steens Basalt Ar-Ar ages by Camp et al. 2013, all recalculated to the Fish Canyon sanidine monitor age of 28.201 Ma of Kuiper et al. 2008 and with 2σ analytical errors), but it is within error of a few lower B Steens Basalt flows that are stratigraphically higher (cf. sample JS-5 = 16.84 ± 0.43 Ma, Camp et al. 2013).

2.5.2 Steens Basalt Flow Morphology, Textures and Petrography

The lower B Steens Basalt package is thickest at Steens Mountain and comprises 35-40 mainly compound flow lobes that are relatively thin (usually 0.5-5 m, as also

described in Bondre and Hart, 2008). The upper Steens Basalt includes more single flows and more a'a and is generally thicker than those of the lower Steens (~5-10 m), but not as thick as typical CRBG (~10-100 m, cf. Long and Wood, 1986; Reidel et al. 2013). The Steens Basalt pahoehoe flows were mainly emplaced by inflation processes (Bondre et al. 2004; Bondre and Hart, 2008; Camp et al. 2013), as were the rest of the much thicker CRBG flows (Self et al. 1996; 2014). Flow tops and bases tend to be vesicular, whereas flow cores are largely non-vesicular and massive with crude columnar to blocky jointing. Diktytaxitic textures are common, as is secondary zeolite mineralization resulting in amygdaloidal textures. Weathering horizons are sometimes present at the contacts between flows or lobes and contain accumulations of red, oxidized sediment, likely from chemical weathering of flow or lobe tops. Development of these horizons is moderate in the lower A Steens Basalt, but generally lacking in the lower B Steens Basalt. Weathering horizons become more abundant between flows and lobes in the upper Steens Basalt, particularly in Kiger Gorge, where they are up to a few cm thick and separate almost all of the uppermost flows. Inasmuch as flow or lobe thickness does not vary radically through the section, eruptive frequency is a proxy for effusion rate. The occurrence of weathering horizons early and late, but not in the middle of the section, demonstrates moderate eruptive frequency at the onset of volcanism, followed by high eruptive frequency, returning to modest frequency near the end of Steens Basalt emplacement.

Textures and modal mineralogy in the Steens Basalt lavas are variable and range from sparsely phyric, to olivine phyric, to plagioclase and olivine phyric, to extremely plagioclase phyric (Fig. 2.7). The abundance of phyric lavas is in stark contrast to the voluminous basaltic andesite members of the CRBG (Grande Ronde Basalt), where flows are sparsely phyric (cf. Hooper, 1982; 1984; Reidel et al. 1989; Takahahshi et al. 1998). Textural types vary from lower to upper Steens Basalt (Fig. 2.7). Lower Steens Basalt flows contain multiple olivine phyric flows (Fig. 2.7A), and modal olivine is typically 2-7%; it reaches 15% in rare cases. In the upper Steens Basalt, olivine is scarcer, making up only a few %, and is only found in tandem with other phenocryst phases. Olivine appears as single microphenocrysts to phenocrysts or in glomerophenocrysts where individual crystals range from 0.5-5 mm. Olivine is typically euhedral but commonly has a cracked

appearance. Chromium spinel and melt inclusions are often found in olivine grains. Resorption (as embayments or resorbed cores) is occasionally present in the phenocrysts from flows with the greatest range of Fo content (see Mineral Compositions) and is more common in the upper Steens Basalt. Phenocrystic clinopyroxene is rare in the lower Steens Basalt but becomes more abundant in the upper Steens Basalt; subophitic to ophitic textures are common in the lower part of the section, where clinopyroxene is dominantly an anhedral oikocryst phase. Plagioclase is found in several distinct size populations: groundmass microlites, microphenocrysts, phenocrysts, and megaphenocrysts (Table 2.2). Crystals of all size populations are largely euhedral and frequently contain oxide mineral inclusions as well as melt inclusions. Disequilibrium textures are infrequent in plagioclase from the lower Steens Basalt, but are pervasive in the upper Steens Basalt flows, most commonly as sieve texture. Oxide minerals are common and include magnetite and ilmenite as groundmass phases and as inclusions in plagioclase and clinopyroxene, as well as chromite inclusions in olivine. We have not identified sulfides or apatite in the lower Steens Basalt. Neither zircon nor baddeleyite has been recovered from large samples (M. Coble and S. Burgess, personal communication, 2017).

The Steens Basalt is known for conspicuous giant plagioclase laths (1-5 cm in diameter). Textures in these giant plagioclase basalts (GPB) are variable and include 1) distinctive radial, snowflake-like plagioclase clusters with olivine trapped at spoke apices (aka "daisy stone" of Annells, 1973; Fig. 2.7B), and 2) sandwich-structured glomerocrysts of plagioclase laths with microphenocrystic olivine trapped between laths. The latter often contains phenocrystic olivine grains or glomerocrysts that are isolated from the plagioclase clusters. Textures 1 and 2 are pervasive in the lower Steens Basalt (Fig. 2.7). Another texture of GPB (3) contains single, isolated plagioclase laths with abundant olivine inclusions (Fig. 2.7C, D, and E); this type more commonly occurs in the upper Steens Basalt. The megaphenocrysts and glomerocrysts are typically 1 cm, but as large as 5 cm in diameter. GPB laths, whether in glomerocrysts or as single isolated crystals, are euhedral and make up a few percent to more than 50% of the rock. GPB are also described for the Deccan and Emeishan flood basalt provinces (e.g. Higgins and

Chandrasekharam 2007, Talusani 2012, Cheng et al. 2014, Sheth 2016), attesting to similar magmatic processes across CFB.

On outcrop scale, GPB erode in a grusy, rounded style that makes them recognizable at a distance. In contrast, sparsely phyric or olivine phyric flows crop out in cliffy vertical ledges with crude columnar to blocky jointing and develop prominent talus slopes. In the lower Steens Basalt, GPB form large packages of compound flow lobes, mostly daisy stone lobes that can be tens to nearly 100 m thick, and these large packages are intercalated with olivine phyric flow lobes a few meters thick (Fig. 2.7). Internally, the GPB flows commonly transition abruptly to more crystal poor textures, either nearly aphyric or containing much smaller and less abundant plagioclase phenocrysts (0.5-2 cm), usually as very thin lenses that we interpret as flow tops. In the upper Steens Basalt, GPB packages are restricted to tens of meters thick and are dominantly single isolated megaphenocryst type flows (Fig. 2.7). The GPB flows there are interbedded with flows that lack phenocrysts or contain sparse microphenocrysts of dominantly plagioclase. Textures in the lower A Steens Basalt section are most like those described for lower B Steens Basalt but have some characteristics common to upper Steens Basalt as well. Olivine is slightly less abundant, and plagioclase is more often resorbed than in the rest of the lower Steens Basalt. Single isolated type GPB flows occur in the lower A section more frequently than in the lower B Steens Basalt, but glomerocrystic type GPB flows occur more frequently in the lower A than in the upper Steens Basalt.

2.5.3 Mineral Compositions

New detailed mineral chemistry on the lower Steens Basalt reveals cryptic variations in olivine, clinopyroxene and plagioclase compositions, signaling temporal changes in magmatic conditions (Fig. 2.8, Table 2.1, Supplement 2). These changes up section are analogous to the cryptic layering typical of LMI (see Discussion below) and are also evident in whole-rock composition (see Major and Trace Element Compositions). Forsterite content (Fo) is homogeneous from core to rim of olivine in some flows (e.g. Fo_{79-78}, Fo_{83-80}, Fo_{84-81}), but heterogeneous in others (e.g. Fo_{85-77}, Fo_{84-63}, Fo_{78-60}; Fig. 2.8). Fo range in individual flows does not necessarily correlate with whole-

rock MgO or Mg# (Mg# = 100*[Mg/(Mg+Fe^T)]); two different flows with >10 wt.% MgO and Mg# ~66 have Fo$_{84-67}$ and Fo$_{84-81}$. However, the maximum Fo content in a given flow does correlate with MgO; the higher the whole-rock MgO, the higher the maximum Fo. The majority of olivine grains are normally zoned with respect to MgO. Reverse zoning is rare and generally restricted to trace elements (particularly Ni) but is notable in the flows with the most homogeneous forsterite content. Average core Fo is greatest in the lower B section and is less in the lower A and upper Steens Basalt sections.

Clinopyroxene is dominantly a late stage groundmass phase present as magnesian augite. As with olivine, Mg# can be quite homogeneous in some flows (Mg# 64-67, 62-68), and heterogeneous in others (Mg# 60-78, 61-77; Fig. 2.8). Typically, but not universally, flows with homogenous olivine compositions also have more restricted ranges of Mg# in clinopyroxene (Fig. 2.8).

Plagioclase compositions vary modestly within or between flows; the full range of core compositions is An$_{78-58}$ and of rims is An$_{76-43}$. Megaphenocrysts larger than 1 cm in GPB flows are remarkably homogeneous; the core to rim variation in An content is typically less than 10 and can be as little as 3. The full range of core compositions from all analyzed megaphenocryst grains is An$_{74-57}$. Phenocrysts (less than 1 cm) and microphenocrysts (larger than 0.5 mm) have a slightly larger compositional variation overall; cores have the full range reported above, and rims range from An$_{74-43}$, with a few exceptions that are <An$_{60}$. The An range within individual flows does not correlate with whole-rock Mg# (i.e., flows with both high and low Mg# have similar plagioclase compositional ranges), and the An range of individual flows does not vary significantly with increasing stratigraphic height (Fig. 2.8).

The extent of compositional heterogeneity tends to correlate across all three mineral phases in the lower Steens Basalt. Flows with restricted compositional ranges in mineral phases alternate with flows characterized by crystals with wider compositional ranges (Fig. 2.8). Mineral compositions for the upper Steens Basalt (Graubard, 2016) document a change into that part of the section (Fig. 2.8). Olivine and clinopyroxene become less magnesian and plagioclase ranges to less calcic compositions. The ΔFo or

ΔMg# in olivine and clinopyroxene, respectively, do not change significantly from lower to upper Steens Basalt, but plagioclase composition, measured as ΔAn (Fig. 2.8) becomes more heterogeneous into the upper Steens Basalt.

2.5.4 Thermobarometry

Olivine-liquid thermometry using olivine and whole-rock compositions from the lower Steens Basalt gives a temperature range of 1180-1350°C for equilibrium samples (Putirka, 2008). None of the few olivine grains analyzed from upper Steens Basalt are in equilibrium with their whole-rock compositions. A new clinopyroxene-liquid thermobarometer (Neave and Putirka, 2017) using clinopyroxene and whole-rock compositions yields a temperature range of 1170-1190°C and a pressure range of 3.4 to 5.6 kbar for lower Steens Basalt equilibrium samples. This same thermobarometer gives a temperature of 1126°C and 5 kbar for the one clinopyroxene grain in equilibrium with its whole-rock sample from all analyzed upper Steens Basalt clinopyroxenes. Oxygen fugacity as estimated from equilibrium Fe-Ti oxide pairs using the ILMAT program (LePage, 2003) range from QFM to QFM-1 for lower Steens Basalt. Fe-Ti oxides have not been analyzed from the upper Steens Basalt; however, best-fit MELTS and Magma Chamber simulator modeling (Moore et al. 2015; Bendaña, 2016; Graubard, 2016) consistently suggest this same range of oxygen fugacity is appropriate for the upper Steens Basalt samples. The pressure estimates given above have also been further constrained by MELTS and MCS modeling (Moore et al. 2015; Bendaña, 2016; Graubard, 2016); pressures above 4 kbar require orthopyroxene as a liquidus phase, but orthopyroxene is absent in all Steens Basalt samples. Best-fit models from computational modeling of samples from all phases of the Steens Basalt consistently suggest the pressure range is limited to 1-4 kbar for the magmatic system.

2.5.5 Major and Trace Element Whole-Rock Compositions

New whole-rock major and trace element analyses clarify the chemical distinctions between lower A, lower B, and upper Steens Basalt, with a zig-zagging pattern of generally less magnesian and more incompatible trace element enriched

compositions at the base (lower A Steens Basalt) and the top (upper Steens Basalt) of the section, but more magnesian and incompatible trace element poor flows in the middle (lower B Steens Basalt). These compositional variations, first recognized by a detailed set of whole-rock data from a transect of samples by Gunn and Watson (1970), reflect changes in magma differentiation processes through time as the Steens Basalt evolved. Whole-rock compositions presented here include all samples collected for this study (Table 2.2, Supplement 3) as well as those samples originally reported by Johnson et al. (1998) and reanalyzed by Wolff et al. (2008), as those samples are from the type section of the Steens Basalt and are the basis for the stratigraphic context of all samples for this study. They are the only other existing samples with a full suite of major and trace element chemistry (major, minor, trace and all REE, all conducted by XRF or ICP-MS at WSU). Also presented is whole-rock chemistry from Kiger Gorge, a section in the upper Steens Basalt, from the MS thesis of Bendaña (2016). There is no evidence for cryptic alteration by anoxic waters, as described for the Sentinel Bluffs Member of the Grande Ronde Basalt (Supplement 5; Sawlan, 2017).

The difference in major element composition between the lower and upper Steens Basalt is evident in the total alkalis versus silica diagram (Fig. 2.9). All of the samples plot in or near the field that encompasses the data of Camp et al. (2013), a large set of XRF analyzed samples from multiple sections located across the entire region of Steens Basalt exposure. The majority of the lower B Steens Basalt samples are subalkaline and tholeiitic, whereas the bulk of upper Steens Basalt samples plot just into the alkaline field and are a combination of basalt, trachybasalt and more evolved basaltic trachy-andesite. This mildly alkaline trend is atypical of all other units comprising the CRBG, particularly for the subalkaline Imnaha and Grande Ronde Basalts (as noted by Camp et al. 2013). Lower A Steens Basalt samples straddle the boundary between alkaline and subalkaline fields, and plot mainly as basalt or trachybasalt. Based on CIPW norms, lower Steens Basalts are olivine tholeiites, whereas the upper Steens Basalt is olivine tholeiites and quartz tholeiites; none are nepheline normative. The dikes sampled in the lower Steens Basalt section have compositional affinities mainly with the upper Steens Basalt flows, consistent with the predominant field relationship where dikes cut the lower or upper

Steens Basalt stratigraphy. One dike of lower Steens Basalt affinity cuts the local basement (Pike Creek Formation). Early alkalic and picritic magmatism typical of other CFB (cf. Deccan, Karoo, Paraná/Etendeka) is lacking in the CRBG, although the lower A Steens Basalt contains some flows that are transitional to mildly alkalic.

Diagrams comparing compositional variation with stratigraphic height further emphasize the distinctions between the lower and upper Steens Basalt (Fig. 2.10A). The eruptive record begins with relatively magnesian compositions in the lower A (~6-8 wt.% MgO), with a range in that section from 3-8.5 wt.%. The MgO range increases and reaches concentrations as high as 12 wt.% in the lower B section, and this range is bracketed by two trends, at high and low MgO, towards increasing MgO early in the section, then becoming less systematic higher in the section (blue bars in Fig. 2.10B). While there may be modest olivine accumulation in some flows, those with the highest MgO do not have the highest modal abundances of olivine; one flow with 15% olivine has 9.5 wt.% MgO (NMSB19; see Supplement 3). High in the lower B section, the high MgO range decreases whereas the low range increases (Fig. 2.10B); eruptions then become less magnesian in the upper Steens Basalt (~3-8 wt.%, Fig. 2.10A). Silica range is moderate in the lower A section (~47-52 wt.%), becomes more restricted in the lower B Steens Basalt (~48-51 wt.%), and reaches the highest values and widest range in the upper Steens Basalt (~48-54.5 wt.%). Incompatible elements (e.g. Rb, Ba) behave similarly, in that the values are lowest and the range most restricted in the lower B Steens Basalt. Incompatible elements are initially heterogeneous/variable in the lower A flows but become more homogeneous up section (Fig. 2.10A). The upper Steens Basalt lavas have the highest incompatible trace element values and largest ranges.

Weighted bootstrap analysis confirms the distinctions in compositional types from the lower A, lower B, and upper Steens Basalt. Compared to lower A and upper Steens Basalt, true and bootstrapped mean values of the lower B section are distinct in most major and trace elements presented, with the exception of Al_2O_3 (Fig. 2.11). The lower A section tends to fall either between the lower B and upper Steens Basalt fields (CaO, Na_2O, Sr, Eu/Eu*) or slightly overlap with the upper Steens Basalt (MgO, FeO*, Rb, REE). There is a clear distinction between the REE true means and bootstrapped values

of the lower B and lower A/upper Steens Basalt, but there is overlap between the REE true means and bootstrapped values of lower A and upper Steens Basalt, particularly in the heavy REE (Fig. 2.12). The true means of the lower A and upper Steens Basalt REE data fall in the center of the bootstrapped values for each, respectively. The lower B true mean is much lower and distinct from those of the lower A and upper Steens Basalt and is also on the high end of the bootstrapped values for that group.

Camp et al. (2013) used Ba versus Cr to distinguish between compositional types from the Steens Mountain type section, in order to use these subtypes to categorize a wide range of Steens Basalt samples from across the entire region of exposure. Three subgroups are defined: lower Steens tholeiitic, upper Steens transitional to mildly alkalic, and upper Steens alkalic (Fig. 2.13). Although there is some slight overlap among fields, the data from this study generally correlate with these fields for the lower B and upper Steens Basalt samples. Samples from the lower A section plot in all three fields, though the majority plot in the upper Steens transitional to mildly alkalic field, demonstrating the variable character of these initial basalt pulses.

Previous workers have used P_2O_5 versus TiO_2 to distinguish different flows of the CRBG (Hooper, 1982; 2002; Camp et al. 2003; Reidel et al. 2013), as the flows tend to fall in distinct fields. Camp et al. (2003) noted that the lower B and upper Steens Basalt have two distinct, sub-parallel and slightly overlapping trends (Fig. 2.14). The fields for the Imnaha and Grande Ronde Basalt flows correlate well to samples of lower B and upper Steens Basalt, respectively, and encompass the majority of the data from the Steens Basalt. Lower B Steens Basalt lavas have Imnaha Basalt like character, whereas lower A and upper Steens Basalt flows generally have Grande Ronde Basalt like character with respect to P_2O_5 versus TiO_2. Thus, we interpret lower B and upper Steens Basalt to be chemically similar to the Imnaha and Grande Ronde formations, respectively. However, some samples of the lower A section straddle the boundary of the Imnaha and Grande Ronde Basalt fields, and one sample plots within the Imnaha Basalt field. Thus, lower A Steens Basalt shares characteristics with lower B and upper Steens Basalt as well as Imnaha and Grande Ronde Basalts.

Collectively, these data support previous interpretations that the Steens Basalt divides into distinct sections; lower B and upper Steens Basalts have been previously divided, and in this study we report a new section, lower A, that shares characteristics of lower B and upper Steens Basalts but may be geographically restricted to a paleovalley in the Steens Mountain source region.

2.6 DISCUSSION

Here, we explore temporal changes in voluminous mafic provinces using stratigraphically controlled whole-rock and mineral chemical data, beginning with the Steens Basalt. We compare the Steens Basalt history to those of the Imnaha and Grande Ronde Basalts of the CRBG, and to temporal variations in the Deccan and Siberian Traps. Finally, we compare Steens Basalt chemical patterns to those in layered mafic intrusions (LMI). The emphasis is on early stages of magmatism during which the plumbing is established to support abundant and frequent eruption of mafic lava.

2.6.1 Steens Magmatic Stages

Based on dominant physical and chemical characteristics of each section, the stack of Steens Basalt lavas at Steens Mountain records three distinct stages of magmatism: lower A, lower B and upper Steens Basalts. The first stage, represented by lower A Steens Basalt, we interpret as an early stage of initially heterogeneous and differentiated magma, signaling early fitful magma ascent, storage, and eruption, and culminating in a magma reservoir capable of delivery of relatively homogenous magma (highest flows in the lower A section, Fig. 2.10A). At this stage, we suggest that the initial thermal state of the crust is relatively cool, magmas stall and crystallize; relatively evolved compositions therefore erupt. Modest development of weathering horizons between flows speaks to a slower eruption rate than during eruption of lower B Steens Basalt. Diversity of lava textures (Fig. 2.7) and compositions that overlap the ranges of lower B and upper Steens Basalt sections (Figs. 2.9-2.14) indicate variable degrees of differentiation and diverse processes acting during this early stage. Toward the top of lower A Steens Basalt, lava composition is more homogeneous and suggests that a

magmatic system capable of erupting relatively homogeneous magma compositions has been established.

The lower B Steens Basalt section lacks weathering horizons, indicating a rapid eruption rate during this time. The section is more mafic overall, with highest MgO and lowest incompatible trace element concentrations (Figs. 2.10-2.13) and textures dominated by olivine phyric and glomerocrystic GPB flows (Fig. 2.7). Mineral chemistry varies up section through the entirety of lower Steens Basalt, from flows with chemically homogeneous phases alternating with flows of heterogeneous mineral compositions (Fig. 2.8). The overall compositional pattern trends to more mafic compositions early in the section (increasing MgO at both high and low ends, highlighted by blue bars in Fig. 2.10B), indicating basalt input to the magma system at a rate faster than differentiation, and then a sweep to less mafic compositions, as the rate of basalt recharge compared to fractionation apparently declines. This general pattern up section is overlain by a zig-zag trend between flows from low to high MgO compositions (black lines connecting flows stratigraphically in Fig. 2.10B), where the excursion range averages ~4-6 wt.% MgO between high and low ends. The sweep to higher MgO signals that initially, recharge outpaces fractionation, and then fractionation outpaces recharge higher (Fig. 2.10B) in the lower B section. Gunn and Watkins (1970) and Camp et al. (2013) also concluded that fractionation and recharge were important processes in the generation of the Steens Basalt.

The upper Steens Basalt records a general change to more evolved compositions, albeit with numerous excursions between more and less mafic compositions, signaling a continued but comparatively lesser role of mafic recharge. The lower estimated volume of the upper Steens Basalt, along with development of weathering horizons especially high in the section, support the idea of a waning magma system. A decrease in olivine, an increase in clinopyroxene, and a higher frequency of the single isolated plagioclase phryic type of GPB (Fig. 2.7) further indicate a change in magmatic regime. The slightly larger average flow thickness in the upper Steens Basalt (5-10 m versus <5 m in the lower Steens) likely reflects the increased silica in the upper Steens Basalt (Fig. 2.10), and hence higher viscosity of the magma.

The upper Steens Basalts lie on a tholeiitic differentiation trend dominated by crystal fractionation and lesser recharge, leading to Fe-rich mildly alkaline, and incompatible element enriched compositions (Fig. 2.9; Camp et al. 2013; cf. Streck and Grunder, 2012). There is also evidence for an additional role of crustal assimilation in the upper Steens Basalt demonstrated through energy constrained and Magma Chamber Simulator modeling (Bendaña et al. 2017; Graubard, 2016), incompatible trace element ratios and whole-rock $^{87}Sr/^{86}Sr$ (Camp et al. 2013; Wolff and Ramos, 2013), and Sr isotopic variations in plagioclase (Ramos et al. 2013). Although a subduction component can mimic crustal contamination, the correlation of increasing Sr isotopic ratios with differentiation indices (decreasing MgO and increasing incompatible elements) lead us to agree with these authors that the trends in the upper section are mainly acquired in the crust. The mineral equilibration pressures for lower and upper Steens Basalt are 1-4 kbar, though abundant shallow crustal staging may mask a deeper history.

Mineral composition also lends insight into the changing nature of the Steens Basalt magmatic system. There are systematic variations of mineral composition, such as correlation between flow MgO and highest Fo in olivine consistent with the overall compositional changes in the lavas. On the other hand, the *range* in mineral composition may be wide or restricted regardless of bulk composition. Variability of olivine composition within single flows is greatest in the lower B Steens Basalt and least in the upper Steens Basalt (largest within flow core range in upper Steens Basalt is Fo_{76-68}, though most flows have cores that vary less than 1 Fo unit; Graubard, 2016). We interpret the variability in the lower B stage to reflect the high rate of recharge, where more primitive basalt repeatedly mixes into resident magma, disturbing the crystallization of equilibrium assemblages. The eruption rate outpaces magma equilibration, leading to more heterogeneous crystal populations. In contrast, during eruption of the upper Steens Basalt, magma has time to equilibrate and is less frequently disturbed by mixing in of recharged magma.

Within each of these stages in the Steens Basalt, a "perched" magma system is established, whereby the system evolves to a characteristic composition after perturbations by recharge, mixing, and/or assimilation. In the lower A section, the magma

perches at ~5 wt.% MgO high in the section, after a period that produces heterogeneity where compositions range from 3 to 8 wt.% MgO (Fig. 2.10A). In lavas of the lower B section up to 600 m, MgO oscillates between low and high values (ΔMgO = 4-5 wt.%), and each "endmember" becomes more magnesian upsection (blue bars in Fig. 2.10B). Excursions to lower MgO suggest that olivine fractionation outpaces recharge, whereas excursions to higher MgO signal episodes of recharge. The system at this stage is dominated by recharge, based on the overall increase in MgO for compositions on both ends of the oscillation. Interestingly, the lower MgO, fractionated lavas are more common, suggesting they are from a more readily tapped, possibly shallower reservoir. In lower B above ~600 m, the range in oscillation declines up section, converging to a narrow range (ΔMgO = ~2 wt.%). In the upper Steens Basalt, compositions are generally less magnesian. Early moderate heterogeneity in MgO is followed by more restricted compositions (950 to 1050 m), followed again by moderate heterogeneity (ΔMgO = ~4 wt.%). The least mafic end decreases to ~3 wt.% MgO, implying an increased role for crystal fractionation and/or assimilation of wall rock; the latter we propose was facilitated by thermal priming of the crust during earlier stages. An increased role for assimilation/fractional crystallization and less input from recharge is supported by upper Steens Basalt flows having the highest concentrations of incompatible trace elements (Figs. 2.10-2.13).

In order to compare the temporal evolution between various CFB and the Steens Basalt, we draw on temporal changes in geochemical data from the CRBG, Deccan Traps, and Siberian Traps, as well as from layered mafic intrusions (LMI; Fig. 2.15 and 2.16). The objective is to compare within suite variation across provinces. The purpose is not to distinguish mantle sources amongst LIP, but rather to tease out commonalities in differentiation processes in time.

Detailed chemostratigraphic comparisons are readily available for LMI; the characteristic layering in these suites has encouraged many workers to study mineral composition, modal and phase changes with stratigraphy. On the other hand, for many CFB, samples are grouped by geochemical magma types rather than stratigraphically.

Because flow-by-flow stratigraphic reconstructions are rare, the following comparisons to other CFB are generalized.

2.6.2 Comparison to Other Large Mafic Systems – Columbia River Basalt Group

Bryan et al. (2010) describe four endmember types of CFB magma petrogenesis, two of which are manifested by large volume basaltic eruptions: type A, which is dominated by olivine phyric lavas with primitive mantle chemical signatures and essentially no crustal staging or contamination; and type B, which has a chemical signature reflective of crustal staging, fractional crystallization and mixing, and assimilation at various levels within the crust. The Steens Basalt, and the CRBG as a whole, represents the type B endmember, having compositions that range from primitive basalts to more evolved basaltic andesites and signatures that suggest a range of differentiation processes modified the lavas.

Textural and geochemical changes with stratigraphy have also been noted for the Imnaha and Grande Ronde Basalt flows of the CRBG (Wolff and Ramos, 2013). The Imnaha Basalt is coeval with the upper Steens Basalt flows and erupted a total volume of 11,000 km^3 (Reidel et al. 2013), whereas the Grande Ronde Basalt erupted a total volume of 150,400 km^3 (Reidel and Tolan, 2013) after the cessation of Steens Basalt volcanism. Dikes related to the Imnaha Basalt and the Grande Ronde Basalt flows erupted from the Chief Joseph Swarm north of the Steens Basalt dike locus and are more proximal to the North American Craton (Fig. 2.2). Imnaha and Grande Ronde Basalt flows are significantly thicker than the Steens Basalt flows and lobes, with an average of ~30 m, but up to ~100 m (Hooper et al. 1984; Reidel and Tolan, 2013). The maximum total thickness of these units is ~3 km, occurring in the Pasco Basin of Washington; the average total thickness is ~1 km (Reidel and Tolan, 2013; Reidel et al. 2013). Imnaha flows are medium- to coarse grained, with sparse olivine or clinopyroxene phenocrysts, and commonly plagioclase-phyric, including many GPB flows (Hooper et al. 1984; Hooper, 1988). The Grande Ronde flows range from virtually aphyric to sparsely phyric to microphyric, with a groundmass of plagioclase and clinopyroxene (Reidel and Tolan, 2013 and references therein). Imnaha Basalt compositions are comparable to the lower

Steens Basalt, although the Imnaha Basalt is generally less primitive than the lower B Steens Basalt (cf. lower Mg# range, Fig. 2.15). The Imnaha Basalt is divided into two chemical types by Hooper et al. (1984); the lower American Bar flows with slightly more evolved compositions (average SiO_2 = 51.5 wt.%, average MgO = 4.8 wt.%, and average Mg# 39), and the upper Rock Creek flows with slightly more mafic compositions (average SiO_2 = 49.7 wt.%, average MgO = 5.5 wt.%, and average Mg# 44). This strengthens similarity to lower Steens Basalt, with a lower subunit (lower A Steens Basalt and American Bar) extending to more evolved compositions below a more mafic sequence (lower B Steens Basalt and Rock Creek). As not all Imanha Basalt data are categorized as either America Bar or Rock Creek types, we do not distinguish these in Figure 2.15. Grande Ronde Basalt compositions overlap with the upper Steens Basalt (Figs. 2.14 and 2.15), but are even more strongly differentiated, as the Grande Ronde Basalt compositions are almost exclusively basaltic andesite. Grande Ronde Basalt follows a subalkaline trend on a TAS diagram (Hooper et al. 2002; Camp et al. 2013) as opposed to the slightly alkaline trend of upper Steens Basalt; significant crustal contamination, as proposed for the Grande Ronde Basalt (Camp et al. 2013; Wolff and Ramos, 2013; Ramos et al. 2013), would drive differentiation to calc-alkalinity (Grove et al. 2003; Streck and Grunder, 2012).

The changes up section from Imnaha to Grande Ronde Basalts are analogous to the Steens Basalt stratigraphic evolution in that fractionation and a stronger contribution of crustal contamination are likely responsible for the shift in composition between the basaltic Imnaha and the more evolved Grande Ronde flows, particularly given the availability of the cratonic crust as a potential contaminant for the Grande Ronde Basalt (Carlson et al. 1981; Carlson, 1984; Wolff et al. 2008; Wolff and Ramos, 2013). This is evident in the lower range of Mg#, coupled with generally higher and more variable Ba/Ta and La/Sm$_N$ in the upper Steens and Grande Ronde Basalts compared with their counterparts, the lower B and Imnaha Basalt, respectively (Fig. 2.15). Effectively, we suggest that part of the differentiation cycle of the Steens Basalt is repeated in a more northerly location. The Imnaha and Grande Ronde Basalt flows ascended and erupted through different basement rocks, and the mantle source ascribed to the Imnaha and

Grande Ronde Basalts is less depleted (Carlson et al. 1981; Carlson, 1984; Wolff et al. 2008; Wolff and Ramos, 2013). Nevertheless, a similar within suite chemical pattern emerges, where the early phase of mafic activity is dominated by recharge without crustal contamination (Imnaha Basalt). This phase is the staging of the mafic magmatic system in the crust, which heats the crust and leads to crustal contamination of subsequent basalts (Grande Ronde Basalt).

Eruptive flux makes for an important distinction between the Steens Basalt and the Imnaha-Grande Ronde Basalt events. The recharge-dominated, lower B Steens Basalt corresponds to the time of maximum eruption rate and largest erupted volume. In contrast, the mafic recharge dominated Imnaha Basalt stage produced flows far less voluminous than the overlying Grande Ronde Basalt (~1:14 Imnaha to Grande Ronde, compared to ~1.5:1 for lower to upper Steens Basalt). We attribute the difference to persistence of basaltic input as well crustal modulation. Together, Imnaha and Grande Ronde volcanism lasted from ~600,000 yr to as long as 1 Myr (Baksi, 2013; Barry et al. 2013), or two to three times the span of the Steens Basalt event. In the Steens Basalt scenario, the initial CRBG pulse impinges on a cold and somewhat refractory crust of accreted oceanic terranes. The mantle input persists long enough to establish a shallow magma reservoir through abundant and rapid basaltic recharge, as evidenced by lower B Steens Basalt compositions. As the mantle flux moves northward (e.g. Camp and Ross, 2004; Jordan et al. 2004; Wolff and Ramos, 2013), eruption rate wanes and produces the fractionation dominated upper Steens Basalt phase, with crustal assimilation owing to thermal priming of a relatively refractory crust. Concurrently, a new locus is established where extensive basaltic injection and recharge produces the Imnaha Basalt, which is similar in volume to lower Steens Basalt (11,000 and 18,600 km^3, respectively). Persistent basalt flux from the mantle heats the more fertile craton-margin crust, which induces crustal assimilation and produces the voluminous Grande Ronde Basalt. High mass rates of assimilation, greatly exceeding crystallization, can be sustained as wet, alkalic partial melts of the crust are added to basalt and lower the liquidus (Reiners et al. 1995), producing crystal-poor basaltic andesite magmas. Although recharge persists, the chemical signature is integrated with crustal assimilation and fractionation processes

during the growth of large magma reservoirs capable of erupting the vast volumes of individual Grande Ronde Basalts (flows up to 10,000 km^3; Reidel and Tolan, 2013).

Regional rhyolite volcanism associated with the CRBG has been recently recognized (Coble and Mahood, 2012; Benson and Mahood, 2016; Benson et al. 2017; Streck et al. 2015; 2016). It begins after the earliest Steens Basalt eruptions (16.69 Ma near McDermitt Caldera; Henry et al. 2017) and continues until at least 15 Ma. This suggests an important role for crustal staging and assimilation in the CRBG. Felsic magmatism is also associated with other CFB, including the Deccan Traps and the Paraná/Etendeka Traps (Lightfoot et al. 1987; Peate, 1997). Rhyolites of the Rooiberg Volcanics are associated with the Bushveld LMI (Twist and French, 1983).

2.6.3 Comparison to Other Large Mafic Systems - Deccan Traps

Other CFB also display systematic variations in time (Fig. 2.15). The Deccan Traps in India, a CFB that was erupted from ~66.5 to 65.5 Ma (Renne et al. 2015), have an estimated original volume of 2×10^6 km^3 (Cortillot and Renne, 2003) and a maximum total thickness of 3.6 km (Richards et al. 2015). The Deccan chemostratigraphy is best established for the Western Ghats region, which is divided into 3 major subgroups: the Kalsubai, Lonavala, and Wai (oldest to youngest). Each subgroup is divided into several formations (Beane et al., 1986; Subbarao and Hooper, 1988). Though the Deccan is dominantly composed of aphyric to sparsely phyric flows of olivine +/- clinopyroxene+/- plagioclase (Beane et al. 1986), GPB are abundant in the Kalsubai; they appear at intervals and define the tops of each individual formation in that subgroup (Beane et al. 1986; Higgins and Chandrasekharm, 2007; Sheth, 2016). Picrites appear throughout the section but are most common in the Kalsubai (Beane et al. 1986). The Deccan Traps share some chemostratigraphic characteristics with the Steens Basalt.

Deccan Trap analogs to Steens Basalt are most evident when considering bulk whole-rock compositional changes in stratigraphy. A decrease in maximum and mean Mg# occurs from the Kalsubai to the Lonavala subgroups, but then maximum Mg# stays consistent from the Lonavala into the Wai subgroup, albeit with a larger overall range in the Wai subgroup (Fig. 2.15). Ba/Ta and La/Sm$_N$ increase in their maximum values,

mean values and ranges from the Kalsubai to the Lonavala, but then decrease in maximum, mean and range into the Wai (Fig. 2.15). This is distinct from the Steens Basalt in that the highest maximum, mean and range for these trace elements are found high in the section, in the upper Steens Basalt (Fig. 2.15). Deccan whole-rock compositional changes up section between the Kalsubai and Lonavala are similar to the transitions between lower B-upper Steens Basalt and Imnaha-Grande Ronde Basalt (red arrows, Fig. 2.15). Much like the lower B Steens Basalt, we suggest the initial heterogeneity and more mafic compositions in the Kalsubai can be explained by a combination of alternating fractionation and recharge, where recharge generally outpaces fractionation. As with the upper Steens Basalt, we suggest that the Lonavala whole-rock compositional characteristics can be explained by fractionation punctuated by periods of magma equilibration with increasing contributions from the crust. The apparent lack of an equivalent of a lower A Steens Basalt section in the Deccan stratigraphy could be because the necessary stratigraphic detail is not sufficiently exposed or has not been sampled. Regardless, the importance of the comparison to the Steens Basalt lies in the suggestion that there is an early, more mafic, recharge-dominated stage during which the system becomes well established in the crust, followed by a period of eruption of more evolved lavas that reflect fractionation and crustal assimilation overprinting mafic recharge.

The Steens Basalt whole-rock compositional analog does not extend to the Wai Subgroup. The return to a more tholeiitic nature in this latest Deccan subgroup (Fig. 2.15; more homogeneous and lower incompatible trace element ratios but similar Mg# range as Lonavala) is distinctive from the shift to a more evolved nature in the latest stages of the Steens Basalt. This likely reflects some fundamental difference in the generation of the final and largest Deccan subgroup. Recent estimates suggest that the Wai represents ~70% of the total volume of the Deccan (Richards et al. 2015). The large volumes in the Wai were fed mainly by inflated sheet flows, in contrast to the dominance of compound pahoehoe flows and rare a'a flows in the Kalsubai and Lonavala subgroups (Bondre et al. 2004, Brown et al. 2011). In this way, the Wai is similar to the most voluminous Grande Ronde phase of the CRBG that also contains enormous inflated flows. The increased

volume in the Wai compared to earlier subgroups implies an increase in magmatic flux in this latest stage of Deccan Traps eruptions. Recent models suggest a difference in the process generating the Wai Subgroup compared to its earlier counterparts (Renne et al. 2015; Richards et al. 2015).

2.6.4 Comparison to Other Large Mafic Systems - Siberian Traps

The great Siberian Traps (Fig. 2.1) may contain a three stage petrogenetic evolution similar to the Steens Basalt, albeit manifested at a grand scale (estimated original volume $>3 \times 10^6$ km^3; Courtillot and Renne, 2003). This CFB erupted between ~252 and 248 Ma (Reichow et al. 2009), but the bulk may have erupted in less than 1 Myr (Burgess and Bowring, 2015; Burgess et al. 2017). The thickest and most voluminous section is found in the Noril'sk region, where individual, mainly simple flows range in thickness from 1 to 100 m. Textures are aphyric to glomeroporphyritic and the mineral assemblage includes plagioclase +/- clinopyroxene +/- olivine. Plagioclase dominates the phenocrystic and glomerophenocrystic lavas, comprising typically 5-10% but rarely up to 20-30% of the volume. Olivine is found most abundantly in picrites, which occur mainly in some of the early formations (Gudchika through Nadezhdinsky, Fig. 2.15; Fedorenko et al. 1996).

Whole-rock compositional data (Fig. 2.15) for the 11 formations of the Noril'sk region show a similar up section trend (Sharma, 1997). The base formation is evolved, with average Mg# 37 and relatively low La/Sm$_N$. The next 4 formations become more mafic (blue arrows, gray shaded region in Fig. 2.15) and oscillate between an average Mg# of 52-65 with a corresponding overall decrease in average La/Sm$_N$. The final 6 formations become slightly more evolved and relatively homogeneous (red arrows, Fig. 2.15). After a transitional stage, represented by the Nadezhdinsky Formation, this section has a range of average Mg# from 48-51, and becomes restricted in average Ba/Ta and La/Sm$_N$ ranges as well. Based on these limited geochemical comparisons, the base formation might represent the first variable pulses of magma with initially heterogeneous and differentiated compositions, similar to lower A Steens. The more mafic formations immediately up section (Syverma through Tuklon, Fig. 2.15) record a recharge dominant

phase, where production of the most mafic lavas occurs due to recharge outpacing fractionation. The oscillations between high and low Mg# "endmembers" among those 4 formations are similar to the within phase oscillations of MgO in the lower B Steens Basalt. Finally, the uppermost and thickest sequence of slightly more evolved formations represents the fractionation and crustal contamination dominated stage that occurs once the system is well established and becomes capable of delivering relatively homogeneous compositions.

2.6.5 Summary of Comparisons to other CFB

The broad comparisons we have made between the Steens Basalt and other CFB suggest that there are comparable petrogenetic phases in these systems, although each province has unique characteristics as well. There is evidence in each, regardless of overall volume, for an earlier recharge dominant stage that produces the most mafic compositions (gray shaded regions in Fig. 2.15) during the waxing pulse of magmatic flux. This is generally followed by a period during which more evolved compositions erupt, once the system is well established (transitions indicated by red arrows, Fig. 2.15). This period of evolved magmatism can be due to fractionation outpacing recharge, abundant crustal assimilation, or both, depending on the persistence and intensity of continued heat input. This general correlation is further supported by the stratigraphic change in MgO of the Mamainse Point Formation from the Keweenawan Flood Basalt Province, where MgO maximum and range are highest early in the section, then decrease and become more homogeneous up section (Klewin and Berg, 1991). Though a range of volumes is represented by the CFB presented here (Fig. 2.1), it appears that a similar evolution of dominant crustal processes occurs in time over the life of CFB provinces.

2.6.6 Comparison to Other Large Mafic Systems – Layered Mafic Intrusions

Layered mafic intrusions (LMI) are complementary to CFB and LIP in that they represent the crystallized and cumulate residua that remains in the crust after fractionation of voluminous mafic magmatism. They have a lower olivine-dominated, layered peridotite section (cf. Stillwater, Bushveld) that is interpreted as evidence of an

early stage of frequent mafic recharge (Wager and Brown, 1967; McBirney and Noyes, 1979; Raedeke and McCallum, 1984). These ultramafic sections are overlain by a plagioclase phyric dominant volume, typically recognized mainly as products of abundant and prolonged fractionation (Wager and Brown, 1967; McCallum et al. 1980; Eales et al. 1986). The Bushveld and Stillwater LMI also contain fine grained dikes, sills and marginal group rocks of norite, gabbro and gabbronorite thought to represent the earliest pulses of magmatism, predating the layered series. These earliest pulses may be analogous to the lower A Steens Basalt and earliest Imnaha Basalt (American Bar) in that they include evolved compositions. Stillwater sills and dikes range from 45.8-51.7 wt. % SiO_2 and 4.1-14.0 wt.% MgO (Helz, 1985) and the Bushveld range from 48.1-57.0 wt. % SiO_2 and 6.8-14.1 wt. % MgO (Wager and Brown, 1967; Barnes et al. 2010), bearing in mind that parental liquid compositions of LMI are more magnesian at given SiO_2 than Phanerozoic flood basalts. The olivine phyric, ultramafic portions of the Bushveld and Stillwater LMI represent ~1/4 to 1/5 of the total thickness (Wager and Brown, 1967; McCallum et al. 1980; Raedeke and McCallum, 1984); this is comparable to the ~1/3 proportion of lower B to upper Steens Basalt. Pressure estimates of crystallization for the Stillwater and Bushveld are restricted to shallow regimes, in the range of 1.5 to 3 kbar (Cawthorn and Davies, 1983; Helz, 1995), comparable to the 1-4 kbar pressure estimates for the Steens Basalt (see thermobarometry).

A characteristic of major LMI are the zig zag patterns in cryptic layering, such as Fo and Ni in olivine, taken to reflect recharge events (Wager and Brown, 1967; McBirney and Noyes, 1979). We compare changes in Fo content and nickel in olivine up section through the lower Steens Basalt (A and B), the Stillwater Ultramafic Series (Raedeke and McCallum, 1984), and the Bushveld Lower Zone (Yudovskaya et al. 2013) in Figure 2.16. Excursions in Fo content through the lower Steens Basalt are much more pronounced (Fo average range: 82-62) than in the Stillwater (Fo range: 84-78) or Bushveld (Fo average range: 92-80) olivine phyric zones. Olivine Ni excursions in the lower Steens Basalt mirror the excursions in average Fo content, and similar excursions can be seen in the Ni content of olivine in the two LMI; that is, from one stratigraphic unit to the next, dramatic changes in Ni are observed. Olivine Ni characteristics are

similar in the lower Steens Basalt and Bushveld: the full range of Ni is similar (2500-500 ppm and 2700-600 ppm respectively), as is the magnitude of the excursions, or the overall change from one stratigraphic height (lava flow or cumulus layer) to the next, viz., a maximum of about 1500 ppm in both (Fig. 2.16). These large fluctuations in mineral composition, particularly in Ni content in olivine, record alternating recharge and fractionation processes up section, where the excursions to high Fo or Ni signal periods where recharge outpaces fractionation.

The comparisons we make between phases of the CRBG are mirrored in the LMI. The most striking commonality is the shallow staging of voluminous basaltic melt with a most mafic recharge dominated phase of activity that heralds the dominant volume. The ultramafic portions of LMI represent this recharge dominant stage. When recharge becomes subordinate to fractionation and the crust is thermally primed, a more evolved stage produces the plagioclase phyric dominant volume of LMI. The large volumes of cumulates generated by extensive crystal fractionation over the life of these voluminous basaltic events remakes the crust by mafic intraplating.

Attempts to quantify the intrusive to extrusive proportions for either LMI, CFB and oceanic LIP are few, but comparisons may illuminate fundamental crustal processes. Cawthorn and Walraven (1998) estimate the Bushveld Complex volume at $3.7 - 6.0 \times 10^5$ km^3 and use this estimate in a thermal cooling and crystallization model to determine the volumes of magma erupted. They arrive at a total magma volume of $7.4 \times 10^5 - 1.2 \times 10^6$ km^3, suggesting the intrusive:extrusive ratio is ~1:1, which seems a lower limit. In contrast, for the Ontong Java Plateau, which is an oceanic LIP, an intrusive:extrusive ratio of ~6:1 is implied by estimates of extrusive and total volume (6×10^6 km^3 and 4.44×10^7 km^3, respectively; Cortillot and Renne, 2003). These I:E ratios suggest that ~50%-85% of the volume of the basaltic pulse of LIP remains behind in the crust. Inasmuch as CFB intersect a lower density crust, the intrusive proportion could be even greater, perhaps explaining why Phanerozoic CFB are typically ~10 times less voluminous than their oceanic counterparts (Fig. 2.1). It is important to quantify intrusive volumes in CFB to determine if mantle flux is similar in both continental and oceanic LIP. The large potential intrusive volume for these settings would not only render the crust more mafic

but may require delamination of deep ultramafic cumulates to maintain a crustal mass balance. Future work will serve to quantify the intrusive to extrusive ratios for the Steens Basalt by estimating volumes of cumulates left in the crust through mass and energy constrained computational modeling using appropriate parental melt compositions.

2.7 CONCLUSIONS

The stratigraphic compositional changes of the Steens Basalt record the thermal waxing and waning of a major pulse of basalt interacting with the crust. The intensity of the thermal input of this event is indirectly recorded in the volume of basalt erupted. The earliest stage of the Steens Basalt (lower A) is dominated by low volume magma flux and fractionation, but the latter part of that stage becomes more homogenous and represents the onset of the early waxing stage of voluminous magma generation. This initial stage gives way to one of rapid magma input and frequent eruption (lower B Steens Basalt), leading to an increasingly mafic magma system dominated by basaltic recharge that outpaces differentiation and contributes to substantial warming of the crust. Differentiation begins to outpace recharge towards the end of the lower B Steens Basalt stage, signaling initiation of the waning period. Now well established, the magmatic system becomes more evolved during the upper Steens Basalt stage, with more time between eruptions and more differentiated compositions indicating reduced basaltic recharge. Crustal assimilation becomes more abundant as the crust is thermally primed; pulses of accompanying felsic magmatism are consistent with a dominant role for crystallization and crustal assimilation. Within each of these stages of the Steens Basalt, a "perched" magma system is established, whereby the system continually evolves to an equilibrium state after perturbations to the system in the form of recharge, mixing, and/or assimilation. As CRBG magmatism migrates north, a comparable pulse of magmatism occurs, represented by the Imnaha and Grande Ronde Basalts.

Chemostratigraphic changes comparable to the Steens Basalt and CRBG are evident in the Deccan Traps, Siberian Traps, and in the Bushveld and Stillwater LMI. Each likely records an early stage of recharge dominance over fractionation, and a later stage of fractionation coupled with crustal melting and assimilation. Few published

studies of CFB provide the detailed stratigraphic control presented here for the Steens Basalt. The generalized comparisons we make to other CFB are a first step toward identifying similarities in petrogenetic evolution among these mafic systems. If oceanic LIP volumes are equivalent to the entire intrusive/extrusive volume of CFB, and LMI roughly represent the intrusive counterparts to CFB remaining in the crust, the proportions suggest that at least 50%-85% of the magma volumes at CFB remain in the crust, effectively remaking the crust of these regions into mafic compositions.

2.8 ACKNOWLEDGEMENTS

2.9 REFERENCES CITED

Annells, R.N., 1973, Proterozoic Flood Basalts of Eastern Lake Superior: the Keweenawan Volcanic Rocks of the Mamainse Point Area, Ontario; Geological Survey of Canada, Paper 72-10, 51 pp.

Baksi, A.K., 2013, Timing and duration of volcanism in the Columbia River Basalt Group: A review of existing radiometric data and new constraints on the age of the Steens through Wanapum Basalt extrusion: Geological Society of America Special Papers, v. 497, p. 67-85.

Barnes, S.J., Maier, W.D., and Curl, E.A., 2010, Composition of the marginal rocks and sills of the Rustenburg Layered Suite, Bushveld Complex, South Africa: implications for the formation of the platinum-group element deposits, Economic Geology, v. 105, p. 1491-1511.

Barry, T.L., Kelley, S.P., Reidel, S.P., Camp, V.E., Self, S., Jarboe, N.A., Duncan, R.A., and Renne, P.R., 2013, Eruption chronology of the Columbia River Basalt Group: Geological Society of America Special Papers, v. 497, p. 45-66.

Beane, J.E., Turner, C.A., Hooper, P.R., Subbarao, K.V., and Walsh, J.N., 1986, Stratigraphy, composition and form of the Deccan basalts, Western Ghats, India: Bulletin of Volcanology, v. 48, p. 61-83.

Bendaña, S.J., 2016, Documenting mantle and crustal contributions to flood basalt magmatism via computational modeling of the Steens Basalt, southeast Oregon [M.S. Thesis]: Central Washington University, 183 p.

Bendaña, S., Bohrson, W.A., Graubard, M.A., Moore, N.E., and Grunder, A.L., 2017, Quantification of Mantle vs. Crustal Contributions to the Steens Flood Basalt Magmatic System, IAVCEI Scientific Assembly, Abstract ME23C-070.

Benson, T.R., and Mahood, G.A., 2016, Geology of the Mid-Miocene Rooster Comb Caldera and Lake Owyhee Volcanic Field, eastern Oregon: silicic volcanism associated with Grande Ronde flood basalt: Journal of Volcanology and Geothermal Research, v. 309, p. 96-117.

Benson, T.R., Mahood, G.A., and Grove, M., 2017, Geology and 40 Ar/39 Ar geochronology of the middle Miocene McDermitt volcanic field, Oregon and Nevada: Silicic volcanism associated with propagating flood basalt dikes at initiation of the Yellowstone hotspot: Geological Society of America Bulletin, v. 129, p. 1027-1051.

Bondre, N. R., Duraiswami, R. A., and Dole, G., 2004, Morphology and emplacement of flows from the Deccan Volcanic Province, India: Bulletin of Volcanology, v. 66, p. 29-45.

Bondre, N.R., and Hart, W.K., 2008, Morphological and textural diversity of the Steens Basalt lava flows, Southeastern Oregon, USA: implications for emplacement style and nature of eruptive episodes: Bulletin of Volcanology, v. 70, no. 8, p. 999-1019.

Brown, R.J., Blake, S., Bondre, N.R., Phadnis, V.M., and Self, S., 2011, Aʹ ā lava flows in the Deccan Volcanic Province, India, and their significance for the nature of continental flood basalt eruptions: Bulletin of Volcanology, v. 73, p. 737-752.

Brueseke, M.E., Heizler, M.T., Hart, W.K., and Mertzman, S.A., 2007, Distribution and geochronology of Oregon Plateau (USA) flood basalt volcanism: The Steens Basalt revisited: Journal of Volcanology and Geothermal Research, v. 161, p. 187-214.

Bryan, S.E., Peate, I.U., Peate, D.W., Self, S., Jerram, D.A., Mawby, M.R., and Miller, J.A., 2010, The largest volcanic eruptions on Earth: Earth-Science Reviews, v. 102, p. 207-229.

Burgess, S.D., and Bowring, S.A., 2015, High-precision geochronology confirms voluminous magmatism before, during, and after Earth's most severe extinction: Science Advances, v. 1, p. e1500470, doi:10.1126/sciadv.1500470.

Burgess, S.D., Muirhead, J.D., and Bowring, S.A., 2017, Initial pulse of Siberian Traps sills as the trigger of the end-Permian mass extinction: Nature communications, v. 8, doi:10.1038/s41467-017-00083-9.

Camp, V.E., and Hanan, B.B., 2008, A plume-triggered delamination origin for the Columbia River Basalt Group: Geosphere, v. 4, no. 3, p. 480.

Camp, V.E., and Ross, M.E., 2004, Mantle dynamics and genesis of mafic magmatism in the Intermontane Pacific Northwest: Journal of Geophysical Research: Solid Earth, v. 109, doi: 10.1029/2003JB002838.

Camp, V.E., Ross, M.E, Duncan, R.A., Jarboe, N.A., Coe, R.S., Hanan, B.B., and Johnson, J.A., 2013, The Steens Basalt: earliest lavas of the Columbia River Basalt Group: Geological Society of America Special Papers, v. 497, p. 87-116.

Camp, V.E., Ross, M.E., and Hanson, W.E., 2003, Genesis of flood basalts and Basin and Range volcanic rocks from Steens Mountain to the Malheur River Gorge, Oregon: Geological Society of America Bulletin, v. 115, p. 105-128.

Carlson, R.W., 1984, Isotopic constraints on Columbia River flood basalt genesis and the nature of the subcontinental mantle: Geochimica et Cosmochimica Acta, v. 48, p. 2357-2372.

Carlson, R.W., and Hart, W.K., 1987, Crustal Genesis on the Oregon Plateau: Journal of Geophysical Research-Solid Earth and Planets, v. 92, no. B7, p. 6191-6206.

Carlson, R.W., Lugmair, G.W., & Macdougall, J.D., 1981, Columbia River volcanism: the question of mantle heterogeneity or crustal contamination: Geochimica et CosmochimicaActa, v. 45, p. 2483-2499.

Cawthorn, R.G., and Davies, G., 1983, Experimental data at 3 kbars pressure on parental magma to the Bushveld Complex: Contributions to Mineralogy and Petrology, v. 83, p. 128-135.

Cawthorn, R.G., and Walraven, F., 1998, Emplacement and crystallization time for the Bushveld Complex: Journal of Petrology, v. 39, p. 1669-1687.

Cheng, L.L., Yang, Z.F., Zeng, L., Wang, Y., and Luo, Z.H., 2014, Giant plagioclase growth during storage of basaltic magma in Emeishan Large Igneous Province, SW China: Contributions to Mineralogy and Petrology, v. 167, p. 1-20.

Coble, M.A., and Mahood, G.A., 2012, Initial impingement of the Yellowstone plume located by widespread silicic volcanism contemporaneous with Columbia River flood basalts: Geology, v. 40, p. 655-658.

Coffin, M.F., Duncan, R.A., Eldholm, O., Fitton, J.G., Frey, F.A., Larsen, H.C., Mahoney, J.J., Saunders, A.D., Schlich, R., and Wallace, P.J., 2006, Large igneous provinces andscientific ocean drilling: Status quo and a look ahead: Oceanography, v. 19, p.150-160.

Coffin, M.F., and Eldholm, O., 1994, Large igneous provinces: crustal structure, dimensions, and external consequences: Reviews of Geophysics, v. 32, p. 1-36. Courtillot, V.E., and Renne, P.R., 2003, On the ages of flood basalt events: Comptes Rendus Geoscience, v. 335, p.113-140.

Cox, K.G., 1980, A model for flood basalt vulcanism: Journal of Petrology, v. 21, p. 629-650.

Cox, C., and Keller, G., 2010, Crustal Structure of the High Lava Plains of the Pacific Northwest Source Seismic and Gravity Modeling, Abstract T41E-07 presented at 2010 Fall Meeting, AGU, San Francisco, CA, 13-17 December.

Eagar, K.C., Fouch, M.J., and James, D.E., 2010, Receiver function imaging of upper mantle complexity beneath the Pacific Northwest, United States: Earth and Planetary Science Letters, v. 297, no. 1, p. 141-153.

Eagar, K.C., Fouch, M.J., James, D.E., and Carlson, R.W., 2011, Crustal structure beneath the High Lava Plains of eastern Oregon and surrounding regions from receiver function analysis: Journal of Geophysical Research: Solid Earth, v. 116 no. B2.

Eales, H.V., Marsh, J.S., Mitchell, A.A., De Klerk, W.J., Kruger, F.J., and Field, M., 1986, Some geochemical constraints upon models for the crystallization of the Upper Critical Zone Main Zone interval, northwestern Bushveld Complex: Mineralogical Magazine, v. 50, p. 567-582.

Fedorenko, V.A., Lightfoot, P.C., Naldrett, A.J., Czamanske, G.K., Hawkesworth, C.J., Wooden, J.L., and Ebel, D.S., 1996, Petrogenesis of the flood-basalt sequence at Noril'sk, north Central Siberia: International Geology Review, v. 38, p. 99-135.

Gao, H., Humphreys, E.D., Yao, H., and van der Hilst, R.D., 2011, Crust and lithosphere structure of the northwestern US with ambient noise tomography: terrane accretion and Cascade arc development: Earth and Planetary Science Letters, v. 304, p. 202-211.

Garfunkel, Z., 2008, Formation of continental flood volcanism - the perspective of setting of melting: Lithos, v. 100, no. 1-4, p. 49-65.

Graubard, M., 2016, Evolution of a Flood Basalt Crustal Magmatic System: In Situ Mineral Data and Computational Modeling of the Steens Basalt [M.S. Thesis]: Central Washington University, 190 p.

Grove, T.L., Elkins-Tanton, L.T., Parman, S.W., Chatterjee, N., Müntener, O., and Gaetani, G.A., 2003, Fractional crystallization and mantle-melting controls on calc-alkaline differentiation trends: Contributions to Mineralogy and Petrology, v. 145, p. 515-533.

Gualda, G.A., Ghiorso, M.S., Lemons, R.V., and Carley, T.L., 2012, Rhyolite-MELTS: a modified calibration of MELTS optimized for silica-rich, fluid-bearing magmatic systems: Journal of Petrology, v. 53, p. 875-890.

Gunn, B.M., and Watkins, N.D., 1970, Geochemistry of the Steens Mountain Basalts, Oregon: Geological Society of America Bulletin, v. 81, p. 1497-1516.

Hawkesworth, C., Kelley, S., Turner, S., le Roex, A., and Storey, B., 1999, Mantle processes during Gondwana break-up and dispersal: Journal of African Earth Sciences, v. 28, no. 1, p. 239-261.

Helz, R.T., 1985, Compositions of fine-grained mafic rocks from sills and dikes associated with the Stillwater Complex, Czamanske, G. K., and Zientek, M. L., eds., The Stillwater complex, Montana: Montana Bureau of Mines and Geology Special Publication 92, p. 97-117.

Helz, R.T., 1995, The Stillwater Complex, Montana: a subvolcanic magma chamber?: American Mineralogist, v. 80, p. 1343-1346.

Henry, C.D., Castor, S.B., Starkel, W.A., Ellis, B.S., Wolff, J.A., Laravie, J.A., McIntosh, W.C., and Heizler, M.T., 2017, Geology and evolution of the McDermitt caldera, northern Nevada and southeastern Oregon, western USA: Geosphere, v. 13, p. 1066-1112.

Higgins, M.D., and Chandrasekharam, D., 2007, Nature of sub-volcanic magma chambers, Deccan Province, India: evidence from quantitative textural analysis of plagioclase megacrysts in the Giant Plagioclase Basalts: Journal of Petrology, v. 48, p. 885-900.

Hofmann, A., 1997, Mantle geochemistry: the message from oceanic volcanism: Nature, v. 385, no. 6613, p. 219-229.

Hooper, P.R., 1982, The Columbia river basalts: Science, v. 215, p. 1463-1468.

Hooper, P.R., 1984, Physical and chemical constraints on the evolution of the Columbia River basalt: Geology, v. 12, p. 495-499.

Hooper, P.R., 1988, Crystal fractionation and recharge (RFC) in the American Bar flows of the Imnaha basalt, Columbia River Basalt Group: Journal of Petrology, v. 29, p. 1097-1118.

Hooper, P.R., 2000, Chemical discrimination of Columbia River basalt flows: Geochemistry, Geophysics, Geosystems, v. 1, no. 6.

Hooper, P.R., Binger, G.B., and Lees, K.R., 2002, Ages of the Steens and Columbia River flood basalts and their relationship to extension-related calc-alkalic volcanism in eastern Oregon: Geological Society of America Bulletin, v. 114, no. 1, p. 43-50.

Hooper, P.R., Camp, V.E., Reidel, S.P., and Ross, M.E., 2007, The origin of the Columbia River flood basalt province: Plume versus non-plume models: Geological Society of America Special Papers, v. 430, p. 635-668.

Hooper, P.R., Kleck, W.D., Knowles, C.R., Reidel, S.P., and Thiessen, R.L., 1984, ImnahaBasalt, Columbia River Basalt Group: Journal of Petrology, v. 25, p. 473 500.

Jarboe, N.A., Coe, R.S., Renne, P.R., and Glen, J.M.G., 2010, The age of the Steens reversal and the Columbia River Basalt Group: Chemical Geology, v. 274, no. 3 4, p. 158-168.

Jarboe, N.A., Coe, R.S., Renne, P.R., Glen, J.M.G., and Mankinen, E.A., 2008, Quickly erupted volcanic sections of the Steens Basalt, Columbia River Basalt Group: Secular variation, tectonic rotation, and the Steens Mountain reversal: Geochemistry Geophysics Geosystems, v. 9, no. 11.

Johnson, J.A., Hawkesworth, C.J., Hooper, P.R., and Binger, G.B., 1998, Major and trace element analyses of Steens Basalt, southeastern Oregon: U.S. Geological Survey Open File Report 98 482, 26 p.

Johnson D.M., Hooper P.R., and Conrey, R.M., 1999, XRF analysis of rocks and minerals for major and trace elements on a single low dilution Li-tetraborate fused bead: Advances in X-Ray Analysis, v. 41, p. 843–867.

Jordan, B.T., Grunder, A.L., Duncan, R.A., and Deino, A.L., 2004, Geochronology of age progressive volcanism of the Oregon High Lava Plains: Implications for the plume interpretation of Yellowstone: Journal of Geophysical Research: Solid Earth, v. 109, p. B10202, doi:101029/2003JB002776.

Kelly, D., 2016, Estimation of analytical error for major, minor and trace elements analyzed by x-ray fluorescence at the Peter Hooper Geoanalytical Laboratory, Washington State University: Geological Society of America Abstracts with Programs, v. 48, no. 7.

Kistler, R.W., and Peterman, Z.E., 1973, Variations in Sr, Rb, K, Na, and initial Sr^{87}/Sr^{86} in Mesozoic granitic rocks and intruded wall rocks in central California: Geological Society of America Bulletin, v. 84, p. 3489-3512.

Klewin, K.W., and Berg, J.H., 1991, Petrology of the Keweenawan Mamainse Point lavas, Ontario: petrogenesis and continental rift evolution: Journal of Geophysical Research: Solid Earth, v. 96, p. 457-474.

Knaack, C., Cornelius, S.B., and Hooper, P.R., 1994, Trace element analyses of rocks and minerals by ICP-MS: GeoAnalytical Lab, Washington State University.

Koppers, A.A.P., 2002, ArArCALC-software for 40Ar/39Ar age calculations: Computers and Geosciences, v. 28, p. 605–619.

Koppers, A.A., Gowen, M.D., Colwell, L.E., Gee, J.S., Lonsdale, P.F., Mahoney, J.J., and Duncan, R.A., 2011, New 40Ar/39Ar age progression for the Louisville hot spot trail and implications for inter–hot spot motion: Geochemistry, Geophysics, Geosystems, v. 12, doi:10.1029/2011GC003804.

Kuiper, K.F., Deino, A., Hilgen, F.J., Krijgsman, W., Renne, P.R., and Wijbrans, J.R., 2008, Synchronizing rock clocks of Earth history: Science, v. 320, p. 500–504.

Lepage, L., 2003, ILMAT: an Excel worksheet for ilmenite-magnetite geothermometry and geobarometry: Computers and Geosciences, v. 29, p. 673-678.

Lightfoot, P.C., Hawkesworth, C.J., and Sethna, S.F., 1987, Petrogenesis of rhyolites and trachytes from the Deccan Trap: Sr, Nd and Pb isotope and trace element evidence: Contributions to Mineralogy and Petrology, v. 95, p. 44-54.

Long, P.E., and Wood, B.J., 1986, Structures, textures, and cooling histories of Columbia River basalt flows: Geological Society of America Bulletin, v. 97, p. 1144-1155.

Luttinen, A.V., Leat, P.T., and Furnes, H., 2010, Bjornnutane and Sembberget basalt lavas and the geochemical provinciality of Karoo magmatism in western Dronning Maud Land, Antarctica: Journal of Volcanology and Geothermal Research, v. 198, no. 1-2, p. 1-18.

Mahood, G.A., and Benson, T.R., 2017, Using 40 Ar/39 Ar ages of intercalated silicic tuffs to date flood basalts: Precise ages for Steens Basalt Member of the Columbia River Basalt Group: Earth and Planetary Science Letters, v. 459, p. 340-351.

Mankinen, E.A., Larson, E.E., Gromme, C.S., Prevot, M., and Coe, R.S., 1987, The Steens Mountain (Oregon) Geomagnetic Polarity Transition: 3. Its regional significance: Journal of Geophysical Research, v. 92, no. B8, p. 8057.

McBirney, A.R., and Noyes, R.M., 1979, Crystallization and layering of the Skaergaard intrusion: Journal of Petrology, v. 20, p. 487-554.

McCallum, I.S., Raedeke, L.D., and Mathez, E.A., 1980, Investigations of the Stillwater Complex: Part I. Stratigraphy and structure of the banded zone. American Journal of Science, v. 280, p. 59-87.

Min, K., Mundil, R., Renne, P.R., and Ludwig, K.R., 2000, A test for systematic errors in 40Ar/39Ar geochronology through comparison with U/Pb analysis of a 1.1-Ga rhyolite: Geochimica et Cosmochimica Acta, v. 64, p. 73–98.

Minor, S.A., Rytuba, J.J., Goeldner, C.A., and Tegtmeyer, K.J., 1987a, Geologic map of the Alvord Hot Springs quadrangle, Harney County, Oregon: U.S. Geological Survey Miscellaneous Field Studies Map MF-1916, scale 1:24,000.

Minor, S.A., Rytuba, J.J., Meulen, D.B., Grubensky, M.J., and Tegtmeyer, K.J., 1987b, Geologic map of the Wildhorse Lake quadrangle, Harney County, Oregon: U.S. Geological Survey Miscellaneous Field studies Map MF-1915, scale 1:24,000.

Moore, N.E., Lytle, K., Bohrson, W.A., and Grunder, A.L., 2015, New Petrologic and Geochemical Insights into Differentiation Processes Required to Produce the Lower Steens Basalt, Columbia River Basalt Province, SE Oregon, Abstract V41C-3090 presented at 2015 Fall Meeting, AGU, San Francisco, CA, 14-18 December.

Neave, D.A., and Putirka, K.D., 2017, A new clinopyroxene-liquid barometer, and implications for magma storage pressures under Icelandic rift zones: American Mineralogist, v. 102, p. 777-794.

Peate, D.W., 1997, The Paraná-Etendeka Province: Large igneous provinces: Continental, oceanic, and planetary flood volcanism, p. 217-245.

Pierce, K.L., and Morgan, L.A., 2009, Is the track of the Yellowstone hotspot driven by a deep mantle plume--Review of volcanism, faulting, and uplift in light of new data: Journal of Volcanology and Geothermal Research, v. 188, p. 1-25.

Putirka, K.D., 2008, Thermometers and barometers for volcanic systems: Reviews in mineralogy and geochemistry, v. 69, p. 61-120.

Raedeke, L.D., and McCallum, I.S., 1984, Investigations in the Stillwater complex: Part II. Petrology and petrogenesis of the ultramafic series: Journal of Petrology, v. 25, p. 395-420.

Reichow, M.K., Pringle, M.S., Al'Mukhamedov, A.I., Allen, M.B., Andreichev, V.L., Buslov, Davies, C.E, , Fedosee, G.S., Fitton, J.G., Inger, S., Medvedev, A.Ya., Mitchell, C., Puchkov, V.N., Safonova, I.Yu., Scott, R.A., and Saunders, A.D., 2009, The timing and extent of the eruption of the Siberian Traps large igneous province: Implications for the end-Permian environmental crisis: Earth and Planetary Science Letters, v. 77, p. 9-20.

Reidel, S.P., Camp, V.E., Tolan, T.L., and Martin, B.S., 2013, The Columbia River flood basalt province: Stratigraphy, areal extent, volume, and physical volcanology: Geological Society of America Special Papers, v. 497, 1-43.

Reidel, S.P., and Tolan, T.L., 2013, The Grande Ronde Basalt, Columbia River Basalt Group: Geological Society of America Special Papers, v. 497, p. 117-153.

Reidel, S.P., Fecht, K.R., Hagood, M.C., Tolan, T.L., and Hooper, P.R., 1989, The geologic evolution of the central Columbia Plateau: Geological Society of America Special Papers, v. 239, p. 247-264.

Reidel, S.P., Tolan, T.L., Hooper, P.R., Beeson, M.H., Fecht, K.R., Bentley, R.D., and Anderson, J.L., 1989, The Grande Ronde Basalt, Columbia River Basalt Group; Stratigraphic descriptions and correlations in Washington, Oregon, and Idaho: Geological Society of America Special Papers, v. 239, p. 21-54.

Reiners, P.W., Nelson, B.K., and Ghiorso, M.S., 1995, Assimilation of felsic crust by basaltic magma: thermal limits and extents of crustal contamination of mantle derived magmas: Geology, v. 23, p. 563-566.

Renne, P.R., Sprain, C.J., Richards, M.A., Self, S., Vanderkluysen, L., and Pande, K., 2015, State shift in Deccan volcanism at the Cretaceous-Paleogene boundary, possibly induced by impact: Science, v. 350, p. 76-78.

Richards, M.A., Alvarez, W., Self, S., Karlstrom, L., Renne, P.R., Manga, M., Sprain, C.J., Smit, J., Vanderkluden, L., and Gibson, S.A., 2015, Triggering of the largest Deccan eruptions by the Chicxulub impact: Geological Society of America Bulletin, v. 127, p. 1507-1520.

Ramos, F.C., Wolff, J.A., Starkel, W., Eckberg, A., Tollstrup, D.L., and Scott, S., 2013, The changing nature of sources associated with Columbia River flood basalts: Evidence from strontium isotope ratio variations in plagioclase phenocrysts: Geological Society of America Special Papers, v. 239, p. 231-257.

Rytuba, J.J., 1988, Volcanism, extensional tectonics, and epithermal mineralization in the Northern Basin and Range Province, California, Nevada, Oregon, and Idaho: U.S. Geological Survey Circular 1035, p. 59-62.

Sawlan, M.G., 2017, Alteration, mass analysis, and magmatic compositions of the Sentinel Bluffs Member, Columbia River flood basalt province: Geosphere, v. 14, no. 4.

Self, S., Schmidt, A., and Mather, T.A., 2014, Emplacement characteristics, time scales, and volcanic gas release rates of continental flood basalt eruptions on Earth: Geological Society of America Special Papers, v. 505, p. 319-337.

Self, S., Thordarson, T., Keszthelyi, L., Walker, G.P.L., Hon, K., Murphy, M.T., and Finnemore, S., 1996, A new model for the emplacement of Columbia River basalts as large, inflated pahoehoe lava flow fields: Geophysical Research Letters, v. 23, p. 2689-2692.

Self, S., Widdowson, M., Thordarson, T., and Jay, A.E., 2006, Volatile fluxes during flood basalt eruptions and potential effects on the global environment: A Deccan perspective: Earth and Planetary Science Letters, v. 248, no. 1, p. 518-532.

Sharma, M., 1997, Siberian Traps, Mahoney, J.J, Coffin. M.J., eds., Large Igneous Provinces, Geophysical Monograph: v. 100, p. 273-295.

Shervais, J.W., Vetter, S.K., Hanan, B.B., 2006, Mafic layered sill complex beneath the eastern Snake River Plain: evidence from cyclic geochemical variations in basalt: Geology, v. 34, no. 5, p. 365-368.

Sheth, H., 2016, Giant plagioclase basalts: Continental flood basalt–induced remobilization of anorthositic mushes in a deep crustal sill complex: Geological Society of America Bulletin, v. 128, p. 916-925.

Streck, M.J., Ferns, M.L., and McIntosh, W., 2015, Large, persistent rhyolitic magma reservoirs above Columbia River Basalt storage sites: The Dinner Creek Tuff eruptive center, eastern Oregon: Geosphere, v. 2, p. 1–10, doi:10.1130/GES01086.1.

Streck, M.J., and Grunder, A.L., 2012, Temporal and crustal effects on differentiation of tholeiite to calcalkaline and ferro-trachytic suites, High Lava Plains, Oregon, USA: Geochemistry, Geophysics, Geosystems, v. 13, no. 11.

Streck, M.J., McIntosh, W., and Ferns, M.L., 2016, Co-CRBG rhyolite volcanism reassessed: Geological Society of America Abstracts with Programs, v. 48, no. 6, doi:10.1130/abs/2016RM-276108.

Subbarao K.V., Hooper P.R., 1988, Reconnaissance map of the Deccan Basalt Group in the Western Ghats, India, In: Subbarao K.V., ed., Deccan flood basalts: Memoirs of the Geological Society of India 10 (enclosure).

Takahahshi, E., Nakajima, K., and Wright, T.L., 1998, Origin of the Columbia River basalts:melting model of a heterogeneous plume head: Earth and Planetary Science Letters, v. 162, no. 1, p. 63-80.

Talusani, R.V.R., 2012, Giant plagioclase basalts from northeastern Deccan volcanic province, India: Implications for their origin and petrogenetic significance: International Journal of Geosciences, v. 3, p. 1027-1032.

Thompson, R., Morrison, M., Dickin, A., and Hendry, G., 1983, Continental flood basalts...arachnids rule OK?: Continental basalts and mantle xenoliths, p. 158-185.

Turner, S., Hawkesworth, C., Gallagher, K., Stewart, K., Peate, D., and Mantovani, M., 1996, Mantle plumes, flood basalts, and thermal models for melt generation beneath continents: Assessment of a conductive heating model and application to the Parana: Journal of Geophysical Research-Solid Earth, v. 101, no. B5, p. 11503-11518.

Twist, D., and French, B.M., 1983, Voluminous acid volcanism in the Bushveld Complex: A review of the Rooiberg Felsite: Bulletin of Volcanology, v. 46, p. 225-242.

Wager, L.R., and Brown, G.M., 1967, Layered igneous rocks, WH Freeman and Company.

Wagner, L., Forsyth, D.W., Fouch, M.J., and James, D.E., 2010, Detailed three-dimensional shear wave velocity structure of the northwestern United States from Rayleigh wavetomography: Earth and Planetary Science Letters, v. 299, no. 3, p. 273-284.

Walker, G.P.L., 1971, Compound and simple lava flows and flood basalts: Bulletin Volcanologique, v. 35, p. 579-590.

Walker, G.W., MacLeod, N.S., Russell, D., and Earnest, P., 1991, Geologic map of Oregon, Geological Survey.

Warren, L.M., Snoke, J.A., and James, D.E., 2008, S-wave velocity structure beneath the High Lava Plains, Oregon, from Rayleigh-wave dispersion inversion: Earth and Planetary Science Letters, v. 274, no. 1-2, p. 121-131.

Wells, R., Bukry, D., Friedman, R., Pyle, D., Duncan, R., Haeussler, P., and Wooden, J., 2014, Geologic history of Siletzia, a large igneous province in the Oregon and Washington Coast Range: Correlation to the geomagnetic polarity time scale and implications for a long-lived Yellowstone hotspot: Geosphere, v. 10, p. 692-719.

Whiteside, J.H., Olsen, P.E., Eglinton, T., Brookfield, M.E., and Sambrotto, R.N., 2010, Compound specific carbon isotopes from Earth's largest flood basalt eruptions directly linked to the end-Triassic mass extinction: Proceedings of the National Academy of Sciences of the United States of America, v. 107, no. 15, p. 6721-6725.

Wolff, J.A., and Ramos, F.C., 2013, Source materials for the main phase of the Columbia River Basalt Group: geochemical evidence and implications for magma storage and transport: Geological Society of America Special Papers, v. 497, p. 273-291.

Wolff, J.A., Ramos, F.C., Hart, G.L., Patterson, J.D., and Brandon, A.D., 2008, Columbia River flood basalts from a centralized crustal magmatic system: Nature Geoscience, v. 1, no. 3, p. 177-180.

Yudovskaya, M.A., Kinnaird, J.A., Sobolev, A.V., Kuzmin, D.V., McDonald, I., and Wilson, A.H., 2013, Petrogenesis of the Lower Zone olivine-rich cumulates beneath the Platreef and their correlation with recognized occurrences in the Bushveld Complex: Economic Geology, v .108, p. 1923-1952.

TABLE 2.1. REPRESENTATIVE LOWER STEENS MINERAL COMPOSITIONS

Sample/Type	Grain_Spot[†]	Grain Type[§]	SiO2	TiO2	Al2O3	FeO*[#]	MnO	MgO	CaO	Na2O	K2O	NiO	Cr2O3	Total	Fo/Mg#[††]	An[§§]
JS22##																
Olivine	2_c	Phenocryst	38.62	0.011	0.061	18.55	0.25	42.19	0.253	0.012	0	0.238	0.036	100.2	80.2	N.A.[†]
Olivine	2_m	Phenocryst	38.95	0.021	0.051	18.44	0.247	42.4	0.258	0.012	0.017	0.266	0.045	100.7	80.4	N.A.
Olivine	2_r	Phenocryst	38.54	0.017	0.078	20.43	0.248	40	0.294	0.004	0.004	0.256	0.041	99.91	77.7	N.A.
Clinopyroxene	2_c	Microphenocryst	50.39	1.432	4.24	9.795	0.009	14.89	18.36	0.395	0	N.A.	0.552	100.1	73.0	N.A.
Clinopyroxene	2_r	Microphenocryst	50.35	1.346	3.004	12.02	0.101	14.32	17.99	0.38	0.014	N.A.	0.042	99.57	68.0	N.A.
Plagioclase	9_c	Phenocryst	48.92	0.057	31.81	0.56	N.A.	0.178	15.44	2.652	0.066	N.A.	N.A.	99.68	N.A.	76.3
Plagioclase	9_m	Phenocryst	49.39	0.068	31.96	0.518	N.A.	0.16	15.16	2.784	0.093	N.A.	N.A.	100.1	N.A.	75.1
Plagioclase	9_r	Phenocryst	49.27	0.069	31.72	0.499	N.A.	0.164	15	2.784	0.082	N.A.	N.A.	99.57	N.A.	74.9
Ilmenite	7_c	Groundmass	0.027	47.45	0.002	48.18	0.526	1.382	0.048	N.A.	N.A.	0	0.029	98.27	N.A.	N.A.
Magnetite	17_c	Groundmass	0.083	24.14	1.623	66.53	0.492	1.938	0.025	N.A.	N.A.	0.048	0.147	96.09	N.A.	N.A.
Chromite	5_c	Inclusion in Ol	0.094	1.571	29.34	31.25	0	11.59	0.023	N.A.	N.A.	0.21	24.28	98.84	N.A.	N.A.
NMSB13																
Olivine	22_c	Microphenocryst	39.12	0.029	0.048	21.76	0.318	39.21	0.257	0.013	0	0.223	0.031	101	76.3	N.A.
Olivine	22_m	Microphenocryst	38.86	0.015	0.028	21.38	0.316	39.65	0.257	0.018	0.014	0.203	0.025	100.8	76.8	N.A.
Olivine	22_r	Microphenocryst	38.56	0.011	0.035	22.1	0.303	39.01	0.27	0.002	0	0.199	0.028	100.5	75.9	N.A.
Clinopyroxene	3_c	Microphenocryst	49.65	2.052	3.92	12.03	0.223	13.68	18.35	0.392	0.006	N.A.	0.061	100.3	67.0	N.A.
Clinopyroxene	3_r	Microphenocryst	48.43	2.573	4.567	13.91	0.236	13.33	17.19	0.425	0.001	N.A.	0.052	100.7	63.1	N.A.
Plagioclase	10_c	Megaphenocryst	50.8	0.071	31.17	0.613	N.A.	0.136	13.79	3.268	0.168	N.A.	N.A.	100	N.A.	70.0
Plagioclase	10_m	Megaphenocryst	52.11	0.07	30.65	0.597	N.A.	0.137	13.49	3.573	0.191	N.A.	N.A.	100.8	N.A.	67.6
Plagioclase	10_r	Megaphenocryst	51.32	0.072	30.73	0.63	N.A.	0.141	13.63	3.414	0.178	N.A.	N.A.	100.1	N.A.	68.8
NMSB18																
Olivine	1_c	Phenocryst	39.67	0.011	0.04	16.62	0.221	42.66	0.238	0.012	0.006	0.287	0.05	99.82	82.1	N.A.
Olivine	1_m	Phenocryst	38.33	0.014	0.058	16.87	0.226	42.68	0.242	0.022	0.007	0.282	0.054	98.78	81.8	N.A.
Olivine	1_r	Phenocryst	38.1	0.017	0.032	17.72	0.187	42.1	0.264	0.006	0	0.234	0.037	98.7	80.9	N.A.
Olivine	4_c	Phenocryst	40.06	0.014	0.058	15.14	0.199	43.87	0.238	0.023	0	0.32	0.053	99.98	83.8	N.A.
Olivine	4_m	Phenocryst	39.41	0.013	0.062	15.64	0.208	43.82	0.257	0.009	0.005	0.339	0.057	99.82	83.3	N.A.
Olivine	4_r	Phenocryst	38.45	0.023	0.052	16.45	0.229	43.42	0.248	0.005	0	0.218	0.049	99.14	82.5	N.A.

Note: All mineral chemistry results for each phase analyzed in this study reported in Supplement 1. N.A. = not applicable

[†]Grain indicates the grain number analyzed from a given sample, spot is the analyzed location on that grain (c = core, m = midpoint, r = rim).

[§]Groundmass grains are <0.5 mm, microphenocrysts are 0.5-1 mm, phenocrysts are 1 mm to 1 cm, megaphenocrysts are >1cm.

[#]Fe is reported as all FeO*.

[††]Fo = forsterite content of olivine; Mg# (for clinopyroxone only) = Mg/(Mg+Fe²⁺).

[§§]An = anorthite content of plagioclase,

[##]Original sample from Johnson et al. 1998 (whole rock reported therein), mineral compositions analyzed in this study.

TABLE 2.2. REPRESENTATIVE WHOLE ROCK MAJOR AND TRACE ELEMENT COMPOSITIONS

Unit	Lower A			Lower B				Upper		
Sample	NMSB-55	NMSB-62	NMSB-69	NMSB-5	NMSB-13	NMSB-18	NMSB-21	NMSB-1	NMSB-2	NMSB-4
Major Elements (wt.%)										
SiO_2	48.14	48.86	48.06	48.66	48.76	47.18	49.96	48.34	52.01	51.72
TiO_2	1.818	1.994	2.744	2.110	1.842	1.752	2.756	2.672	2.623	2.580
Al_2O_3	15.69	16.16	14.61	15.09	18.46	13.42	14.24	15.22	13.38	13.44
$FeO*^{\dagger}$	11.30	11.27	13.08	11.74	9.90	11.36	12.82	14.36	13.43	13.33
MnO	0.171	0.176	0.200	0.186	0.154	0.183	0.200	0.201	0.214	0.211
MgO	7.36	6.04	5.23	8.53	6.03	10.62	5.34	5.40	3.90	3.96
CaO	9.86	9.02	8.16	9.45	10.63	9.88	9.07	8.59	7.64	7.66
Na_2O	2.90	3.13	3.34	2.88	3.01	2.28	2.97	3.45	3.53	3.30
K_2O	0.66	1.08	1.39	0.74	0.51	0.46	1.40	1.17	1.76	1.74
P_2O_5	0.288	0.365	0.553	0.334	0.250	0.217	0.391	0.418	0.401	0.372
Mg#§	56.3	51.5	44.2	59.0	54.7	64.9	45.2	42.7	36.5	37.0
Total	98.19	98.08	97.36	99.73	99.54	97.36	99.15	99.82	98.89	98.32
LOI%	0.75	1.47	1.40	N.A.$^{\#}$	N.A.	N.A.	N.A.	N.A.	N.A.	N.A.
Trace Elements by XRF (ppm)										
Ni	150	94	58	233	126	302	63	78	13	16
Cr	221	106	48	554	191	812	118	58	68	75
V	308	315	403	295	294	298	405	420	418	420
Ga	19	20	21	20	21	16	21	22	22	23
Cu	190	140	235	140	135	140	204	318	203	184
Zn	96	103	125	107	88	96	119	134	135	137
Trace Elements by ICP-MS (ppm)										
La	11.87	16.36	23.43	16.08	12.00	11.41	21.11	19.96	21.79	20.47
Ce	28.89	37.77	54.97	37.04	27.69	26.67	47.67	44.30	47.99	45.18
Pr	4.19	5.32	7.74	5.27	4.02	3.87	6.77	6.37	7.00	6.55
Nd	19.59	23.74	34.30	23.37	18.10	17.41	30.13	28.73	31.53	28.95
Sm	5.24	5.99	8.56	5.91	4.89	4.69	7.71	7.41	8.11	7.59
Eu	1.83	2.02	2.70	2.02	1.73	1.64	2.50	2.32	2.47	2.38
Gd	5.40	6.21	8.69	6.13	5.15	5.13	8.16	7.62	8.55	7.95
Tb	0.89	1.01	1.38	1.00	0.83	0.85	1.32	1.18	1.40	1.29
Dy	5.41	6.09	8.37	5.92	4.91	5.12	7.95	7.32	8.51	8.00
Ho	1.07	1.22	1.62	1.15	0.97	0.99	1.57	1.45	1.70	1.61
Er	2.77	3.12	4.33	2.91	2.47	2.53	3.97	3.72	4.42	4.16
Tm	0.38	0.43	0.59	0.41	0.34	0.35	0.56	0.52	0.62	0.59
Yb	2.28	2.70	3.57	2.37	2.01	2.06	3.25	3.15	3.74	3.58
Lu	0.34	0.41	0.54	0.38	0.30	0.31	0.51	0.49	0.56	0.54
Ba	238	393	491	289	210	178	397	470	580	597
Th	0.97	2.01	2.55	1.80	1.13	1.41	3.00	2.56	3.72	3.60
Nb	7.42	9.14	12.85	10.73	7.85	7.63	12.47	10.06	10.91	10.60
Y	26.34	30.14	40.87	28.68	24.02	24.37	38.72	35.80	42.55	39.79
Hf	3.24	4.01	5.54	3.93	3.25	3.32	5.26	4.98	5.58	5.33
Ta	0.48	0.61	0.85	0.72	0.53	0.52	0.87	0.68	0.75	0.72
U	0.34	0.69	0.83	0.40	0.24	0.27	0.93	0.75	1.42	1.33
Pb	2.37	4.02	5.55	3.20	2.17	2.26	4.94	5.16	7.43	7.18
Rb	10.6	18.4	23.4	9.4	6.4	7.8	25.5	18.2	36.9	37.1
Cs	0.36	0.21	0.33	0.17	0.10	0.11	0.59	0.26	1.25	1.28
Sr	481	462	448	427	510	325	395	474	366	373
Sc	30.6	29.1	32.7	28.4	24.0	30.7	32.4	31.9	39.8	40.4
Zr	119	151	210	154	123	126	203	191	211	203

Note: All whole rock compositons obtained in this study reported in Supplement 3.

†Fe is reported as all $FeO*$.

§Mg# = Mg/(Mg+Fe2+), Fe2+ is calculated as 0.90 $FeO*$.

$^{\#}$N.A. = not applicable
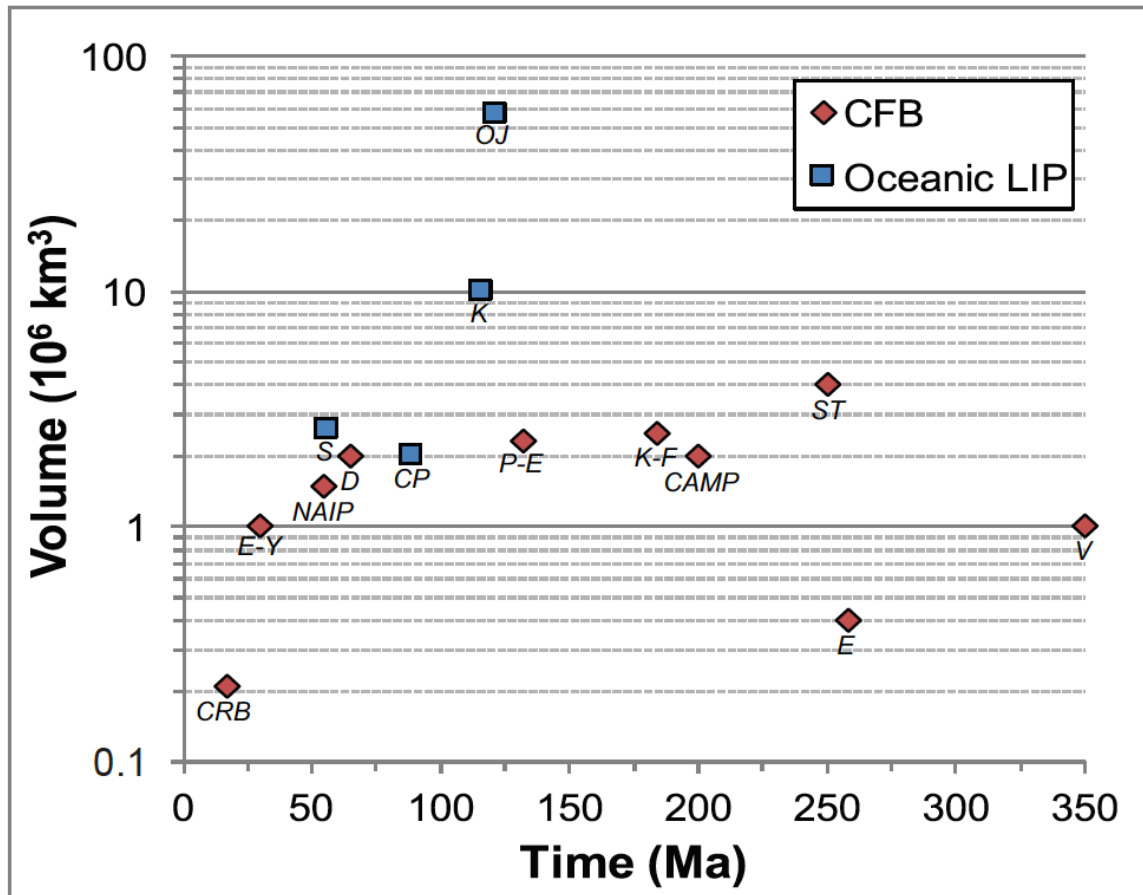
Figure 2.1. Volume versus age record of Phanerozoic continental flood basalt (CFB) and oceanic large igneous provinces (LIP) for select major provinces. Volume and age estimates from Cortillot and Renne, 2003; Encyclopedia of Volcanoes, 2015; Wells et al. 2014. The Precambrian Keweenawan Province (1100 Ma), though well outside of this timespan, plots near the volumetric average of Phanerozoic LIP (~2 x10^6 km^3). CAMP = Central Atlantic Magmatic Province, CP = Caribbean Plateau, CRB = Columbia River Basalt (including the Steens Basalt), D = Deccan Traps, E = Emeishan Traps, E/Y = Ethiopia/Yemen CFB, K = Kerguelen Plateau, K/F = Karoo/Ferrar Provinces, NAIP = North Atlantic Igneous Province, OJ = greater Ontong Java (Ontong Java, Manihiki and Hikurangi Plateaus), P/E = Paraná/Etendeka Traps, S = Siletzia-Crescent Terrane, ST = Siberian Traps, V = Viluy Traps.
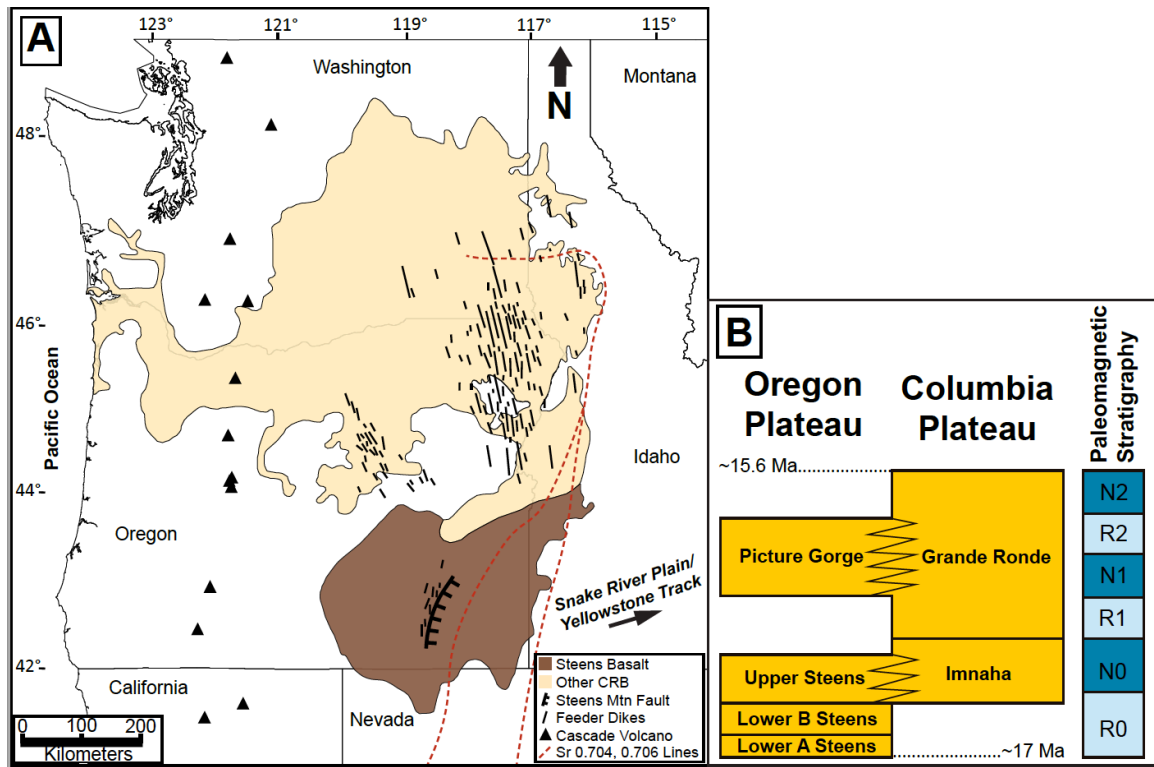
Figure 2.2. (A) Regional map of the CRBG. Brown shaded region shows the full extent of Steens Basalt; tan is the remainder of the CRBG. Heavy black lines are feeder dikes, hatched curved line is the Steens Mountain escarpment, black triangles are the major Cascade volcanoes. Red dashed lines are the initial $^{87}Sr/^{86}Sr$ 0.704 (western line) and 0.706 (eastern line) isopleths from Pierce and Morgan (2009). The analyses of plutonic rocks that define the 0.706 line reflect crustal sources, so it is the inferred western boundary of the North American craton (Kistler and Peterman, 1973). After Camp et al. 2013. (B) Schematic regional stratigraphy for the informally designated main phase eruptions of the CRBG, which compose ~93% of the total CRBG eruptive volume (Reidel et al. 2013; Camp et al. 2013). The Steens Reversal (R0 to N0) occurred at 16.73 Ma. Paleomagnetic stratigraphy and Steens Reversal age from Jarboe et al. (2008; 2010), upper limit of Grande Ronde volcanism from Barry et al. (2013). Modified from Camp & Ross (2004), Camp & Hanan (2008) and Wolff & Ramos (2013).
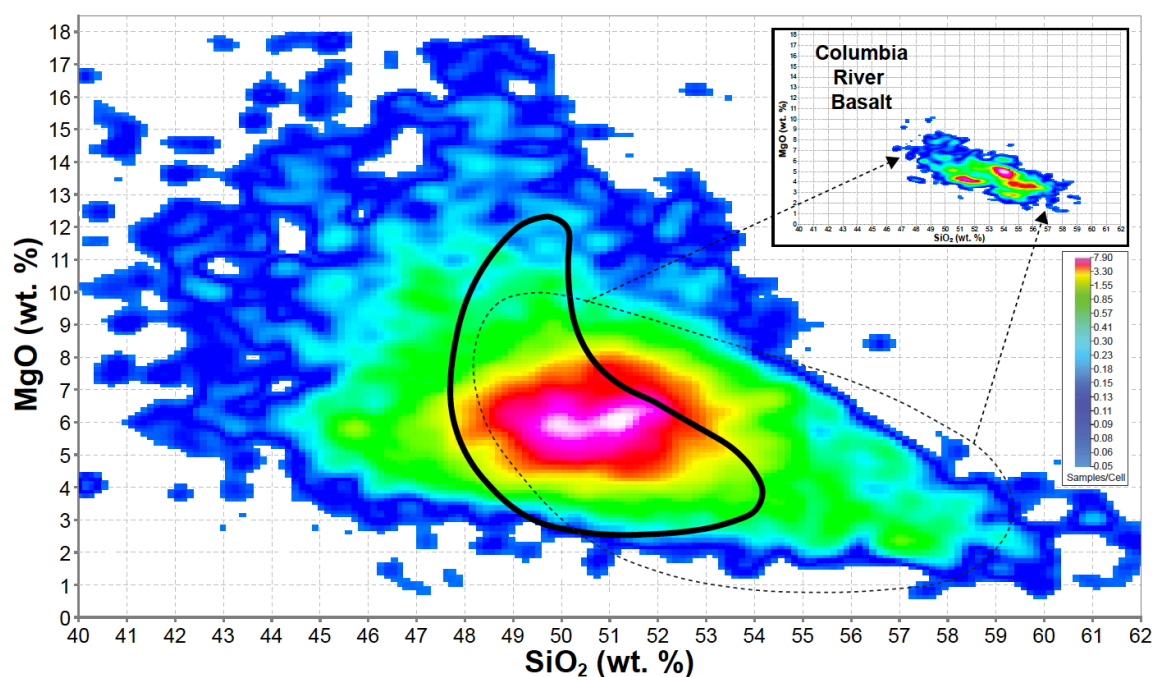
Figure 2.3. Comparison of MgO versus SiO_2 for Continental Flood Basalts. Density contours on main figure are the bulk of CFB (Siberian Traps, Deccan Traps, Parana, Karoo and Ferrar, Emeishan, Central Atlantic Magmatic Province), solid black line encompasses Steens Basalt data, dashed black line represents the field of all other CRBG. Inset shows density contours for all other CRBG. Density contours are color coded as shown on inset, by number of samples per cell, where each cell is 0.1 wt.% on all sides, and warmest colors represent highest sample density. Data from precompiled files of each province from the GeoRoc database, accessed June 2016.
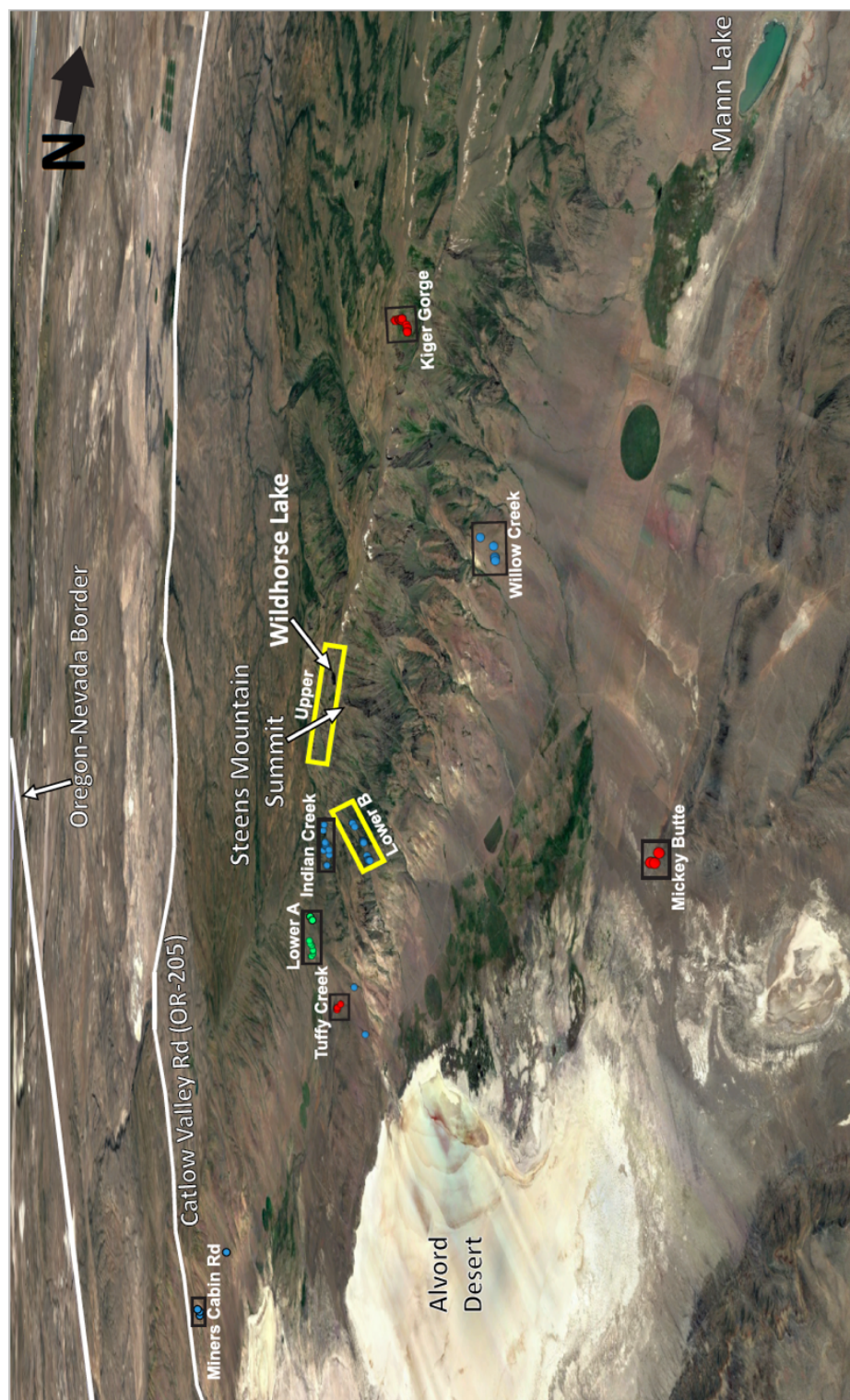
Figure 2.4. Oblique view of Steens Mountain from Google Earth looking southwest, showing Steens Basalt sample locations (circles) from this study, color-coded to chemical affinity (green = lower A, blue = lower B, red = Upper). Yellow rectangles outline the transect of Johnson et al. 1998, the type section of Steens Basalt. Black rectangles outline additional sections sampled for this study, and detailed in Figure 5. The 3 solitary blue sample points are from dikes sampled for this study that cross cut basement. North-south distance along the scarp from Mann Lake to the southernmost samples is 55 km.
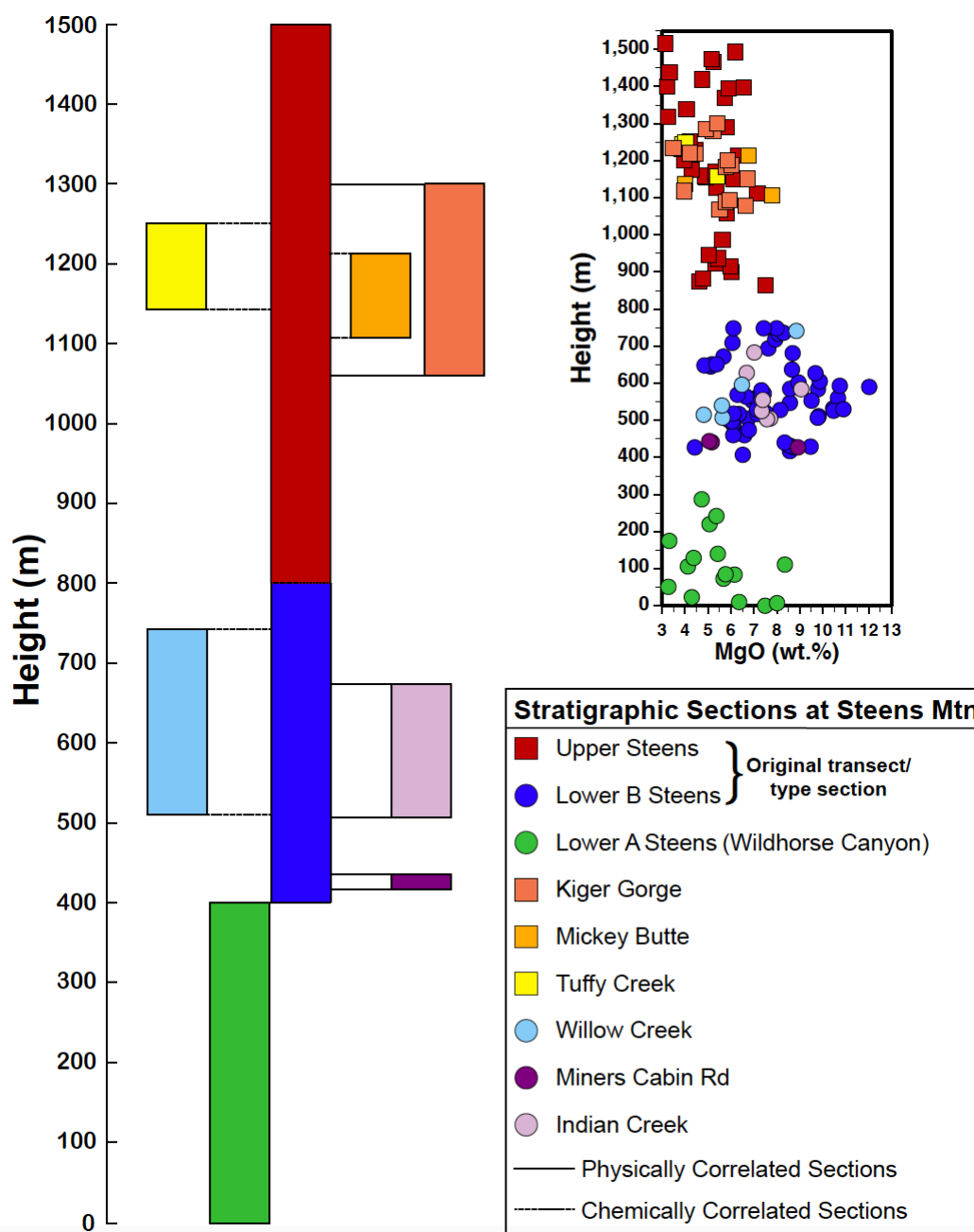
Figure 2.5. Correlation of new sample sections with the original transect/type section of the Steens Basalt. The original type section at Steens Mountain is shown in blue and red (lower B and upper Steens, respectively). The sections that were both physically and chemically correlated to the type section are shown with solid lines, whereas those that were chemically correlated only have dashed lines. Finer dashed line between lower B and upper Steens Basalt reflects the uncertainty in the location of transition between these two phases. See text for further explanation. Inset of MgO wt.% versus stratigraphic height establishes the chemical correlation of these sections, which is also evident in many other major and trace elements; see text for discussion.
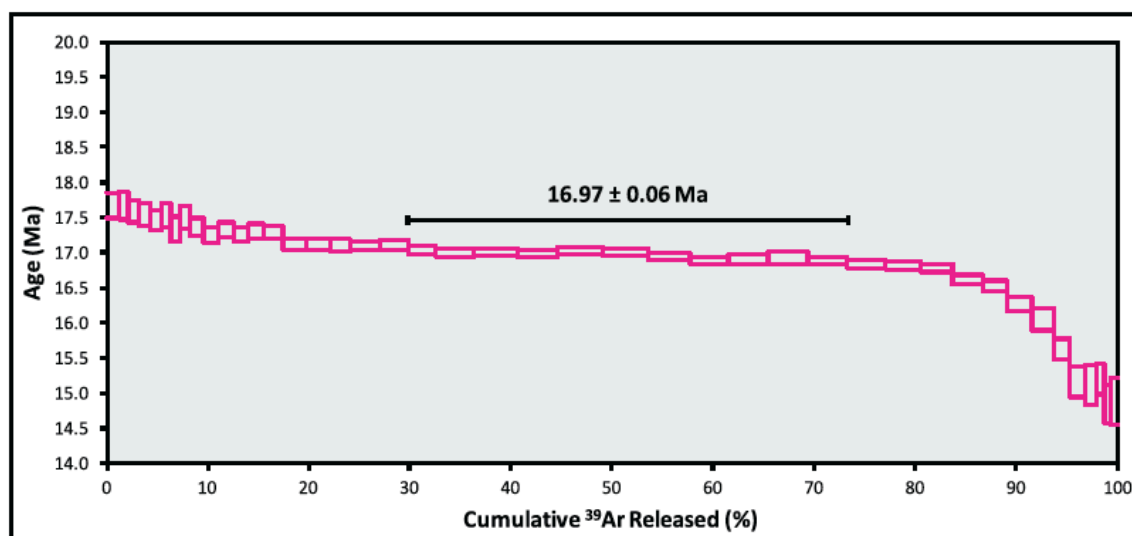
Figure 2.6. Age spectrum for groundmass Ar-Ar incremental age determination on sample NMSB55. The weighted plateau age is 16.97±0.06 Ma (error is ±2σ) and was calculated from 11 contiguous heating steps that contained ~45% of the total [39]Ar released.
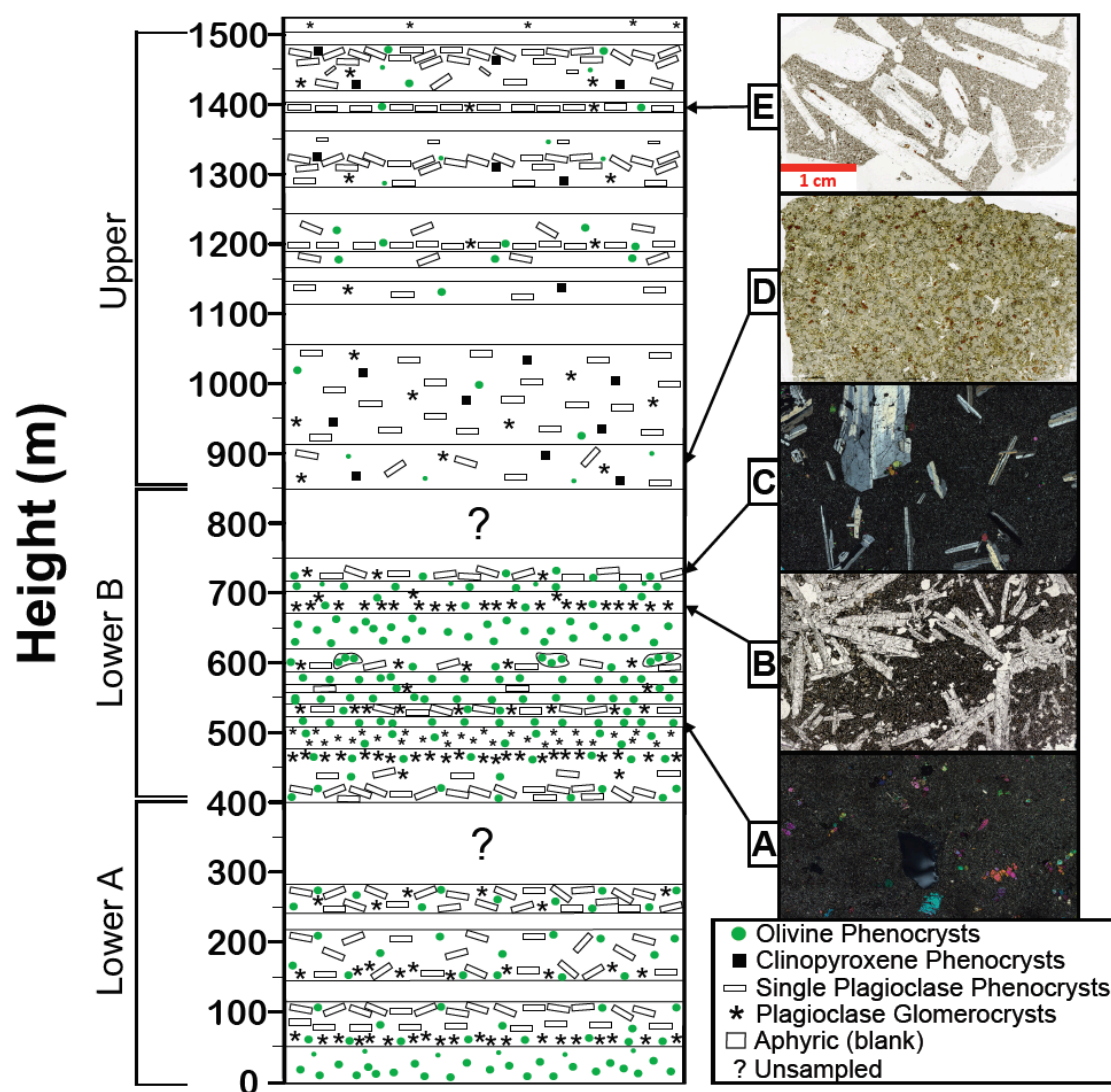
Figure 2.7. Textural changes with stratigraphic height and photomicrographs of representative Steens Basalt textures. Extent/thickness of each chemical section is shown on the far left. Systematic variations in textural types and phenocryst phases occur up section (e.g. olivine phenocryst phase decreases up section as clinopyroxene appears as a phenocryst phase up section, see text for details). We use the term phenocrysts to denote crystals large enough to see in hand sample, with no genetic implications. Photomicrographs of full thin sections display some of the most common textural types, 1 cm scale bar applies to all: (A) Olivine phyric with very fine groundmass, (B) daisy stone type plagioclase glomerocrysts with sparse olivine phenocrysts and abundant olivine microphenocrysts between laths, (C) single-isolated type plagioclase phenocrysts with occasional glomerocrysts, sparse olivine and cryptocrystalline groundmass, (D) single isolated and glomerocrysts of plagioclase microphenocrysts with abundant clinopyroxene, and (E) very large, flow aligned single-isolated type plagioclase with rare olivine.
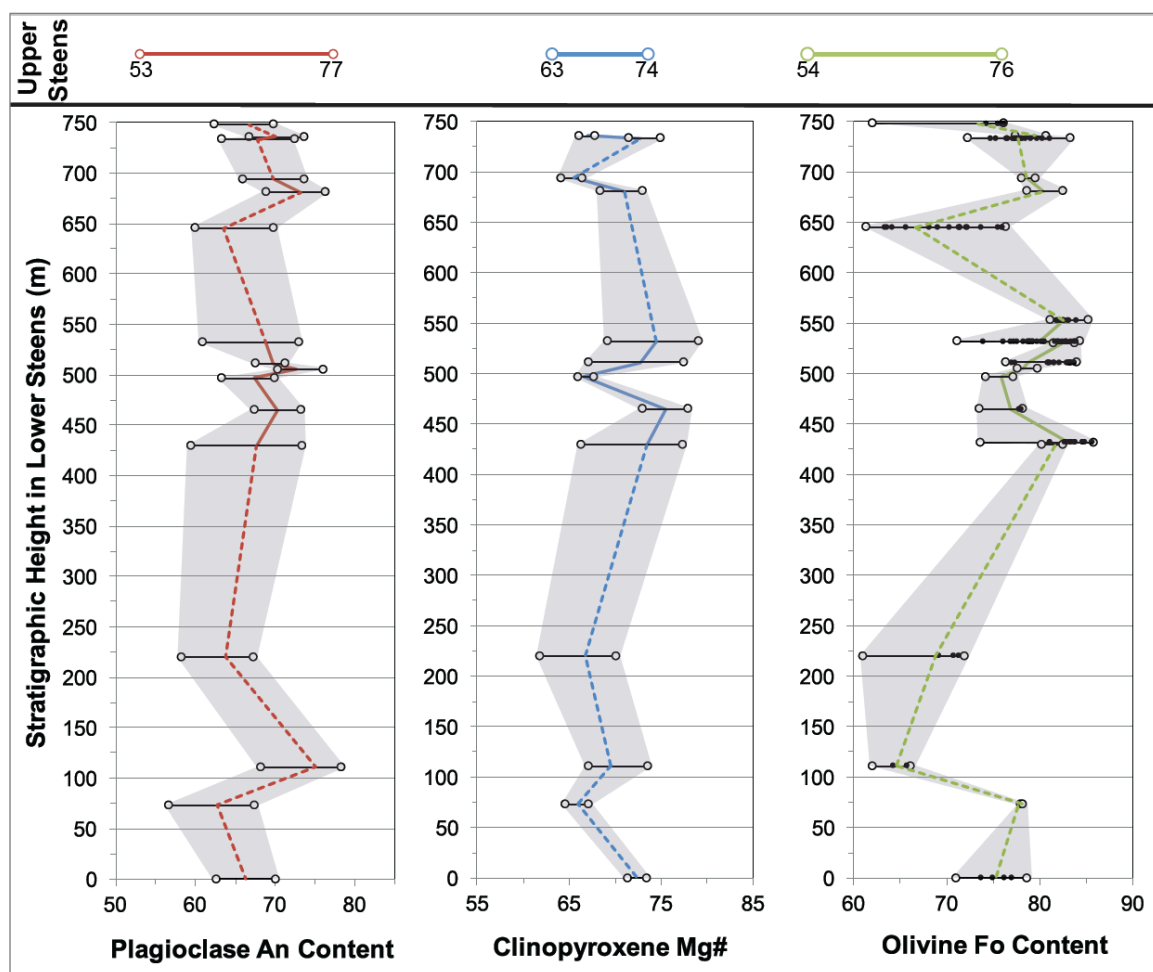
Figure 2.8. Olivine, clinopyroxene and plagioclase mineral composition versus stratigraphic height for the lower Steens (lower A and B), in comparison to full ranges for the upper Steens. An = anorthite content, Fo = forsterite content. Open circle end caps connected by solid horizontal black lines represent maximum and minimum values from grain core analyses within a sample (flow) at a given stratigraphic height. Colored lines connect mean core compositional values between flows and are solid connecting stratigraphically continuous flows or dashed where all variability between flows is not captured (unsampled or unanalyzed flows). Small black circles in the olivine composition diagram are individual data points for all analyzed cores in the flows with more heterogeneity (not shown for clinopyroxene as that phase is less common and there are few analyses, or for plagioclase because the data are generally evenly spread across the range for that phase). Gray fields to outline the excursions and how the compositional ranges change from analyzed flow to analyzed flow up section. Olivine analyses are limited from the lower A section (4 lowest samples) because the flows in that section are typically highly altered. At the top of the figure, the full range of An, Mg#, and Fo content for minerals of the upper Steens (Graubard, 2016) records a change upsection to less magnesian olivine and slightly lower Mg# in clinopyroxene, but a similar range of An content.
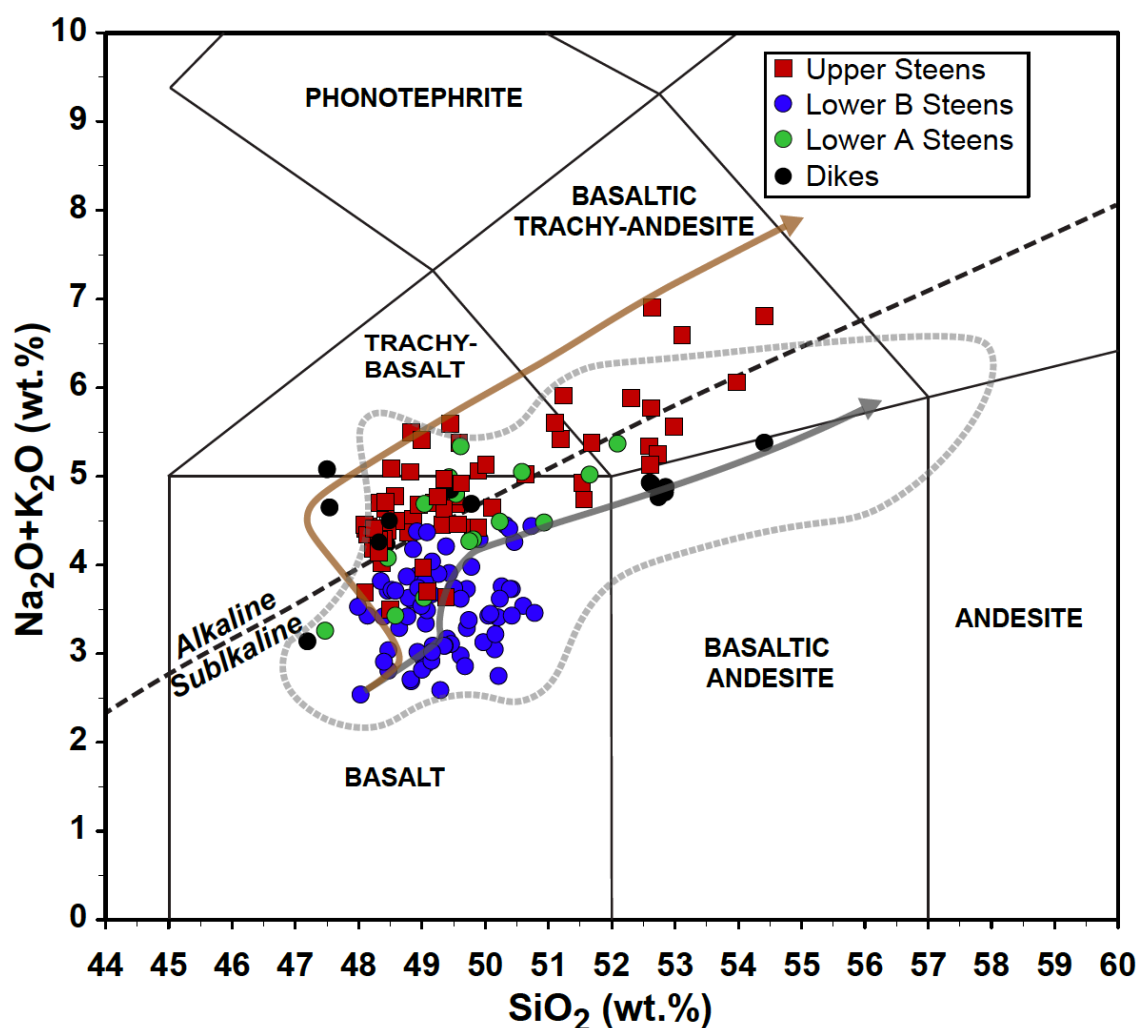
Figure 2.9. Total alkalis versus silica discrimination diagram. Lower B Steens is dominantly subalkaline basalt, whereas upper Steens also contains alkaline basalt, trachybasalt and basaltic trachy-andesite. The lower A Steens flows overlap with both lower B and upper Steens. Dikes tend to have upper Steens compositional affinity, consistent with field relations in which dikes dominantly cross cut lower or upper Steens stratigraphy. Light gray dashed line is the data field of Camp et al. 2013, a large set of XRF analyzed samples across the entire region of Steens Basalt exposure (beyond Steens Mountain). Dark gray and brown transparent lines represent crystal fractionation trends at 1 and 4 kbar, respectively, using the MELTS program (Gualda et al. 2012) and 0.5 wt.% H_2O in the parent magma. Data from this study, Johnson et al. 1998 and Wolff et al. 2008 are shown. Upper Steens data includes a new transect from Kiger Gorge (Bendaña, 2016). Alkaline versus subalkaline boundary from Irvine & Baragar, 1971.
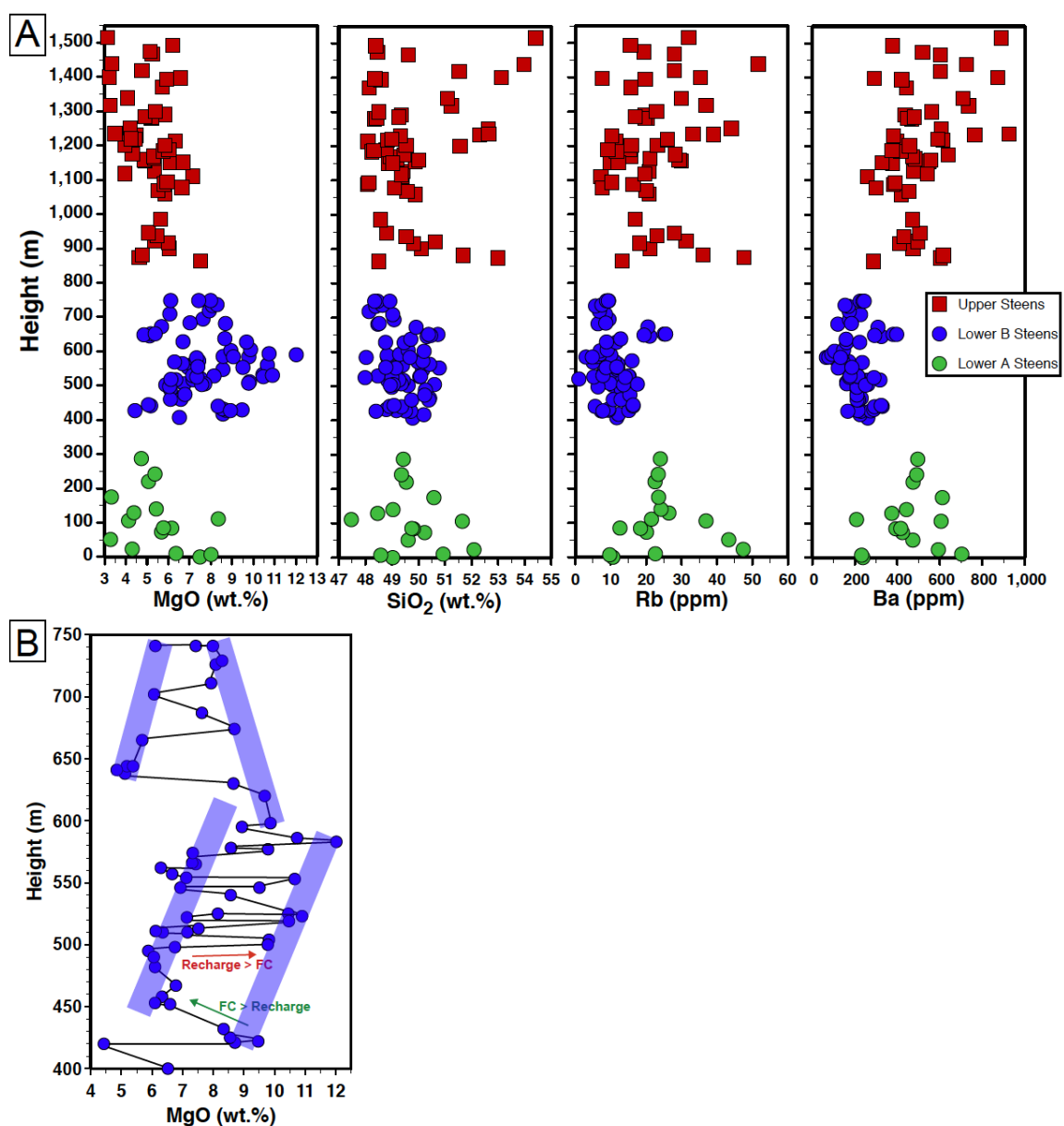
Figure 2.10. (A) Stratigraphic height versus MgO, SiO$_2$, Rb, and Ba. Systematic variations up section are evident, which has led to the informal designation of lower Steens, herein lower B Steens (blue circles), and upper Steens (red squares) chemical groups. The lower A Steens (this study) is distinguishable from both the lower B and upper Steens chemical types. (B) Zoomed in view of MgO variation in lower B Steens section with height. Black lines connect flows by stratigraphic height to reveal the zig zag pattern between flows. Transparent blue bars highlight the high and low extremes of MgO (wt. %) and show that both of these increase up section to ~600 m. Higher in the section, the extremes are less systematic; the low extreme increases slightly up section whereas the high extreme decreases.
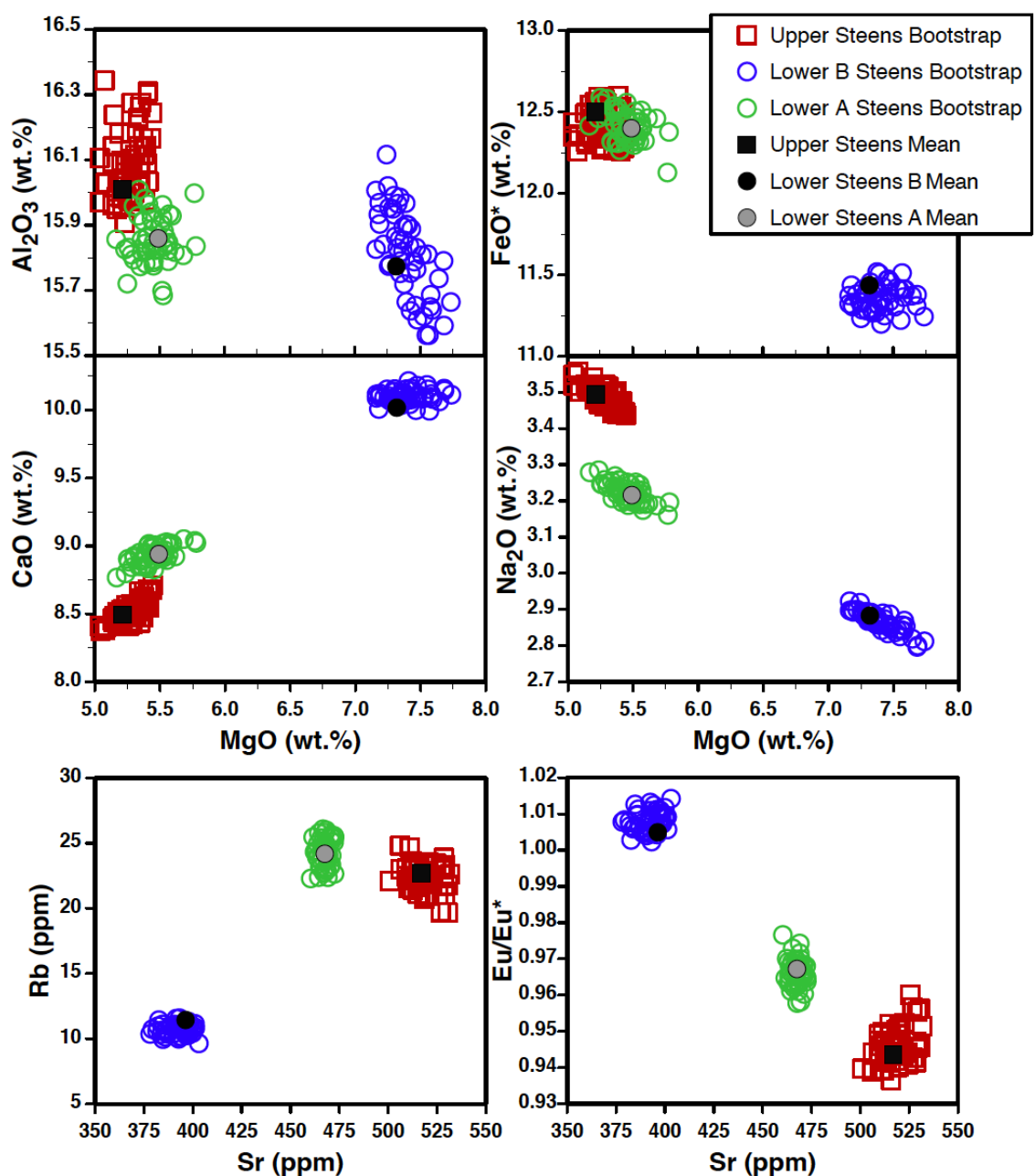
Figure 2.11. Bootstrapped mean values for select major elements versus MgO and trace elements versus Sr from the three Steens Basalt subgroups. The mean of the compositional data from each subgroup is shown in black (upper = squares, lower B = circles) or gray (lower A = circles) to demonstrate that these values are consistent with the bootstrap calculated mean values. See text for a discussion of the bootstrapping technique.
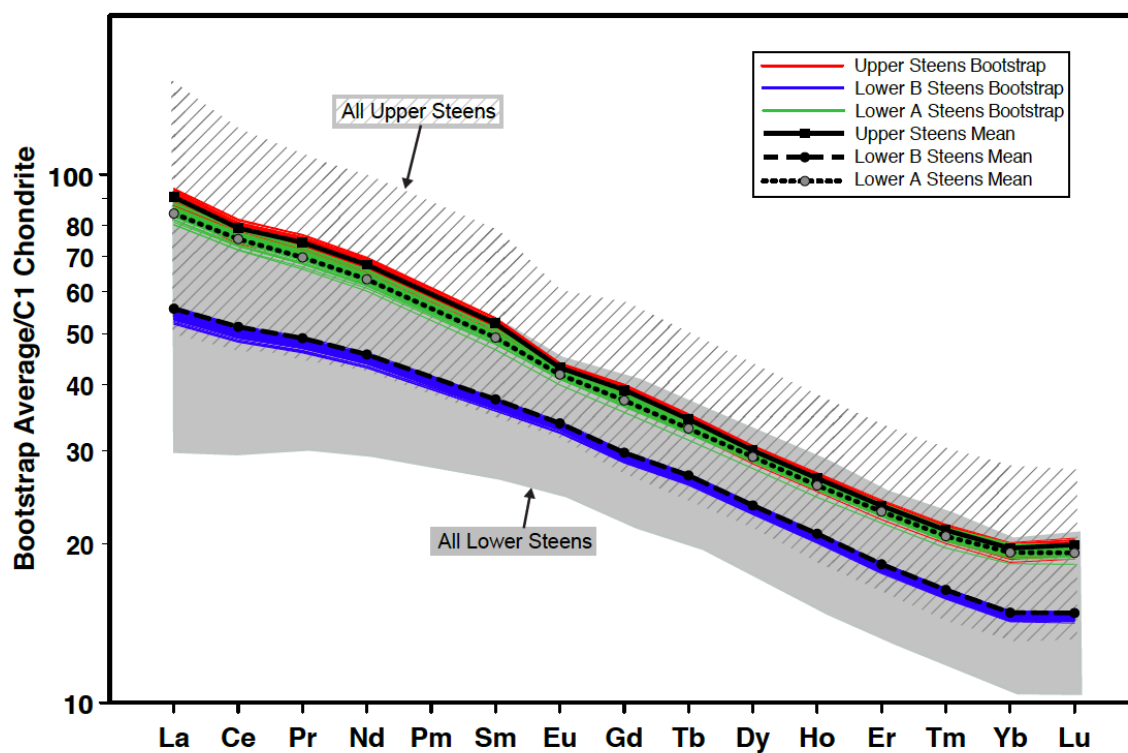
Figure 2.12. Chondrite normalized REE diagram of all analyzed Steens Basalt and bootstrapped mean values from the Steens subgroups. Gray field outlines the full range of lower Steens REE compositions, pattered field with diagonal lines encompasses the full range of upper Steens REE compositions.
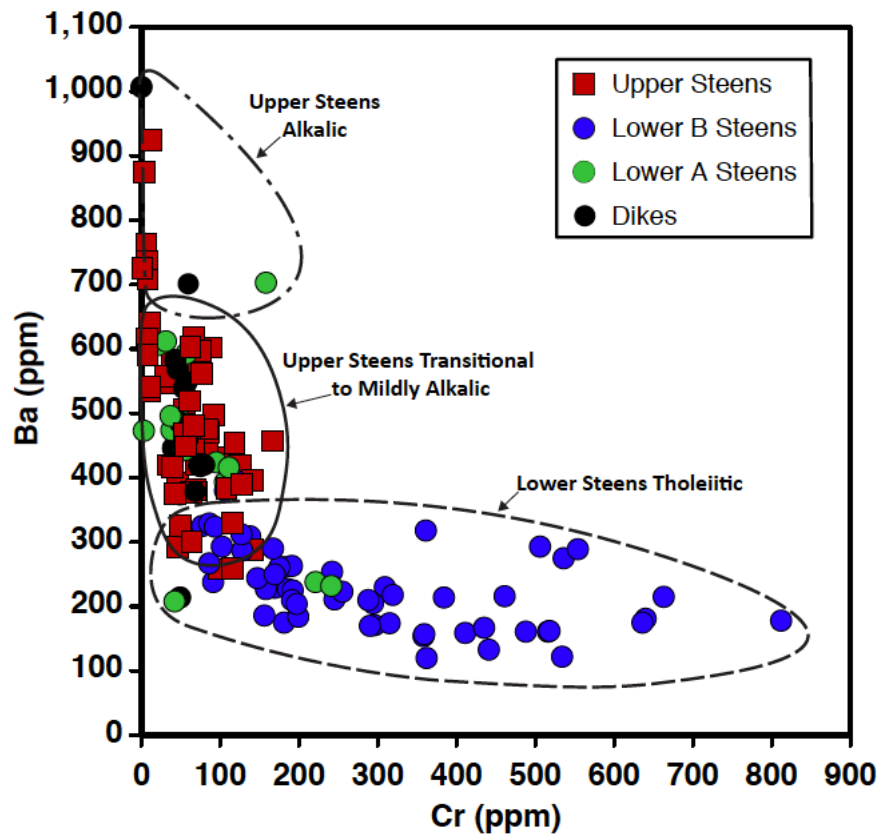
Figure 2.13. Ba versus Cr as a discriminant between lower and upper Steens, after Camp et al. 2013. All lower B Steens samples from this study fall within the Lower Steens Tholeiitic field, whereas the lower A Steens and upper Steens samples fall in all three fields.
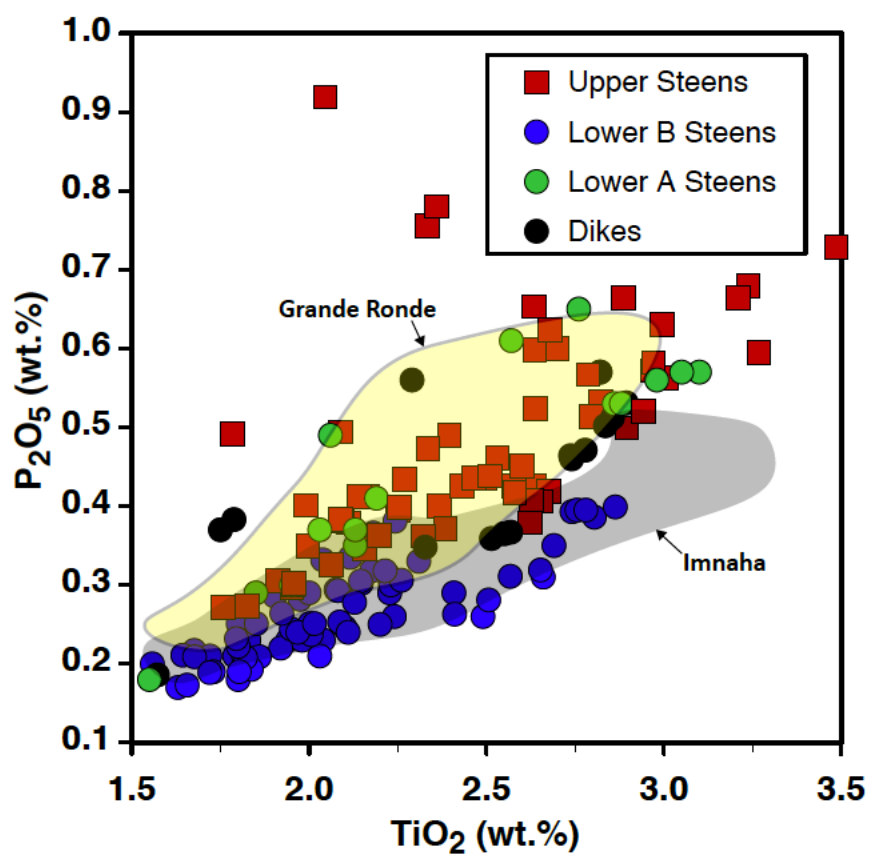
Figure 2.14. P_2O_5 versus TiO_2 for the lower A, lower B and upper Steens subgroups and dikes. Gray and yellow fields outline data from the Imnaha and Grande Ronde flows of the Columbia River Basalt Group, respectively. Imnaha and Grande Ronde compositional data from a precompiled file of CRBG chemistry in the GeoRoc database (accessed January 2017).
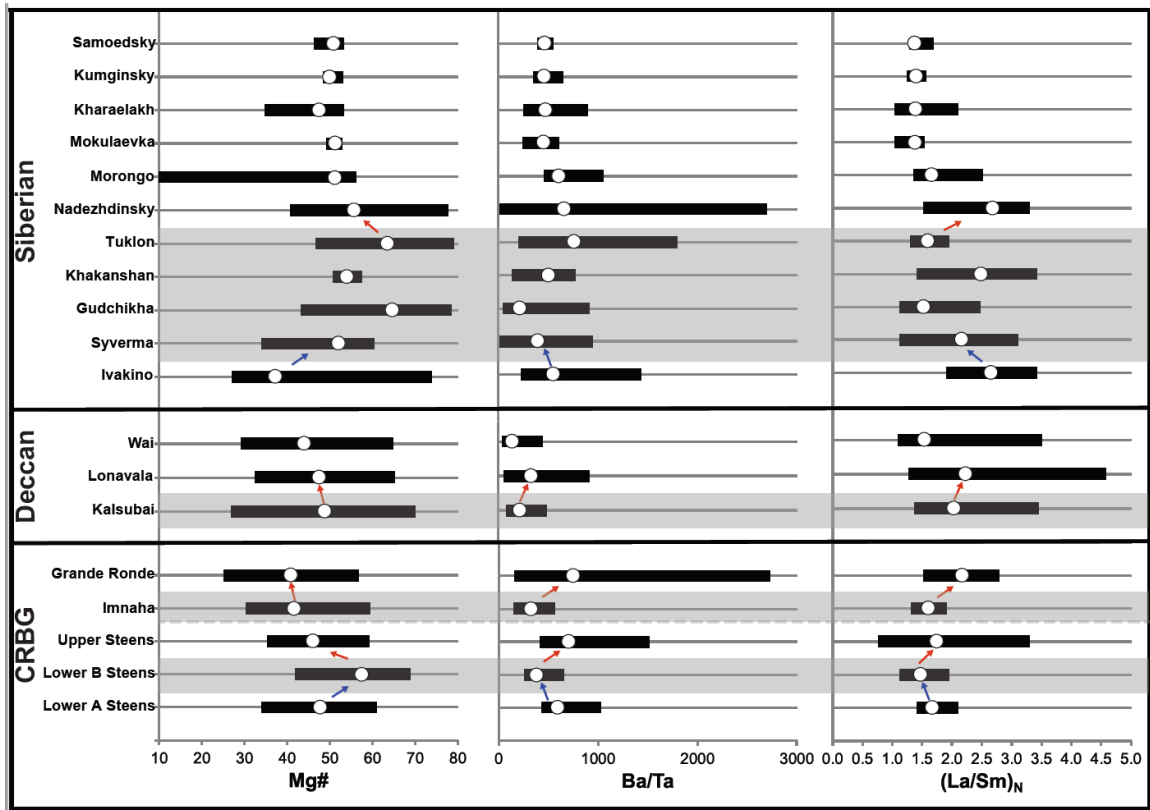
Figure 2.15. Temporal evolution of whole-rock Mg#, Ba/Ta and $(La/Sm)_N$ for the CRGB, Deccan Traps and Siberian Traps. Black bars represent the full range of values from each formation or subgroup; white circles represent the mean of each data range. Gray shaded regions highlight sections of each CFB where a mafic, recharge phase is evident. The individual CFB are ordered from most voluminous at the top (Siberian Traps), to least voluminous at the bottom (Steens Basalt). Formations are ordered stratigraphically within each CFB; the dashed gray line at the base of the Imnaha Basalt denotes a transition to the northward section of the CRBG. Blue arrows indicate a shift to a mafic compositional range within CFB (similar to the lower A-lower B Steens transition), whereas red arrows highlight a shift to more evolved compositional ranges (similar to the lower B-upper Steens transition). Imnaha Basalt, Grande Ronde Basalt, Deccan Traps, and Siberian Traps data from GeoRoc precompiled files (accessed June 2016 and January 2017).
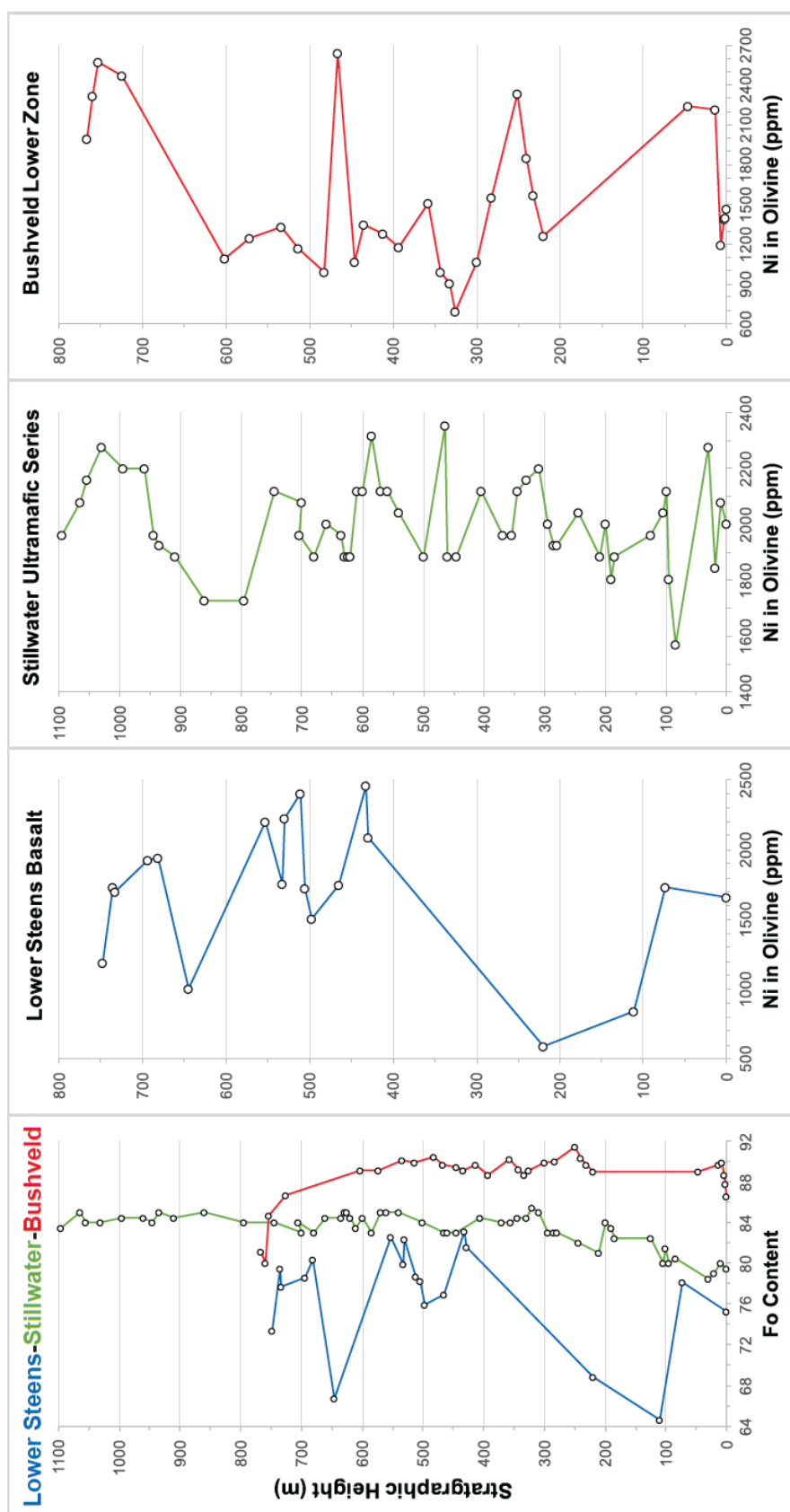
Figure 2.16. Changes in forsterite (Fo) and nickel (Ni) content (ppm) of olivine with stratigraphic height in the Steens Basalt, Stillwater Complex Ultramafic Series and Bushveld Lower Zone. Colored lines are coded blue for lower Steens, green for Stillwater, red for Bushveld. For the lower Steens and Bushveld, colored lines connect average Fo content at a given stratigraphic height, and open circles emphasize the location of these averages. For the Stillwater, the line and open circles represent one olivine composition at each given height from a section analyzed by Raedeke and McCallum, 1984. In the nickel content panels, the same symbology is followed, but instead each location has a separate panel. Note that the scales vary for both stratigraphic height and nickel content in each location. Bushveld data from the Turfspruit Section Lower Zone of Yudovskaya et al. 2013.

CHAPTER 3

Mantle sources and effects of crustal passage on the Steens Basalt

Moore, N.E.[1], Grunder, A.L.[1], Bohrson, W.A.[2], Carlson, R.W.[3]

[1]College of Earth, Ocean and Atmospheric Sciences, Oregon State University, Corvallis, OR 97331

[2]Department of Geological Sciences, Central Washington University, Ellensburg, WA 98926

[3]Department of Terrestrial Magnetism, Carnegie Institution for Science, Washington DC 20015

3.1 ABSTRACT

Mantle source characterization is an important step in developing conceptual models for the generation and evolution of large igneous provinces. Characterizing the mantle input into the generation of these large volumes of mafic lavas can lead to a better understanding of how these types of magma systems are initiated. The Steens Basalt (~16.9 Ma) in southeast Oregon is the oldest formation of the Columbia River Basalt Group, representing the onset of this continental flood basalt (CFB). Radiogenic isotopic compositions least affected by crustal processes serve as important indicators of mantle contributions, particularly in CFB where lavas experience modification during passage through thicker crust, in comparison to their oceanic counterparts. We re-evaluate the mantle and crustal sources required to generate the Steens Basalt based on new and existing Sr, Nd, Pb, Hf, Os and O isotopic compositions as well as whole-rock major and trace element data. We concur with previous interpretations that the Steens Basalt was generated by melting of a combination of depleted upper mantle, and a more enriched, mantle endmember, and by contamination of continental crust. Two component mixing models suggest that the mantle sources contribute roughly equal proportions up through the waxing stage of the Steens Basalt, and then the depleted mantle component increases as magmatism begins to wane. Residual sulfides in the mantle source or sulfides fractionated early in the Steens Basalt magmatic system and incorporated into later melts are required to explain high Os concentrations in lavas from the waxing stage of magmatism. During the latest stage, when the crust has been thermally primed by continued magmatism, crustal contamination by mafic accreted terranes contributes to magma composition. Other geochemical effects from crustal passage are evident in a subset of lavas. Cryptic deep fractionation of abundant clinopyroxene results in enrichment of δ^{18}O in some flows, that is enhanced by later shallow fractionation of olivine ± clinopyroxene ± plagioclase. The three-stage petrogenesis of the Steens Basalt is further elucidated from these interpretations, presenting a schematic view of the magmatic system evolution from mantle through crust.

3.2 INTRODUCTION

The generation of large volumes of mafic magmas expressed as large igneous provinces (LIP) remains contentious. While largely agreed that buoyant, thermally or compositionally driven mantle upwelling anomalies are responsible, models for creating these anomalies range from mantle plumes (aka hotspots, e.g. Richards et al. 1989) to meteorite impacts (e.g. Ingle and Coffin, 2004). Others suggest that LIP may occur after delamination of dense lithospheric crustal roots and resulting mantle upwelling (Anderson, 2005; Elkins-Tanton, 2005). Volumes of magmas produced, areas inundated, and timescales of eruption vary among LIPs. Additionally, contributions from various mantle reservoirs and crustal components vary among and between oceanic LIPs and their crustal counterparts, continental flood basalts (CFB).

The relatively primitive nature of most LIP and CFB (Coffin and Eldholm, 1994) allows for deciphering mantle source characteristics using isotopic compositions. In comparison to oceanic LIP, CFB are typically more modified from their original mantle parentage due to storage and differentiation within the crust, which may permit contamination by the thick continental crusts through which they must ascend before erupting. CFB provinces include high-Mg primitive lavas, but also contain compositions consistent with crustal differentiation from high-Mg melts (e.g., Cox 1980; Thompson et al. 1983; Garfunkel 2008). It has also been proposed that melt from metasomatized mantle sources (e.g., Turner et al. 1996; Hawkesworth et al. 1999) or of eclogite (e.g., Takahahshi et al. 1998; Camp and Hanan 2008; Luttinen et al. 2010) can account for CFB compositions with lower MgO (~8 wt.% MgO) and Ni (<200 ppm). Still, isotopic characteristics can elucidate potential contributions from crustal versus mantle sources (cf. Melluso et al. 2006, Camp and Hanan, 2008; Wolff et al. 2008; Wolff et al. 2013; Heinonen et al. 2016). While the smallest and youngest CFB worldwide, study of the mantle source character and petrogenesis of the Columbia River Basalt Group (CRBG), particularly with reference to the earliest and most primitive phase, viz., the Steens Basalt, provides a detailed analysis of CFB generation, in contrast to much larger CFB provinces such as the Deccan and Siberian Traps. The Steens Mountain exposure offers a unique opportunity within a flood basalt province to study the evolution of an eruptive

system from a restricted area during the initiation of the magmatic event. Given the enormity of flood basalt provinces, such detailed flow-by-flow studies through the whole stratigraphy of a CFB event are difficult and often lead complicated interpretation as a consequence of the many processes that produce and modify magmas over the scale of a whole CFB province.

Many workers have studied the isotopic character of the Columbia River Flood Basalt Group (CRBG, Fig. 3.1) to interpret mantle source characteristics and crustal contribution to the generation of the lavas. Carlson (1984) suggested that three mantle reservoirs are responsible for the Sr, Nd, Pb and O isotopic character of Columbia Plateau formations of the CRBG: a depleted mantle endmember (C1, Fig. 3.2), a depleted mantle contaminated by young subducted sediment (C2, Fig. 3.2), and subcontinental lithospheric mantle enriched in incompatible trace elements by an ancient crustal or subduction source. He proposed that the extensive melting in this region was caused by back arc extension generated by subduction of the Juan de Fuca Plate. Isotopic and whole-rock characteristics of the Steens Basalt, now formally recognized as the earliest formation of the CRBG (Camp et al. 2013), led Hart and Carlson (1987) to suggest that the Steens Basalt is derived from a depleted mantle source and the parental magmas were contaminated by the arc related rocks that constitute the accreted basement terranes of eastern Oregon. Hooper and Hawkesworth (1993) demonstrated that the Picture Gorge Basalt (Fig. 3.2) is isotopically distinct from the other formations of the CRBG, shares affinity with high alumina olivine tholeiites of the High Lava Plains and other basalts formed by Basin and Range extension, and therefore has the largest proportion of depleted mantle input of all the CRBG. Wolff et al. (2008) and Wolff and Ramos (2013) suggested that the isotopic and trace element characteristics of the Steens and Picture Gorge Basalts can be produced by mixing various proportions of a mantle plume and depleted mantle component similar to Pacific mid-ocean ridge basalt (MORB), with contamination by either arc derived fluids (Picture Gorge) and/or mafic accreted terranes (Steens). They interpret the Imnaha Formation as dominantly representing an enriched, ocean island basalt (OIB)-like component (the "Imnaha Component", IC in Fig. 3.2), with the later Grande Ronde lavas (Fig. 3.2) sourced by the same IC mantle component

but extensively contaminated by cratonic crust. The Chief Joseph dikes, the source of the Imnaha and Grande Ronde Basalts, are in close proximity to the boundary of the craton (i.e., just west of the $^{87}Sr/^{86}Sr$ 0.706 line, Fig. 3.1). They further suggest that all CRBG lavas contain at least a minor subduction/arc component, and that this is likely due to contamination by accreted mafic terranes that make up the crust through which the bulk of the lavas traversed. Camp and Hanan (2008) presented new isotopic and trace element data on the Steens and Imnaha Basalts along with compiled data on the other informally designated main stage formations of the CRBG (Fig. 3.3), building on previous interpretations of mantle source and contamination components to suggest that a best fit genetic model for the CRBG is a mantle plume impinging on an extensional setting, which ultimately facilitated delamination of deep eclogitic crustal roots.

Although previous studies have produced radiogenic isotope data for a selection of Steens Basalts (Fig. 3.2), the study presented here is based on a comprehensive sampling of the entire Steens Basalt stratigraphy. The coupling of isotope data to detailed geochemical interpretation of the three-phase evolution of the Steens Basalt (Moore et al. 2018, in press) can better resolve the changing mantle and crustal contributions that influence the compositions of these flood basalt magmas. In addition, a new distinct chemical stage of the Steens Basalt has been discovered (Moore et al. 2018, in press) for which isotopic compositions were not previously available. For this purpose, we here present new Sr, Nd, Pb isotopes (Fig. 3.2) and the first ever Hf, Os and $\delta^{18}O$ isotopic data from stratigraphically constrained samples of the Steens Basalt, to provide new description and quantification of the mantle and crustal components that contribute to generation of this earliest formation of the CRBG.

3.3 GEOLOGIC SETTING AND PETROLOGIC CONTEXT

The Steens Basalt (~16.9 Ma) of SE Oregon represents the onset of Columbia River Flood Basalt volcanism. These flows cover an area of 53,000 km^2 and have a total estimated volume of 31,800 km^3, or ~15% of the 210,000 km^3 estimated volume of the entire CRBG (Camp et al. 2013; Reidel et al. 2013). Eruptions emanated from dikes centered at Steens Mountain, where the Steens Basalt is the thickest and compositional

range is the widest (Fig. 3.3; Johnson et al. 1998; Camp et al. 2013; Moore et al. 2018, in press). The crust of eastern Oregon is made of accreted Paleozoic to Mesozoic mafic arc terranes stitched with Mesozoic plutons (Walker et al. 1991). Just to the northeast of Steens Mountain, the mid-crustal basement rocks are composed of the late Triassic to Cretaceous Olds Ferry arc terrane (Kurz et al. 2017). The earliest flows of the Steens Basalt are of reversed polarity and transition to normal polarity around the 16.7-16.5 Ma Steens magnetic reversal (Jarboe et al. 2008; 2010; Mahood and Benson, 2017) during the later stage of upper Steens Basalt eruptions (Fig. 3.3). Shortly after the magnetic reversal and coeval with the waning stage of the Steens eruptions, volcanism of the CRBG shifted northward to the Columbia plateau where flows emanated from the Chief Joseph Dike Swarm to first produce the Imnaha Basalt, and then the most voluminous of the CRBG formations, the Grande Ronde flows (Figs. 3.1 and 3.3). The Picture Gorge Basalt erupted coeval with the Grande Ronde Basalt, but from the Monument Dike Swarm in north central Oregon (Figs. 3.1 and 3.3). These units represent the bulk of CRBG volcanism, though eruptions continued through ~6 Ma (Reidel et al. 1989).

The type section of Steens Basalt at Steens Mountain (Camp et al. 2013) has been well sampled and studied (Johnson et al. 1998; Moore et al 2018, in press), and thus the data illustrate stratigraphic changes through time. Compositional distinctions between the early and later flows are evident from major, trace element and isotopic compositions, resulting in an informal designation between "lower" and "upper" units (Johnson et al. 1998, Camp et al. 2003, Camp et al. 2013). The Steens Basalt is known for flows with very large (>1cm) and abundant plagioclase phenocrysts, or giant plagioclase basalts (GPB). These flows are present in each Steens Basalt stage, but vary in textural type throughout the section (Moore et al. 2018, in press). $^{87}Sr/^{86}Sr$ of plagioclase from a variety of lava textures in the lower B and upper Steens Basalt are generally in equilibrium with whole-rock $^{87}Sr/^{86}Sr$, suggesting these crystals grew within the Steens magmatic system and are not xenocrystic (Toth, 2018). GPB are abundant in the Imnaha Basalt (Hooper et al. 1984; Reidel et al. 2013) and are also present in the Picture Gorge Basalt (Bailey, 1989).

A detailed stratigraphic petrologic and compositional analysis of the Steens Basalt that includes sampling of multiple sections at Steens Mountain records a three-stage evolution of the thermal waxing and waning of a major pulse of basalt interacting with the crust (Moore et al. 2018, in press). The earliest stage, the lower A Steens Basalt, is dominated by low volume magma flux and is characterized by initially heterogeneous compositions from variable recharge and fractionation, and culminates in homogeneous compositions (Fig. 3.3). The lower A stage represents early waxing of voluminous magma generation, that gives way to the next stage of rapid magma input and frequent eruption. This waxing stage, represented by the lower B Steens Basalt, yields an increasingly mafic magma system dominated by basaltic recharge that outpaces differentiation and contributes to substantial warming of the crust. This stage contains the most primitive and dominantly olivine phyric lavas, with compositions that are tholeiitic and incompatible trace element poor. Recharge dominates early in this stage, evident in the overall increasing MgO low in the section (Fig. 3.3), followed by dominance of fractional crystallization late in the stage, evident in the more evolved compositions up section (Fig. 3.3). This increase in differentiated character late in the lower B stage signals initiation of a waning stage with less frequent eruptions, called the upper Steens Basalt. During the upper Steens stage the magmatic system becomes more evolved, producing more alkalic compositions that are higher in trace element concentrations with more radiogenic Sr and Pb isotopic compositions (Figs. 3.2 and 3.3) as a consequence of reduced basaltic recharge and a contribution by crustal assimilation after prolonged magmatism has thermally primed the region. This interpretation of changes in differentiation processes through time in the Steens Basalt stages is supported by changes in mineral composition analogous to the cryptic variations in mineral phases up section in layered mafic intrusions, and similar changes are evident in other CFB (Moore et al. 2018, in press).

Computational modeling of the Steens Basalt magmatic system has further constrained the processes responsible for compositional modification of the magmas in time and served as an initial basis for quantification of the masses of recharge, fractional crystallization, and assimilation in the lower B and upper Steens Basalt. Results of

Energy-Constrained Recharge, Assimilation and Fractional Crystallization (EC-RAFC) models focused on Sr concentrations and $^{87}Sr/^{86}Sr$ in both the lower B and upper Steens Basalt suggest subequal masses of both recharge and crustal assimilation for these two stages (Bendaña, 2016). In contrast, major element modeling of the lower B and upper Steens Basalt stages using the Magma Chamber Simulator (MCS) suggest that recharge masses in the lower B Steens are nearly double that of the upper Steens, and conversely fractional crystallization masses are nearly double in the upper Steens compared to the lower B stage (Graubard, 2016). These MCS models do not require crustal assimilation in the lower B stage, but suggest a significant contribution by crustal melts to the generation of the more evolved upper Steens lavas. An important outcome of both the initial EC-RAFC and MCS modeling is that a single magma chamber model is untenable, given that the volumes of recharge required to raise MgO to nearly primitive compositions from lavas that have fractionated to the low MgO end are too vast to accommodate such a model. Crustal staging of the Steens Basalt must occur in a tiered, multi-level magmatic system rather than a single chamber.

MCS modeling focused on the geochemical changes upsection within the waxing, lower B Steens Basalt stage (Chapter 4) seeks to characterize the generation of two distinct MgO trends; a high and low MgO trend, which displays consistent ΔMgO (the change in MgO content between stratigraphically continuous samples from low to high MgO) of ~4-5 wt.% as MgO increases in both trends early during the stage (Fig. 3.3). These models reveal that frequent and increasingly voluminous recharge events, up to 7 times the volume of the existing magma chamber, with small intervals of cooling and crystal fractionation between recharge events, produces the initially increasing magnesian character upsection in the high MgO trend. Declining MgO in the remainder of the high MgO trend is consistent with a combination of fractionation, olivine gabbro cumulate entrainment, and magma + cumulate mixing with a variety of lower B Steens Basalt high MgO compositions at mid to upper crustal levels. Some of the lower B Steens high MgO trend samples in this declining MgO stage display a secondary trend towards high Al_2O_3 with decreasing MgO and Rb that cannot be explained by fractional crystallization alone (Fig. 3.4), and are consistent with mixing of an evolved, iron and titanium rich melt with

40% plagioclase cumulate entrainment (Chapter 4). Compositions on the low MgO trend are consistent with ~15% fractionation of a parent magma from the high MgO trend, with storage at shallower, upper crustal levels. Low MgO trend GPB compositions are produced by entrainment of troctolite cumulates into the ~15% fractionated melts of the low MgO trend. The shallower reservoirs in which the low MgO trend magmas fractionate are pulsed by periodic recharge from the primitive reservoir to produce the increasingly magnesian character in this trend that mirrors the high MgO trend at consistent ΔMgO early in the lower B Steens stage (Chapter 4).

Though the petrochemical changes evident through time within the Steens Basalt stages have been shown to be partially due to variations in dominant differentiation processes, magma input volumes and eruption rates (Moore et al. 2018, in press), there is undoubtedly variability that results from differences in mantle source and partial melt generation and/or crustal contributions, as shown by many other workers (Fig. 3.2). Given the geochemical stratigraphic control available, the Steens Basalt presents an exceptional opportunity to study changes in mantle and crustal input through time during this stage of the CRBG, and adding more detailed stratigraphically controlled isotopic data aids in constraining and quantifying contributions identified through textural and geochemical analysis and petrologic modeling.

3.4 ANALYTICAL METHODS

New isotopic data are presented from samples collected for this study from several stratigraphic sections along Steens Mountain (Moore et al. 2018, in press), and from samples collected by Johnson et al. (1998) from the type section at Steens Mountain (Camp et al. 2013). Whole-rock major and trace element compositions for NMSB- series samples are reported in Moore et al. (2018, in press), and for the JS- and MF94- series samples in Johnson et al. (1998) and Wolff et al. (2008).

3.4.1 Radiogenic Isotopes

Preparation and analysis of samples for Sr, Nd, Pb, Hf and Os were performed at Carnegie Institution for Science Department of Terrestrial Magnetism (DTM) and for Sr,

Nd, and Pb at New Mexico State University's Analytical Geochemistry Research Laboratory (NMSU). Analytical methods for NMSU are detailed in Bendaña (2016). For work conducted at DTM, fresh rock chips from each sample were powdered in an alumina ceramic dish to avoid contamination of metals. To digest powders for Sr, Nd, Pb and Hf, approximately 50 mg of powder was weighed from each sample and dissolved in a mix of ~2 mL of concentrated HNO_3 and ~4 mL concentrated HF. The mixture was sealed in 15 mL Savillex Teflon beakers and placed on a 90°C hotplate overnight. The solutions were evaporated to dryness and redissolved twice in 1 mL of concentrated HNO_3. To ensure complete dissolution, the samples were dissolved again in 4 mL of 4M HCl, evaporated to dryness, dried two more times with 0.5 mL of 0.5N HBr, and redissolved in 3 mL of 0.5N HBr.

Following digestion, Sr, Nd, Pb and Hf were separated and purified by column chromatography. Lead was first separated following the protocol of Carlson et al. (2006), by loading the samples on 0.04 mL Teflon columns with AG1-X8 100-200 mesh anion-exchange resin using HNO_3 and HBr as eluants. The Pb fraction collected in HNO_3 was purified by running it though the columns a second time. The HBr fraction that contained all other elements was evaporated, oxidized with 0.5 mL of concentrated HNO_3 to drive off HBr, evaporated again to dryness, redissolved in 5 mL of 0.1N HF-1N HCl, and allowed to sit on a 90 °C hotplate for one hour. The samples were centrifuged, the liquid was carefully removed from any precipitate, then loaded on 0.6 x 20 cm columns with AG50W-X8 200-400 mesh cation-exchange resin. Hafnium was separated following a procedure modified from that of Patchett and Tatsumoto (1980), first by collecting the initial solution and an additional 5 mL of 0.1N HF-1N HCl. Next, 30 mL of 2.5N HCl was loaded and discarded, then Sr was collected with 14 mL of the same solution. 14 mL of 4N HCl was loaded and discarded, then Sm-Nd were collected in 16 mL of the same solution. Hafnium was purified using the procedure of Münker et al. (2001) on 0.6 x 10 cm columns using Eichrom LN 100-150 μm resin. The sample was loaded in 5 mL of 2.5N HCl and rinsed with 10 mL 2.5N HCl, 10 mL 6N HCl, 4 mL of Milli-Q water, 60 mL of 0.09 N Citric acid-0.45M HNO_3-1wt.% H_2O_2, 5 mL of 0.09 N Citric acid-0.45M HNO_3, and 20 mL of 6N HCL-0.06N HF. The purified Hf fraction was collected in 8 mL

of 6N HCl-0.4N HF. Strontium was purified on 0.25 mL Teflon columns with Eichrom Sr resin by loading in 1.5 mL of 2N HNO_3 and rinsing with 2 mL of the same solution. The purified Sr fraction was collected in 2 mL of 0.05M HNO_3. Neodymium was separated from the other REE following the procedure of Garcon et al. (2017) on columns with 50-10 μm LN spec resin. The sample was loaded in 0.2 mL 0.173M HCl, rinsed with 10.75 mL 0.173M HCl, and the Nd fraction was collected in 9 mL of the same solution.

Strontium, Nd and Os were measured on the Thermo-Fisher Triton thermal ionization mass spectrometer. Strontium was loaded on Re filaments in 1μL 4N HNO_3 along with 0.5 μL H_3PO_4-HF-Ta_2O_5 slurry (Birck, 1986). Each ratio reported in Table 3.1 is the average of 200-300 ratios obtained using 8 second integrations with a signal size from 3 to 27 x 10^{-11} amps of ^{88}Sr. Potential Rb interference was monitored at ^{85}Rb, for which the $^{85}Rb/^{86}Sr$ was below 1 x 10^{-5} for all analyses. Mass fractionation was corrected using exponential mass dependency and $^{86}Sr/^{88}Sr = 0.1194$. The Sr standard NBS987 was measured multiple times during analytical sessions and averaged 0.710243 ± 0.000002 for n = 10, where uncertainty is 2σ. Uncertainties for the samples are provided in Supplement 6. In all cases, the uncertainty on $^{87}Sr/^{86}Sr$ was <0.00003.

Neodymium was loaded on double Re filaments and analyzed with ^{140}Ce and ^{147}Sm as interference monitors. Each ratio reported in Table 3.1 is the average of 240-270 ratios obtained using 8 second integrations with a signal size from 1.1 to 2.6 x 10^{-11} amps of ^{144}Nd. Mass fractionation was corrected using exponential mass dependency and $^{146}Nd/^{144}Nd = 0.7219$. The Nd standard JNdi was measured multiple times during analytical sessions and averaged 0.5121213 ± 0.0000018 (n = 2), 0.5121027 ± 0.0000015 (n = 2), 0.5121150 ± 0.0000018 (n = 5), with the differences in values reflecting the ageing of the faraday cups between the different analytical sessions. The reported uncertainties are 2σ. Data for the samples are adjusted to a JNdi value of 0.512115 (Tanaka et al. 2000) based on the average value determined for JNdi during the separate analytical sessions. Uncertainties for the samples are provided in Supplement 6. In all cases, the uncertainty on $^{143}Nd/^{144}Nd$ was <0.000024.

Lead and Hf isotopic compositions were measured on the Nu HR multicollector ICP-MS and Nu Plasma II multicollector ICP-MS. Lead samples were introduced into the plasma in 0.5 mL 0.4N HNO_3 using a Teflon nebulizer with a 50 mL/min uptake and a glass cyclonic spray chamber. Each ratio reported in Table 3.1 is the average of 41-50 ratios obtained using 10 second integrations. ^{208}Pb signals ranged from 0.1 to 5.5 x 10^{-11} amps, and Tl was added to generate a ^{205}Tl signal of ~1 x 10^{-11} amps. Mass fractionation was corrected first to $^{205}Tl/^{203}Tl = 2.3875$, and then adjusted for the difference between the NBS981 Pb standards measured every 3 samples and the reported value for the standard (Todt et al. 1996). Average values for NBS981 obtained during analytical sessions for n = 13 measurements were $^{208}Pb/^{204}Pb = 36.701 \pm 0.005$, $^{207}Pb/^{204}Pb = 15.492 \pm 0.002$, and $^{206}Pb/^{204}Pb = 16.940 \pm 0.002$ where uncertainty is 2σ. Uncertainties for the samples are provided in Supplement 6. In all cases, the uncertainty on $^{208}Pb/^{204}Pb$ was <0.07, on $^{207}Pb/^{204}Pb$ <0.03, on $^{206}Pb/^{204}Pb$ <0.03, on $^{208}Pb/^{206}Pb$ <0.0002, and on $^{207}Pb/^{206}Pb$ <0.0002.

Hafnium isotopic compositions were measured by introducing samples into the plasma in 0.08N HNO3 – 0.06N HF via a Teflon nebulizer with a 50 mL/min uptake and an MCN-6000 desolvating nebulizer, and analyzed with ^{173}Yb, ^{175}Lu, ^{181}Ta, and ^{183}W as interference monitors. $^{175}Lu/^{177}Hf$ and $^{173}Yb/^{177}Hf$ were less than 6.8 x 10^{-4} for all runs (Supplement 6). The Hf standard JMC475 was Yb doped to improve these corrections by adjusting the $^{173}Yb/^{176}Yb$ ratio to achieve the most accurate correction for ^{176}Yb on ^{176}Hf. Each ratio reported in Table 3.1 is the average of 52-80 ratios obtained using 10 second integrations where signal size of ^{178}Hf ranged from 0.8 to 10.9 x 10^{-11} amps. Mass fractionation was corrected to $^{179}Hf/^{177}Hf = 0.7325$. The average of JMC475 obtained during analytical sessions for n = 13 measurements were $^{176}Hf/^{177}Hf = 0.282166 \pm 0.000002$ where uncertainty is 2σ. Reported $^{176}Hf/^{177}Hf$ (Table 3.1) were adjusted by the offset between the average of the JMC475 standards run in each session and the reported value of 0.282160, which overlaps within uncertainty with the value of 0.282163 reported by Blichert-Toft et al. (1997). Uncertainties for the samples are provided in Supplement 6. In all cases, the uncertainty on $^{176}Hf/^{177}Hf$ was <0.000007.

For Os isotopic determinations, approximately 2 g of sample was weighed and spiked with mixed ^{185}Re-^{190}Os enriched spikes. Samples were digested in HNO_3-HCl following the modified Carius tube procedure of Shirey and Walker (1995). Os was extracted with CCl_4 using procedures described by Carlson et al. (2006). The Os was further purified by the microdistillation procedure described by Roy-Barman and Allègre (1994). Os isotopic compositions reported in Table 3.2 were measured by negative thermal ionization on a Thermo-Fisher Triton thermal ionization mass spectrometer. Samples were loaded on Pt filaments with $BaOH_2$ and analyzed by peak hopping on an electron multiplier measuring all Os isotopes and ^{185}Re for potential interference. Mass fractionation was corrected to ^{192}Os/^{188}Os = 3.08259. The Os standard JMOs was measured multiple times during analytical sessions and averaged ^{187}Os/^{188}Os = 0.17383 ± 0.00006 for n = 3 where uncertainty is 2σ. Replicate Os isotopic analyses on two separate dissolutions of two samples indicate reproducibility in Os concentration and ^{187}Os/^{188}Os of 4% and 0.8% respectively for NMSB5, and 6% and 1.4% respectively for NMSB18. Re was separated by the method described in Carlson et al. (2006) using AG1-X8 anion exchange resin, and isotopic compositions reported in Table 3.2 were measured on the ThermoFisher iCap-Qc RF quadrupole. Signal size for ^{185}Re and ^{187}Re ranged from ~56,000 to 108,000 and ~62,000 to 136,000 counts per second, respectively. A Re standard made from dissolved Re metal was measured multiple times during the analytical session and averaged ^{185}Re/^{187}Re = 0.593 ± 0.004 for n = 4 where uncertainty is 2σ. This standard value was used to correct sample measurements for instrumental mass fractionation.

To test for interlaboratory bias, sample JS44 was analyzed at both DTM and NMSU. The isotopic standards used at both labs are identical for Sr, Nd, and Pb. Reproducibility between laboratories for ^{87}Sr/^{86}Sr, ^{143}Nd/^{144}Nd, ^{206}Pb/^{204}Pb, ^{207}Pb/^{204}Pb, and ^{208}Pb/^{204}Pb are 0.007%, 0.002%, 0.6%, 0.4%, 0.3%, respectively. Samples with reported values for ^{176}Hf/^{177}Hf in Table 3.1 are those analyzed at DTM, the remainder were analyzed at NMSU.

3.4.2 Oxygen Isotopes

Plagioclase mineral separates were extracted from crushed samples from 15 flows. The crushed samples were sieved to a grain size >0.3 mm, magnetically separated to remove groundmass, and the freshest plagioclase was hand-picked under plain light. Oxygen isotopes were measured in plagioclase samples via an integrated CO_2 laser fluorination MAT 253 isotope ratio mass spectrometer (IRMS) system at the University of Oregon (Bindeman, 2008; Loewen and Bindeman, 2015). The range of material analyzed from each sample was 1.2 to 1.5 mg. The Gore Mountain Garnet standard (UOG, accepted $\delta^{18}O$ = 6.52‰) was measured multiple times (n = 5) during the analytical session to correct for instrumental drift (Loewen and Bindeman, 2015). Analytical precision of UOG analyses from the session was 0.08% (2σ). Some slight variability between replicate analyses from separate aliquots of four samples is likely due to within sample variability in plagioclase.

3.4.3 Helium Isotopes

Helium isotope analyses on olivine separates from two samples were performed using a Nu Instruments noble gas mass spectrometer at Oregon State University, following procedures described in Graham et al. (2014). Helium concentrations were determined by peak height comparison to standards of known size. Over the course of this study the ^4He blank level was 2.2×10^{-11} std cm^3. Blank-corrected ^4He concentrations in the samples (NMSB19 olivine, 243 mg, and NMSB49 olivine, 101 mg) were 0.72 and 0.86 $\times 10^{-9}$ std cm^3/g, respectively. Both analyses were below the ^3He detection limit of 2.5×10^{-16} std cm^3 (6700 atoms), which is estimated from the ^3He blank variability (defined as 3 standard deviations about the mean). The maximum $^3He/^4He$ ratio in the samples is therefore 0.25 R_A ($[2.5 \times 10^{-16}/0.72 \times 10^{-9}]/1.4 \times 10^{-6}$), indicating that at such low helium concentration levels, crustal/radiogenic helium is dominant.

3.5 RESULTS

3.5.1 Sr, Nd, Pb and Hf Isotopes

Steens Basalt samples generally plot as an array between MORB-like (global/Pacific MORB fields) and more enriched OIB-like compositions in most isotopic space (Figs. 3.2 and 3.5). All samples fall within the mantle array field (Hart et al. 1986) in $^{143}Nd/^{144}Nd$ versus $^{87}Sr/^{86}Sr$ (Fig. 3.5A), and near the mantle array line (Graham et al. 2006) in $^{143}Nd/^{144}Nd$ versus $^{176}Hf/^{177}Hf$ (Fig. 3.5B). At a given $^{206}Pb/^{204}Pb$, the lower Steens tends to have higher $^{87}Sr/^{86}Sr$ (Fig. 3.2) and lower $^{143}Nd/^{144}Nd$ and $^{176}Hf/^{177}Hf$ than the upper Steens. In general, samples from the lower B Steens Basalt fall closer to the MORB fields, whereas most upper Steens Basalt lavas plot within the OIB fields. The lower A Steens Basalt compositions fall near the overlap of samples from the other two stages but tend to be more similar to lower B stage lavas (Fig. 3.5). In comparison to the other formations of the CRBG, lower B Steens Basalt overlaps with some Picture Gorge Basalt compositions, though the Picture Gorge Basalt has more MORB-like character overall. The upper Steens Basalt overlaps with Imnaha Basalt compositions but does not range to as high values of $^{87}Sr/^{86}Sr$ and $^{206}Pb/^{204}Pb$ (Figs. 3.2 and 3.5). These results are consistent with previous isotopic data reported for the Steens Basalt (Camp and Hanan, 2008; Wolff et al. 2008), but the new data exhibit an expanded range of compositions (Fig. 3.2).

3.5.2 Os Isotopes and Concentrations

$^{187}Os/^{188}Os$ for lower B Steens Basalt samples are remarkably homogenous (Fig. 3.6). Though the lavas span MgO compositions from ~6-11 wt.%, $^{187}Os/^{188}Os$ only ranges from 0.1292 to 0.1311 and $^{187}Os/^{188}Os_i$ from 0.1282 to 0.1296 (Figs. 3.6 and 3.7, Table 3.2). This limited range of $^{187}Os/^{188}Os$ falls at the low end of reported compositions for both global MORB and OIB (Fig. 3.6), and therefore does not distinguish lower B Steens Basalt as having more MORB or OIB-like character. Although $^{187}Os/^{188}Os$ is restricted in this stage of the Steens Basalt, the samples span the full range of $^{87}Sr/^{86}Sr$ for all lower B Steens Basalt (Figs. 3.2 and 3.7). The lower B Steens Basalt plots within or near the field of Pacific MORB in both $^{187}Os/^{188}Os$ versus $^{87}Sr/^{86}Sr$ and $^{187}Os/^{188}Os$

versus $^{206}Pb/^{204}Pb$ (Fig. 3.7). A decrease in $^{87}Sr/^{86}Sr$ and $^{206}Pb/^{204}Pb$ is roughly correlated with an increase in stratigraphic height within this stage of the Steens Basalt (Fig. 3.7). Compared to worldwide MORB and the Imnaha Basalt of the CRBG, Os concentrations are uniquely high in the lower B Steens Basalt (~300-900 ppt) with values higher than the bulk of MORB and OIB (blue and purple fields, Fig. 3.6).

$^{187}Os/^{188}Os$ from the upper Steens Basalt is much more radiogenic (0.2824) than in the lower B Steens Basalt stage; Os concentration is also very low (1.5 ppt). The upper Steens Basalt flow analyzed for Re-Os is located approximately 250 m into the upper Steens Basalt section at Steens Mountain, where the total thickness of that stage is ~650 m. The MgO content of the sample is ~7 wt.%, comparable to the lower end of MgO among samples analyzed for Re-Os from the lower B Steens Basalt (Fig. 3.6). Even so, the upper Steens Basalt is higher in $^{187}Os/^{188}Os$, as well as $^{87}Sr/^{86}Sr$ and $^{206}Pb/^{204}Pb$, than the lower B Steens Basalt (Figs. 3.2, 3.5 and 3.7). $^{187}Os/^{188}Os$ and Os concentration in upper Steens Basalt are similar to those in the Grande Ronde Basalt, though are slightly less radiogenic (Fig. 3.6).

Osmium generally behaves compatibly in the Steens Basalt, and correlates with other compatible elements; Os decreases with MgO, Ni and Cr (Fig. 3.8, MgO not shown). It also correlates broadly with other chalcophile elements such as FeO and Cu. Sulfides have not been identified in any sample of the Steens Basalt. Os concentrations in the lower B Steens Basalt range to higher values than are found in either the Imnaha or Grande Ronde Basalt, but most samples among the these three CRBG stages have similar FeO* and Cu content overall (Fig. 3.8).

3.5.3 Oxygen Isotopes

$\delta^{18}O$ in plagioclase from Steens Basalt lavas is somewhat restricted, with most values ranging from 5.9 to 6.6‰ (Figs 3.7, 3.8 and 3.9, Table 3.1). When compared to other members of the CRBG, the Steens Basalt is most similar to those with low $\delta^{18}O$ (Fig. 3.11), viz., the Imnaha and Picture Gorge Basalts. Higher values of 7.4‰ in the stratigraphically highest sample of the lower B Steens Basalt, and 8.5‰ from a dike in the upper Steens Basalt (Fig. 3.9) are more akin to the less mafic members of the CRBG,

the Grande Ronde, Wanapum and Saddle Mountain Basalts, that range from 5.9-8.5‰. Overall, most of the formations of the CRBG have elevated $\delta^{18}O$ compared to the bulk of basaltic magmas, which range from 5.5-5.9‰ (Bindeman, 2008).

Compositions for upper Steens Basalt are barely higher on average than lower B Steens Basalt; upper Steens lavas have a mean of 6.4‰ (mode = 6.2‰), compared to a mean of 6.3‰ (mode = 6.1‰) for lower B Steens lavas. An initial increase in $\delta^{18}O$ with stratigraphic height occurs in the lower B Steens Basalt samples, which is followed by a decrease upsection until reaching the highest, outlier value high in that stage (Fig. 3.9). There is no systematic change in $\delta^{18}O$ upsection within the upper Steens Basalt (Fig. 3.9).

There are two trends in $\delta^{18}O$ versus MgO and SiO_2 (Fig. 3.10). Most of the data define slightly increasing $\delta^{18}O$ (5.9 to 6.3‰) over 48-53 wt.% SiO_2, with a corresponding decrease in MgO from 9.5 to 4 wt. %. A second trend has markedly higher $\delta^{18}O$ (5.9 to 8.5‰) over the same SiO_2 range. We attribute the first trend to crystal fractionation and the second to crustal contamination.

Crystal fractionation of mafic phases can cause an increase in $\delta^{18}O$ of remaining melt. Fractionation of an assemblage of olivine, clinopyroxene and plagioclase from a magma with a starting composition of 6.0‰ would increase $\delta^{18}O$ by ~0.2‰ (Bindeman, 2008) over the given range of MgO and SiO_2 in Figure 3.10. These ranges of MgO and SiO_2 represent 60% and 70% crystallization, respectively, from a starting composition of 11 wt.% MgO and 48 wt.% SiO_2 (a primitive Steens Basalt sample composition) using the rhyolite-MELTS program (Gualda et al. 2012). The crystal fractionation trend closely follows the first trend noted in the bulk of the data (Fig. 3.10).

3.6 DISCUSSION

Radiogenic isotope compositions provide a unique window into interpreting mantle components responsible for generation of basalts. This is true even for magmas that have experienced significant differentiation in the crust, as is the case for most CFB, as they have a thick crustal gauntlet to traverse prior to eruption. Characterization of the mantle and crustal components in other well-studied CFB remains contentious. Fields that encompass the isotopic data for the two most voluminous CFB in the world, the

Deccan and Siberian Traps, are shown on Figure 12. Using radiogenic and stable isotope compositions, Peng et al. (1994) proposed that the mantle source of the Deccan Traps is a combination of a depleted upper mantle similar to Indian Mid-Ocean Ridge Basalt (near DS in Fig. 12) and an enriched, deeper mantle similar to the source of the Reunion hotspot (near ES in Fig.12). The primitive lavas from the Deccan are divided into high and low Ti types, which are suggested to result from deeper melting in the garnet stability field and shallower melting in the spinel stability field, respectively. These workers also propose that the bulk of Deccan lavas are contaminated by up to 40% melts of the local crust, composed of Archean amphibolite (Peng et al. 1994). In contrast, Melluso et al. (2006) suggest that there is little evidence for an enriched mantle source in the bulk of the Deccan Trap lavas, given the Reunion hotspot signature is limited to geographically restricted picrites from the north/northeast region of the Deccan Traps, and propose that the contaminant is subcontinental lithospheric mantle that has been modified by subducted sediment or fluids. They prefer a single "hybrid" mantle component, one that is similar to depleted Indian MORB mixed with a modified subcontinental lithospheric mantle, to explain the more radiogenic isotope compositions as well as elevated large ion lithophile and light rare earth element compositions (Melluso et al. 2006). For the Siberian Traps, Wooden et al. (1993) added greatly to the database of Lightfoot et al. (1990; 1993), all these studies reaching a similar conclusion that an enriched, deep mantle source is the primary contributor to partial melt generation for that CFB. Wooden et al. (1993) prefer a scenario in which extensive crustal processing and assimilation generate the more radiogenic compositions in the Siberian Traps, whereas Lightfoot et al. (1990; 1993) attribute these characteristics to a contribution by subcontinental lithospheric mantle. A Division of high and low Ti types, similar to the one proposed for the Deccan Traps, exists for Siberian Trap lavas, which are also explained by deep versus shallow partial melting in the mantle (Sharma, 1997). Given these characteristics, Sharma (1997) proposed that the high Ti, deeper mantle melts are from an enriched, plume source whereas the shallower, low Ti melts are from a depleted MORB like source, and that contamination comes from the subcontinental lithospheric mantle rather that the continental crust due to what he describes as relatively unradiogenic Pb values (Fig. 12).

Though the model for generation of both of these flood basalts is overwhelmingly attributed to an enriched mantle plume source, there appears to be a significant role for more depleted upper mantle contribution in both cases.

We present the most comprehensive isotopic data set for the Steens Basalt to date, in conjunction with existing whole-rock major, trace element and isotopic data, with the goal of further elucidating relative contributions by mantle and crustal components to the generation of the Steens Basalt, and ultimately quantifying the contributions by each component. These data confirm the interpretation by previous workers that two mantle sources contribute to generation of the lavas, a depleted and an enriched source, as is also suggested for other CFB such as the Deccan and Siberian Traps. These data verify that crustal contamination modifies primitive magma compositions during ascent through the crust, especially during the upper Steens Basalt stage, and suggest that additional crustal processes have affected the petrogenesis of subsets of lavas within the Steens Basalt stages. We provide quantification of the contributions by various components in time throughout the Steens Basalt magmatic evolution to infer a schematic model of the crustal processes and changes in crustal architecture during each stage of the Steens Basalt, as well as the contribution made to the crust by abundant crystal fractionation.

3.6.1 Mantle and Crustal Sources

Lower A Steens Basalt isotopic compositions overlap with the lower B and upper Steens Basalt lavas in Sr, Nd, Pb and Hf isotopic spaces (Figs. 3.5, 3.12 and 3.13) but are most similar to lower B stage lavas. This earliest stage was dominated by magmas stalling and fractionating in the crust (Moore et al. 2018, in press). Trace element data show the lower A Steens basalts have slightly higher ratios of LILE to HFSE elements (e.g. Ba/Ta and La/Ta) ratios compared to the lower B Steens basalts (Fig. 3.14). High LILE/HFSE ratios are typically associated with convergent margin magmas, continental crust and the sediments derived from the continents. Mixing such materials with typical mantle peridotite would be expected to exert a strong isotopic imprint simply because the Sr, Nd and Pb concentration of crustal materials is so much higher than typical mantle materials. The lack of an obvious isotopic distinction between the lower A and B Steens

Basalts suggests that a high Ba/Ta component could be added by assimilation of crustal wall-rock, which in the Steens area is primarily Paleozoic-Mesozoic accreted oceanic terranes, that have only a limited isotopic distinction compared to modern mantle. However, this may reflect repeated episodes of prolonged cooling and fractionation in the crust punctuated by periodic recharge events (Fig. 3.15). A model with episodes of prolonged fractional crystallization (40%) punctuated by periodic recharge from a primitive lower B Steens Basalt starting composition explain some lower A Steens Basalt Ba, Ta and Sr compositions (Fig. 3.15). The majority of lower A Steens Basalt compositions can be reached by a similar model of alternating fractionation and recharge from a starting composition of the most mafic upper Steens Basalt sample (Fig. 3.15). Ba increases 10-fold while Ta only increases 4-fold over the fractionation-recharge models, leading to the much higher Ba/Ta ratios in the lower A Steens Basalt. The models can also explain the increase in Sr over the range of Steens Basalt compositions. Given that fractionation outpaces recharge in the lower A Steens stage (Moore et al. 2018) and that the increase in Ba and Ta is controlled by abundant fractionation, this explains why higher LILE/HFSE ratios occur in the lower A but not lower B stage. More voluminous and frequent recharge keeps the incompatible trace elements low during the waxing, lower B stage. There is however one lower A Steens Basalt sample with anomalously high Ba/Ta at ~6 wt.% MgO that is a likely candidate for crustal contamination, given all samples from the other stages at that MgO content have much lower Ba/Ta (Figs. 3.14 and 3.15).

From the base through about halfway up the lower B Steens Basalt section, MgO increases in both minimum and maximum value at a relatively consistent ΔMgO of 4-5 wt.% (400-600 m, Fig. 3.3); this trend is interpreted to represent a recharge-dominated waxing stage of magmatism (Moore et al. 2018, in press). The highest MgO samples on this trend also have the lowest $^{87}Sr/^{86}Sr$ and $^{206}Pb/^{204}Pb$, suggesting that an enriched (ES) mantle source makes its greatest contribution early during the stage. Contributions from an incompatible element depleted mantle source (DS) component then increase in time within the lower B Steens Basalt section, as a decrease in both $^{87}Sr/^{86}Sr$ and $^{206}Pb/^{204}Pb$ roughly correlates increasing stratigraphic height, moving closer to or within the Pacific

MORB field (Fig. 3.7). This occurs during the waning stages of the lower B Steens Basalt, where fractionation begins to outpace recharge (Moore et al. 2018, in press) and maximum MgO decreases (above 600 m in Fig. 3.3). Given the lower B Steens Basalt lies on or very near the trend expected for mixing between DS and ES in Sr, Nd, Pb and Hf isotopic spaces (Figs. 3.2, 3.5, and 3.12), has mantle values of $^{187}Os/^{188}Os$ (Figs. 3.6 and 3.7), and low LILE/HFSE (Ba/Ta) ratios, little to no crustal contamination has affected the lavas of this stage.

The homogeneity in $^{187}Os/^{188}Os$ among samples of the lower B Steens Basalt over a range of MgO (Figs. 3.6 and 3.7) represents variable contributions by DS and ES components, suggesting that both of these sources have a similar $^{187}Os/^{188}Os$ signature. Given the small range of $^{187}Os/^{188}Os$, a significant amount of pyroxenite is not present in the Steens Basalt mantle source, as is suggested for some CFB (e.g. Pertermann and Hirschmann, 2003; Rogers et al. 2010; Heinonen et al. 2013), because pyroxenite tends towards high Re/Os ratios and hence evolves to high $^{187}Os/^{188}Os$ on even relatively short time scales.

The upper Steens Basalt lavas have higher $^{87}Sr/^{86}Sr$ and $^{207}Pb/^{204}Pb$, but lower $^{143}Nd/^{144}Nd$ at a given $^{206}Pb/^{204}Pb$ than the lower B Steens Basalt (Figs. 3.12 and 3.13). This trajectory is similar to, but not as pronounced as that of the Grande Ronde Basalts (Fig. 3.12), which are interpreted to have significant cratonic crustal contamination (Wolff et al. 2008; Wolff and Ramos, 2013). This trajectory in the upper Steens Basalt, coupled with high $^{187}Os/^{188}Os$ (much higher than lower B Steens Basalt samples at similar MgO) and both Ba/Ta and La/Ta ratios that are similar to the crustally contaminated Grande Ronde Basalt (Fig. 3.14), reflects the addition of a crustal component during the latest Steens Basalt stage. However, as shown for the lower A Steens Basalt, a model of repeated episodes of prolonged fractionation punctuated by periods of recharge can account for most of the elevated Ba/Ta ratios in the upper Steens Basalt (Fig. 3.15), and thus suggests relatively minor amounts of crustal contamination occurred during this stage. Given the location of the eruptive center at Steens Mountain and the relatively limited range in the isotopic composition of upper Steens Basalts compared to the Grande Ronde Basalt (Figs. 3.12 and 3.14; i.e. significantly higher and

more variable $^{87}Sr/^{86}Sr$ in the Grande Ronde lavas), mafic accreted terranes are the most likely contaminant for the Steens Basalt, rather than the suggested cratonic crust contaminant for Grande Ronde lavas. Assimilation of mafic crust by the Steens Basalt results in muted changes to Sr, Nd, Pb, and Hf isotopic compositions, and lower SiO_2 than the dominantly basaltic andesite compositions of the Grande Ronde Basalt (Hooper, 2000). Basaltic rocks, however, generally have very high Re/Os ratios in comparison to mantle peridotite and thus evolve to radiogenic Os quickly, allowing even young accreted mafic terranes to be characterized by sufficiently high $^{187}Os/^{188}Os$, and thus can serve as the contaminant of the upper Steens basalt measured here.

In an attempt to further characterize potential mantle source components that contribute to the generation of the Steens Basalt, isotopically distinct mantle endmembers originally defined by Zindler and Hart (1986) are shown in Figure 3.12. An additional component, ES (as defined by Rooney et al. 2012, based on the "C" mantle component of Hanan and Graham, 1996) is similar to the Imnaha component (Wolff and Ramos, 2013) and represents an enriched mantle source. There is no evidence for direct mixing from either EMI or HIMU to the Steens Basalt; none of the samples plot near or towards these endmembers in any isotopic space (Fig. 3.12). Contributions from an EMII component are unlikely as well. While the Steens Basalt samples, particularly those from the upper Steens Basalt, trend toward EMII for some isotopic combinations (Fig. 3.12A, B), this is not the case in all isotopic space (Fig. 3.12D-G).

Wolff and Ramos (2013) used incompatible trace element ratios in tandem with isotopic compositions in the CRBG to assist in deciphering mantle versus crustal contributions to the generation of the formations of the main stage (Steens, Imnaha, Grande Ronde and Picture Gorge Basalts). They noted that correlations between isotopes and LILE/HFSE in the Steens Basalt are weak (Fig. 3.14), but that La/Ta strongly correlates with Ba/Ta. They further note that the range of Ba/Ta in the lower B Steens Basalt is very small but increases in range and value in the upper Steens, increasing dramatically with decreasing MgO and slight increase in $^{87}Sr/^{86}Sr$ in the latter. They suggest this is most easily explained by contamination of accreted terranes as opposed to a subduction component in the mantle source. All new data presented in this study are

consistent with these trends. Given the low values and narrow range of Ba/Ta in the lower B Steens (Fig. 3.14), combined with Sr, Nd, and Pb isotopic values that are lower than expected for such a contaminant, a subduction component in the mantle source for this stage is not required.

3.6.2 Isotopic Mixing and AFC Models

To quantify mantle contributions to the generation of Steens Basalt, the most primitive Steens Basalt compositions (lower B Steens Basalt) are evaluated in light of various proportions of mixing between 5% partial melts from a depleted mantle source (DS), similar to a MORB source, and an enriched mantle source (ES), similar to but slightly more enriched than the Imnaha Component (Figs. 3.2, 3.5 and 3.7; Wolff and Ramos, 2013). Next, isotopic trends in the upper Steens Basalt, away from the mantle mixing curves are modeled by mixing of a crustal contaminant represented by 5% partial melts of compositions from the Olds Ferry Terrane.

For two components, 1 and 2, with different isotopic ratios and different concentrations of elements a and b, two component mixing can be calculated using the equations:

$$R_{mix}^a = R_1^a X_1^a + R_2^a (1 - X_1^a)$$

and

$$R_{mix}^b = R_1^b \left[\frac{X_1^a}{r(1 - X_1^a) + X_1^a} \right] + R_2^b \left[\frac{r(1 - X_1^a)}{r(1 - X_1^a) + X_1^a} \right]$$

and

$$r = \frac{(C^b/C^a)_2}{(C^b/C^a)_1}$$

where R_i is the isotopic ratio of component i, X_i is the elemental fraction contributed to the mixture from component i, and C is the concentration of element a or b in component i (DePaolo, 1981; as derived in Graham et al. 1992). Isotopic and elemental compositions used for mixing endmembers and elemental concentrations calculated for the 5% partial melts of each component are reported in Table 3.3. Partial melting of all endmember components was calculated by batch melting.

Parabolic mixing curves for 5% partial melts of both DS and ES are presented for all analyzed isotope systems in Figure 3.12 (A-H) and at a finer scale to show data detail for select isotopic systems in Figure 3.13. Steens Basalt compositions can be accounted for by a range of mixing proportions between the mantle sources, from 40DS:60ES to 70DS:30ES (Figs. 3.12 and 3.13). Lower A and B Steens Basalt compositions appear to have subequal contributions of DS and ES for the bulk of the data, but some lower B Steens have a larger DS contribution (70%); these are the samples highest in that section (Fig. 3.7); thus, the models confirm that basalt with a more depleted mantle source signature increasingly contributed to magmatism as the system waxed. The small deviations of some lower A and B Steens basalt samples away from the mantle melt mixing curves can be accounted for by a slightly different starting composition of DS or ES components, or, more likely, by slight contamination of partial melts from a third component represented by compositions from the Olds Ferry Terrane as in the upper Steens Basalt (Figs. 3.12 and 3.13). Upper Steens Basalt compositions plot farther from the DS-ES mantle melt mixing curves and have higher $^{87}Sr/^{86}Sr$ and $^{207}Pb/^{204}Pb$ but lower $^{143}Nd/^{144}Nd$ and $^{207}Pb/^{204}Pb$ at a given $^{206}Pb/^{204}Pb$ than strict mixing of DS-ES mantle melts would predict.

Nearly linear trends of the Steens Basalt along or tangential to DS-ES melt mixing curves exist in some models (Figs. 3.12E-F, 3.13D), suggesting that upper Steens Basalt samples could represent magmas sourced from 100% ES. However, upper Steens Basalt has been demonstrably affected by crustal contamination (see discussion above), and assimilation of partial melts from the Olds Ferry Terrane could produce similar trends that are either indistinguishable from the DS-ES melt mixing curves or cannot be assessed due to lack of data for the Olds Ferry compositions (i.e. for $^{176}Hf/^{177}Hf$ and $^{187}Os/^{188}Os$; Fig. 3.12).

The deviations from the DS-ES mantle mixing curves, particularly for the upper Steens Basalt, can be explained by mixing with 5% partial melts of compositions from the Olds Ferry Terrane (Kurz et al. 2017). Mixing was modeled between DS-ES melt mixtures and partial melts from the Olds Ferry Terrane for each isotopic system, where 2 mixing curves bracket the bulk of the data at a high and low end. For example, in

$^{87}Sr/^{86}Sr$ versus $^{206}Pb/^{204}Pb$, the calculated mixed melt compositions at 40DS:60ES and 50DS:50ES were each separately mixed with the Olds Ferry partial melt to create 2 mixing curves that bracket the bulk of the data (Fig. 3.13). Given that absolute concentrations of elements in the DS-ES mantle sources are uncertain, *r* for these crustal contamination models was adjusted so that the mixing curves capture the trends in the Steens Basalt data.

While a contribution of as much as 30% Olds Ferry partial melt component is suggested by the mixing curves for a few lower A and B Steens Basalt compositions, the bulk of the compositions from these stages do not require addition of a crustal component (Fig. 3.13). This is consistent with whole-rock major and trace element compositions as well as computational modeling (Graubard, 2016; Moore et al. 2018, in press; Chapter 4). In contrast, the upper Steens Basalt compositions fall on the mixing curves at 30-70% mixing of Olds Ferry partial melts to the DS-ES mantle melt mixes. This range of crustal melt addition is inconsistent with the major element compositions in the upper Steens Basalt. The 5% partial melts of Olds Ferry are tonalitic with ~69 wt.% SiO_2, and thus a contribution by 30% or more of this melt composition to a starting composition of 48 wt.% SiO_2 (a reasonable parent composition, see Chapter 4) would result in melts with silica compositions above 54 wt.%, the maximum value for the upper Steens lavas (Moore et al. 2018, in press). Therefore, the amount of crustal contamination must be less than 30%. However, the real composition of the crustal contaminant may be slightly different than the estimates used here, and the amount of partial melting of the crust could vary as well.

Comparing isotopic systems with elemental concentrations provides additional evidence of the required mantle and crustal components to the generation of Steens Basalts. Binary mixing between only DS melts and OF crustal melts plus fractionation can explain all the trends in the data for $^{87}Sr/^{86}Sr$ and $^{143}Nd/^{144}Nd$ versus 1/Sr and 1/Nd, respectively (Fig. 3.16). Fractionation drives compositions off the DS melt-OF melt mixing lines towards higher Sr and Nd (or lower 1/Sr and 1/Nd). However, the data straddle the DS melt-OF melt mixing curves in $^{87}Sr/^{86}Sr$ versus Ba and in all Pb isotopes versus 1/Pb (Fig. 3.16), ruling out the possibility that magma generation is solely

attributable to DS and OF components. The most primitive lower B Steens samples, those that most convincingly lack a crustal assimilation signature, instead display a trend between ES and DS melts, and the bulk of the other Steens Basalt data can be explained by fractionation from these most primitive samples (Fig. 3.16).

Abundant fractionation is clear in not only the isotopic versus trace element signature, but in the $\delta^{18}O$ compositions of the Steens Basalt as well. Compositions presented here are from plagioclase rather than whole-rock. A small fractionation factor exists between plagioclase and basaltic melt, resulting in a Δplagioclase-melt of ~0.2‰ (Zhao and Zheng, 2003), which suggests the Steens Basalt melt compositions are ~0.2 less than the values measured for this study. Accounting for this, the bulk of the data suggest a melt range of 5.8-6.0‰ (Fig. 3.11), which requires significant fractional crystallization from parental magmas that likely had initial $\delta^{18}O$ of 5.5‰. Fractionation of $\delta^{18}O$ between basaltic melt and clinopyroxene and olivine yield a Δclinopyroxene-melt and Δolivine-melt of ~0.4‰ and 1‰, respectively, making fractionation of these phases much more efficient at increasing $\delta^{18}O$ in the melt. Given that fractionation of the mineral assemblage in the Steens Basalt (olivine, clinopyroxene and plagioclase) only increases $\delta^{18}O$ by ~0.2‰ (Bindeman, 2008) over the given range of MgO and SiO_2 in the magmas, fractionation of large volumes of either clinopyroxene or olivine likely occurred prior to the shallow crustal staging recorded by barometry and suggested by modeling for the Steens Basalt magmatic system (Graubard, 2016; Moore et al. 2018; Chapter 4).

The mineral assemblage of the Steens Basalt changes with pressure/depth. Using rhyolite-MELTS (Gualda et. al 2012) and a parent magma of primitive lower B Steens composition (NMSB18; Moore et al. 2018), fractionation was modeled over the range of crustal pressures corresponding to the crustal thickness in the Steens Mountain region to determine the mineral assemblage at various depths (Fig. 3.17). From ~6-10 kbar, clinopyroxene is the sole liquidus phase, and fractionates alone until 40-45% crystallization. From ~4-5 kbar, olivine is the liquidus phase, but orthopyroxene, which is not part of the phase assemblage of the Steens Basalt, appears after only a few percent crystallization of olivine. From ~2-3 kbar, olivine is the liquidus phase until clinopyroxene begins fractionating after ~11% crystallization. From 0-1 kbar, olivine is

the liquidus phase until plagioclase begins fractionating after ~11% crystallization. Olivine has the largest Δmineral-melt and thus is most efficient at increasing the $\delta^{18}O$ of remaining melt; however, fractionation of 27-30% olivine alone is required to raise $\delta^{18}O$ of melt from 5.5‰ to 5.8-6.0‰. Because either clinopyroxene or plagioclase join olivine as crystallizing phases after only 11% fractionation in the upper crust, there is not enough olivine only fractionation at shallow depths to account for the bulk of the data. However, fractionation of ~45-60% clinopyroxene alone can account for the same increase in $\delta^{18}O$. Thus, the $\delta^{18}O$ range for the bulk of Steens Basalt lavas measured here can be accounted for by a combination of voluminous deep crustal fractionation of clinopyroxene followed by shallow fractionation of other phases. Given the phase equilibria, clinopyroxene fractionation must have taken place at greater depth than the mid to upper crustal levels where the basalts last equilibrated. The existing mineral assemblage is largely in equilibrium with the host rocks, so shallower fractionation overprinted any deeper crustal history recorded in the minerals. This combination of abundant clinopyroxene fractionation at depth and of olivine ± clinopyroxene ± plagioclase at shallow crustal levels can explain the bulk of measured $\delta^{18}O$ in the Steens Basalt, and much of the range of the other main phase CRBG as well (Fig. 3.11).

Some samples are too high in $\delta^{18}O$ to be explained by fractionation alone (Fig. 3.10), and likely reflect some type of open system process. One lower B Steens Basalt sample has elevated $\delta^{18}O$ (~7.4‰; Fig. 3.11), although there is otherwise little evidence to support significant contamination by crustal melts during this stage of magma generation (see discussion above). This sample is the highest stratigraphic sample in the lower B Steens stage, and thus could represent a transition to increasing crustal contamination into the upper Steens stage.

To further elucidate the contribution by crustal melt assimilation, simple AFC models using the equations of DePaolo (1981) are presented in Figure 3.16. Comparing trace element compositions that are affected strongly by crustal assimilation with isotopic compositions provides additional constraints on the amount of crustal melt contribution in the basalts. Assimilation of a 5% partial melt of Olds Ferry composition (Table 3.3) into a fractionating melt of primitive lower B Steens Basalt composition with an r = 0.1

(fractionation at 10 times the rate of assimilation) is shown in Figure 3.16. Even at such low rates of assimilation, once fractionation has progressed to F = 90%, compositions reach ~54 wt.% SiO_2 (not shown), which is too high to account for the overwhelming majority of the Steens Basalt data (Moore et al. 2018, in press). Though assimilation at this rate is too high to account for the major element concentrations in the bulk of the samples, this rate is conversely too low to account for the highest $\delta^{18}O$ compositions in the lower B and upper Steens (7.4‰ and 6.8 to 8.5‰, respectively; Fig. 3.16). Strictly speaking, a binary mix between a parent magma of 6‰ $\delta^{18}O$ (represented by the bulk of the Steens Basalt data; Fig. 3.11) and a contaminant with 10‰ $\delta^{18}O$ (from rhyolites coeval with the CRGB; Colon et al. 2015) would require 15 to 25% contamination by crustal melts to produce the highest $\delta^{18}O$ values in the Steens Basalt. This range of crustal melt contamination into a primitive Steens composition with 48 wt.% SiO_2 (as described above) would result in melts with silica contents of 51-54 wt.% SiO_2, within the range of the more evolved Steens Basalt samples (Moore et al. 2018, in press). This simple binary mixing calculation does not consider fractionation that is likely occurring simultaneously, but puts a probable upper limit of 25% crustal melt addition to the crustally contaminated Steens Basalt lavas measured here.

3.6.3 High Os in the Lower B Steens Basalt and Implications for an Os-Rich Source

While Os concentrations range to over 1 ppb for some OIB (Hauri, 2002), perhaps reflecting accumulation of disaggregated peridotite, typical ranges are 0.01 to 0.5 ppb for most OIB and 0.001 to 0.05 ppb for most MORB (Fig. 3.6; Shirey and Walker, 1998). Most lower B Steens Basalt samples measured here have Os concentrations higher than typical basalts (~0.3-0.9 ppb; Fig. 3.6). Osmium is extraordinarily compatible in sulfide minerals (Mungall and Brenan, 2014), but there is no petrographic evidence of sulfides in any analyzed sample of the Steens Basalt. This suggests that the lower B Steens lavas are sulfide undersaturated.

It is unlikely that the high Os concentrations of the lower B Steens Basalt are contributed by the crust. If crustal contamination had affected the generation of the lower B Steens Basalt, $^{187}Os/^{188}Os$ should be higher than the mantle-like, homogenous range

found in these lavas, given the crust of the region is composed of Mesozoic accreted terranes that likely have elevated $^{187}Os/^{188}Os$ due to their age. The upper Steens Basalt clearly demonstrates the crustal contamination effect, with elevated $^{187}Os/^{188}Os$ and very low Os concentration (Fig. 3.6). Therefore, the $^{187}Os/^{188}Os$ and elevated Os concentrations of the lower B Steens Basalt must come from either their mantle source or accumulation of an Os-rich mineral phase. This is supported by the fact that the lower B Steens Basalt samples with the highest Os concentrations are also those with the highest MgO, suggesting Os is being carried by the recharge magma from the source, or that the recharge magma dissolves Os-rich minerals precipitated from prior fractionation. Furthermore, given the homogeneity of $^{187}Os/^{188}Os$ in the lower B Steens and the variable input of DS and ES mantle source components, these mantle sources likely have similar $^{187}Os/^{188}Os$, and one or both may contain a phase with elevated Os concentrations that contributes to melt generation. Attributing the high Os concentrations in the lower B Steens Basalt to their mantle source is difficult given that Os acts compatibly during mantle melting. The most likely explanation is consumption of an Os-rich phase, such as sulfide, during melting, or alternatively, accumulation of an Os-rich phase produced by prior fractionation in the Steens Basalt magmatic system.

Some workers have proposed that accumulation of lithospheric and/or xenocrystic olivine can also produce magmas with high Os concentrations (Reisberg et al. 1993). Partition coefficients estimated for Os in olivine/melt range from 1 to 20, with one value from a disequilibrium case as high as 200 (Hart and Ravizza, 1993; 1996; Martin et al. 1994). Though Os is compatible in this mineral phase, partition coefficients are at least 1000 times lower than those estimated for Os in sulfide/melt (see below). Hart and Ravizza (1996) report Os concentrations in olivine from mantle lherzolite and primitive basalts mostly ~0.2 ppb, but one analysis from an olivine in lherzolite contains ~2.4 ppb. Addition of olivine with Os concentrations ~0.2 ppb is insufficient to raise Os to the values in the lower B Steens Basalt; addition of ~35% olivine with Os concentrations of 2.4 ppb would be required to raise a melt of ~0.05 ppb (an average basalt) to 0.9 ppb. This is an unreasonable amount of olivine accumulation given the required increase in MgO that would accompany such a process, producing a new melt + cumulates of ~20

wt.% MgO (from a starting melt of ~9 wt.% MgO). Some lower B Steens Basalt samples may contain accumulated cognate olivine, but as a very minor component given MgO is ≤12 wt.%, textures lack evidence of xenocrystic olivine, and forsterite compositions of olivine are homogeneous within crystals (Moore et al. 2018, in press). $^{187}Os/^{188}Os$ is homogeneous in the lower B Steens Basalt, so variable contributions by accumulated lithospheric olivine is unlikely as it would result in higher and variable $^{187}Os/^{188}Os$; additionally, olivine in the lower B Steens Basalt is not in equilibrium with the mantle as would be expected if olivine was accumulated from a lithospheric component (Fo ≤86 in lower B Steens, Moore et al 2018, in press). Given the lack of evidence of accumulative olivine in the petrographic and geochemical data, we suggest that this is an unlikely scenario for obtaining the elevated Os concentrations in the lower B Steens Basalt.

One possible scenario for producing high Os concentrations in the lower B Steens Basalt is a case where small amounts of residual mantle sulfides are completely consumed. Os is enormously compatible in sulfide, with sulfide/melt partition coefficient estimates from $3.52 \times 10^5 - 1.15 \times 10^6$ (Mungall and Brenan, 2014). Hart and Ravizza (1996) report Os concentrations of 4.1 ppm in sulfides from Kilbourne Hole lherzolites; if this is a typical value for Os in mantle sulfide, then very minor sulfide consumption can produce the range of Os compositions found in OIB (up to 1 ppb). Melt from the modeled ES mantle (similar to what produces OIB) is likely generated at a higher pressure in comparison to melt from the modeled DS mantle (similar to what produces MORB). Decreasing pressure during magma ascent will increase sulfide solubility, causing sulfide saturated melts to become undersaturated (Mavrogenes and O'Neill, 1999). If a sulfide undersaturated melt encounters residual sulfides in the surrounding mantle as it ascends, it will scavenge the sulfides (Mavrogenes and O'Neill, 1999). During the waxing lower B Steens Basalt stage, the recharge magma has a stronger ES contribution, as the samples with the highest Os concentrations and high MgO have elevated $^{87}Sr/^{86}Sr$ and $^{206}Pb/^{204}Pb$. $^{87}Sr/^{86}Sr$ and $^{206}Pb/^{204}Pb$ decrease late in the lower B Steens section, where the DS component contribution increases, and Os concentrations decrease (Figs. 3.6 and 3.7). If the DS source does contribute to the high Os signature, the phase contributing the high Os must be mostly consumed over the early waxing part of the lower B Steens stage.

An alternative scenario is one in which sulfides are precipitated from prior fractionation in the Steens Basalt system and consumed by later ascending recharge melts. Minimal and preliminary compositional data from melt inclusions in olivine of two lower B Steens Basalt flows have a range of 0-700 ppm S (Supplement 7). For basaltic melts at 1200°C and shallow crustal levels (~0-3 kbar), sulfide saturation is achieved at ~1000 ppm S (Mavrogenes and O'Neill, 1999). This further supports the notion that the lower B Steens Basalt lavas are sulfide undersaturated. However, extensive fractionation (~60%) could cause a melt of ~700 ppm S to become sulfide saturated (Mavrogenes and O'Neill, 1999). If a sulfide undersaturated recharge magma is introduced into a chamber that has extensively fractionated to the point of sulfide saturation/precipitation of sulfides, the recharge magma would consume the sulfides that precipitated from the evolved melt. Given the range of MgO compositions in the lower B Steens Basalt (as low as ~4.5 wt.% MgO), up to 70% fractionation in the more evolved melts is supportable. Therefore, consumption of an Os-rich mineral phase, such as sulfide, during magma ascent or crustal staging is a plausible explanation for high Os concentrations in the lower B Steens Basalt.

3.6.4 Mantle Source and Crustal Process Summary

The three-stage crustal process evolution described for the Steens Basalt (Moore et al. 2018, in press) coupled with the mantle sources characteristics and crustal processes interpreted here as well as the results of computational modeling (Chapter 4) produce a schematic view of the mantle to crust for the Steens Basalt magmatic system (Fig. 3.18). The mantle source of the Steens Basalt represents variable mixtures between a depleted and an enriched mantle component. These mantle sources contribute melts in nearly equal proportions to the generation of the lower A Steens Basalt, during which fractional crystallization dominates over recharge and magma volumes are relatively low. During the lower B Steens stage, the mantle sources initially contribute subequal proportions to magma generation during the waxing, recharge dominated period evident early in the section. Melts incorporate a high Os phase, perhaps residual sulfides in the mantle source or from accumulation of cognate sulfides in the crust. The depleted mantle component begins to play a larger role late in the lower B Steens stage, and recharge becomes

subordinate to fractionation. Fractionation occurs at varying levels within the crust, including deep (6-10 kbar) fractionation of up to 45% clinopyroxene and shallow fractionation of olivine ± clinopyroxene ± plagioclase, which continues into the upper Steens stages. Additional crustal processes evolve the magmas of the lower B stage, ultimately producing FeTi rich melts containing abundant crystallized plagioclase that mix with more primitive compositions to produce some giant plagioclase basalts, and cumulate entrainment of olivine gabbro at mid crustal levels and of troctolite at upper crustal levels to produce some of the less magnesian flows in the lower B Steens Basalt (Chapter 4). Finally, during the waning upper Steens Basalt stage, the depleted and enriched mantle source contributions return to subequal proportions, and voluminous fractionation continues. Shoaling of the system occurs because the abundant products of crystallization are left behind as a layered mafic series in the crust. The mafic accreted terrane crust, now thermally primed from extended magmatism, contaminates the magmas with crustal partial melts. The combination of a more depleted and a more enriched mantle source coupled with variable crustal melt assimilation though time proposed for the Steens Basalt is similar to models proposed for generation of other CFB, such as the Deccan and Siberian Traps, suggesting that the petrogenetic and evolutionary history at CFB provinces over a variety of scales is comparable.

3.7 CONCLUSIONS

New and existing radiogenic isotopic compositions require at least two distinct mantle sources for the Steens Basalt: an enriched and a depleted mantle component. There is little evidence for direct mixing from other proposed mantle endmembers such as EMI, EMII or HIMU. A third component is required by isotopic compositions of some Steens Basalt lavas; contamination by mafic accreted terrane crust, similar in composition to the Olds Ferry Terrane, is likely responsible for this trend.

The lower A Steens Basalt isotopic compositions can be modeled by mixing of roughly equal proportions of DS and ES mantle sources. These lavas show little evidence of crustal assimilation, given that relatively high Ba/Ta ratios can largely be explained by repeated episodes of fractionation and recharge. Mixing of the DS and ES mantle sources

in approximately equal proportions continues into the waxing stage, the lower B Steens Basalt. The homogeneity of $^{187}Os/^{188}Os$ in the lower B Steens Basalt lavas suggest that the $^{187}Os/^{188}Os$ ratio of DS and ES mantle sources are similar. Input of the DS component increases in time within the lower B Steens Basalt and contributes as much as 70% of the mantle source for some lavas erupted later in the stage, during initiation of the waning period, when fractionation begins to outpace recharge. Lower B Steens Basalt Os concentrations require a contribution from an Os-rich source, either residual sulfide from the mantle source or from consumption of a Os-rich cognate mineral phase while staged in the crust. Lower B Steens Basalt generally lacks isotopic and trace element signatures reflective of assimilation of crustal melts, and crustal contamination is not required for most lavas from this stage by isotopic mixing models. Voluminous fractionation at both deep and shallow crustal levels occurs during this stage, elevating $\delta^{18}O$ above parental basaltic melt values, which continues into the upper Steens stage.

During the upper Steens Basalt stage, the DS and ES mantle endmembers contribute subequal proportions, with some samples suggesting a greater contribution by the ES mantle. The system is now well established in this stage; magmatism has thermally primed the mafic accreted terrane crust in which the magmas have stalled and fractionated. This allows for melting of mafic terrane crust, similar in composition to the Olds Ferry Terrane, which assimilate with mantle melts that together generate the upper Steens Basalt.

The data presented here further resolves changing mantle source and crustal effects during the three-stage petrochemical evolution proposed for the Steens Basalt. A more detailed schematic view from the mantle through the crust in the Steens Basalt magmatic system is elucidated. The Steens Basalt mantle source and crustal contamination model presented here is similar to models proposed for other CFB, and suggests that CFB provinces share a similar generation and evolution history.

3.8 ACKNOWLEDGEMENTS

3.9 REFERENCES CITED

Anderson, D.L., 2005, Large igneous provinces, delamination, and fertile mantle: Elements, v.1 p. 271-275.

Arndt, N.T., Czamanske, G.K., Wooden, J.L., and Fedorenko, V.A., 1993, Mantle and crustal contributions to continental flood volcanism: Tectonophysics, v. 223, p. 39-52.

Bailey, M.M., 1989, Revisions to stratigraphic nomenclature of the Picture Gorge Basalt Subgroup, Columbia River Basalt Group: Geological Society of America Special Papers v. 239, p. 67-84.

Barry, T.L., Kelley, S.P., Reidel, S.P., Camp, V.E., Self, S., Jarboe, N.A., Duncan, R.A., and Renne, P.R., 2013, Eruption chronology of the Columbia River Basalt Group: Geological Society of America Special Papers, v. 497, p. 45-66.

Bellieni, G., Comin-Chiaramonti, P., Marques, L.S., Melfi, A.J., Piccirillo, E.M., Nardy, A.J.R., and Roisenberg, A., 1984, High-and low-TiO2 flood basalts from the Paraná plateau (Brazil): petrology and geochemical aspects bearing on their mantle origin: Neues Jahrbuch für Mineralogie Abhandlungen, v. 150, p. 273-306.

Bendaña, S.J., 2016, Documenting mantle and crustal contributions to flood basalt magmatism via computational modeling of the Steens Basalt, southeast Oregon [M.S. Thesis]: Central Washington University, 183 p.

Bindeman, I., 2008, Oxygen isotopes in mantle and crustal magmas as revealed by single crystal analysis. Reviews in Mineralogy and Geochemistry, v. 69, p. 445-478.

Birck J.L., 1986, Precision K–Rb–Sr isotopic analysis: application to Rb–Sr chronology: Chemical Geology, v. 56, p. 73-83.

Blichert-Toft, J., Chauvel, C., and Albarède, F., 1997, Separation of Hf and Lu for high precision isotope analysis of rock samples by magnetic sector-multiple collector ICPMS: Contributions to Mineralogy and Petrology, v. 127, p. 248-260.

Brandon, A.D., Hooper, P.R., Goles, G.G., and Lambert, R.S.J., 1993, Evaluating crustal contamination in continental basalts: the isotopic composition of the Picture Gorge Basalt of the Columbia River Basalt Group: Contributions to Mineralogy and Petrology, v. 114, p. 452-464.

Camp, V.E., and Hanan, B.B., 2008, A plume-triggered delamination origin for the Columbia River Basalt Group: Geosphere, v. 4, no. 3, p. 480.

Camp, V.E., and Ross, M.E., 2004, Mantle dynamics and genesis of mafic magmatism in the Intermontane Pacific Northwest: Journal of Geophysical Research: Solid Earth, v. 109, doi:10.1029/2003JB002838.

Camp, V.E., Ross, M.E, Duncan, R.A., Jarboe, N.A., Coe, R.S., Hanan, B.B., and Johnson, J.A., 2013, The Steens Basalt: earliest lavas of the Columbia River Basalt Group: Geological Society of America Special Papers, v. 497, p. 87-116.

Camp, V.E., Ross, M.E., Duncan, R.A., and Kimbrough, D.L., 2017, Uplift, rupture, and rollback of the Farallon slab reflected in volcanic perturbations along the Yellowstone adakite hot spot track: Journal of Geophysical Research: Solid Earth, v. 122, p. 7009-7041.

Camp, V.E., Ross, M.E., and Hanson, W.E., 2003, Genesis of flood basalts and Basin and Range volcanic rocks from Steens Mountain to the Malheur River Gorge, Oregon: Geological Society of America Bulletin, v. 115, p. 105-128.

Carlson, R.W., 1984, Isotopic constraints on Columbia River flood basalt genesis and the nature of the subcontinental mantle: Geochimica et Cosmochimica Acta, v. 48, p. 2357-2372.

Carlson, R.W., Lugmair, G.W., & Macdougall, J.D., 1981, Columbia River volcanism: the question of mantle heterogeneity or crustal contamination: Geochimica et CosmochimicaActa, v. 45, p. 2483-2499.

Carlson, R.W., Czamanske, G., Fedorenko, V., and Ilupin, I., 2006, A comparison of Siberian meimechites and kimberlites: Implications for the source of high-Mg alkalic magmas and flood basalts: Geochemistry, Geophysics, Geosystems, v. 7, doi:10.1029/2006GC001342.

Chesley, J.T., and Ruiz, J., 1998, Crust–mantle interaction in large igneous provinces: implications from the Re–Os isotope systematics of the Columbia River flood basalts: Earth and Planetary Science Letters, v. 154, p. 1-11.

Coffin, M.F., and Eldholm, O., 1994, Large igneous provinces: crustal structure, dimensions, and external consequences: Reviews of Geophysics, v. 32, p. 1-36.

Colón, D.P., Bindeman, I.N., Stern, R.A., and Fisher, C.M., 2015, Isotopically diverse rhyolites coeval with the Columbia River Flood Basalts: evidence for mantle plume interaction with the continental crust: Terra Nova, v. 27, p. 270-276.

Cox, K.G., 1980, A model for flood basalt vulcanism: Journal of Petrology, v. 21, p. 629-650.

DePaolo, D.J., 1981, Trace element and isotopic effects of combined wallrock assimilation and fractional crystallization: Earth and Planetary Science Letters, v. 53, p. 189-202.

Drignon, M., 2018, An experimental and analytical investigation of the parameters that influence measured CO_2 in Plagioclase-Hosted Melt Inclusions in MORBs [Doctoral Dissertation]: Oregon State University, 96 p.

Eagar, K.C., Fouch, M.J., James, D.E., and Carlson, R.W., 2011, Crustal structure beneath the High Lava Plains of eastern Oregon and surrounding regions from receiver function analysis: Journal of Geophysical Research: Solid Earth, v. 116 no. B2.

Elkins-Tanton, L.T., 2005, Continental magmatism caused by lithospheric delamination: Geological Society of America Special Papers, v. 388, p. 449-462.

Gannoun, A., Burton, K.W., Parkinson, I.J., Alard, O., Schiano, P., and Thomas, L.E., 2007), The scale and origin of the osmium isotope variations in mid-ocean ridge basalts: Earth and Planetary Science Letters, v. 259, p. 541-556.

Garfunkel, Z., 2008, Formation of continental flood volcanism - the perspective of setting of melting: Lithos, v. 100, no. 1-4, p. 49-65.

Gaschnig, R.M., Vervoort, J.D., Lewis, R.S., and Tikoff, B., 2011, Isotopic evolution of the Idaho batholith and Challis intrusive province, northern US Cordillera: Journal of Petrology, v. 52, p. 2397-2429.

Graham, D.W., Blichert-Toft, J., Russo, C.J., Rubin, K.H., and Albarède, F., 2006, Cryptic striations in the upper mantle revealed by hafnium isotopes in southeast Indian ridge basalts: Nature, v. 440, p. 199-202.

Graham, D.W., Hanan, B.B., Hémond, C., Blichert-Toft, J., and Albarède, F., 2014, Helium isotopic textures in Earth's upper mantle: Geochemistry, Geophysics, Geosystems, v. 15, p. 2048-2074, doi:10.1002/2014GC005264.

Graham, D.W., Jenkins, W.J., Schilling, J.G., Thompson, G., Kurz, M.D., and Humphris, S.E., 1992, Helium isotope geochemistry of mid-ocean ridge basalts from the South Atlantic: Earth and Planetary Science Letters, v. 110, p. 133-147.

Graubard, M., 2016, Evolution of a Flood Basalt Crustal Magmatic System: In Situ Mineral Data and Computational Modeling of the Steens Basalt [M.S. Thesis]: Central Washington University, 190 p.

Grunder, A.L., 1987, Low δ 18 O silicic volcanic rocks at the Calabozos caldera complex, southern Andes: Contributions to Mineralogy and Petrology, v. 95, p. 71-81.

Gualda, G.A., Ghiorso, M.S., Lemons, R.V., and Carley, T.L., 2012, Rhyolite-MELTS: a modified calibration of MELTS optimized for silica-rich, fluid-bearing magmatic systems: Journal of Petrology, v. 53, p. 875-890.

Hanan, B.B., and Graham, D.W., 1996, Lead and helium isotope evidence from oceanic basalts for a common deep source of mantle plumes: Science, v. 272, p. 991-995.

Hart, S.R., Gerlach, D.C., and White, W.M., 1986, A possible new Sr-Nd-Pb mantle array and consequences for mantle mixing: Geochimica et Cosmochimica Acta, v. 50, p. 1551-1557.

Hart, S.R., Hauri, E.H., Oschmann, L.A., and Whitehead, J.A., 1992), Mantle plumes and entrainment: isotopic evidence: Science, v. 256, p. 517-520.

Hart, S.R., and Ravizza, G., 1993, Os partitioning in lherzolite and basalt: v. 74, p. 120.

Hart, S.R., and Ravizza, G.E., 1996, Os partitioning between phases in lherzolite and basalt: Geophysical Monograph, v. 95, p. 23-134.

Hart, W.K., and Carlson, R.W., 1987, Tectonic controls on magma genesis and evolution in the northwestern United States: Journal of Volcanology and Geothermal Research, v. 32, p. 119-135.

Hauri, E.H., 2002, Osmium isotopes and mantle convection: Philosophical Transactions of the Royal Society of London A: Mathematical, Physical and Engineering Sciences, v. 360, p. 2371-2382.

Hauri, E.H., Whitehead, J.A., and Hart, S.R., 1994, Fluid dynamic and geochemical aspects of entrainment in mantle plumes: Journal of Geophysical Research: Solid Earth, v. 99, p.24275-24300.

Hawkesworth, C., Kelley, S., Turner, S., le Roex, A., and Storey, B., 1999, Mantle processes during Gondwana break-up and dispersal: Journal of African Earth Sciences, v. 28, no. 1, p. 239-261.

Heinonen, J.S., Luttinen, A.V., and Bohrson, W.A., 2016, Enriched continental flood basalts from depleted mantle melts: modeling the lithospheric contamination of Karoo lavas from Antarctica: Contributions to Mineralogy and Petrology, v. 171, no. 9.

Heinonen, J.S., Luttinen, A.V., Riley, T.R., and Michallik, R.M., 2013, Mixed pyroxenite peridotite sources for mafic and ultramafic dikes from the Antarctic segment of the Karoo continental flood basalt province: Lithos, v. 177, p. 366-380.

Hooper, P.R., 2000, Chemical discrimination of Columbia River basalt flows: Geochemistry, Geophysics, Geosystems, v. 1, no. 6.

Hooper, P.R. and Hawkesworth, C.J., 1993, Isotopic and geochemical constraints on the origin and evolution of the Columbia River basalt: Journal of Petrology, v. 34, p.1203-1246.

Hooper, P.R. and Swanson, D.A., 1990, The Columbia River Basalt Group and associated volcanic rocks of the Blue Mountains province: US Geological Survey Professional Paper 1437, p. 63-99.

Ingle, S., and Coffin, M.F., 2004, Impact origin for the greater Ontong Java Plateau?: Earth and Planetary Science Letters, v. 218, p.123-134.

Hooper, P.R., Kleck, W.D., Knowles, C.R., Reidel, S.P., and Thiessen, R.L., 1984, Imnaha Basalt, Columbia River Basalt Group: Journal of Petrology, v. 25, p. 473-500.

Jarboe, N.A., Coe, R.S., Renne, P.R., and Glen, J.M.G., 2010, The age of the Steens reversal and the Columbia River Basalt Group: Chemical Geology, v. 274, no. 3 4, p. 158-168.

Jarboe, N.A., Coe, R.S., Renne, P.R., Glen, J.M.G., and Mankinen, E.A., 2008, Quickly erupted volcanic sections of the Steens Basalt, Columbia River Basalt Group: Secular variation, tectonic rotation, and the Steens Mountain reversal: Geochemistry Geophysics Geosystems, v. 9, no. 11.

Johnson, J.A., Hawkesworth, C.J., Hooper, P.R., and Binger, G.B., 1998, Major and trace element analyses of Steens Basalt, southeastern Oregon: U.S. Geological Survey Open File Report 98 482, 26 p.

Kurz, G.A., Schmitz, M.D., Northrup, C.J., and Vallier, T.L., 2017, Isotopic compositions of intrusive rocks from the Wallowa and Olds Ferry arc terranes of northeastern Oregon and western Idaho: Implications for Cordilleran evolution, lithospheric structure, and Miocene magmatism: Lithosphere, v. 9, p. 235-264.

Lightfoot, P.C., Hawkesworth, C.J., Hergt, J., Naldrett, A.J., Gorbachev, N.S., Fedorenko, V.A., and Doherty, W., 1993, Remobilisation of the continental lithosphere by a mantle plume: major-, trace-element, and Sr-, Nd-, and Pbisotope evidence from picritic and tholeiitic lavas of the Noril'sk District, Siberian Trap, Russia: Contributions to Mineralogy and Petrology, v. 114, p. 171-188.

Lightfoot, P.C., Naldrett, A.J., Gorbachev, N.S., Doherty, W., and Fedorenko, V.A., 1990, Geochemistry of the Siberian Trap of the Noril'sk area, USSR, with implications for the relative contributions of crust and mantle to flood basalt magmatism: Contributions to Mineralogy and Petrology, v. 104, p. 631-644.

Luttinen, A.V., Leat, P.T., and Furnes, H., 2010, Bjornnutane and Sembberget basalt lavas and the geochemical provinciality of Karoo magmatism in western Dronning Maud Land, Antarctica: Journal of Volcanology and Geothermal Research, v. 198, no. 1-2, p. 1-18.

Mahood, G.A., and Benson, T.R., 2017, Using 40 Ar/39 Ar ages of intercalated silicic tuffs to date flood basalts: Precise ages for Steens Basalt Member of the Columbia River Basalt Group: Earth and Planetary Science Letters, v. 459, p. 340-351.

Mankinen, E.A., Prevot, M., Gromme, C.S., and Coe, R.S., 1985, The Steens Mountain (Oregon) Geomagnetic Polarity Transition: 1. Directional history, duration of episodes, and rock magnetism: Journal of Geophysical Research, v. 90, no. NB12, p. 393-416.

Martin, C.E., Carlson, R.W., Shirey, S.B., Frey, F.A., and Chen, C.Y., 1994, Os isotopic variation in basalts from Haleakala Volcano, Maui, Hawaii: A record of magmatic processes in oceanic mantle and crust: Earth and Planetary Science Letters, v. 128, p. 287-301.

Mavrogenes, J.A., and O'Neill, H.S.C., 1999, The relative effects of pressure, temperature and oxygen fugacity on the solubility of sulfide in mafic magmas: Geochimica et Cosmochimica Acta, v. 63, p. 1173-1180.

Melluso, L., Beccaluva, L., Brotzu, P., Gregnanin, A., Gupta, A.K., Morbidelli, L., and Traversa, G., 1995: Constraints on the mantle sources of the Deccan Traps from the petrology and geochemistry of the basalts of Gujarat State (Western India): Journal of Petrology, v. 36, p. 1393-1432.

Melluso, L., Mahoney, J.J., and Dallai, L., 2006, Mantle sources and crustal input as recorded in high-Mg Deccan Traps basalts of Gujarat (India): Lithos, v. 89, p. 259-274.

Moore, N.E., Grunder, A.L. and Bohrson, W.A., in press 2018, The three-stage petrochemical evolution of the Steens Basalt compared to large igneous provinces and layered mafic intrusions: Geosphere.

Mungall, J.E., and Brenan, J.M., 2014, Partitioning of platinum-group elements and Au between sulfide liquid and basalt and the origins of mantle-crust fractionation of the chalcophile elements: Geochimica et Cosmochimica Acta, v. 125, p. 265-289.

Münker, C., Weyer, S., Scherer, E., Mezger, K., 2001, Separation of high field strength elements (Nb, Ta, Zr, Hf) and Lu from rock samples for MC-ICPMS measurements: Geochemistry Geophysics Geosystems v. 2, doi:10.1029/2001GC000183.

Nelson, D.O., 1983, Implications of oxygen-isotope data and trace-element modeling for a large- scale mixing model for the Columbia River Basalt: Geology, v. 11, p. 248-251.

Patchett, P.J., and M. Tatsumoto, 1980, Lu–Hf total-rock isochron for the eucrite meteorites: Nature, v. 288. p. 571.

Peng, Z.X., Mahoney, J., Hooper, P., Harris, C., and Beane, J., 1994, A role for lower continental crust in flood basalt genesis? Isotopic and incompatible element study of the lower six formations of the western Deccan Traps: Geochimica et Cosmochimica Acta, v. 58, p. 267-288.

Pertermann, M., and Hirschmann, M.M., 2003, Partial melting experiments on a MORB like pyroxenite between 2 and 3 GPa: Constraints on the presence of pyroxenite in basalt source regions from solidus location and melting rate: Journal of Geophysical Research: Solid Earth, v. 108, p. B2, doi:10.1029/2000JB000118.

Pierce, K.L., and Morgan, L.A., 2009, Is the track of the Yellowstone hotspot driven by a deep mantle plume?--Review of volcanism, faulting, and uplift in light of new data: Journal of Volcanology and Geothermal Research, v. 188, p. 1-25.

Roy-Barman, M. and Allègre C.J., 1994, ^{187}Os/^{188}Os ratios of mid-ocean ridge basalts and abyssal peridotites, Geochimica et Cosmochimica Acta, v. 58, p. 5043–5054.

Richards, M.A., Duncan, R.A., Courtillot, V.E., 1989, Flood basalts and hot-spot tracks: plume heads and tails: Science, v. 246, p.103–107.

Reidel, S.P., Camp, V.E., Tolan, T.L., and Martin, B.S., 2013, The Columbia River flood basalt province: Stratigraphy, areal extent, volume, and physical volcanology: Geological Society of America Special Papers, v. 497, 1-43.

Reidel, S.P., Fecht, K.R., Hagood, M.C., Tolan, T.L., and Hooper, P.R., 1989, The geologic evolution of the central Columbia Plateau: Geological Society of America Special Papers, v. 239, 247-264.

Reisberg, L., Zindler, A., Marcantonio, F., White, W., Wyman, D., and Weaver, B., 1993, Os isotope systematics in ocean island basalts: Earth and Planetary Science Letters, v. 120, p. 149-167.

Rogers, N.W., Davies, M.K., Parkinson, I.J., and Yirgu, G., 2010, Osmium isotopes and Fe/Mn ratios in Ti-rich picritic basalts from the Ethiopian flood basalt province: No evidence for core contribution to the Afar plume: Earth and Planetary Science Letters, v. 296, p. 413- 422.

Rooney, T.O., Hanan, B.B., Graham, D.W., Furman, T., Blichert-Toft, J., and Schilling, J.G., 2011, Upper mantle pollution during Afar plume–continental rift interaction: Journal of Petrology, v. 53, p. 365-389.

Sharma, M., 1997, Siberian traps: In: Mahoney, J.J., Coffin, M.F. (Eds.), Large Igneous Provinces: Continental, Oceanic, and Planetary Flood Volcanism: AGU Monograph, v. 100, p. 273–295.

Shirey, S.B. and Walker, R.J., 1995, Carius tube digestion for low-blank rhenium osmium analysis: Analytical Chemistry, v. 67, p. 2136-2141.

Shirey, S.B., and Walker, R.J., 1998, The Re-Os isotope system in cosmochemistry and high temperature geochemistry: Annual Review of Earth and Planetary Sciences, v. 26, p. 423- 500.

Stracke, A., Bizimis, M., and Salters, V. J., 2003, Recycling oceanic crust: Quantitative constraints: Geochemistry, Geophysics, Geosystems, v. 4, no. 3.

Stracke, A., Hofmann, A.W., and Hart, S.R., 2005, FOZO, HIMU, and the rest of the mantle zoo: Geochemistry, Geophysics, Geosystems, v. 6, no. 5, doi:10.1029/2004GC000824.

Sun, S.S., and McDonough, W.S., 1989, Chemical and isotopic systematics of oceanic basalts: implications for mantle composition and processes, In: Saunders, A.D., and Norry, M.J. (Eds.), Magmatism in the Ocean Basins: Geological Society of London Special Publications, v. 42, p.313-345.

Takahahshi, E., Nakajima, K., and Wright, T.L., 1998, Origin of the Columbia River basalts:melting model of a heterogeneous plume head: Earth and Planetary Science Letters, v.162, no. 1, p. 63-80.

Tanaka, T., Togashi, S., Kamioka, H., Amakawa, H., Kagami, H., Hamamoto, T., Yuhara, M., Orihashi, Y., Yoneda, S., Shimizu, H. and Kunimaru, T., 2000, JNdi 1: a neodymium isotopic reference in consistency with LaJolla neodymium: Chemical Geology, v. 168, p. 279-281.

Thompson, R., Morrison, M., Dickin, A., and Hendry, G., 1983, Continental flood basalts... arachnids rule OK?: Continental basalts and mantle xenoliths, p. 158-185.

Todt, W., Cliff, R.A., Hanser, A., Hofmann, A.W., 1996, Evaluation of a 202Pb–205Pb double spike for high precision lead isotope analysis, In: Hart, S.R., Basu, A. (Eds.), Earth Processes: Reading the Isotope Code, pp. 429–437.

Toth, C., 2018, Giant plagioclase in the Steens Basalt, SE Oregon: Cumulate entrainment revealed by textural and in situ chemical analysis [M.S. Thesis]: Central Washington University, 105 p.

Turner, S., Hawkesworth, C., Gallagher, K., Stewart, K., Peate, D., and Mantovani, M., 1996, Mantle plumes, flood basalts, and thermal models for melt generation beneath continents: Assessment of a conductive heating model and application to the Parana: Journal of Geophysical Research-Solid Earth, v. 101, no. B5, p. 11503-11518.

Walker, J.A., Gmitro, T.T., and Berg, J.H., 2002, Chemostratigraphy of the Neoproterozoic Alona Bay lavas, Ontario: Canadian Journal of Earth Sciences, v. 39, p. 1127-1142.

Walker, G.W., MacLeod, N.S., Russell, D., and Earnest, P., 1991, Geologic map of Oregon, Geological Survey.

Walker, R.J., Shirey, S.B., Hanson, G.N., Rajamani, V., Horan, M.F., 1989, Re–Os, Rb Sr, and O isotopic systematics of the Archean Kolar schist belt, Karnataka, India: Geochimica et Cosmochimica Acta v. 53, p. 3005–3013.

Wooden, J.L., Czamanske, G.K., Fedorenko, V.A., Arndt, N.T., Chauvel, C., Bouse, R.M., and Siems, D.F., 1993, Isotopic and trace-element constraints on mantle and crustal contributions to Siberian continental flood basalts, Noril'sk area, Siberia: Geochimica et Cosmochimica Acta, v. 57, p. 3677-3704.

Wolff, J.A., and Ramos, F.C., 2013, Source materials for the main phase of the Columbia River Basalt Group: geochemical evidence and implications for magma storage and transport: Geological Society of America Special Papers, v. 497, p. 273-291.

Wolff, J.A., Ramos, F.C., Hart, G.L., Patterson, J.D., and Brandon, A.D., 2008, Columbia River flood basalts from a centralized crustal magmatic system: Nature Geoscience, v. 1, no. 3, p. 177-180.

Workman, R.K., and Hart, S.R., 2005, Major and trace element composition of the depleted MORB mantle (DMM): Earth and Planetary Science Letters, v. 231, p. 53-72.

Xiao, L., Xu, Y.G., Mei, H.J., Zheng, Y.F., He, B., and Pirajno, F., 2004, Distinct mantle sources of low-Ti and high-Ti basalts from the western Emeishan large igneous province, SW China: implications for plume–lithosphere interaction: Earth and Planetary Science Letters, v. 228, p. 525-546.

Zhao, Z.F., and Zheng, Y.F., 2003, Calculation of oxygen isotope fractionation in magmatic rocks: Chemical Geology, v. 193, p. 59-80.

Zindler, A., and Hart, S., 1986, Chemical geodynamics: Annual review of earth and planetary sciences, v. 14, p. 493-571.

Table 3.1

Sr, Nd, Pb, Hf and O Isotopic Compositions for the Steens Basalt

Sample[a]	$^{87}Sr/^{86}Sr$	$^{143}Nd/^{144}Nd$	εNd	$^{208}Pb/^{204}Pb$	$^{207}Pb/^{204}Pb$	$^{206}Pb/^{204}Pb$	$^{208}Pb/^{206}Pb$	$^{207}Pb/^{206}Pb$	$^{204}Pb/^{206}Pb$	$^{176}Hf/^{177}Hf$	εHf	$δ^{18}O$
Lower A Steens												
NMSB-55	0.703621	0.512960	6.3	38.45	15.58	18.84	2.0403	0.8270	0.0531	0.283140	12.5	
NMSB-64	0.703547	0.512981	6.7	38.45	15.57	18.92	2.0326	0.8231	0.0528	0.283119	11.8	
NMSB-69	0.703708	0.512930	5.7	38.49	15.59	18.88	2.0389	0.8259	0.0530	0.283111	11.5	
NMSB-70	0.703957	0.512861	4.4	38.58	15.61	18.94	2.0362	0.8240	0.0528	0.283056	9.5	
Lower B Steens												
MF9463	0.703547	0.512943	5.9	38.39	15.58	18.82	2.0400	0.8278				
MF9464	0.703530	0.512963	6.3	38.44	15.58	18.83	2.0412	0.8275	0.0530	0.283110	11.5	
MF9466	0.703805	0.512910	5.3	38.92	15.75	19.11	2.0365	0.8240				6.07
MF9467	0.703880	0.512930	5.7	38.61	15.62	18.95	2.0374	0.8243				6.24
MF9468	0.703670	0.512930	5.7	38.62	15.61	18.99	2.0342	0.8224				
MF9469	0.703693	0.512951	6.1	38.58	15.61	18.94	2.0367	0.8241				
MF9471a	0.703560	0.512950	6.1	38.55	15.63	18.92	2.0376	0.8263				
MF9471b	0.703560	0.512940	5.9	38.91	15.77	19.09	2.0377	0.8262				
MF9472	0.703640	0.512930	5.7	38.53	15.60	18.93	2.0352	0.8240				6.49
JS19	0.703700	0.512920	5.5	38.52	15.59	18.90	2.0382	0.8250				6.24
JS22	0.703331	0.513028	7.6	38.48	15.62	18.81	2.0451	0.8302	0.0524	0.283170	13.6	6.15
JS23	0.703560	0.512890	4.9	38.43	15.60	18.86	2.0374	0.8269				
JS26	0.703480	0.512970	6.5	38.62	15.69	18.92	2.0413	0.8291				5.96
JS29	0.703600	0.512950	6.1	38.64	15.68	18.96	2.0378	0.8268				
NMSB-5	0.703850	0.512916	5.4	38.64	15.63	18.95	2.0396	0.8244	0.0525	0.283080	10.4	
NMSB-13	0.703590	0.512916	5.4	n.a.[b]	n.a.[b]	n.a.[b]	n.a.[b]	n.a.[b]	n.a.[b]	0.283120	11.8	
NMSB-18	0.703727	0.512943	6.0	38.58	15.60	18.91	2.0397	0.8249	0.0528	0.283100	11.1	
NMSB-19	0.703463	0.512993	6.9	38.60	15.60	18.94	2.0382	0.8239	0.0525	0.283180	13.9	
NMSB-20A	0.703660	0.512921	5.5	38.61	15.61	18.93	2.0404	0.8248	0.0528	0.283110	11.5	
NMSB-21	0.703739	0.512925	5.6	38.61	15.61	18.93	2.0405	0.8248	0.0528	0.283090	10.8	
NMSB-23	0.703531	0.512981	6.7	38.64	15.65	19.00	2.0344	0.8236	0.0506	0.283140	12.5	
NMSB-25	0.704021	0.512895	5.0	38.80	15.70	19.09	2.0324	0.8227	0.0515	0.283080	10.4	
NMSB-36	0.703468	0.513000	7.1	38.40	15.60	18.79	2.0436	0.8301	0.0528	0.283130	12.2	
Upper Steens												
JS31	0.703770	0.512930	5.7	38.52	15.62	18.91	2.0371	0.8260				
JS32	0.703850	0.512870	4.5	38.53	15.60	18.98	2.0303	0.8219				
JS34	0.703690	0.512900	5.1	38.54	15.60	18.97	2.0315	0.8225				6.19
JS39	0.703680	0.512910	5.3	38.51	15.61	18.91	2.0368	0.8254				6.12
JS41	0.703970	0.512890	4.9	38.51	15.93	18.43	2.0350	0.8244				6.15
JS44	0.704095	0.512916	5.4	38.69	15.60	19.00	2.0363	0.8212	0.0526	0.283000	7.6	6.75
JS45	0.703740	0.512910	5.3	38.47	15.60	18.88	2.0372	0.8259				5.91
JS46	0.703840	0.512900	5.1	38.46	15.60	18.88	2.0372	0.8264				
JS52	0.703780	0.512900	5.1	38.45	15.59	18.87	2.0379	0.8261				
JS55	0.703690	0.512920	5.5	38.63	15.67	18.95	2.0387	0.8268				
JS57	0.703860	0.512860	4.3	38.57	15.61	18.98	2.0324	0.8226				6.25
JS58	0.703890	0.512870	4.5	38.77	15.70	19.05	2.0353	0.8243				6.18
JS60	0.704020	0.512840	3.9	38.54	15.60	18.93	2.0358	0.8241				
JS62	0.704040	0.512870	4.5	38.58	15.62	19.00	2.0307	0.8219				8.5
JS63	0.703890	0.512900	5.1	38.60	15.63	18.97	2.0348	0.8242				
JS66	0.703950	0.512870	4.5	38.55	15.61	18.95	2.0348	0.8240				
NMSB-2	0.704030	0.512892	5.0	38.62	15.62	19.02	2.0312	0.8214	0.0526	0.283080	10.4	
STM 6	0.703758	0.512928	5.7	38.54	15.61	18.90	2.0391	0.8257	0.0529	0.283100	11.1	
STM 15	0.703686	0.512932	5.7	38.48	15.59	18.87	2.0391	0.8262	0.0530	0.283097	11.0	
STM 20	0.703758	0.512927	5.6	38.54	15.61	18.90	2.0395	0.8259	0.0529	0.283100	11.1	
STM 33	0.703714	0.512936	5.8	38.48	15.59	18.85	2.0407	0.8270	0.0530	0.283100	11.1	
STM 34	0.703693	0.512929	5.7	38.46	15.59	18.84	2.0408	0.8271	0.0530	0.283102	11.2	
STM 37	0.703898	0.512853	4.2	38.50	15.60	18.88	2.0395	0.8265	0.0529	0.283050	9.3	
STM 44	0.703781	0.512914	5.4	38.60	15.63	18.94	2.0373	0.8250	0.0527	0.283090	10.8	

Note: δ18O of plagioclase in per mil. Though samples are divided by stage, they are listed in numerical and not stratrigraphic order within each stage. Uncertainties are presented in Supplement 6.

[a]Samples with reported $^{176}Hf/^{177}Hf$ were analzyed at DTM, all others at NMSU.

[b]Signal strength of ^{208}Pb was negligible on two separate aliquots of sample NMSB13.

Table 3.2

Re-Os Isotopic Compositions for the Steens Basalt

Sample	Re (ppb)	Os (ppb)	$^{187}Re/^{188}Os$	$^{187}Os/^{188}Os$	2σ Error	$^{187}Os/^{188}Os_i$
Lower B Steens						
JS22	0.4469	0.5962	3.61	0.12921	0.00007	0.12820
NMSB-5	0.2829	0.7296	1.86	0.13011	0.00006	0.12878
NMSB-13	0.4868	0.2889	8.12	0.13113	0.00005	0.12887
NMSB-18	0.3798	0.8617	2.12	0.13002	0.00006	0.12943
NMSB-19	0.3041	0.6747	2.17	0.13018	0.00005	0.12958
Upper Steens						
JS44	0.3438	0.0015	1126	0.28215	0.00046	

Note: Calculated $^{187}Os/^{188}Os_i$ for JS44 is negative, likely due to slight Os loss.

Table 3.3

Input for Isotope Mixing Models

	ES	DS	Olds Ferry	5% Melt ES	5% Melt DS	5% Melt OF
$^{87}Sr/^{86}Sr$	0.7040	0.7026	0.7047	0.7040	0.7026	0.7047
$^{143}Nd/^{144}Nd$	0.51285	0.51313	0.51277	0.51285	0.51313	0.51277
$^{206}Pb/^{204}Pb$	19.50	18.28	19.04	19.50	18.28	19.04
$^{207}Pb/^{204}Pb$	15.60	15.49	15.64	15.60	15.49	15.64
$^{208}Pb/^{204}Pb$	39.20	37.30	38.77	39.20	37.30	38.77
$^{176}Hf/^{177}Hf$	0.28304	0.28326		0.28304	0.28326	
$^{187}Os/^{188}Os$	0.1325	0.1250		0.1325	0.1250	
Sr (ppm)	21.1	7.6	1025	420	190	695
Nd (ppm)	1.4	0.6	11.5	23	10	77
Pb (ppm)	0.07	0.02	16.77	12	0.4	70
Hf (ppm)	0.31	0.16		2.90	1.50	
Os (ppm)	0.00040	0.00005		0.00004	0.000005	
Ba (ppm)	6	0.6	436	114	11.4	1860
D_{Sr}				0	0	1.5
D_{Nd}				0.01	0.01	0.1
D_{Pb}				0	0	0.2
D_{Hf}				0.06	0.06	
D_{Os}				12	12	
D_{Ba}				0.01	0.01	0.2

Note: ES - enriched source, DS - depleted source, OF - Olds Ferry Terrane. Olds Ferry composition is sample DC08-01 of Kurz et al. 2017. Elemental concentrations for ES and DS from Sun and McDonough, 1989; Shirey and Walker, 1998; Workman and Hart, 2005. Other data sources as listed in Fig. 12 caption. 5% melts of each source calcualted from batch melting equation. See text for discussion.
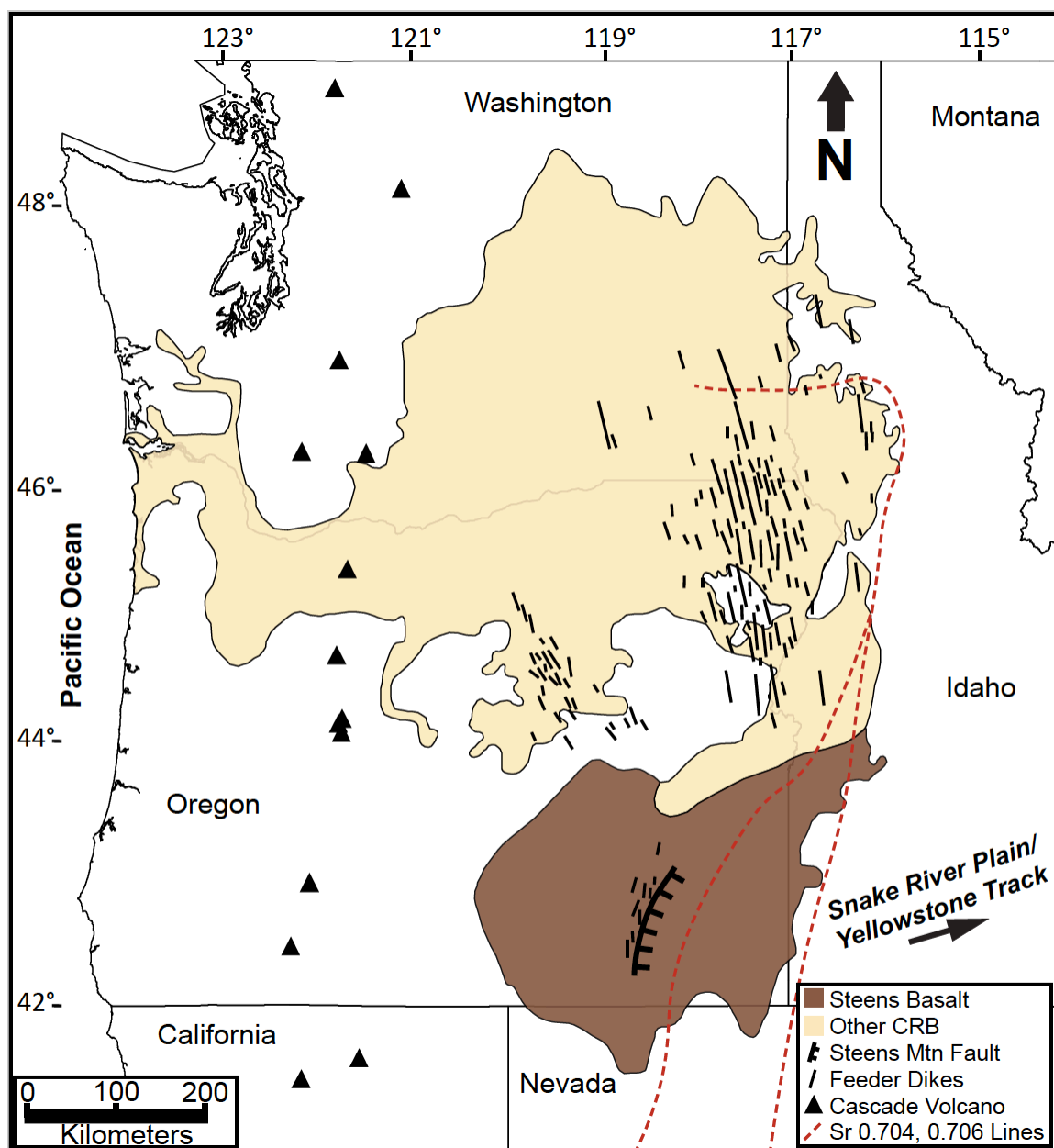
Figure 3.1. Regional map of the CRBG. Brown shaded region shows the full extent of Steens Basalt; tan region is the remainder of the CRBG. Solid black lines are feeder dikes; the Steens dikes near Steens Mountain, the Chief Joseph swarm in NE Oregon and SE Washington, and the Monument swarm in north central Oregon. Hatched curved black line is the highest relief segment of Steens Mountain escarpment along the Steens Fault, one of several NNE-striking normal faults in the northern Basin and Range province. Black triangles are the major Cascade volcanoes. Red dashed lines are the $^{87}Sr/^{86}Sr_i$ 0.704 (western line) and 0.706 (eastern line) isopleths (Pierce and Morgan, 2009); the 0.706 line is the inferred western boundary of the North American craton (Kistler and Peterman, 1973).
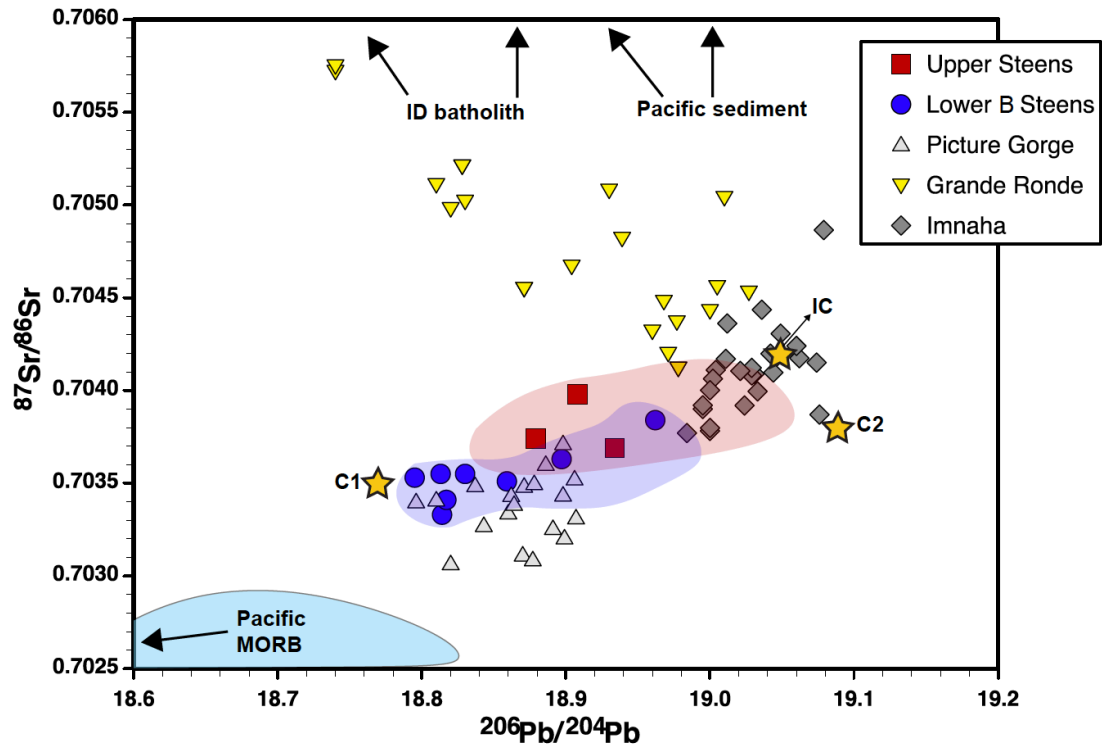
Figure 3.2. $^{87}Sr/^{86}Sr$ versus $^{206}Pb/^{204}Pb$ diagram for the main eruptive stages of the Columbia River Basalt Group. CRBG data from Hooper and Hawkesworth, 1993; Camp and Hanan, 2008; Wolff et al. 2008. Lower B (blue circles) and upper (red squares) Steens basalt samples are those that existed prior to this study, blue and red fields encompass the full range of lower B (blue) and upper (red) Steens Basalt data presented in this study, lower A samples overlap both fields. C1 and C2 are mantle endmember components of Carlson, 1984. IC is the Imnaha component defined by Wolff et al. 2013. Black arrows show the direction toward Idaho Batholith (Gaschnig et al. 2011) and Pacific sediment compositions, after Wolff et al. 2013. The Pacific MORB field (Stracke et al. 2003) extends to lower $^{87}Sr/^{86}Sr$ and $^{206}Pb/^{204}Pb$ beyond the scale of this diagram.
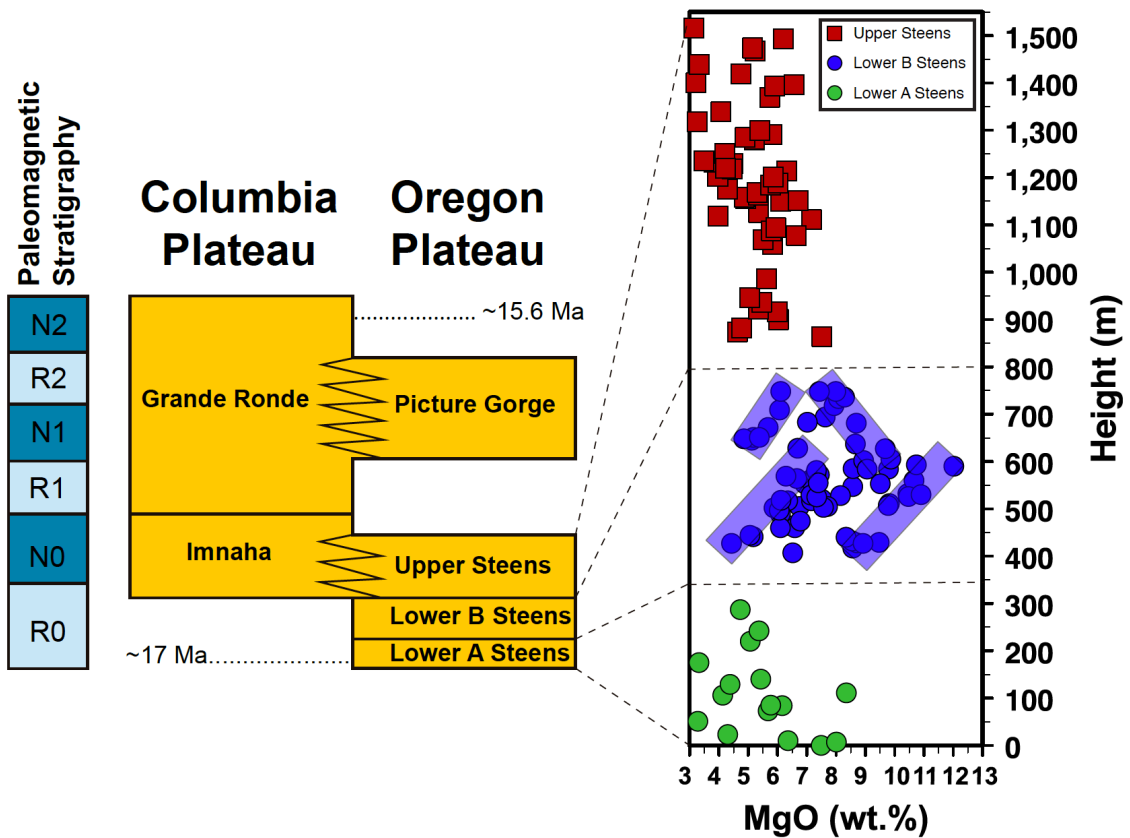
Figure 3.3. Schematic regional stratigraphy for the informally designated main stage eruptions of the CRBG and MgO compositional data for the 3 stages of the Steens Basalt. The Steens Reversal (R0 to N0) is estimated at 16.7 (Jarboe et al. 2010) and revised to 16.5 Ma (Mahood and Benson, 2017). Blue transparent bars highlight the high and low MgO trends in the lower B Steens stage, and emphasize the early increasing magnesian character at consistent ΔMgO. Paleomagnetic stratigraphy from Jarboe et al. (2008; 2010). Age of initiation of Steens Basalt, MgO data and Steens Basalt stage designations from Moore et al. (2018, in press). Upper limit of Grande Ronde volcanism from Barry et al. (2013). Modified from Camp & Ross (2004), Camp & Hanan (2008) and Wolff & Ramos (2013).
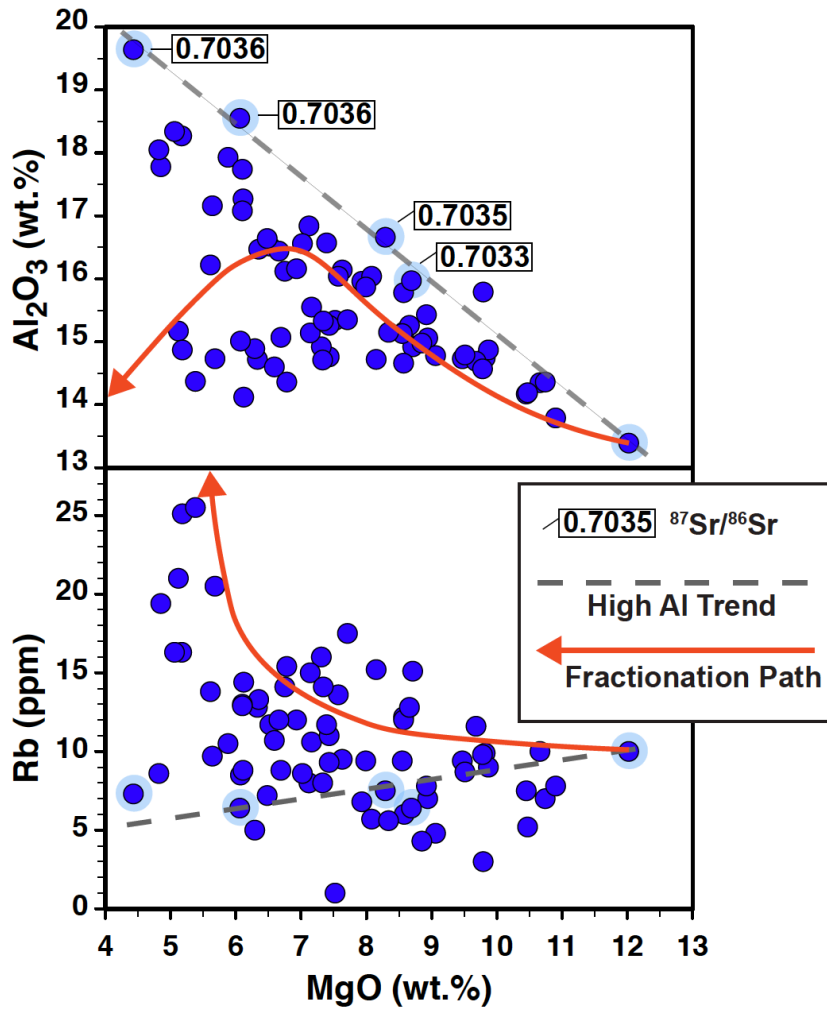
Figure 3.4. Al_2O_3 and Rb versus MgO for the lower B Steens Basalt. Data from Moore et al. (2018, in press). Gray dashed line shows a trend in the lower B Steens data toward high Al_2O_3 but low Rb. Red lines show the fractionation trend from a basaltic parent of 12 wt.% MgO and 0.5 wt.% H_2O at 4 kbar, calculated using the MELTS program (Gualda et al. 2012); the arrow points in the direction of increasing amounts of fractionation. Samples outlined in light blue define the high Al_2O_3 trend and have [87]Sr/[86]Sr compositions as shown in the black outlined boxes.
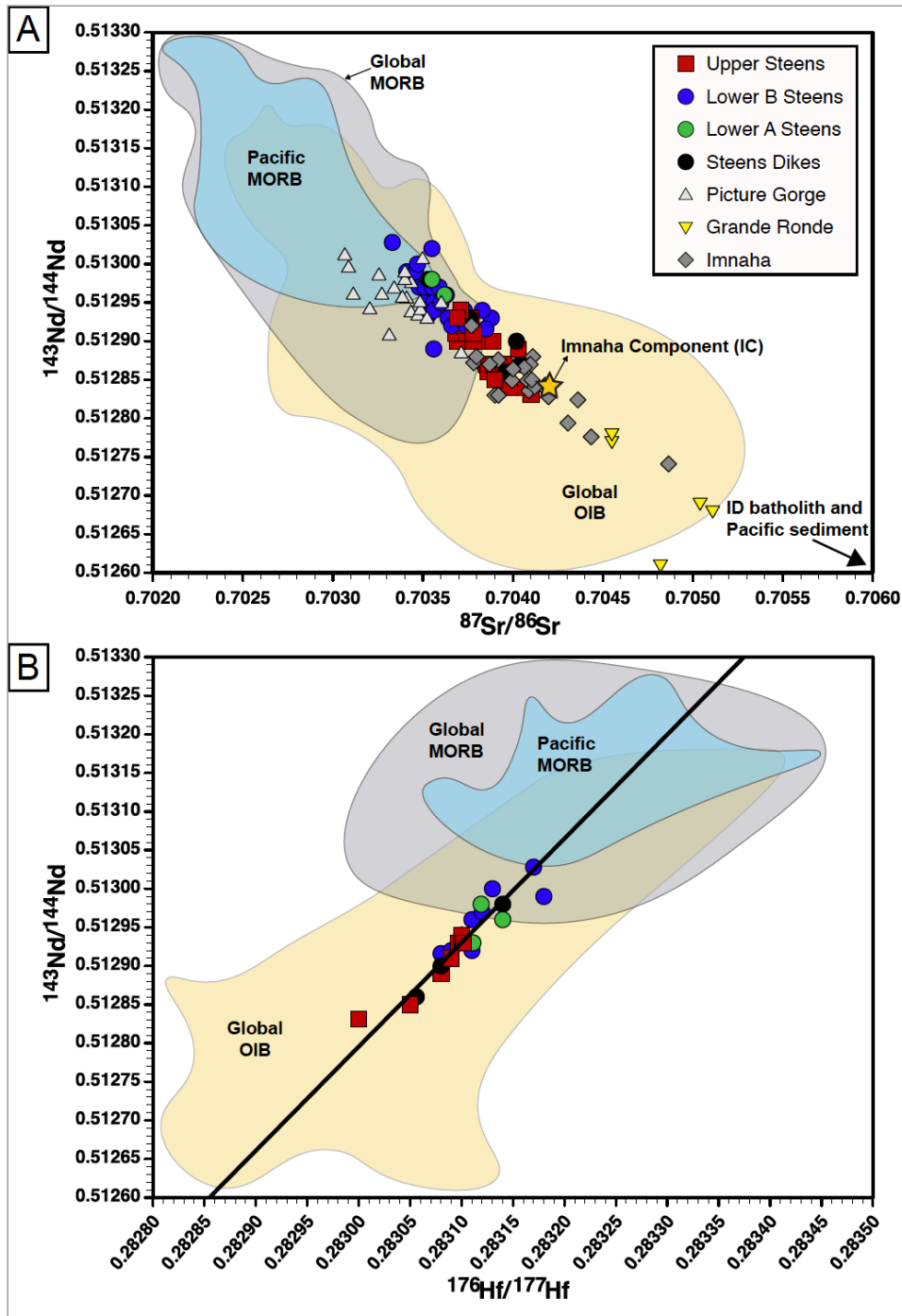
Figure 3.5. $^{143}Nd/^{144}Nd$ versus (A) $^{87}Sr/^{86}Sr$ and (B) $^{176}Hf/^{177}Hf$ for the Steens Basalt and other main stage formations of the CRBG. Some Steens Basalt data and all other CRBG data from Hooper and Hawkesworth, 1993; Camp and Hanan, 2008; Wolff et al. 2008. Global OIB, global MORB, and Pacific MORB fields from Stracke et al. 2003. IC is the Imnaha component defined by Wolff et al. 2013. Black arrow shows the direction toward Idaho Batholith (Gaschnig et al. 2011) and Pacific sediment compositions, after Wolff et al. 2013. Mantle array in (B) from Graham et al. 2006.
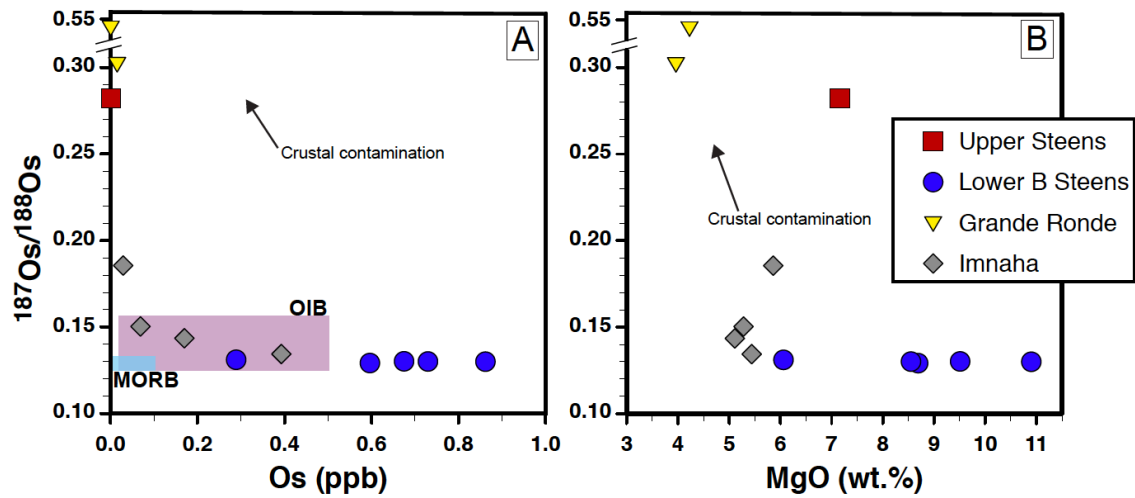
Figure 3.6. $^{187}Os/^{188}Os$ versus (A) Os concentration and (B) MgO for the Steens, Imnaha, and Grande Ronde Basalts. Imnaha and Grande Ronde Basalt data from Chesley and Ruiz (1998). MORB and OIB fields represent the bulk of uncontaminated global basalts from Shirey and Walker (1998) and Hauri (2002). Black arrow points in the direction that crustal contamination can drive Os isotopes and concentrations. Note the scale break at high values of $^{187}Os/^{188}Os$.
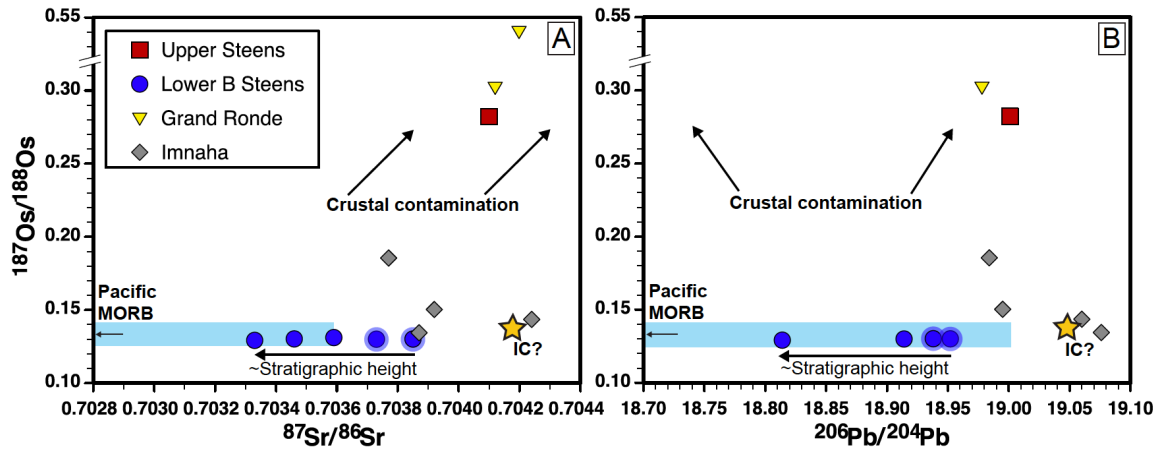
Figure 3.7. $^{187}Os/^{188}Os$ versus (A) $^{87}Sr/^{86}Sr$ and (B) $^{206}Pb/^{204}Pb$ for the Steens, Imnaha, and Grande Ronde Basalts. Lower B Steens Basalt samples highlighted with transparent blue circles have the highest Os concentrations and MgO. Decreasing $^{87}Sr/^{86}Sr$ and $^{206}Pb/^{204}Pb$ at ~constant $^{187}Os/^{188}Os$ roughly correlates with increasing stratigraphic height in the lower B Steens samples, as indicated by single black arrow. IC is the Imnaha component defined by Wolff et al. 2013, which was not defined in terms of $^{187}Os/^{188}Os$ and is therefore approximated here. Double black arrows point in the directions that crustal contamination can drive Os isotopes and concentrations. Imnaha and Grande Ronde Basalt data from Hooper and Hawkesworth, 1993; Chesley and Ruiz, 1998. Pacific MORB field from Gannoun et al. (2007). Note the scale break at high values of $^{187}Os/^{188}Os$.
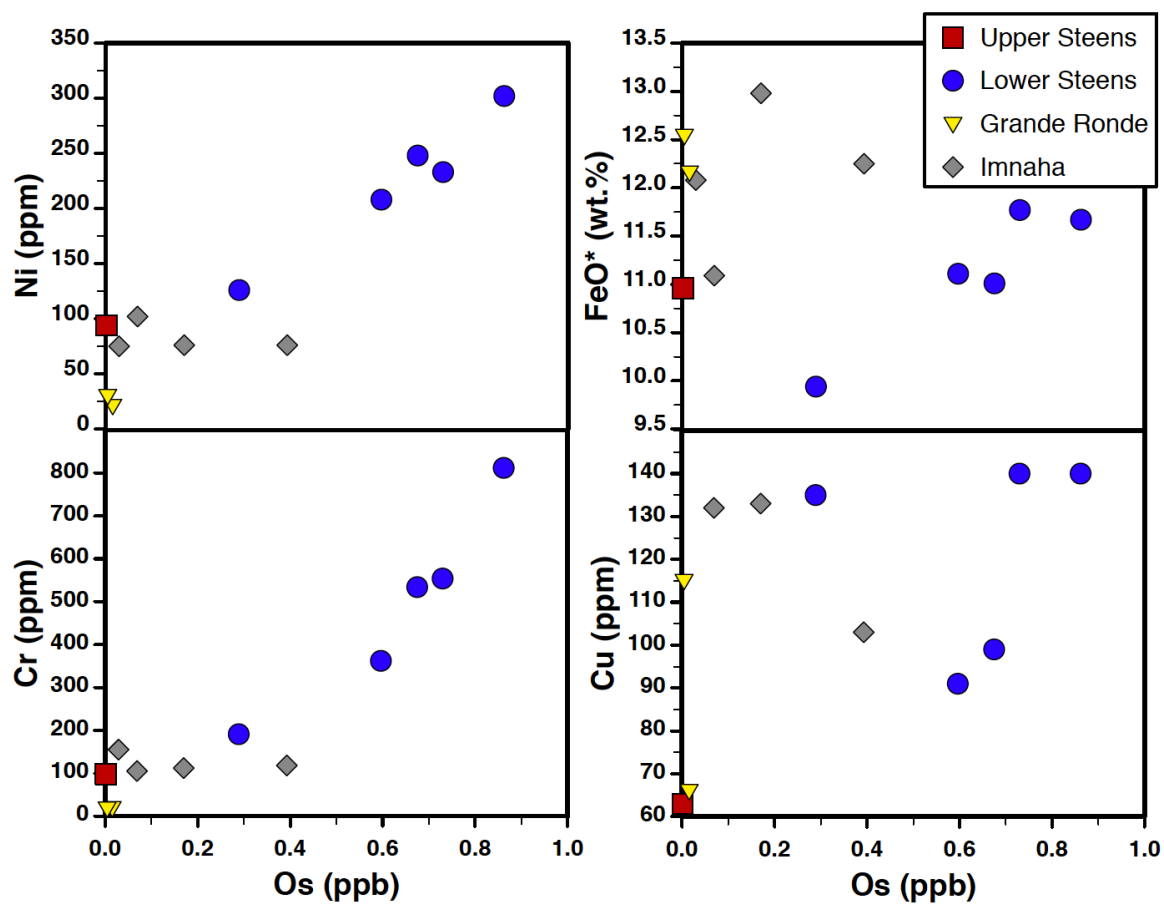
Figure 3.8. Select major and trace elements versus Os concentration for the Steens, Imnaha, and Grande Ronde Basalts. Imnaha and Grande Ronde Basalt data from Hooper and Hawkesworth, 1993; Chesley and Ruiz, 1998.
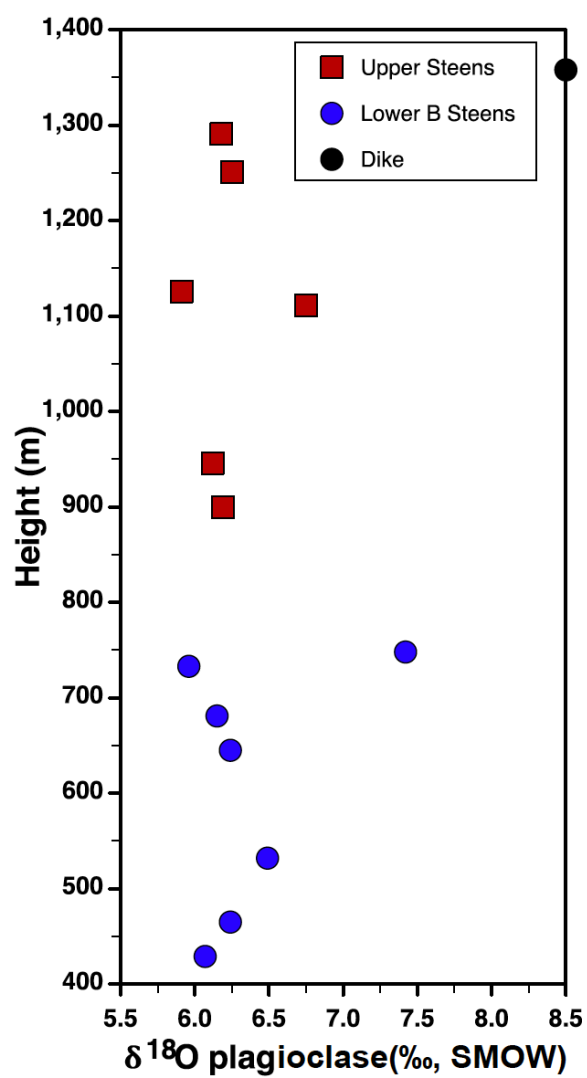
Figure 3.9. Stratigraphic height versus $\delta^{18}O$ of plagioclase for the Steens Basalt.
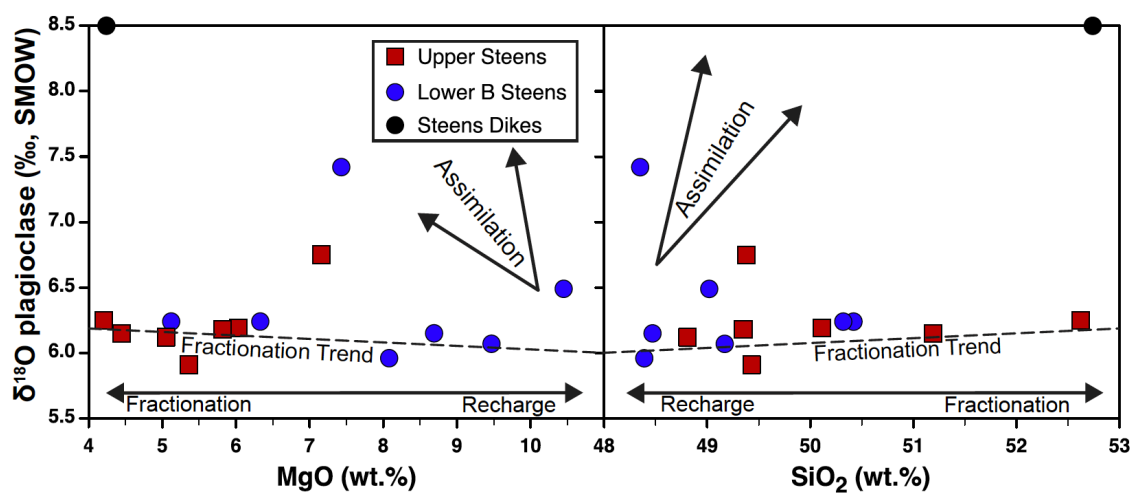
Figure 3.10. $\delta^{18}O$ of plagioclase versus MgO and SiO_2 for the Steens Basalt. Dashed black lines are fractionation trends from a parent of 11 wt. % MgO, 48 wt.% SiO_2 and 6‰ $\delta^{18}O$, calculated as described in the text. Double black arrows indicate the directions crustal contamination can drive compositions. Double headed black arrow shows the directions recharge or fractionation can drive compositions.
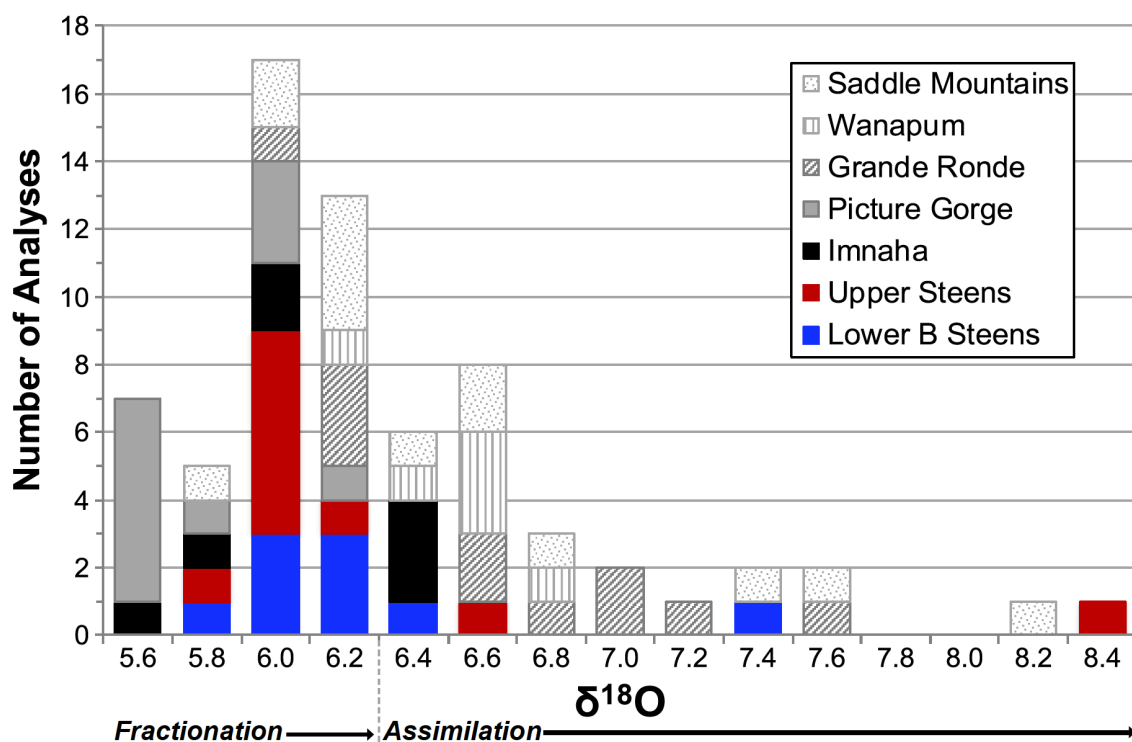
Figure 3.11. Histogram of $\delta^{18}O$ from select formations of the CRBG. The Steens Basalt $\delta^{18}O$ analyses are from plagioclase, all other CRBG $\delta^{18}O$ are from whole-rock analysis. See text for discussion of fractionation versus assimilation compositions. CRBG data from Nelson, 1983; Carlson, 1984; Hooper and Swanson, 1990; Brandon et al. 1993.
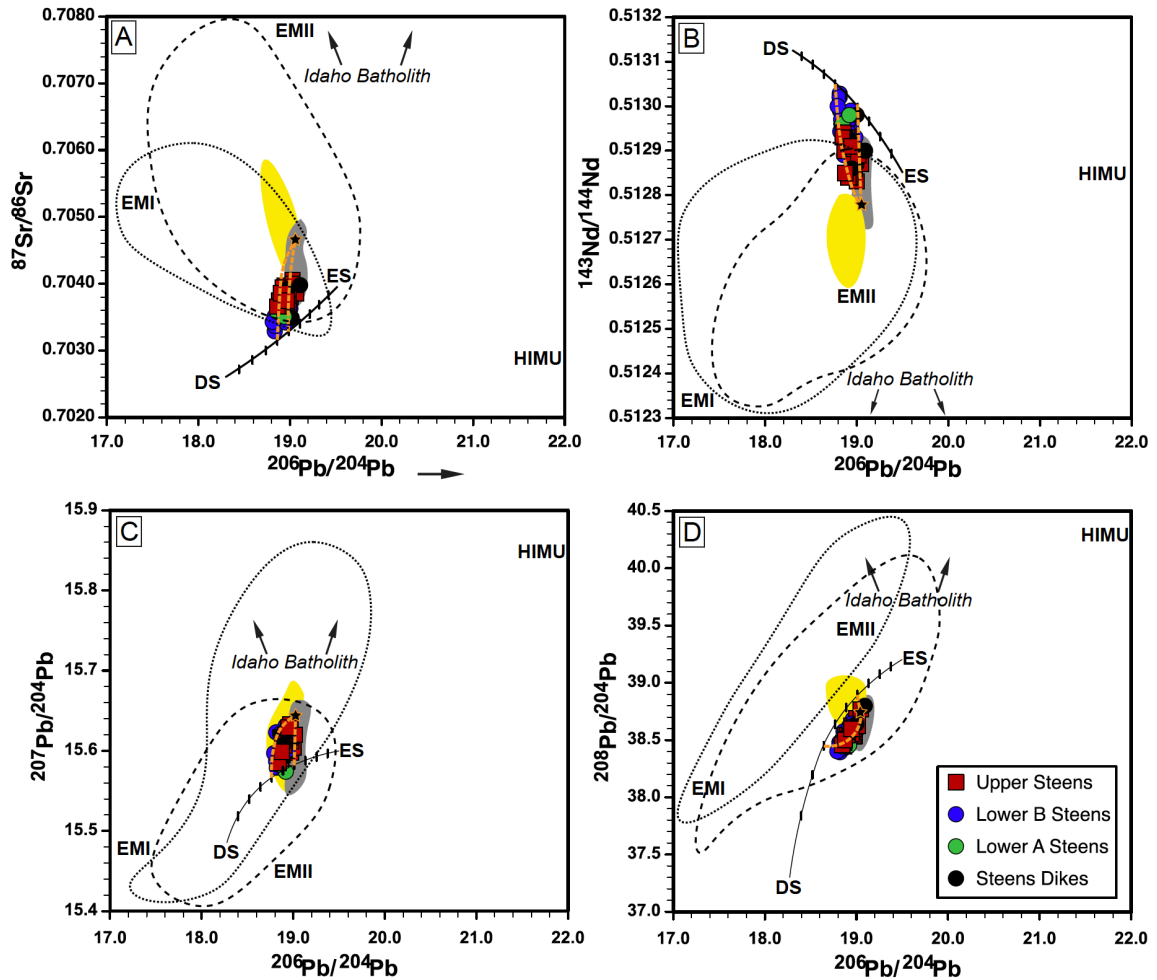
Figure 3.12, Part 1. Mantle melt isotopic mixing models for the Steens Basalt. Black arrows show the direction toward Idaho Batholith compositions (Gaschnig et al. 2011). DS (depleted mantle, low ^{87}Sr/^{86}Sr and ^{206}Pb/^{204}Pb, high ^{143}Nd/^{144}Nd), EMI (enriched mantle I, moderate ^{87}Sr/^{86}Sr, low ^{143}Nd/^{144}Nd, and high ^{206}Pb/^{204}Pb), EMII (enriched mantle II, high ^{87}Sr/^{86}Sr, low ^{143}Nd/^{144}Nd, and high ^{206}Pb/^{204}Pb), and HIMU (high μ, low ^{87}Sr/^{86}Sr and ^{143}Nd/^{144}Nd, very high ^{206}Pb/^{204}Pb) are the mantle components of Zindler and Hart (1986), revised by Hart et al. 1992, Hauri et al. 1994, and Stracke et al. 2005. ES = enriched source based on the "C" component of Hanan and Graham (1996) as modified by Rooney et al. (2012). Isotopic mixing curves between 5% partial melts of both DS and ES are shown with tick marks at 10% mixing increments, calculated as described in text. Gray and yellow fields encompass the data from Imnaha and Grande Ronde Basalts, respectively. Black dashed and dotted fields encompass data from the Siberian and Deccan Traps, respectively (from GeoRoc precompiled data files, accessed June, 2016). Black and orange star represents two Olds Ferry Terrane samples (Kurz et al. 2017) as a reasonable crustal contaminant. There is no reported ^{176}Hf/^{177}Hf or ^{187}Os/^{188}Os for the Olds Ferry Terrane, and only sparse data for these ratios in the Siberian and Deccan CFB. Note the break in scale at high ^{187}Os/^{188}Os in panels (G) and (H). Uncertainties (see Supplement 6) are much smaller than symbol size for all Steens Basalt data. See figure 13 for zoomed in detail of Steens Basalt data and modeled mixes.
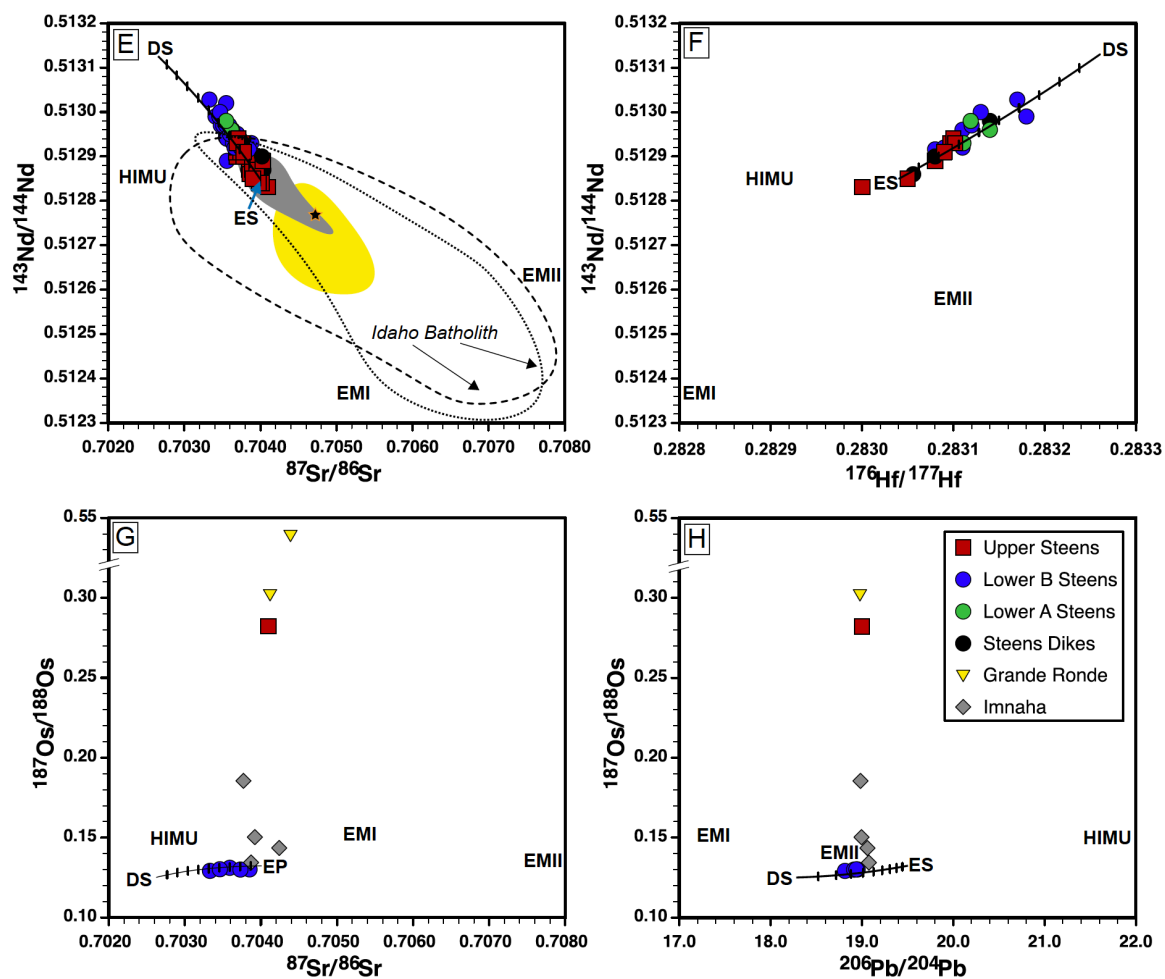
Figure 3.12, Part 2. See caption for 3.12, Part 1.
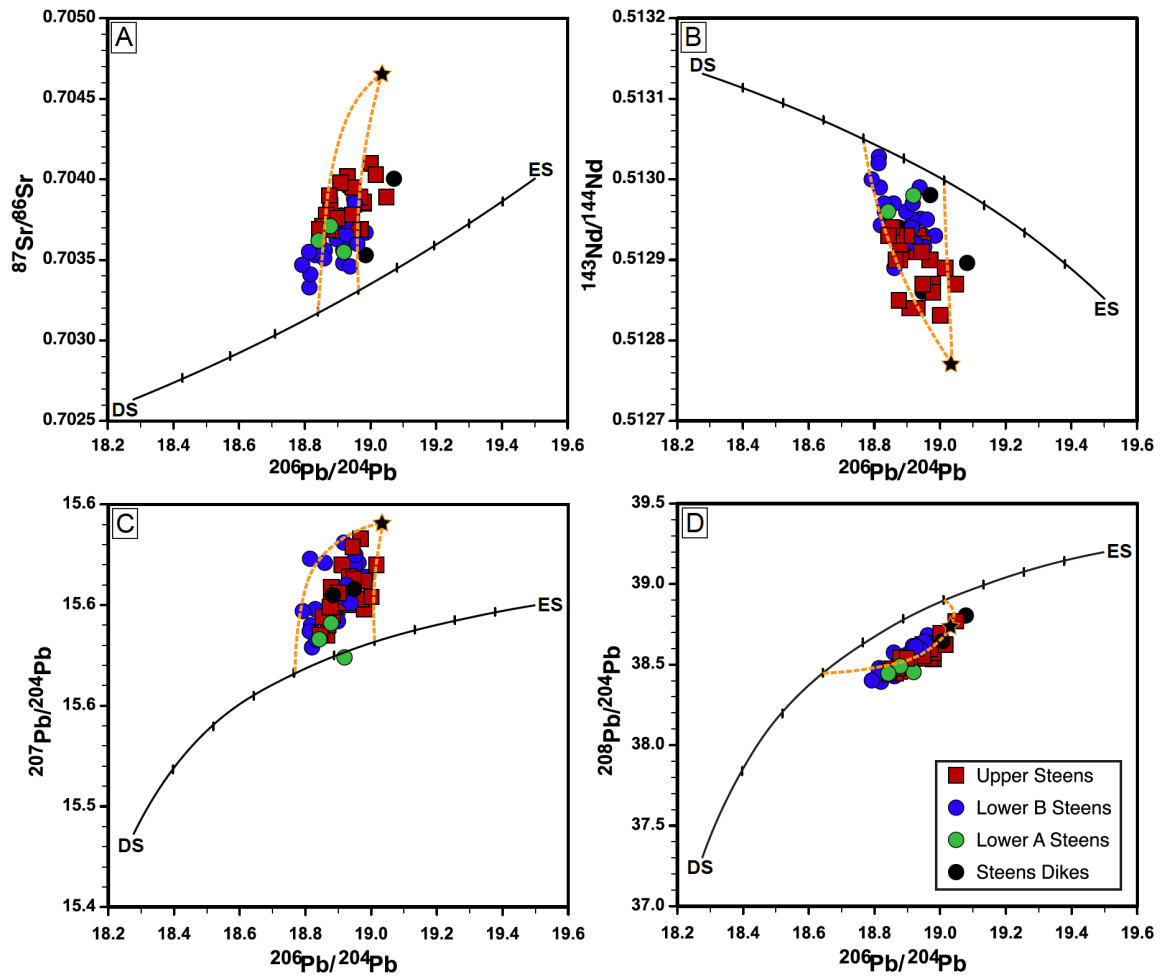
Figure 3.13. Crustal melt isotopic mixing models for the Steens Basalt. Orange dashed lines are calculated mixing curves between 5% partial melt of Olds Ferry Terrane (Kurz et al. 2017; Table 3.3) and various proportions of DS-ES partial melt mixes. Isotopic mixing curves between DS and ES from Figure 12 are replicated, and each tick mark represents 10% increments. See text for discussion.
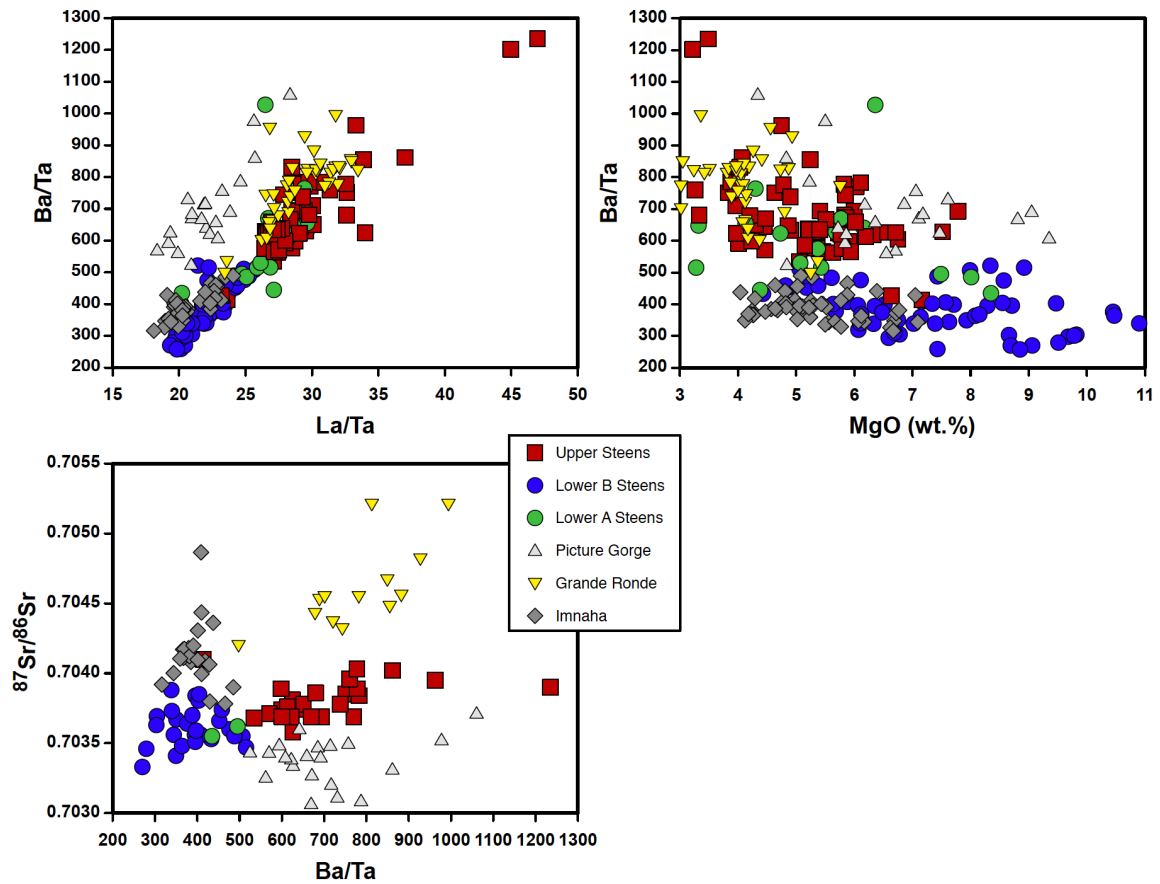
Figure 3.14. Comparison of LILE/HFSE ratios, $^{87}Sr/^{86}Sr$, and MgO for the Steens Basalt and other main stage formations of the CRBG. Data from Moore et al. (2018, in press); Camp and Hanan, 2008; Wolff et al. 2008.
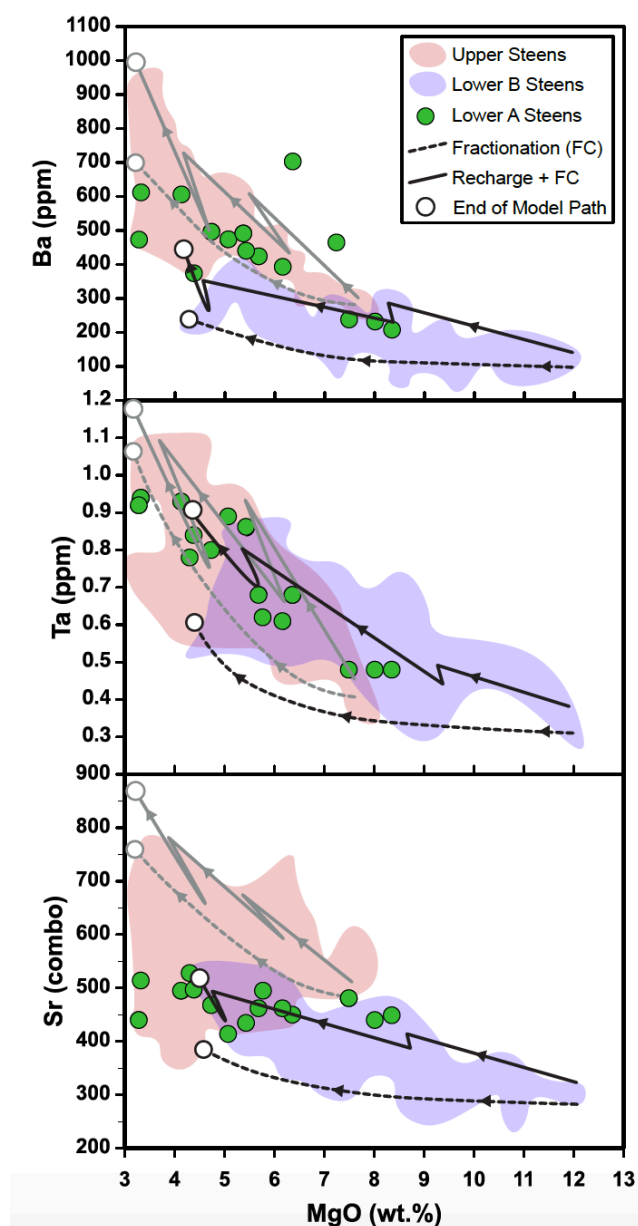
Figure 3.15. Fractionation and fractionation-recharge models for enrichment of select Steens Basalt trace elements. Fractionation only models are dashed lines, fractionation plus recharge models are solid lines; recharge events occur after 40% fractional crystallization and appear where excursions to higher MgO are indicated along the path, using a recharge composition as calculated in Chapter 4 (Table 4.1). Black lines are lower B Steens models using sample NMSB18 as a parent, and gray lines are upper Steens models using NMSB45 as a parent (Moore et al. 2018, in press). Modeled trends were ended (open black circles) when compositions reached the maximum values of MgO content in the lower B and upper Steens Basalts, respectively. Silica content (not shown) for all model paths stays within range of both lower B and upper Steens Basalts, respectively.
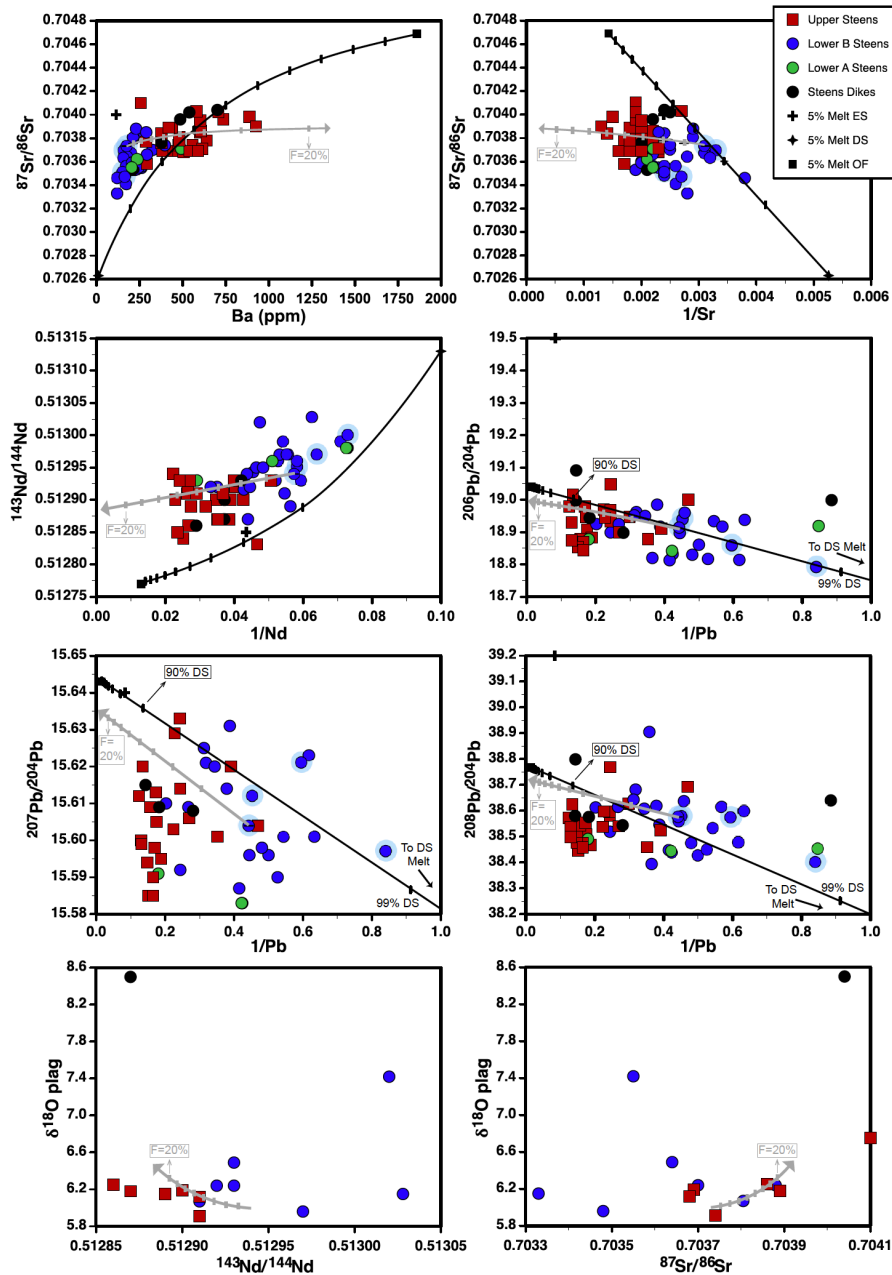
Figure 3.16. AFC of primitive lower B Steens melt and DS-OF mixing curves for select isotope and trace element compositions. Gray lines are AFC models, with tick marks at 10% decrements of remaining melt, where models end at 20% remaining melt, just beyond the maximum amount of fractionation allowable to reach the most evolved Steens Basalt compositions. Parent magma for the AFC model is NSMB18 (Moore et al. 2018, in press) and the crustal contaminant is a 5% partial melt of OF (Table 3.3). Black lines are binary mixing between 5% partial melts of DS and OF, where tick marks represent 10% increments of mixing, except for the Pb-Pb plots, where ticks for 99% DS-1% OF are also shown. Light blue highlighted samples are the most primitive samples from the lower B stage, those on the high MgO trend.
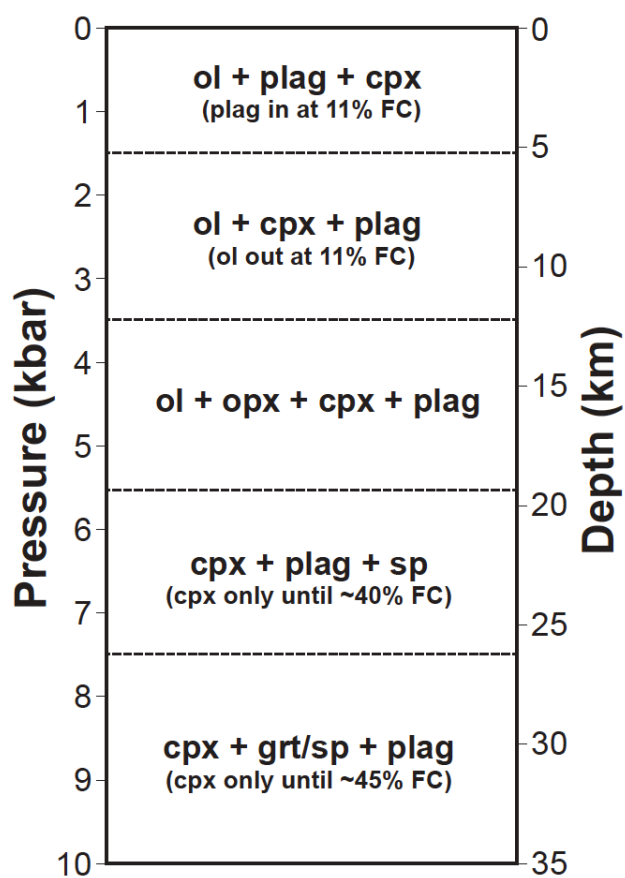
Figure 3.17. Mineral assemblage changes with pressure in primitive Steens Basalt. Phase equilibria at the range of pressures shown were calculated using rhyolite-MELTS (Gualda et al. 2012) from a parent magma composition of sample NMSB18 (Moore et al. 2018, in press). Ol = olivine, cpx = clinopyroxene, plag = plagioclase, opx = orthopyroxene, sp = spinel, grt = garnet, FC = fractional crystallization.
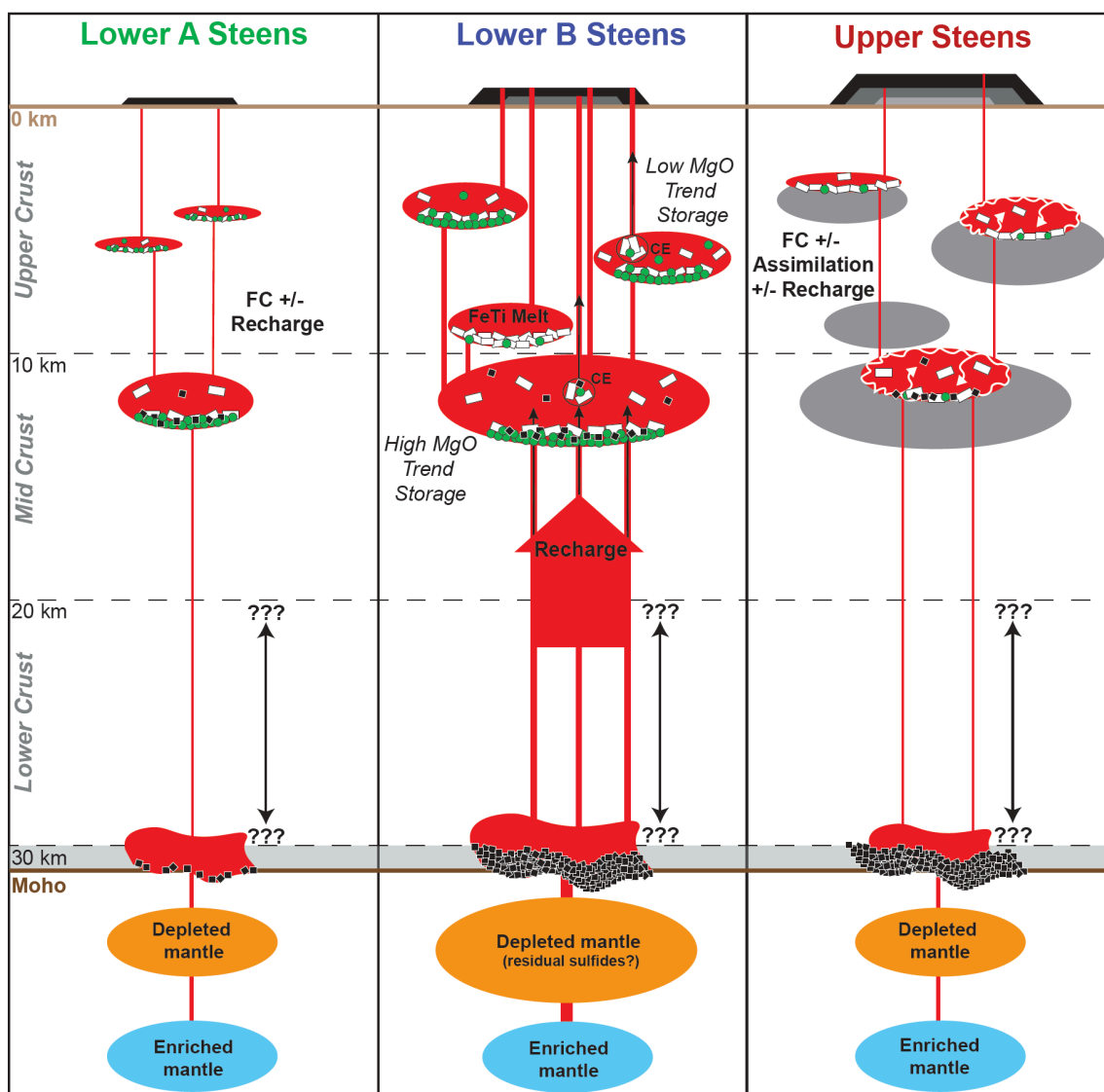
Figure 3.18. Schematic summary of mantle sources, crustal process and contributions to the three-stage evolution of the Steens Basalt. Green circles represent olivine crystallization, black squares are clinopyroxene, and white rectangles are plagioclase. FC = fractional crystallization; CE = cumulate entrainment; FeTi melt = iron and titanium rich melt; see text for discussion of processes. Question marks in lower crust reflect uncertainty of exact depth of cryptic clinopyroxene only crystallization, as clinopyroxene is the sole liquidus phase through 40% crystallization from ~30 up to ~20 km. Light gray transparent range at the base of the crust represents the ~3 km thick region seismically imaged to have higher velocity and density (~7.2-7.4 m/s and 2.95 /cm^3; Eagar et al. 2011), which coincides with a proposed region of abundant clinopyroxene only fractionation from this study. White curves and arrows indicate assimilation of crustal melts. Gray magma chambers in upper Steens panel represent the solid cumulate residue of prolonged fractionation of olivine, clinopyroxene, and plagioclase.

CHAPTER 4

The role of mafic recharge during onset of Continental Flood Basalts: Computational modeling of the Steens Basalt integrated with field and petrochemical constraints

4.1 ABSTRACT

Development of computational modeling over the past several decades is an important advancement for petrologic interpretation of magmatic systems. These tools allow the user to model petrologic processes with intensive parameters constrained by geochemical and textural data and add support to quantitative interpretations of the processes that contribute to magma generation. The Magma Chamber Simulator provides the most rigorous approach to petrologic computational modeling, in a software package that allows for energy-constrained open-system modeling that tracks simultaneous recharge, assimilation, and fractional crystallization of a magmatic system using whole-rock major, trace element, and isotope compositions. We here apply MCS modeling to evaluate the processes acting during the onset of flood basalt volcanism. It is axiomatic that a large pulse of basalt volcanism must have underlying processes that initiate the event. Detailed examination and modeling of stratigraphically controlled data provides insight into the growing magma imprint into and through the crust during these events.

The lower B Steens Basalt stage has been previously interpreted to represent the waxing of the basaltic pulse of Steens Basalt magmatism, itself an early stage of the Columbia River Basalt Flood Basalt event. We focus on modeling the lower Steens B section, during which magmatism was dominated by high recharge volumes and subordinate crystal fractionation and perhaps minor assimilation. Focused modeling of compositions from this stage of the Steens Basalt using the Magma Chamber Simulator confirms the dominance of recharge and constrains the relative energy budget and mass balance dictated by recharge, fractionation and assimilation in the lower B Steens Basalt.

Initial modeling using the family of MELTS software constrains the best fit intensive parameters for the lower B Steens Basalt. A range of pressure from 1-3 kbar, initial H_2O content from 0.5 to 1.0 wt. % of parent and recharge magmas, and oxygen fugacity from QFM to QFM-1 is indicated by computational modeling and is supported by previous thermobarometry results.

The composition of lower B Steens Basalt oscillates between two parallel trends, separated by ~5 wt.% MgO, which increase in MgO with stratigraphic height to a maximum of ~7.5 and ~11 wt.% MgO. The two trends then decline in MgO and converge

upsection. Best fit models using the Magma Chamber simulator for the more primitive MgO trend suggest that compositions on this trend are produced largely by recharge of primitive magma, with consecutive recharge events increasing in mass, and only minor amounts of cooling and crystallization in between recharge events. Samples in the upper part of the lower B Steens section on the primitive MgO trend decrease in MgO, and are consistent with a combination of fractionation, cumulate entrainment, and magma mixing among various primitive melt compositions. The more evolved MgO trend is composed of flows that are either sparsely phyric or giant plagioclase basalts that contain abundant large plagioclase phenocrysts. Models suggest the sparsely phyric flows are likely the result of fractionation from a primitive, high MgO parent at shallower crustal levels, whereas the giant plagioclase basalts are formed by cumulate entrainment into fractionated melts. These shallower, dominantly fractionating reservoirs are periodically pulsed by magmas from the recharge dominated primitive MgO trend, so that both the primitive and evolved MgO trend lavas increase in MgO over the interval during which recharge is dominant and volumetrically increases. Models including assimilation of anatectic wallrock melts are not consistent with the observed compositions.

An integrated mass balance calculation yields intrusive to extrusive ratios of ~8:1 to 14:1, with associated cumulate addition to the crust of 5-28 km. This initial attempt at a Steens Basalt mass balance suggests that significant gabbroic underplating occurs over the life of the flood basalt event, perhaps requiring foundering and delamination of deep crustal roots into the overlying mantle.

4.2 INTRODUCTION

Over the last 40 years, advances in the use of petrologic modeling for igneous rock suites have provided a means to substantiate qualitative interpretations of the processes that contribute to generation of magmatic systems. Though volcanic eruptions give a snapshot of magma petrogenesis, they are a partial sampling of a much larger flux of heat and mass from the mantle, the bulk of which may remain behind as igneous rocks in the crust. Whether erupted or stalled in the crust, magmas are affected to various degrees by passage through the crust, by differences in contributions of recharge (R) and

associated magma mixing, crustal assimilation (A), and fractional crystallization (FC). Computational modeling that simulates magmatic conditions and processes can be used as a complement to traditional methods, providing additional evidence for interpretation of the relative contributions of magmatic processes, as well as quantification of the relative masses of melts, fluids and crystals produced in the magma reservoir(s). In this way, temporal variations in sources and processes, as well as the impact of magmatic throughput on the growth and evolution of crust can be described and quantified.

In this study, I present computational modeling results using the new Magma Chamber Simulator for the generation of the Steens Basalt. The objective is two-fold: 1) to understand the mass and energy balance related to the passage of a pulse of magmatism from the mantle through the crust, as related to the onset of Steens Basalt volcanism, itself the herald of the Columbia River Flood Basalt event; and 2) to test the effectiveness and flexibility of the MCS model in light of the detailed temporal, textural, mineral chemical and compositional (major element, trace element and isotopic) constraints we have on the system. The focus here is on modeling of the lower Steens Basalt, particularly the lower B Steens Basalt, which is the stage of Steens Basalt volcanism that represents the persistent injection of basalt to create a mid to shallow crustal magma plexus. In particular, modeling is aimed at teasing out the processes responsible for oscillations between high and low MgO trends in the lower B Steens Basalt (Fig. 4.1), and the accompanying increase in magnesian character of both trends initially upsection. Petrologic modeling of the detailed, stratigraphically controlled textural and compositional data obtained for the lower B Steens Basalt provides important evidence for the development of a large, mafic magmatic system staged in the mid to shallow crust and the magmatic processes that operated during the onset of vigorous flood basalt volcanism. The goal of this computational modeling is a quantitative rendering of the temporal evolution of depth of differentiation, the relative importance of RAFC processes, the variations in mass and energy contributions from the mantle, and the response of the crust, as recorded in the lower B Steens Basalt. This approach has application for understanding the waxing stages of other continental flood basalt (CFB) events by comparison.

4.3 THE FOUNDATION OF THE MAGMA CHAMBER SIMULATOR

Early iterations of quantitative petrologic modeling include equations to assess trace element/isotope mixing and assimilation coupled with crystal fractionation (AFC) by DePaolo (1981; 1985), which recognize the importance of the energy link between assimilation and crystallization, expressed as the parameter "r", or the ratio of rate of assimilation to rate of crystallization. The MELTS family of software packages (MELTS, p-MELTS, rhyolite-MELTS) provide a next step forward for computational modeling, allowing the user to model thermodynamically consistent AFC processes driven by phase equilibra. These programs calculate equilibrium states of coexisting solids, liquids and fluids from thermodynamic models of relevant phases and track the changing major element compositions of both liquids and solids (Ghiorso and Sack, 1995; Ghiorso et al. 2002; Gualda et al. 2012). MELTS tracks changing melt composition and relative masses of melt + solid ± fluid during cooling and crystallization, while simultaneously tracking the changing crystallizing assemblage and mineral compositions. Input parameters for the MELTS program are the parent magma composition, initial H_2O content, pressure constraints, and oxygen fugacity. The ability to track changing trace elements and isotope compositions with energy conservation between the magma and the entire system was introduced with Energy-Constrained Recharge, Assimilation, and Fractional Crystallization (EC-RAFC; Bohrson and Spera, 2001; 2003; Spera and Bohrson, 2001; 2002; 2004). The gap between the latter two modeling packages is the combined modeling of major and trace elements, isotopes and phase equilibria simultaneously for RAFC processes in a multicomponent, multiphase system. The most recent advance in petrologic computational modeling combines the power of the MELTS family of software (major elements and phase equilibria) with EC-RAFC (trace elements and isotopes) into one program via the Magma Chamber Simulator (MCS; Bohrson et al. 2014). MCS is a thermodynamic, energy and mass constrained tool for calculating how composition, mass, and thermal constraints in a crustal magmatic system vary in response to recharge, assimilation, and crystallization. All of these steps have led to the ability to rigorously model petrologic processes and quantify their relative contributions in a thermodynamically and self-consistent manner.

The MCS software package allows for energy-constrained open-system modeling that tracks simultaneous RAFC of a magmatic system using whole-rock major and trace element and isotope compositions. Input includes parental magma, recharge magma(s), and wallrock compositions and the initial H_2O content and oxygen fugacity of each. The simulation is isobaric, so a system pressure is also required for the magma body, as well as masses for wallrock and recharge magma(s). Additional input includes the temperature of the recharge magma(s) upon recharge into the magma body and the initial temperature of the wallrock, as well as masses for wallrock and recharge magma(s). The program tracks changing compositions of all components in the system (melts + solids ± fluids) along user defined temperature decrements for the magma body. With each temperature step, MCS calculates the equilibrium conditions for the melts + solids ± fluids of the parent magma, recharge magma, and wallrock. Recharge events occur at a user set temperature or after a user set cooling interval. Up to 5 recharge events can be included in one simulation. As the system cools, heat is transferred to the wallrock; once heated beyond the solidus, anatectic wallrock melts are added when a set critical wallrock melt volume fraction is reached (i.e., a percolation threshold (Bohrson et al. 2014). The detailed compositional and mass changes tracked throughout the simulations can then be compared to a suite of igneous samples.

4.4 GEOLOGIC SETTING OF THE STEENS BASALT

The Steens Basalt began erupting at ~16.9 Ma at Steens Mountain (Moore et al. 2018, in press) and is the oldest member of the Columbia River Flood Basalt Group (CRBG). The Steens Basalt section is thickest at Steens Mountain and crops out in ~200 thin flows and compound flow lobes. In order to capture flow-by-flow variations in composition, detailed sampling has been conducted at multiple stratigraphic sections that cover most of the lateral extent of Steens Mountain (Johnson et al. 1998, Bendaña, 2016; Moore et al. 2018, in press). Changes in chemical composition of the lavas upsection have prompted distinction between the lower and upper Steens Basalt flows (Camp et al. 2013). These geochemical changes are attributed to differences in relative amounts of fractional crystallization and recharge through time (Gunn and Watkins, 1970); more

recently, they have been attributed to varying contributions of RAFC through time (Camp et al. 2013; Wolff and Ramos, 2013; Moore et al. 2018, in press).

The Steens Basalt whole-rock major and trace element compositions, mineral compositions, textural characteristics and field relations record a three-stage magmatic history (Moore et al. 2018, in press). The first, stratigraphically deepest stage is the lower A Steens Basalt. Lavas of this stage occur in a paleovalley near the southern end of Steens Mountain (Moore et al. 2018, in press) and are interpreted as early fitful magma ascent and eruption where crystal fractionation dominates over recharge. The lower B Steens Basalt is a ~350-m thick stack of lava flows lacking significant weathering horizons and accounting for more about 2/3 of the volume of the Steens Basalt. Lower B Steens Basalt contains the most primitive compositions of the Steens Basalt and of the CRBG as a whole. This stage represents waxing of the Steens basaltic pulse when recharge played the largest role. Compositions oscillate between a primitive high and more evolved low MgO basalt with a ΔMgO of ~4-5 wt.% (Fig. 4.1); both suites become more magnesian upsection in the lower part of the lower B Steens Basalt, signaling a period dominated by recharge over fractional crystallization. This stage closes with declining oscillations in MgO to produce more homogeneous compositions (6-8 wt.% MgO; Fig. 4.1), marking the transition to lesser recharge and more extensive fractional crystallization. The third and final stage is represented by the upper Steens Basalt. Upper Steens lavas range to basaltic andesite and as a group are less magnesian, more Fe-rich and incompatible trace element enriched than the basalt lavas produced during the waxing lower B Steens pulse. Fractional crystallization dominates over recharge and is accompanied by modest crustal assimilation. The upper Steens stage represents the waning of the Steens Basalt pulse as flood basalt volcanism migrated north (Moore et al. 2018, in press).

Though the Steens Basalt contains the most primitive basalts of the CRBG, it is also known for containing flows that have very large (>1cm) and abundant plagioclase phenocrysts comprising up to 40% of the mode, called giant plagioclase basalts (GPB). GPB basalt flows occur also in the Imnaha Basalt of the CRBG (Hooper et al. 1984; Reidel et al. 2013), and likely in all other flood basalt provinces, including the Deccan

Traps (e.g. Higgins and Chandrasekharam 2007; Talusani 2012; Sheth 2016), Emeishan Traps (e.g. Cheng et al. 2014) and Keewenawan (Walker et. al 2002). GPB flows are present in each of the Steens Basalt stages (lower A, lower B, and upper), but vary in textural type throughout the section (Moore et al. 2018, in press). GPB flows are on the evolved end of the Steens Basalt compositional spectrum ($\leq$8 wt.% MgO), but their geochemical characteristics cannot be reproduced solely by equilibrium or fractional crystallization from more primitive Steens Basalt compositions. Trace element compositions in plagioclase from GPB in lower B Steens Basalt are low relative to those in upper Steens Basalt, and $^{87}Sr/^{86}Sr$ in plagioclase from GPB of both stages is largely in equilibrium with the host rock (Toth, 2018).

4.5 MODELING APPROACH

The overall objectives of computational modeling were 1) to establish pressure, initial H_2O content and oxygen fugacity of the Steens Basalt system during its development, and 2) to simulate the parents and processes that make a self-consistent model that reasonably reproduces the stratigraphic variations in lava and mineral composition in the Steens Basalt. Initial computational modeling was conducted in rhyolite-MELTS (Gualda et al. 2012) to constrain best-fit intensive parameters (pressure, initial H_2O content, oxygen fugacity) for later input into MCS simulations. Calculations using a variety of mineral-melt thermobarometers (Moore et al. 2018, in press) served as a basis for the initial range of intensive parameters used as input into rhyolite-MELTS simulations. A variety of parental magma compositions were used to test the range of pressure, H_2O content, and oxygen fugacity conditions that prevailed in the Steens magmatic system. Pressure was varied from 1-10 kbar*, initial H_2O content from 0 to 1.5 wt.%, and oxygen fugacity from QFM+2 to QFM-1. Results of the simulations were compared to the lower B Steens Basalt whole-rock compositions to arrive at the range of conditions most applicable to the full range of observed samples. Determination of these best-fit parameters inform initial MCS simulations. MCS models major element and

*Kilobars (kbar) are used as the unit measure of pressure throughout this chapter instead of the International System of Units recommended Gigapascals (GPa) due small ranges in upper crustal pressures for the lower B Steens Basalt. Note that 10 kbar = 1 GPa.

phase equilibria constraints first; these results inform calculation of open-system trace element and isotopic constraints.

Computational modeling with MCS was conducted to constrain the RAFC processes responsible for generation of the lower B Steens Basalt compositions, and to determine the relative mass contributions of the individual RAFC processes. In particular, for this study, the model results can be compared to the stratigraphically controlled, upsection variations observed in the lower B Steens Basalt section. The changing character of both the high and low MgO trends of the lower B Steens Basalt (Fig. 4.1) are modeled as separately evolving entities, in contrast to the approach of Graubard (2016), where excursions from high MgO compositions to low MgO compositions (and vice versa) were modeled. In this way, these models test the idea of separately evolving magma chambers or distinct reservoirs for the high and low MgO lavas. The lower B and upper Steens Basalt crops out over 53,000 km^2, of which the basalts at Steens Mountain are a small portion, therefore individual sections may not catch the entire range geochemical variability present. Some of the detailed geochemical excursions in stratigraphy may be an artifact of sampling of a particular section, but as a whole, there are patterns that persist from section to section. The goal of this modeling is not to capture every flow to flow compositional excursion, but to elucidate a plausible scenario to explain the overall variability upsection in the lower B Steens Basalt stage.

Compositional input for parent and recharge magmas, wallrock assimilant, typical mineral compositions for plagioclase, olivine and clinopyroxene that were used to calculate potential cumulate compositions, potential cumulate compositions, and cumulate plus melt compositions are in Table 4.1. Partition coefficients used in trace element modeling are reported in Table 4.2. The parental magma composition used for both the low and high MgO trends, sample MF9466 (Johnson et al. 1998), is one of the more mafic lower B Steens Basalt samples, appears early in the section, falls on the high MgO trend (Fig. 4.1). The recharge magma composition used in simulations is calculated from lower B Steens Basalt sample NMSB18 with the addition of 4% lower B Steens Basalt olivine of Fo$_{86}$ composition (whole-rock and mineral compositions from Moore et al. 2018, in press). Sample NMSB18 is one of the most primitive among lower B Steens

Basalt samples, contains 7% modal olivine and lacks textures suggestive of olivine accumulation. The 4% olivine was added in an attempt to achieve a composition that is close to a primitive mantle melt prior to olivine fractionation. While this forsterite composition is not in equilibrium with mantle compositions, it is the highest forsterite composition observed in Steens Basalt. The resulting recharge magma composition is slightly more magnesian than the most magnesian sample from the lower B Steens Basalt, JS13 (Johnson et al. 1998), but falls on a trend that projects backward (to higher MgO) from 3 kbar fractionation models. These 3 kbar FC models are a good fit to most of the primitive lower B Steens Basalt samples (Fig. 4.2). JS13 was not used to calculate the recharge magma composition given that only XRF data are available for it; MCS modeling for this study includes major, trace and isotopic compositions, all of which are available for NMSB18. Though assimilation is not expected in lower B Steens Basalt based on whole-rock compositional interpretations for this study (Moore et al. 2018, in press; Chapter 3), model runs testing addition of wallrock were conducted for both the high and low MgO trends. The assimilant composition used in simulations is an intermediate (basaltic andesite) sample from the Olds Ferry Terrane (Table 4.1; sample 99AQ-07 of Tumpane, 2010; $^{87}Sr/^{86}Sr$ composition from Kurz et al. 2017). Olds Ferry is the mafic accreted terrane that composes the basement rock just to the northeast of Steens Mountain (Kurz et al. 2017). Sample 99AQ-07 was used as the wallrock composition for assimilation models that reasonably explain some compositional trends in the upper Steens Basalt (Graubard, 2016). As a test for the possibility of cumulate or cumulate plus melt entrainment to explain some lower B Steens Basalt compositions, various potential compositions were calculated. Cumulate entrainment was modeled using compositions of average lower B Steens Basalt plagioclase + olivine + clinopyroxene in the proportions of 60%/15%/25%, and plagioclase + olivine in the proportions of 89%/11%; selection of proportions of these minerals were informed by fractionation models in initial rhyolite-MELTS calculations. The average plagioclase, olivine and clinopyroxene mineral compositions used to calculate these bulk cumulate compositions are An_{66}, Fo_{76}, and Mg#75, respectively (Table 4.1; major elements averaged from the mineral composition data of Moore et al., 2018, in press; trace element compositions of average plagioclase

composition from Toth, 2018). Because concentrations of the trace elements modeled in MCS simulations (Sc, Rb, Sr, Ba, and Ce) are not available for lower B Steens Basalt olivine and clinopyroxene, Rb, Sr, Ba and Ce (ppm) were all assumed to be zero for both olivine and clinopyroxene given these elements are incompatible in both phases (Table 4.2). A 30 ppm estimate for Sc in clinopyroxene is included given this element is compatible in clinopyroxene. This estimate is from the average clinopyroxene composition of the Kakanui, New Zealand augite Smithsonian Microbeam Standard NMNH 122142 (Mason and Allen, 1973). Lastly, the composition estimated for a FeTi rich melt plus cumulate plagioclase in Chapter 3 was used to test the simple mixing models proposed for this component and a primitive lower B Steens Basalt composition.

Simulations using the parent and calculated recharge magma compositions were run over the range of best-fit intensive parameters determined from rhyolite-MELTS models to further constrain these parameters. As a first step, simulations of whole-rock major element and mineral compositions of the appropriate phases present in the lower B Steens Basalt (olivine, spinel, clinopyroxene, plagioclase, and Fe-Ti oxides) were compared to observed samples. Once the best-fit major element models were constrained, modeling of whole-rock trace and isotope compositions was conducted. Viable models include those that reproduce the appropriate excursions in individual elemental compositions for each scenario, where concentrations are similar between the models and model targets, though not necessarily identical (but close to or within analytical error).

4.6 MODELING RESULTS

4.6.1 Best-Fit Intensive Parameters

Best-fit intensive parameters, including pressure, oxygen fugacity, and initial H_2O content, for both the high and low MgO trend models of the lower B Steens Basalt are in Table 4.3. These best fit parameters were determined based on evaluation of hundreds of simulations in both rhyolite-MELTS and MCS. Results from both are consistent and predict that mid to upper crustal conditions control the compositional characteristics evident in the lower B Steens Basalt.

Pressures are constrained to 1 to 3 kbar by both rhyolite-MELTS and MCS modeling for the range of lower B Steens Basalt compositions. Fractionation models at 4 kbar and above predict orthopyroxene as a liquidus phase, but this mineral phase does not appear in any Steens Basalt flows. Fractionation models at 3 kbar are most appropriate to explain the range of compositions on the high MgO trend; lower pressure suppresses plagioclase as a fractionating phase to well below the MgO content where plagioclase is present in these flows (i.e. plagioclase appears in the high MgO trend samples at ~7-8 wt.% MgO, but at 2 kbar and below, plagioclase first occurs at ~6.3 wt. % MgO). Fractionation models at 1 kbar are most appropriate to explain the range of sparsely phyric flows in the low MgO trend (Fig. 4.3). Though higher pressures are consistent with some elemental compositions of sparsely phyric low MgO target samples (e.g. FeO, CaO at 3 kbar; Fig. 4.3) and some of the GPB-low MgO targets (e.g. CaO), 3 kbar FC cannot explain the full range of both sparsely phyric and GPB compositions on the low MgO trend. The 1 kbar FC model is a good fit to most of the sparsely phyric targets, and so this pressure is used in modeling those targets on the low MgO trend. A separate process is invoked to explain the GPB compositions. The modeled, best fit pressure results generally agree with thermobarometric calculations from mineral-melt compositions of the lower B Steens Basalt, which suggest a pressure range of 1-4 kbar (Moore et al. 2018, in press). Given these results, 3 kbar was used for the high MgO trend models, and 1 kbar was used for the low MgO trend models.

Oxygen fugacity is constrained to the Quartz-Fayalite-Magnetite buffer; the range from QFM-1 to QFM is consistent with the bulk of the lower B Steens Basalt data. Slightly more oxidizing conditions represented by QFM+1 predict Fo_{89} in olivine, which is higher than any analyzed forsterite from the lower B Steens Basalt (Fo_{86} is the maximum). QFM+2 yields orthopyroxene in the mineral assemblage, appearing after olivine in the sequence at 9 wt.% MgO. This suggests QFM and below is the best-fit oxygen fugacity for the system. Because the bulk of oxygen fugacity calculations from Fe-Ti oxide mineral compositions of the lower B Steens Basalt give QFM-1 (Moore et al. 2018, in press), this is the oxygen fugacity set for all models of both the high and low MgO trends.

Initial H_2O content of both the parent and recharge magmas is constrained to 0.5 to 1.0 wt.%. For the parent magma, initial H_2O content below 0.5 wt.% yields orthopyroxene in the mineral assemblage at 8.5 wt.% MgO, second to olivine as a crystallizing phase. Initial H_2O content of the parent magma above 1 wt.% suppresses plagioclase as a crystallizing phase until ~4 wt.% MgO, whereas plagioclase is found in abundance in lavas from 7-8 wt.% MgO and below. For the recharge magma, initial H_2O content of less than 0.5 wt.% yields mineral compositions inconsistent with those from the lower B Steens Basalt (plagioclase is too albitic and clinopyroxene is too Mg-rich) and predicts whitlockite in the crystallizing assemblage beginning at 7.3 wt.% MgO. initial H_2O content higher than 1 wt.% in the recharge magma suppresses plagioclase crystallization until ~4 wt.% MgO. The best fit initial H_2O content results from modeling are consistent with calculations from the plagioclase hygrometer of Lange et al. (2009), which predicts 0.5 wt.% H_2O for the range of plagioclase compositions in the lower B Steens Basalt (Moore et al. 2018, in press). Thus, an initial H_2O content of 0.5 wt.% was used in the parent and recharge magma for all models of both the high and low MgO trends.

4.6.2 High MgO Trend RAFC Models

The punctuated sweep to increasingly magnesian character among the lavas defining the high-MgO trend in the lower B Steens Basalt section (Fig. 4.1) is best modeled by a series of increasingly voluminous recharge events with small amounts of intervening fractional crystallization. The subsequent (upsection) punctuated decline in MgO is modeled by more extensive fractional crystallization (Figs. 4.1 and 4.4) with lesser recharge. Total system, recharge and fractionation masses and normalized masses resulting from the best fit model (described in detail below) are summarized in Table 4.4. The model begins with 100 g of the parent magma composition at a liquidus of 1282°C, and cools by ΔT of 50 °C to fractionally crystallize ~3 g of olivine. Intervening cooling and crystallization are simulated to represent the time interval suggested by the stratigraphic distance between the parent and the next high-MgO sample in the trend at ~9.75 wt.% MgO (orange circle, Figs. 4.1 and 4.4), which is the target composition of

recharge event 1.At 1232 °C, recharge event 1 is triggered and adds 55 g of recharge magma to the resident magma after cooling. The recharge magma for each event is added at a T of 1300 °C, just above the liquidus for that composition. Recharge event 2 is triggered after a ΔT of 10 °C, to simulate the shorter stratigraphic interval that occurs between the target for recharge 1 and the target for recharge 2 (~10.5 wt.% MgO, green circle Figs. 4.1 and 4.4). Approximately 2.5 g of olivine is fractionally crystallized during the cooling interval before 105 g of recharge magma is added to the resident magma during recharge event 2. Recharge event 3 is triggered after a ΔT of only 5 °C to represent the very short stratigraphic interval between the recharge 2 target and the recharge 3 target (~11 wt.% MgO, light blue circle, Figs. 4.1 and 4.4). Cooling of this small temperature increment results in fractional crystallization of ~3 g of additional olivine, and then 170 g of recharge magma is added during recharge event 3. There is a decrease in MgO of the next high MgO trend sample to ~10.6 wt.% (light blue open circle, Figs. 4.1 and 4.4), and thus cooling of ΔT = 15 °C is simulated before recharge event 4 is triggered; an additional 7 g of olivine is fractionated over this cooling interval. 3100 g of recharge magma is then added during recharge event 4 to capture the recharge 4 target (~12 wt.% MgO, black circle, Figs. 4.1 and 4.4). Following this last recharge event, the system is allowed to cool and fractionate to low MgO to capture the lower MgO target compositions in the upper stratigraphic portion of the high MgO trend (open black circles, Figs. 4.1 and 4.4). At the final/stratigraphically highest target composition (~8 wt.% MgO, open black circle, Figs. 4.1 and 4.4) an additional 402 g of olivine is crystallized. The ending total system mass is 3530 g (Table 4.4).

The target compositions for each recharge event are generally well matched to the model results for most major and trace elements (Fig. 4.4). Some exceptions include: 1) slightly higher SiO_2 in all recharge targets; 2) lower FeO, Sr, Ba, and higher K_2O in recharge target 1; and 3) higher K_2O in recharge target 4, each compared to their modeled counterparts. Silica content variations are likely due to differences between the model parent and recharge compositions and the true parent and recharge compositions. To simplify the model a constant recharge composition is assumed, but this composition may vary in time, which may also account for some of the variation between model results and

target samples. Because the recharge composition chosen is only slightly more magnesian than the most primitive lower B Steens Basalt sample target, recharge mass necessarily increases for the increasingly magnesian MgO target samples. Models that include assimilation (RAFC) do not produce addition of anatectic wallrock melts until the crust is sufficiently heated, which occurs after recharge event 4, and thus assimilation of this composition at the modeled parameters is not feasible to explain the deviations from RFC model results and the recharge targets (Figure 4.5).

Larger discrepancies exist between FC model results and FC targets, particularly for the FC targets after recharge event 4 (open black circles, Fig. 4.4). These samples have higher Al_2O_3, Na_2O, K_2O, NiO and Sr but lower CaO, Cr_2O_3, Ce, Sc and $^{87}Sr/^{86}Sr$ than the modeled fractional crystallization trend predicts (black squares, Fig. 4.4). FeO, P_2O_5, Rb, and Ba are variably enriched or depleted relative to the FC trend among the target samples. The modeled FC trend reaches Al_2O_3 content comparable to these target samples, but at much lower MgO; the modeled FC trend reaches appropriate Al_2O_3 at 6-7 wt.% MgO, whereas the samples are 8-8.7 wt.% MgO). Plagioclase does not crystallize until ~6.5 wt.% in the FC model, but all three of the post recharge 4 FC target samples contain plagioclase at much higher MgO content. AFC models including addition of a reasonable wallrock anatectic melt yield compositions that are too Si and Cr rich and too Al and Na poor to be consistent with the FC targets (Fig. 4.5). FC from the parent magma rather than from the recharge 4 target better captures some of the elemental trends in some of the FC targets; FeO, CaO, Na_2O, NiO, Rb, and Ba are more consistent with compositions of some, though not all target samples in this case (red squares, Figure 4.6). Several other models were attempted that did not successfully reproduce the trends evident in the FC targets, including cumulate entrainment of plagioclase and plagioclase + olivine to the FC modeled liquids (small black squares, Fig. 4.4), high pressure (8-10 kbar) fractional crystallization of substantial clinopyroxene from a parental high MgO magma (the recharge magma composition used in RFC models) with subsequent fractional crystallization of residual liquids at low pressure (1-3 kbar), and high pressure (8-10 kbar) fractional crystallization of substantial clinopyroxene from a parental high

MgO magma with subsequent cumulate entrainment to residual liquids at low pressure (1-3 kbar).

Two additional models were attempted to reproduce the compositions of the post recharge event 4 FC targets: entrainment of cumulate plagioclase + olivine + clinopyroxene into a more mafic parental composition and mixing of this more mafic parental composition with a FeTi rich melt + plagioclase. In these models, the resident/parent magma composition used is the recharge magma composition estimated for RFC models (Table 4.1).

Entrainment of a near solidus cumulate composed of 60% plagioclase, 15% olivine and 25% clinopyroxene into a resident magma that consists of the recharge composition (Table 4.1) generates a mixed magma that is higher in Al_2O_3 and Sr than the FC trend and thus reaches compositions similar to the FC targets for those elements (Fig. 4.6). This model can also account for lower FeO, P_2O_5, Rb, Ba, Ce, and Sc in the FC target samples. However, the cumulate entrainment model yields CaO even higher than the FC trend, which cannot explain the CaO compositions of the FC target samples (Fig. 4.6). MCS predicts that all of the plagioclase and ~85% of the clinopyroxene in the cumulate is resorbed when the cumulate is entrained into the resident magma. Given the high CaO content of both plagioclase and clinopyroxene (14.0 and 17.9%, respectively; Table 4.1), resorption of these phases causes the new magma to be high in CaO, too high to account for the relatively low CaO in the FC targets.

A trend of some lower B Steens samples towards high Al_2O_3 with decreasing MgO and Rb cannot be the result of fractional crystallization alone, and require the addition of a component that drives more primitive lower B Steens Basalt compositions to these values (Fig. 4.7). The component cannot be plagioclase alone, as the plagioclase in the Steens Basalt contains an average of 30 wt.% Al_2O_3 and 0 wt.% MgO, but the best fit trend of the samples on the high Al_2O_3 trajectory reaches only 24 wt.% Al_2O_3 at 0 wt.% MgO (Fig. 4.7). Additionally, the best fit trend of these data reaches 5 ppm Rb at 0 wt.% MgO, though plagioclase contains 0 ppm Rb (Fig. 4.7). Lastly, at 0 wt.% MgO the trend has both TiO_2 and FeO that are much too high (1.8 and 8.5 wt.%, respectively, not shown) to suggest that plagioclase alone is the added component, and instead indicates

that a high FeO and TiO_2 melt combined with cumulate plagioclase mixes with primitive lower B Steens Basalt melts to produce the observed trend.

Evolved melts rich in FeO and TiO_2 (FeTi melts) are produced from significant fractionation of olivine ± clinopyroxene ± plagioclase from primitive lower B Steens Basalt compositions, and thus are an abundant product of the magmatic system over time. Lavas of this type are abundant in the upper Steens Basalt stage (Moore et al. 2018, in press). To estimate the composition of a high FeTi melt + plagioclase rich mixing endmember, first a FeTi melt was estimated based on an average of Fe- and Ti-rich compositions from the upper Steens Basalt (Table 4.5). Next, a mixing line was created between average Steens Basalt plagioclase compositions and the estimated FeTi melt for SiO_2, TiO_2, Al_2O_3, FeO, CaO, Na_2O, K_2O, Rb (ppm), and Sr (ppm) versus MgO (dashed lines, Fig. 4.7, all elements not shown). Where these mixing lines cross the high Al_2O_3 trend in the lower B Steens Basalt (open circles, Fig. 4.7) is assumed to be the composition of the FeTi melt-plagioclase mixing endmember ("target FeTi melt-plagioclase mix", Table 4.5). Next, a simple two-component mix of average Steens Basalt plagioclase and the estimated FeTi melt was calculated at various proportions. The composition achieved at a mix of 60% FeTi melt plus 40% average Steens Basalt plagioclase was the best match to the target FeTi melt-plagioclase mix (gray highlighted compositions, Table 4.5). Thus, the endmember component that mixes with primitive lower B Steens Basalt magmas to produce the high Al_2O_3 trend is similar to a 60/40 mix of FeTi melt and Steens Basalt plagioclase, respectively.

Model simulations starting with a parent magma of the recharge composition mixing with a component that is 60% FeTi rich melt and 40% plagioclase can account for some of the FC target compositions (Fig. 4.6). This model is consistent with higher Al_2O_3, FeO, Na_2O, K_2O, NiO, Sr, and Ba but lower CaO, Cr_2O_3, Rb and Sc of the FC targets. All of the plagioclase from the FeTi rich melt + plagioclase component is resorbed after the mixing event, but the lack of cumulate clinopyroxene in this component and the abundance of FeTi melt (8 wt.% CaO; Table 4.1) drives CaO down in the resulting magma.

The best-fit RFC model yields a normalized recharge mass of ~9.1 and a normalized fractional crystallization mass of ~0.2 (Table 4.4). This calculation includes the assumptions that the FC targets represent some degree of fractional crystallization and that the potential cumulates entrained are not part of the crystallized masses from the model events. The mass results demonstrate that the increasing MgO phase of the high MgO trend is strongly recharge dominated, whereas the decrease in MgO upsection in the high MgO trend is FC dominated and is derived from the high-MgO trend. The amount of crystallization required to maintain the ΔMgO ~5 wt.% is 10-15%. Overall, the high MgO trend models show that crystallization must be far subordinate to recharge to account for the increasing MgO upsection.

4.6.3 Low MgO Trend RAFC Models

Best-fit models for the low MgO trend of the lower B Steens Basalt include a combination of fractional crystallization from the high MgO trend parent coupled with cumulate entrainment of plagioclase + olivine. Fractional crystallization of the parent magma at 1 kbar (Fig. 4.8) is a good fit for the two transitional high MgO samples just upsection from the parent on the low MgO path (blue filled circles, Figs. 4.1 and 4.8) and most of the sparsely phyric low MgO targets (open purple circles, Figs. 4.1 and 4.8). Elemental concentrations of some GPB can also be explained by fractional crystallization at 1 kbar from the parent magma (i.e. SiO_2, CaO, Na_2O, Cr_2O_3), with notable exceptions in Al_2O_3, FeO, TiO_2, NiO, Rb, Sc, Sr and Ba (Fig. 4.8). As previously noted (see Best-Fit Intensive Parameters), some elemental concentrations in both the sparsely phyric and GPB targets are consistent with an FC path at 3 kbar, but there is no consistency to which elements are a good fit to the models among these two distinct textures (Fig. 4.3). Additionally, 3 kbar FC models have a crystallization sequence of olivine + clinopyroxene + plagioclase, whereas in the 1 kbar FC model plagioclase begins crystallizing before clinopyroxene. Clinopyroxene in both the sparsely phyric and GPB target samples is an anhedral oikocryst phase that encloses plagioclase, or a groundmass phase only. These textural characteristics require plagioclase crystallization before clinopyroxene.

Given that continued fractional crystallization beyond the sparsely phyric sample compositions does not fit the GPB target compositions, assimilation of anatectic wallrock melts was modeled in an attempt to match the GPB targets through combined AFC processes. Assimilation of anatectic wallrock melts can account for lower FeO and TiO_2 in the GPB, but not the higher Al_2O_3, Na_2O, NiO and lower K_2O of the GPB relative to the 1 kbar FC trend (Fig. 4.8). Assimilation cannot account for the bulk of the elemental concentrations in the sparsely phyric samples, particularly in FeO and TiO_2, although the AFC trend is similar to the FC trend for Al_2O_3 and CaO (Fig. 4.8).

Other simulations invoking cumulate entrainment into a resident magma of the sparsely phyric target compositions are more consistent with the GPB target compositions. Entrainment of a cumulate consisting of plagioclase only cannot account for the GPB compositions, because at appropriate MgO (~6 wt.%), Al_2O_3 and NiO are too low and FeO and TiO_2 are too high (Fig. 4.9). Addition of 40 g of plagioclase + olivine in troctolite proportions (89 to 11%, respectively; Table 4.1) into 100g of resident magma consisting of sparsely phyric target sample compositions can explain the higher Al_2O_3, CaO, NiO, and Sr but lower FeO, K_2O, TiO_2, Cr, Rb, Sc, Ba and Ce of the GPB relative to the 1 kbar FC trend (Fig. 4.9). We tested models of entrainment of the plagioclase + olivine cumulates into two sparsely phyric parent magma compositions, those with the lowest and MgO, respectively (6.3 and 6.8 wt.% MgO, respectively; Fig. 4.9). The composition plotted is the combined melt + cumulates in order to show the composition of a resulting phyric lava.

In an attempt to model continuously upsection in the low MgO trend from one sample to the next in the stratigraphic sequence (as was attempted for the high MgO trend), recharge from the first GPB sample to the sparsely phyric sample stratigraphically above was attempted (Figs. 4.1 and 4.8). The resulting compositions are too high in Al_2O_3 and NiO and too poor in FeO and TiO_2 at appropriate MgO content. Given the inability to produce compositions similar to the sparsely phyric samples from a resident magma similar to the GPB, no further attempt was made to continuously model upsection through the remainder of the low MgO trend.

4.7 DISCUSSION

Collaborative studies aimed at modeling the Steens Basalt chemostratigraphic excursions have been focused on the flood basalt as a whole, from lower through upper Steens Basalt. Bendaña (2016) modeled excursions in Sr concentrations and $^{87}Sr/^{86}Sr$ from lower B through upper Steens Basalt using EC-RAFC, with the goal of quantifying changes in recharge, fractional crystallization and crustal assimilation upsection. The results of this modeling suggest sub-equal contributions (by mass) of recharge and crustal assimilation in both the lower B and upper Steens Basalt stages. Crustal assimilation is not invoked in more qualitative interpretations of the general geochemical characteristics of the lower B Steens Basalt (Gunn and Watkins, 1970; Camp et al. 2013; Wolff and Ramos, 2013; Moore et al. 2018, in press; Chapter 3). Later work by Bendaña et al. (2017) using MCS to model the same excursions in Sr concentrations and $^{87}Sr/^{86}Sr$ negates early models, and suggests that recharge is dominant and requires only a minor role for crustal assimilation in the lower B Steens Basalt, and shows the upper Steens Basalt is dominated by assimilation coupled with a significant decrease in recharge. Additionally, an important outcome of this work is that the volumes of recharge required to reconstruct the MgO excursions on a flow by flow basis are enormous, which is the basis for modeling the more evolved and more primitive MgO trends separately in this study. Graubard (2016) was the first to use the MCS approach to model changes in major element and mineral compositions from lower B through upper Steens Basalt. This modeling was focused on select packages within each the latter two Steens Basalt stages. Modeled masses for the select packages and estimated masses for unmodeled flow by flow excursions suggest that the lower B Steens Basalt is dominated by recharge coupled with equilibrium and fractional crystallization, whereas the upper Steens Basalt is dominated by crystallization and crustal assimilation. Recharge mass estimates for the lower B Steens Basalt in these initial MCS models are double those of the upper Steens Basalt; conversely, estimated masses of crystallization and assimilation are more than double for the upper Steens Basalt stage. Computational modeling to date consistently suggests that the mantle input was greatest during the lower B Steens Basalt phase, and

this waxing stage of magmatic input sufficiently heated the crust so that a larger contribution by crustal assimilation occurs during the waning, upper Steens Basalt stage.

4.7.1 Interpretation of High MgO Trend RAFC Processes

The best-fit RFC model for the high MgO trend is a good compositional match to the recharge targets in the initial part of the lower B Steens section where MgO increases with stratigraphic height (Figs. 4.1 and 4.4). The FC target samples on the high MgO trend that decrease in MgO with stratigraphic height (Fig. 4.1) are not entirely consistent with fractionation after the final recharge event in the best-fit RFC model (Fig. 4.4); in other words, fractional crystallization of the magma after recharge 4 at 3 kbar cannot alone account for the composition of these three target samples. Fractionation from the original parent composition at 3 kbar is consistent with some elemental concentrations in the FC targets (CaO, K_2O; Fig. 4.6), but does not produce compositions consistent with all elements in each FC target. Though the FC target samples range from 8-8.7 wt.% MgO and all contain plagioclase, the FC modeled magmas do not produce plagioclase until differentiated to ~6.5 wt.% MgO. Cognate plagioclase cumulate entrainment is one explanation, and is suggested by high Al_2O_3, Na_2O, and Sr. However, CaO is depleted rather than enriched in the samples relative to the fractionation trend, and in the case of plagioclase entrainment, CaO should be higher in the resulting mixed magma. Plagioclase + olivine cumulate entrainment cannot account for the compositions, because Ni concentrations in the target samples match the FC trend, but addition of olivine would result in increasing the Ni content over the FC trend.

The here preferred explanation for the compositions observed in the FC target samples is mixing with a FeTi rich melt + plagioclase cumulates. This model is particularly useful to explain the FC target sample compositions with the most elevated FeO, Na_2O, K_2O and most depleted CaO, TiO_2 Rb, and Sc (Fig. 4.6).

The cumulate entrainment model can explain the range and the variation among some of the FC target samples. Entrainment of olivine + clinopyroxene + plagioclase in olivine gabbro proportions is potentially reasonable, as this assemblage is consistent with crystallization at 3 kbar. However, clinopyroxene crystallizes before plagioclase in the

FC models at 3 kbar, but clinopyroxene is not a phenocryst phase in any of the target compositions. This requires that clinopyroxene fractionation be very efficient, completely removing the phase, or that clinopyroxene is not stable at shallower pressures and is completely resorbed during ascent or later shallower crustal staging. In the cumulate entrainment models at 3 kbar, entrained clinopyroxene is largely resorbed, and at shallower levels (1 kbar) all of the entrained clinopyroxene is resorbed. Clinopyroxene is unstable when entrained into the most primitive compositions at mid to upper crustal levels, which explains the lack of clinopyroxene as a phenocryst phase in the eruptive products. Ascent through the crust after entrainment, or short term shallower magma staging allows the clinopyroxene to be completely resorbed, so that it only appears as a late stage anhedral groundmass phase.

Invoking shallower crystal fractionation cannot explain the FC target compositions, as a 1 kbar fractionation model from a starting composition of the recharge 4 magma is nearly identical to fractionation of that composition at 3 kbar; exceptions are that the 1 kbar model is even more depleted in Al_2O_3 and more enriched in CaO at a given MgO than the 3 kbar model, contrary to the trends of the target samples. It is possible to explain the compositions by addition of a different plagioclase composition than the average plagioclase used in the models, but this seems unlikely. The lowest CaO of analyzed plagioclase in the lower B Steens Basalt is 10.5 wt.%, which is the same as the CaO composition of the two of the FC targets. Given the target compositions have CaO lower than the FC trend, mixing of magmas from the FC model trend with plagioclase that has CaO *lower* than the target samples is the only way to achieve the CaO concentrations in the FC targets. Assimilation of anatectic wallrock melts increases SiO_2 and Cr_2O_3 but decreases Al_2O_3 and Na_2O relative to the FC target samples and the FC model trend, so is also not a reasonable explanation for the sample compositions (Fig. 4.5).

A combination of RFC and cumulate entrainment with magma mixing is consistent with compositions of the high MgO trend and suggests that a distinct mid to upper crustal reservoir or reservoirs of primitive magma experience periodic influx of increasing volumes of primitive magma in time with short intervals of cooling and minor

fractionation between recharge events during the early part of the lower B Steens Basalt stage. Later in time, the decreasing MgO character suggests that the magmas experience more fractionation (Figs. 4.1, 4.5, 4.6). The decreasingly mafic compositions upsection in the high MgO trend may be generated by some combination of fractionation, cumulate entrainment of an olivine gabbro, and/or mixing of a FeTi rich melt + cumulate plagioclase with variable high MgO primitive compositions.

Despite high recharge volumes and accompanying high heat influx indicated by the RFC models for the high MgO trend, assimilation of anatectic melts of wallrock are not supported by AFC models (Fig. 4.5). Likely, the volumes of recharge are so high that a comparatively small amount of contamination by anatectic wallrock melt is not recognizable, as it is swamped by the primitive magma input. Alternatively, the cumulates produced during cooling and fractionation between recharge events may armor the magma reservoirs and effectively insulate the magma as well as prevent infiltration by the small volumes of crustal melt. Boundary layer crystallization along the walls and roof of magma chambers has long been thought to be an important intrusive process (McBirney et al. 1985; Marsh, 1988; Nielsen and DeLong, 1992). Abundant crystal accumulation along the margins of the magma chamber would provide a physical and thermal boundary between the magma and the country wallrock. Later heat influx from magma recharge may cause entrainment or partial melting of the cumulate residue on the walls, which would produce compositions similar to those of the FC targets in the decreasingly mafic part of the section (Figs. 4.1 and 4.6). A refractory wallrock, one of mafic composition with little or no hydrous phases, would also lead to very minor amounts of crustal contamination. Computational modeling (Graubard, 2016) suggests that assimilation and cumulate entrainment are both important processes during the upper Steens Basalt phase. As magma reservoirs become increasingly crystal rich with continued fractionation and waning recharge, shoaling of the system may occur in time as new injections penetrate the solidifying mass. Shoaling would allow more contact between the magma reservoir and unarmored crust and ultimately facilitate more thermal exchange and assimilation, as suggested for the upper Steens Basalt stage. Shoaling may also facilitate stoping of chamber roof blocks.

4.7.2 Interpretation of Low MgO Trend RAFC Processes

Because the low MgO trend is systematically more evolved than the high-MgO trend, and because it mimics the sweep to increasing and then decreasing MgO, we posit that the low MgO trend magmas were derived from parents on the high MgO line of descent. Low pressure (1 kbar) fractional crystallization from a high MgO trend parent magma reasonably explains the compositions of sparsely phyric low MgO samples, but cannot account for GPB flow compositions. Cumulate entrainment of a troctolite into resident magmas with the compositions of the sparsely phyric low MgO target samples produces compositions similar to the GPB targets. Continuing upsection from the first GPB sample in the low MgO trend, an increase in MgO to the next sparsely phyric flow occurs (Fig. 4.1); however, recharge of a more mafic magma into the GPB compositions does not produce compositions similar to the sparsely phyric flows (Fig. 4.8). The modeled section of the low MgO trend is representative of the remainder of the low MgO trend, in that continuing upsection, the lowest MgO flows tend to be GPB and their slightly higher MgO counterparts are sparsely phyric (Fig 4.1). This suggests that a portion of the primitive magmas from the high MgO trend ascend to shallower depths (from 3 to 1 kbar) and stall, fractionating to produce the sparsely phyric low MgO flows. Some of these fractionated liquids then entrain troctolite cumulates to form the GPB. Plagioclase and olivine are reasonable as the sole phases in a cumulate residue for this depth/pressure, given the crystallization sequence in the models is olivine + plagioclase + clinopyroxene; the final phase does not crystallize until liquids reach ~6.5 wt.% MgO. Perhaps entrainment occurs during ascent prior to eruption, preventing fractionation of the entrained cumulates. In other words, a magma of sparsely phyric composition previously staged at 1 kbar entrains the cumulates just before or during ascent, carrying the entrained solids to the surface. The GPB overall contain abundant olivine phenocryst clusters and glomerocrystic plagioclase, reminiscent of cumulate textures. There is a general lack of disequilibrium textures, equilibrium between whole-rock and mineral major and trace element (Moore et al. 201, in press) and Sr isotopic compositions (Toth, 2018) in the phenocryst phases of the GPB. Additionally, both plagioclase and olivine are relatively homogeneous from core to near the rim, with rim compositions that decrease in

An or Fo relative to the rest of the crystal. This variable rim composition could result from brief entrainment into magma prior to eruption, giving the grain only a short period during which to grow a rim of slightly different composition. This is consistent with the model of Toth (2018), who suggests that the lower B Steens GPB flows are the result of abundant cumulate entrainment in which most of the cumulate clinopyroxene and plagioclase are resorbed upon entrainment, subsequently causing a bloom of new plagioclase after saturating the melt in plagioclase components. If the GPB and sparsely phyric magmas evolve in this way, they are likely produced in distinct reservoirs residing above the primitive reservoir producing the high MgO trend lavas, as the pressure of differentiation is systematically lower (1 versus 3 kbar; Fig.4.10).

4.7.3. Summary of RAFC Processes for the Lower B Steens Basalt

Figure 4.10 presents a schematic summary of the processes and crustal structure suggested by the MCS models that are consistent with the compositional trends of the lower B Steens Basalt. Models for the high MgO trend in the lower B Steens Basalt suggest that the increasing MgO in the base of the section is the result of increasingly voluminous recharge through time with subordinate fractionation between recharge events at mid to upper crustal levels (3 kbar). Fractionation at this depth produces olivine gabbro cumulates. The decreasing MgO character stratigraphically upsection in the high MgO trend is a consequence of fractionation, cumulate entrainment and magma mixing into variable primitive magma compositions. Fractionation of primitive magmas at shallower crustal levels (1 kbar) and cumulate entrainment into the fractionated liquids produce low MgO trend compositions. Fractionation at this depth yields troctolite cumulates. The low MgO trend increases in MgO upsection initially along with high MgO trend at a relatively consistent ΔMgO (~4-5 wt.%; Fig. 4.1); this is likely because the low MgO reservoirs are fed by the more deeply staged primitive magmas, albeit at shallower levels and less frequently recharged, allowing for more cooling and crystallization. Assimilation is unlikely to contribute to generation of flows in the lower B Steens Basalt based on model results.

4.7.4. Recharge, Fractional Crystallization, and Intrusive Mass Calculations for Lower B Steens Basalt

A desired outcome of MCS modeling for the Lower B Steens Basalt stage is a quantification of mass estimates for recharge and fractional crystallization. Because the relative masses contributed by those processes have been constrained by modeling of the section, I describe a preliminary attempt at calculating a mass balance, or total magma supply for the entire lower B Steens Basalt section (reported in Table 4.6; see Supplement 8 for spreadsheet of calculations). The calculation attempts to quantify cumulate, recharge and intrusive masses informed by the best-fit MSC models of the high and low MgO trends.

The mass balance calculations begin at flow 2 (Fig. 4.11) at the base of the lower B Steens Basalt section and continue through the informal boundary between lower B and upper Steens Basalt (at ~750 m; Figs. 4.1 and 4.11). It is assumed that the 66 analyzed flows represent the full suite of lower B Steens Basalt (i.e. that all flows are sampled). Assuming that each of the 66 flow erupts an equal volume and using 18,600 km^3 as the volume estimated for lower B Steens Basalt (Moore et al. 2018, in press), the eruptive volume of each of the 66 flows is estimated at ~280 km^3. Flows are grouped into packages for which calculations can be conducted in a step by step manner, where MgO compositions could be averaged into 1 to 3 groups for simplification (Fig. 4.11, Table 4.6). Where a transition from high MgO to low MgO occurs, the amount of crystallization necessary to reach the appropriate ΔMgO was estimated in MELTS. Low MgO flows are assumed to represent eruption of the entire magma reservoir, so that only cumulates remain intrusively from those flows. Thus, these volume estimates are minima, as it is likely there are small amounts of trapped residual melt within the cumulate residue. The first 18 flows, which occur stratigraphically before recharge events begin in the high MgO trend model, were used to scale an "intrusive" melt volume that remains in the crust after eruptions. This scaling is based on the number of high MgO flows in that section, with the rationale that a larger volume of liquid resides in the more primitive magma reservoir where recharge occurs. A 6:1 intrusive to extrusive ratio (I:E) is assumed, as proposed by Moore et al. (2018, in press) for CFB. As an example of this

scaling process for flow numbers 4 to 15 (Table 4.6), 7 of the flow are considered to be low MgO eruptions that were produced by an average of 15% crystallization, and 5 are considered to be high MgO flows erupted without significant fractionation that represents a 6:1 intrusive to extrusive volume. For this step, the total high MgO volume erupted is 564 km^3 (5 flows x 282 km^3), which requires 1692 km^3 of melt to remain "intrusively" in the crust. This scaling is an attempt to begin with a reasonable volume of magma, given there is no way to infer a starting volume.

Calculations for the flow packages through the remainder of the section are not scaled to an I:E of 6:1. The remaining intrusive liquid calculated after eruption of the first 18 flows is used as the starting volume for the next package (package 4; Fig. 4.11), and the mass of the first recharge event is calculated as a proportion of that starting volume of intrusive liquid. For example, R1 in the high MgO trend model is 55 g, so must add 55% to the existing volume. The beginning magma chamber volume for package 4 is 10,152 km^3 (Table 4.6; carried over from initial scaling steps), so the recharge magma volume for that step is 5584 km^3, yielding a new total magma reservoir volume of 15,736 km^3. The eruptive volumes for the total number of flows in that package is subtracted from the new total magma chamber volume; in the continued example, the eruptive volume of the 7 flows in package 4 is 7 x 282 km^3, or 1974 km^3). The cumulates produced by crystallization of the low MgO flows are calculated and also subtracted from the total magma chamber volume (in the example, 15,736 km^3 - 1974 km^3 - 157 km^3 = 13,605 km^3). The remaining liquid after all eruptions and cumulate removal is then carried over as the beginning primitive magma reservoir volume for the next package/step. The calculation continues in this manner until the last flow in the section is reached. Recharge events cease after flow 45, as predicted by the high MgO trend best-fit model results.

The total volume of cumulates produced in this calculation is 2023 km^3. Though this is small compared to the total eruptive volume (18,600 km^3), it is not unexpected given the lower B Steens Basalt stage is dominated by recharge rather than fractionation. It is also inherent in the assumptions, given the cumulate residue is only calculated by fractionation from the eruptive volumes of low MgO flows. It is probable that not all remaining liquid after fractionation erupts in the low MgO events but proceeding with the

calculation in this manner forces the primitive magma reservoir to be most voluminous and partitioning some remaining liquid to a low MgO reservoir presents an additional unknown factor. A larger primitive magma reservoir is reasonable given the increasing amounts of recharge required by the model, up to 7 times the existing magma chamber volume (i.e. recharge event 4, Tables 4.4 and 4.6).

The total calculated intrusive volume after all eruptions of the lower B Steens Basalt is 251,522 km^3, which includes total cumulates plus remaining liquid after the final eruption. This yields an I:E of ~14:1, much higher than predicted. Much of this remaining liquid likely contributes to later upper Steens Basalt eruptions, and indeed given that recharge has been modeled to be subordinate to fractionation during the upper Steens Basalt stage (Graubard, 2016), this could be close to the total intrusive volume for the entire Steens Basalt. There is likely continued minor recharge during upper the Steens Basalt stage to keep the system thermally viable, but eventually this recharge ceases, a large mush zone continues to fractionate, and final eruptions of the remaining liquid herald the end of volcanism. Using the total eruptive volume of 31,800 km^3 for the Steens Basalt to calculate an I:E yields ~8:1, a ratio close to the predicted value. Assuming that the entire intrusive volume cools and crystallizes over time, the full volume is added to the crust. Using the calculated intrusive volume and the full outcrop area of the Steens Basalt is 53,000 km^2, this suggests ~5 km is added to the crust during the lower B Steens Basalt stage, or potentially over the life of the flood basalt event. On the other hand, it is unlikely that the crustal magma reservoir system exists under the entire outcrop area, as the Steens Basalt flows spread tens to just over 100 km away from the dike swarm that fed them. ~9000 km^2 is the area of Steens Mountain where the dike swarm is mapped; using this area instead of the full Steens outcrop area suggests as much as 28 km of crust is added during the lower B Steens Basalt stage, or potentially over the full duration of Steens Basalt eruptions. Though abundant gabbroic underplating has been suggested in the region (Carlson and Hart, 1987), the maximum estimate seems high. Given the total thickness of the crust in this area is ~32 km, the maximum estimated intrusive volume would require foundering and delamination of substantial amounts of crust/cumulates into the mantle.

This is a preliminary foray into a potential mass balance calculation for the lower B Steens Basalt and Steens Basalt as a whole. Future revisions and honing of the mass balance will include allowance for variable amounts of recharge and fractionation in order to get a sense of the full range of variability that may exist, given that some parameters are not well constrained.

4.7.5 Magma Supply Rates

Studies estimating magma supply rates for volcanic systems are few. Magma supply rates represent the total mass of magma input to the system over the life of the magmatic system, or the combined erupted and intrusive magma volumes over a given time interval. Because intrusive or stored volumes cannot be directly observed, magma supply rates can only be estimated indirectly (Poland et al. 2014). Evidence for magma storage in the crust comes from a variety of data, including geochemical/petrologic characteristics, seismology, and surface deformation. The latter two are applicable to active systems, and as such for the Steens Basalt, the only evidence for crustal storage is the somewhat differentiated character of many of the flows. The range to more evolved basaltic compositions demonstrates that some magma storage at depth occurred to alter the compositional characteristics from the original mantle parentage.

In active systems, some studies have calculated magma supply rates by measuring heat flow or heat loss at the surface and estimating the mafic flux necessary to sustain that heat flow over a given time interval (Bacon, 1982; Francis et al. 1993). The few other studies that calculate magma supply rates do so over a long period of observed volcanic activity (long on human times scales, not geologic time scales) in active systems with a combination of evidence that includes eruption rate, gas emissions, and deformation data (e.g. Lowenstern and Hurwitz, 2008; Allard et al. 2006; Anderson and Poland, 2016), though none exist for CFB. Therefore, there are limited magma supply rate estimates by which an applicable comparison can be made to the Steens Basalt. On the other hand, eruption rates provide a minimum magma supply rate, and are available for all systems with eruptive volume estimates and age constraints. Most volcanic systems historically observed (i.e. Hawaiian volcanism, Icelandic volcanism, Cascade

stratovolcanoes) are episodic, but over long periods of time provide average eruption rates. Steens Basalt likely also erupted episodically, but average rate was greatest during the waxing stage (lower B Steens Basalt), where lack of soil development between flows suggests very minimal eruption intervals (Moore et al. 2018, in press).

Eruption rates for the Steens Basalt vary from ~0.1 to 0.6 km^3/yr based on the total estimated volume of 31,800 km^3 (Camp et al. 2013) and an eruption duration from 50,000 to 300,000 years, respectively (Mankinen et al. 1985; Jarboe et al. 2008; Camp et al. 2013). Recent estimates of total volume and duration of the main phase eruptions of the CRBG (Steens, Imnaha, Grande Ronde and Picture Gorge Basalts) are 194,200 km^3 (Reidel et al. 2013) and ~1 Myr (Baksi, 2013), respectively, suggesting an overall eruption rate of ~0.2 km^3/yr for bulk of the CRBG. Estimates of eruption rates at other CFB, including the Deccan Traps, Karoo Province, and the Parana-Etendeka range from 0.75-1.5 km^3/yr (Richards et al. 1989); the minimum estimate for these other CFB is of the same order of magnitude as the maximum estimate for the Steens Basalt, though these other CFB are all significantly more voluminous (see Moore et al. 2018, in press). The magma supply rates for the Steens Basalt, based on mass balance calculations and the 50,000 to 300,000-year estimated eruption duration, is 0.9 to 5.6 km^3/yr.

One fairly well constrained example of a volcano with estimated eruption rates and magma supply rates that may be comparable to the Steens Basalt is for Kilauea. Calculated eruption rates at Kilauea range from 0.02 to 0.19 km^3/yr, with an average of 0.1 km^3/yr (as compiled in Poland et al. 2014), comparable to the minimum Steens Basalt eruption rate estimate. Magma supply rate estimates range from 0.08 to 0.28 km^3/yr for the 2000-2012 eruptive interval. The estimates for the Steens Basalt are significantly higher than for Kilauea. Kilauea is fed by a hotspot that has persisted for ~85 Ma (Regelous et al. 2003), and may represent a more steady-state plume heat flux, as opposed to the Steens Basalt, which may represent the initiation or resurgence of the Yellowstone plume and waxing heat flux to the mantle. Models suggest that large igneous provinces are formed during initial impingement of very large diameter plume heads, whereas hotspot tracks such as the Hawaii/Emperor Seamount chain and Tristan de Cunha result from melting by much smaller diameter plume tails (White and

McKenzie, 1989; Campbell and Griffiths, 1990), which would imply initially higher magma supply rates during plume impingement.

4.7.6 Potential Crustal Inflation, Implications for Magma Reservoir Size, Shape and Number

Large volumes of magma recharge implied by the high MgO trend models need to be accommodated by the crust. Given these large recharge masses implied by MCS models, significant doming or uplift of the surface might be expected. Though deformation may accompany magma intrusion at depth, as is inferred to be the case for the inflation of South Sister that began in 1997 and culminated in 2004-2006 (Dzurisin et al. 2009), other studies suggest that magma compressibility may accommodate significant amounts of magma intrusion depending on host rock strength and volatile content. Johnson et al. (2000) demonstrate the 75-80% of the magma volume intruded during the 1983-1986 eruptive period of Kilauea was accommodated by magma compression, and only 20-25% of the volume was accommodated by increasing the magma reservoir size and subsequent surface inflation. Thus, if volatile content is significant and host rocks are strong (Johnson et al. 2000), large recharge volumes can be accommodated with relatively minor amounts of deformation.

Other questions remain about the crustal structure of the Steens Basalt magmatic system. Estimates of individual magma reservoir size for a variety of magmatic systems range from hundreds of km^3 for the Yellowstone Caldera (Christiansen, 2001) to 1 km^3 for Kilauea (Poland et al. 2009). Reservoir size is uncertain for the Steens Basalt magmatic system, but a minimum can be estimated from the volume of a single flow. Individual flows of the CRBG have volumes as great as ~14,000 km^3, with areal extents and thicknesses of ~84,000 km^2 and 160 m, respectively (Reidel and Tolan, 2013). The Steens Basalts have not been mapped in such detail. Individual flows, however, at Hart Mountain, 100 km to the west are as thick as 5 m and almost certainly have their source at Steens Mountain. If the distribution of individual flows covers the full areal extent of the Steens Basalt as a disc of a 100 km radius, then a maximum flow volume for a 5 m thick flow is ~50 km^3. If flows are considered as a wedge shape within the disc, then

minimum volume is several to tens of km^3. The magma reservoir size likely increases in time to accommodate the increasingly large recharge volumes suggested for the lower B Steens Basalt. Most models for reservoir shape are elliptical or spheroidal (e.g. Davis, 1986; Annen et al. 2006; Gudmundsson, 2012), though the elongated direction can vary from horizontal (Gudmundsson, 2012) to vertical (Scandone and Malone, 1985). Chamber shape is typically inferred from seismicity/earthquake foci, and thus remains an unknown for the Steens Basalt. The overall crustal structure suggested by the best fit models for the Steens Basalt implies that the reservoirs, which we envision as a crystal rich matrix hosting horizontal lenses of largely liquid magma, exist at multiple levels in the mid to upper crust and that multiple types of reservoirs allow for a variety of crustal processes to modify the primitive magmas (Fig. 4.10).

The separate but linked evolution of the high and low MgO trends in the lower B Steens Basalt suggests that multiple magma reservoirs are more likely than one very large chamber (Fig. 4.10). Reservoir size, shape, number, and crustal deformation are best constrained by seismology and geodesy at active volcanoes. Because these cannot be directly observed for CFB, continued work through geochemical analysis, petrologic modeling and perhaps seismic tomography is necessary to help resolve these open questions for the Steens Basalt and other CFB provinces.

4.8 CONCLUSIONS

This study documents the waxing of a shallow mafic magmatic system in the continental crust by integrating field, petrologic, and computational modeling data. Computational modeling using the Magma Chamber Simulator provides supportive evidence to previous interpretations of the balance RAFC processes responsible for imparting geochemical characteristics to the lower B Steens Basalt, which including waxing recharge early in the stage, coupled with subordinate recharge, then waning recharge coupled with increasing fractionation late. MCS modeling also suggests that additional processes beyond RAFC serve to modify the compositions of the magmas, including cumulate entrainment and magma mixing, and quantifies the relative mass

contributions of recharge and fractional crystallization to the generation of the high MgO trend.

Periodic recharge events with small intervals of cooling and crystal fractionation between events is consistent with the initially increasing magnesian character upsection in the high MgO trend. Masses of recharge events increase upsection until the most magnesian flows are erupted. Declining MgO in the remainder of the high MgO trend is consistent with a combination of fractionation, olivine gabbro cumulate entrainment, and magma + cumulate mixing with a variety of lower B Steens Basalt high MgO compositions at mid to upper crustal levels.

The compositions of the sparsely phyric flows in the low MgO trend are consistent with fractionation of a parent magma similar to that of the high MgO trend, with storage at shallower crustal levels (upper crust). GPB compositions can be closely approximated by entrainment of troctolite cumulates into fractionated melts similar in composition to the sparsely phyric flows. The shallower reservoirs in which the low MgO trend magmas stage must be pulsed by periodic recharge from the primitive reservoir, given the low MgO trend lavas also become increasingly magnesian in the recharge dominated portion of the section along with the high MgO trend flows, and ΔMgO between the high and low MgO trends remains relatively consistent, owing to a relatively consistent amount of fractionation from the high MgO primitive parent magmas (~10-15%).

Recharge masses from the RFC models far surpass crystallization masses. This emphasizes the importance of recharge during the lower B Steens Basalt stage and supports the idea that this is the waxing stage of magmatic input. A preliminary total mass balance calculation for the entire lower B Steens Basalt package suggests a range of 5-28 km of crustal cumulate addition. Given the thickness of crust in this region, the maximum estimate would require foundering and delamination of crustal roots into the upper mantle. Uncertainty in the possible range of variability of recharge and fractionation masses and the many assumptions made in this first attempt at a total mass balance calculation for the lower B Steens Basalt must be refined, but this calculation provides an initial basis for integrating masses upsection for the Steens Basalt and

ultimately other CFB. Magma supply rates for the lower B Steens Basalt suggested by the integrated mass balance calculations are 11 to 70 times those of Kilauea, which suggests an inherent difference in the volume of magma input for large igneous provinces and hotspot tracks. Magma reservoir size and shape likely varies in time throughout the Steens Basalt stages, with thick crystal rich mush overlain by thinner, sill like lenses of melt. These reservoirs are staged at multiple levels within the crust, to produce the compositional variety of flows.

4.9 ACKNOWLEDGMENTS

4.10 REFERENCES CITED

Allard, P., Behncke, B., D'Amico, S., Neri, M., and Gambino, S., 2006, Mount Etna 1993–2005; anatomy of an evolving eruptive cycle: Earth-Science Reviews, v. 78, p. 85-114.

Anderson, K.R., and Poland, M.P., 2016, Bayesian estimation of magma supply, storage, and eruption rates using a multiphysical volcano model: Kīlauea Volcano, 2000–2012: Earth and Planetary Science Letters, v. 447, p.161-171.

Annen, C., Blundy, J.D., and Sparks, R.S.J., 2005, The genesis of intermediate and silicic magmas in deep crustal hot zones. Journal of Petrology, v. 47, p. 505-539.

Bacon, C.R., 1982, Time-predictable bimodal volcanism in the Coso Range, California: Geology, v. 10, p. 65-69.

Baksi, A.K., 2013, Timing and duration of volcanism in the Columbia River Basalt Group: A review of existing radiometric data and new constraints on the age of the Steens through Wanapum Basalt extrusion: Geological Society of America Special Papers, v. 497, p. 67-85.

Bendaña, S.J., 2016, Documenting mantle and crustal contributions to flood basalt magmatism via computational modeling of the Steens Basalt, southeast Oregon [M.S. Thesis]: Central Washington University, 183 p.

Bendaña, S., Bohrson, W.A., Graubard, M.A., Moore, N.E., and Grunder, A.L., 2017, Quantification of Mantle vs. Crustal Contributions to the Steens Flood Basalt Magmatic System, IAVCEI Scientific Assembly, Abstract ME23C-070.

Bohrson, W.A. and Spera, F.J., 2001, Energy-constrained open-system magmatic processes II: application of energy-constrained assimilation-fractional crystallisation (EC-AFC) model to magmatic systems: Journal of Petrology, v. 42, p. 1019-1041.

Bohrson, W.A., and Spera, F.J., 2003, Energy-constrained open-system magmatic processes IV: Geochemical, thermal and mass consequences of energy-constrained recharge, assimilation and fractional crystallization (EC-RAFC): Geochemistry, Geophysics, Geosystems, v. 4, doi:10.1029/2002GC000316.

Bohrson, W.A., Spera, F.J., Ghiorso, M.S., Brown, G.A., Creamer, J.B., and Mayfield, A., 2014, Thermodynamic model for energy-constrained open-system evolution of crustal magma bodies undergoing simultaneous recharge, assimilation and crystallization: The magma chamber simulator: Journal of Petrology, v. 55, p. 1685-1717.

Camp, V.E., Ross, M.E, Duncan, R.A., Jarboe, N.A., Coe, R.S., Hanan, B.B., and
Johnson, J.A., 2013, The Steens Basalt: earliest lavas of the Columbia River
Basalt Group: Geological Society of America Special Papers, v. 497, p. 87-116.

Campbell, I.H., and Griffiths, R.W., 1990, Implications of mantle plume structure for the
evolution of flood basalts: Earth and Planetary Science Letters, v. 99, p. 79-93.

Carlson, R.W., and Hart, W.K., 1987, Crustal Genesis on the Oregon Plateau: Journal of
Geophysical Research-Solid Earth and Planets, v. 92, no. B7, p. 6191-6206.

Cheng, L.L., Yang, Z.F., Zeng, L., Wang, Y., and Luo, Z.H., 2014, Giant plagioclase
growth during storage of basaltic magma in Emeishan Large Igneous Province,
SW China: Contributions to Mineralogy and Petrology, v. 167, p. 1-20.

Christiansen, R.L., 2001, The Quaternary and Pliocene Yellowstone Plateau volcanic
field of Wyoming, Idaho, and Montana: U.S. Geological Survey Professional
Paper 729–G, 145 p.

Davis, P.M., 1986, Surface deformation due to inflation of an arbitrarily oriented triaxial
ellipsoidal cavity in an elastic half space, with reference to Kilauea volcano,
Hawaii: Journal of Geophysical Research, v. 91, p. 7429–7438.

DePaolo, D.J., 1981, Trace element and isotopic effects of combined wallrock
assimilation and fractional crystallization: Earth and Planetary Science Letters, v.
53, p. 189-202.

DePaolo, D. J., 1985, Isotopic studies of processes in mafic magma chambers: I. The
Kiglapait Intrusion, Labrador: Journal of Petrology, v. 26, p. 925-951.

Dzurisin, D., Lisowski, M., and Wicks, C.W., 2009, Continuing inflation at Three Sisters
volcanic center, central Oregon Cascade Range, USA, from GPS, leveling, and
InSAR observations: Bulletin of Volcanology, v. 71, p. 1091.

Francis, P., Oppenheimer, C., and Stevenson, D., 1993, Endogenous growth of
persistently active volcanoes: Nature, v. 366, p. 554-557.

Ghiorso, M.S., Hirschmann, M.M., Reiners, P.W., and Kress, V.C. III, 2002, The
pMELTS: a revision of MELTS for improved calculation of phase relations and
major element partitioning related to partial melting of the mantle to 3 GPa:
Geochemistry, Geophysics, Geosystems, v. 3, doi:10.1029/2001GC000217.

Ghiorso, M.S. and Sack, R.O., 1995, Chemical mass transfer in magmatic processes IV: A revised and internally consistent thermodynamic model for the interpolation and extrapolation of liquid-solid equilibria in magmatic systems at elevated temperatures and pressures: Contributions to Mineralogy and Petrology, v. 119, p. 197-212.

Graubard, M., 2016, Evolution of a Flood Basalt Crustal Magmatic System: In Situ Mineral Data and Computational Modeling of the Steens Basalt [M.S. Thesis]: Central Washington University, 190 p.

Gualda G.A.R., Ghiorso, M.S., Lemons, R.V., and Carley, T.L., 2012, Rhyolite-MELTS: a modified calibration of MELTS optimized for silica-rich, fluid-bearing magmatic systems: Journal of Petrology, v. 53, p. 875-890.

Gudmundsson, A., 2012, Magma chambers: Formation, local stresses, excess pressures, and compartments: Journal of Volcanology and Geothermal Research, v. 237, p. 19-41.

Gunn, B.M., and Watkins, N.D., 1970, Geochemistry of the Steens Mountain Basalts, Oregon: Geological Society of America Bulletin, v. 81, p. 1497-1516.

Higgins, M.D., and Chandrasekharam, D., 2007, Nature of sub-volcanic magma chambers, Deccan Province, India: evidence from quantitative textural analysis of plagioclase megacrysts in the Giant Plagioclase Basalts: Journal of Petrology, v. 48, p. 885-900.

Hooper, P.R., 1984, Physical and chemical constraints on the evolution of the Columbia River basalt: Geology, v. 12, p. 495-499.

Jarboe, N.A., Coe, R.S., Renne, P.R., Glen, J.M.G., and Mankinen, E.A., 2008, Quickly erupted volcanic sections of the Steens Basalt, Columbia River Basalt Group: Secular variation, tectonic rotation, and the Steens Mountain reversal: Geochemistry Geophysics Geosystems, v. 9, no. 11.

Johnson, J.A., Hawkesworth, C.J., Hooper, P.R., and Binger, G.B., 1998, Major and trace element analyses of Steens Basalt, southeastern Oregon: U.S. Geological Survey Open File Report 98-482, 26 p.

Johnson, D.J., Sigmundsson, F., and Delaney, P.T., 2000, Comment on "Volume of magma accumulation or withdrawal estimated from surface uplift or subsidence with application to the 1960 collapse of Kīlauea volcano" by P.T. Delaney and D.F. McTigue: Bulletin of Volcanology, v. 61, p. 491–493.

Kurz, G.A., Schmitz, M.D., Northrup, C.J., and Vallier, T.L., 2017, Isotopic compositions of intrusive rocks from the Wallowa and Olds Ferry arc terranes of northeastern Oregon and western Idaho: Implications for Cordilleran evolution, lithospheric structure, and Miocene magmatism: Lithosphere, v. 9, p. 235-264.

Lange, R.A., Frey, H.M., and Hector, J., 2009, A thermodynamic model for the plagioclase-liquid hygrometer/thermometer: American Mineralogist, v. 94, p. 494-506.

Lowenstern, J.B., and Hurwitz, S., 2008, Monitoring a supervolcano in repose; heat and volatile flux at the Yellowstone caldera: Elements, v. 4, p. 35-40.

Mankinen, E. A., Prevot, M., Grommé, C.S., and Coe, R. S., 1985, The Steens Mountain (Oregon) geomagnetic polarity transition: 1. Directional history, duration of episodes, and rock magnetism: Journal of Geophysical Research: Solid Earth, v. 90, no. B12, p. 10393-10416.

Mason, B. and Allen, R.O., 1973, Minor and trace elements in augite, hornblende and pyrope megacrysts from Kakanui, New Zealand: New Zealand Journal of Geology and Geophysics, v. 16, p. 935-947.

Marsh, B.D., 1988, Crystal capture, sorting, and retention in convecting magma: Geological Society of America Bulletin, v. 100, p. 1720-1737.

McBirney, A.R., Baker, B.H., and Nilson, R.H., 1985, Liquid fractionation. Part I: Basic principles and experimental simulations: Journal of Volcanology and Geothermal Research, v. 24, p. 1-24.

Moore, N.E., Grunder, A.L. and Bohrson, W.A., in press 2018, The three-stage petrochemical evolution of the Steens Basalt compared to large igneous provinces and layered mafic intrusions: Geosphere.

Nielsen, R.L., and DeLong, S.E., 1992, A numerical approach to boundary layer fractionation: application to differentiation in natural magma systems: Contributions to Mineralogy and Petrology, v. 110, p. 355-369.

Poland, M.P., A. Miklius, and Montgomery-Brown, E.K., 2014, Magma supply, storage, and transport at shield-stage Hawaiian volcanoes: U.S. Geological Survey Professional Paper 1801, p. 179-235.

Poland, M.P., Sutton, A.J., and Gerlach, T.M., 2009, Magma degassing triggered by static decompression at Kīlauea Volcano, Hawai'i: Geophysical Research Letters, v. 36, L16306, doi:10.1029/2009GL039214.

Regelous, M., Hofmann, A.W., Abouchami, W., and Galer, S.J.G., 2003, Geochemistry of lavas from the Emperor Seamounts, and the geochemical evolution of Hawaiian magmatism from 85 to 42 Ma: Journal of Petrology, v. 44, p. 113-140.

Reidel, S.P., Camp, V.E., Tolan, T.L., and Martin, B.S., 2013, The Columbia River flood basalt province: Stratigraphy, areal extent, volume, and physical volcanology: Geological Society of America Special Papers, v. 497, 1-43.

Reidel, S.P., and Tolan, T.L., 2013, The Grande Ronde Basalt, Columbia River Basalt Group: Geological Society of America Special Papers, v. 497, p. 117-153.

Richards, M.A., Duncan, R.A., and Courtillot, V.E., 1989, Flood basalts and hot-spot tracks: plume heads and tails. Science, v. 246, p. 103-107.

Scandone, R., and Malone, S.D., 1985, Magma supply, magma discharge and readjustment of the feeding system of Mount St. Helens during 1980: Journal of Volcanology and Geothermal Research, v. 23, p. 239–262.

Sheth, H., 2016, Giant plagioclase basalts: Continental flood basalt–induced remobilization of anorthositic mushes in a deep crustal sill complex: Geological Society of America Bulletin, v. 128, p. 916-925.

Spera, F.J. and Bohrson, W.A., 2001, Energy-constrained open-system magmatic processes I: general model and energy-constrained assimilation–fractional crystallisation (EC-AFC) formulation: Journal of Petrology, v. 42, p. 999-1018.

Spera, F.J. and Bohrson, W.A., 2002, Energy-constrained open-system magmatic processes III: energy-constrained recharge, assimilation, and fractional crystallisation (EC-RAFC): Geochemistry Geophysics Geosystems, v. 3, doi: 10.1029/2002GC000315.

Spera, F.J. and Bohrson, W.A., 2004, Open-system magma chamber evolution: an energy constrained geochemical model incorporating the effects of concurrent eruption, recharge, variable assimilation and fractional crystallization (EC-E′RA χFC): Journal of Petrology, v. 45, p. 2459-2480.

Talusani, R.V.R., 2012, Giant plagioclase basalts from northeastern Deccan volcanic province, India: Implications for their origin and petrogenetic significance: International Journal of Geosciences, v. 3, p. 1027-1032.

Toth, C., 2018, Giant plagioclase in the Steens Basalt, SE Oregon: Cumulate entrainment revealed by textural and in situ chemical analysis [M.S. Thesis]: Central Washington University, 105 p.

Tumpane, K.P., 2010, Age and isotopic investigations of the Olds Ferry terrane and its relations to other terranes of the Blue Mountains province, eastern Oregon and west-central Idaho [M.S. thesis]: Boise State University, 220 p.

Walker, J.A., Gmitro, T.T., and Berg, J.H., 2002, Chemostratigraphy of the Neoproterozoic Alona Bay lavas, Ontario: Canadian Journal of Earth Sciences, v. 39, p. 1127-1142.

White, R., and McKenzie, D., 1989 Magmatism at rift zones: the generation of volcanic continental margins and flood basalts: Journal of Geophysical Research: Solid Earth, v. 94, p. 7685-7729.

Wolff, J.A., and Ramos, F.C., 2013, Source materials for the main phase of the Columbia River Basalt Group: geochemical evidence and implications for magma storage and transport: Geological Society of America Special Paper 497, p. 273-291.

Table 4.1

Compositional Input for MCS RAFC Models

	Parent Magma	Recharge Magma	Average Plag (An$_{66}$)	Average Olivine (Fo$_{76}$)	Average Cpx (Mg# 75)	Estimated FeTi Melt	Cumulate Plag+ Olivine+Cpx	Cumulate Plag + Olivine	FeTi Rich Melt + Plag (60/40)	Wallrock Assimilant
SiO$_2$	49.17	48.10	51.0	38.50	50.52	50	49.01	49.63	50.40	56.26
TiO$_2$	1.82	1.73	0.10	0.02	1.64	2.50	0.47	0.09	1.50	1.17
Al$_2$O$_3$	14.73	13.24	30.0	0.35	3.46	15	18.92	26.74	21.00	14.09
FeO*	11.22	11.74	0.50	20.70	11.39	13	6.25	2.72	8.00	10.94
MnO	0.18	0.19	0	0.30	0.17	0.20	0.09	0.03	0.12	0.57
MgO	9.47	12.29	0.25	38.90	14.67	5	9.65	4.50	3.00	4.88
CaO	10.09	9.75	14.0	0.40	17.9	8	12.94	12.50	10.40	7.64
Na$_2$O	2.50	2.24	3.50	0	0.37	3.25	2.19	3.12	3.35	3.70
K$_2$O	0.59	0.45	0.25	0	0.01	0.45	0.15	0.22	1.00	0.48
P$_2$O$_5$	0.23	0.21	0	0	0	0.45	0	0	0.27	0.27
NiO	0.032	0.049	0	0.21	0	0.010	0.030	0.023	0.006	0
Cr$_2$O$_3$	0.100	0.117	0	0.03	0.180	0.005	0.005	0.003	0.003	0
H$_2$O	0.50	0.50	0	0	0	0.6	0	0	0.36	
Sc (ppm)	31.7	29.5	4	0	30.0	34	9.9	3.6	22.0	
Rb (ppm)	9.4	7.5	0	0	0	5	0	0	5.0	
Sr (ppm)	341	312	800	0	0	500	540	623-801	580	
^{87}Sr/^{86}Sr	0.7038	0.7038	0.7037	0	0	0.7037	0.7037	0.7037	0.7037	
Ba (ppm)	215	171	60	0	0	500	36	53	324	
Ce (ppm)	27.6	25.6	1.5	0	0	50	0.9	1.3	30.6	

Note: Parent magma composition is sample MF9466 from Johnson et al. 1998. Recharge magma was calculated by adding 4% lower B Steens Fo$_{86}$ olivine to the whole rock composition of sample NMSB18. Cumulate plagioclase + olivine + clinopyroxene was calculated by using average plagioclase, olivine and clinopyroxene compositions from the lower B Steens Basalt mixed in the proportions 60% plag/15% olivine/25% cpx. Cumulate plagioclase + olivine composition was calculated by using the average plagioclase and olivine compositions mixed in the proportions 89% plagioclase/11% olivine. FeTi rich melt + plagioclase composition calculated from an estimated FeTi rich melt reported in Chapter 3 and the average plagioclase composition, mixed in the proportions 60% FeTi rich melt/40% plagiolcase as in the Chapter 3 simple mixing calculations. Whole rock and mineral compositions used for calculating recharge, cumulate and FeTi melt + cumulate compositions from Moore et al. 2018, in review and Toth, 2018. Wallrock assimilant is Olds Ferry Terrane sample 99AQ-07 from Tumpane, 2010. Plag = plagioclase, Cpx = clinopyroxene.

Table 4.2

Partition Coefficients used in MCS Models

	Olivine K_D	Cpx K_D	Plag K_D	Spinel K_D	Rhom-oxide K_D
Sc (ppm)	0.3	3.0	0.01	0	0.73
Rb (ppm)	0.00018	0.011	0.07	0.029	0
Sr (ppm)	0.00019	0.1	2	0	0
Ba (ppm)	0	0.002	0.20	0	0
Ce (ppm)	0.0001	0.1	0.20	0.01	0

Note: Partition coefficients for basalt from the Geochemical Earth Reference Model (GERM) Database. Cpx = clinopyroxene, Plag = plagioclase, Rhom-oxide = rhombohedral oxides.

Table 4.3

Best Fit Intensive Parameters for MCS Modeling

	Range	Rationale
Pressure	1 - 3 kbar	At 4 kbar and above, orthopyroxene is a liquidus phase, which is not part of Steens Basalt mineral assemblage.
		3 kbar is best fit for high MgO path models because at lower pressure, plag is suppressed and appears below MgO contents of actual samples that contain plag.
		1 kbar is best fit for low MgO path models due to the good correlation of the model trend with the sparsely phyric flow data (see Fig. 4.3).
fO_2	QFM-1 to QFM	QFM+1 yields forsterite contents that are too high (Fo_{89}). QFM+2 yields orthopyroxene in the mineral assemblage.
		QFM-1 fits the modeled paths and is suggested by the bulk of Fe-Ti mineral compositions, but QFM cannot be ruled out.
H_2O content	Parent Magma 0.5 to 1 wt.%	<0.5 wt.% yields orthopyroxene in the mineral assemblage.
		>1 wt.% suppresses plagioclase below MgO contents of actual samples that contain plag.
	Recharge Magma 0.5 to 1 wt.%	<0.5 wt.% yields incorrect mineral compositions for multiple phases and whitlockite in the mineral assemblage.
		>1 wt.% suppresses plagioclase below MgO contents of actual samples that contain plag.

Note: See *Results-Best-Fit Intensive Parameters* section for further discussion.

Table 4.4
Modeled Recharge and Fractionation Masses for High MgO Trend of Lower B Steens Basalt

Event	Total System Mass (g)	Recharge (g)	Fractional Crystallization (g)	Cumulative Fractional Crystallization (g)	Normalized Recharge Mass	Normalized FC Mass
Initial Parent Magma	100	—	2.8	2.8	—	0.03
R1	155	55	2.6	5.4	0.55	0.02
R2	260	105	2.9	8.3	0.68	0.01
R3	430	170	7.0	15.3	0.65	0.02
R4	3530	3100	402.0	417.3	7.21	0.12
Total	**3530**	**3430**	**417.3**	**417.3**	**9.09**	**0.19**

Note: R1 = Recharge Event 1, etc. Some cooling of the parent magma/resident magma between recharge events and after recharge events leads to crystallization of cumulate olivine. See *Results-High MgO Trend RAFC* Models section for explanation.

Table 4.5

Mixing Models of Plagioclase Rich FeTi Melt and Primitive Lower Steens Basalt

Sample	SiO$_2$	TiO$_2$	Al$_2$O$_3$	FeO	MgO	CaO	Na$_2$O	K$_2$O	Rb (ppm)	Sr (ppm)
Lower Steens High Al$_2$O$_3$ Samples										
MF9464	49.7	1.80	19.6	9.5	4.4	10.8	3.2	0.6	7	523
JS27	48.6	1.64	16.7	10.7	8.3	10.4	2.7	0.6	8	416
NMSB-13	49.0	1.85	18.6	9.9	6.1	10.7	3.0	0.5	6	510
Modeling Endmembers										
Average Steens Plagioclase	51.0	0.00	30.0	0.5	0.0	14.0	3.5	0.3	0	700
Estimated FeTi Melt[a]	50.0	2.50	15.0	13.0	5.0	8.0	3.3	1.5	5	500
JS13 (Lower B Steens Parent)	48.8	1.72	13.4	11.3	12.0	9.6	2.1	0.6	10	301
Target FeTi Melt-Plagioclase Mix[b]	50.5	1.80	21.0	8.8	1.0 - 4.0	12.5	3.3	0.4	5	580
Mixing FeTi Melt + Plag										
40/60 FeTi - Plag	50.6	1.00	24.0	5.5	2.0	11.6	3.4	0.8	2	620
50/50 FeTi - Plag	50.5	1.25	22.5	6.8	2.5	11.0	3.4	0.9	3	600
60/40 FeTi - Plag	50.4	1.50	21.0	8.0	3.0	10.4	3.4	1.0	3	580
Mixing JS13 + 60/40 FeTi - Plag										
20/80 JS13 + 60/40 FeTi - Plag	50.1	1.54	19.5	8.7	4.8	10.2	3.1	0.9	4	524
25/75 JS13 + 60/40 FeTi - Plag	50.0	1.56	19.1	8.8	5.3	10.2	3.0	0.9	5	510
50/50 JS13 + 60/40 FeTi - Plag	49.6	1.61	17.2	9.7	7.5	10.0	2.7	0.8	7	441

Note: Whole-rock major and trace element and mineral composition data from Moore et al. (in press). Fill colors denote model and target pairs.

[a]Estimated from the range of FeTi melt samples in the upper Steens Basalt. Data from Moore et al. (in press).

[b]This target composition lies at the point where the trendline of lower B Steens Basalt to high Al$_2$O$_3$ crosses the trendline between the estimated FeTi melt and average Steens plagioclase compostion in all major and trace element spaces considered in this model. See text for discussion.
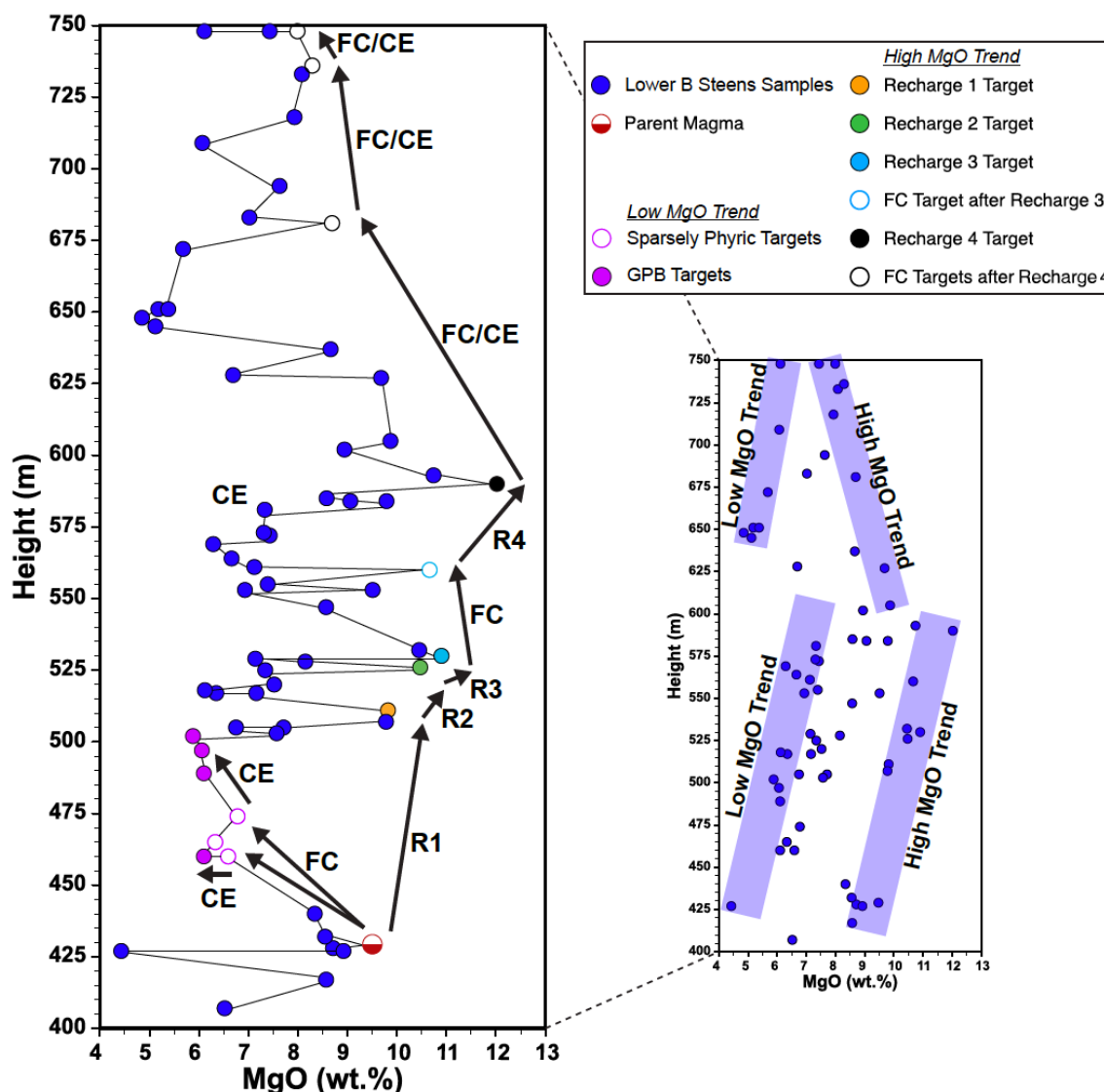
Table 4.6

Mass Balance of Potential Intrusive and Extrusive Volumes for the Lower B Steens Basalt

Package # and Flows in Package (see Fig. 4.10)	Sample Numbers of Flows in Package	Total Flows in Package	High MgO Eruptions (# flows)	Low MgO Eruptions (# flows)	% FC to Low MgO (avg for flows)	% Liquid Remaining Low MgO (erupted portion)	High MgO Eruption Volume (km^3)	Low MgO Eruption Volume (km^3)	Total Eruption Volume (km^3)	Cumulates Produced (km^3)	Expected I:E (6:1)	Total Scaled Intrusive Liquid Expected
Pkg 1, Flows 2-3	JS07-01 to MF9464	2	1	1	25	75	282	282	564	94	6	1692
Pkg 2, Flows 4-15	MF9465 to MF9470	12	5	7	15	85	1410	1974	3384	348	6	8460
Pkg 3, Flows 16-18	NMSB34 to NMSB35	3	0	3	5	95	0	846	846	45	6	0
Totals		**17**	**6**	**11**			**1692**	**3102**	**4794**	**487**		**10152**

No Scaling Next Steps

Package # and Flows in Package (see Fig. 4.10)	Sample Numbers of Flows in Package	Total Flows in Package	High MgO Eruptions (# flows)	Low MgO Eruptions (# flows)	% FC to Low MgO (avg for flows)	% Liquid Remaining Low MgO (erupted portion)	High MgO Eruption Volume (km^3)	Low MgO Eruption Volume (km^3)	Total Eruption Volume (km^3)	Cumulates Produced (km^3)	Calculated I:E	Resident High MgO Magma km^3	Recharge Event	Recharge % (decimal) of Resident Magma	Recharge Mamga Added (km^3)	Total High MgO Magma Before Eruptions (km^3)	Liquid Remaining After High MgO Eruptions	Liquid Remaining After Low MgO Eruptions
Pkg 4, Flows 19-25	NMSB11 to NMSB51	7	2	5	10	90	564	1410	1974	157	7:1	10152	R1	0.55	5584	15736	15172	13605
Pkg 5, Flows 26-28	NMSB15 to NMSB17	3	1	2	10	90	282	564	846	63	26:1	13605	R2	0.68	9251	22856	22574	21948
Pkg 6, Flows 29-44	NMSB18 to JS12	16	3	13	10	90	846	3666	4512	407	7:1	21948	R3	0.65	14266	36214	35368	31294
Pkg 7, Flows 45-51	JS13 to JS18	6	2	4	5	95	564	1128	1692	59		31294	R4	7.20	225319	256613	256049	254861
Pkg 7, Flows 50-56	NMSB24 to JS21	6	0	6	25	75	0	1692	1692	564	75:1	254861	R4 (cont.)	-	-	-	-	252605
Pkg 8, Flows 57-62	JS22 to JS26	6	1	5	10	90	282	1410	1692	188	148:1	252605	n/a - FC only	-	-	252605	252323	250725
Pkg 9, Flows 63-66	JS27 to JS30	4	2	2	6	92	564	564	1128	98	221:1	250725	n/a - FC only	-	-	250725	250161	249499
Totals									**18330**	**2023**								**251522**

Figure 4.1. Compositional paths modeled in MCS for the lower B Steens Basalt. Main diagram shows changing MgO wt.% with stratigraphic height in the lower B Steens Basalt, with thin black lines connecting the samples in sequential stratigraphic order. Outset of stratigraphic height versus MgO highlights the specific paths defined as high and low MgO trends, and the upsection variations in MgO that distinguish the two trends. The parent magma (red half-filled circle) is the starting composition for MCS modeling of both the high and low MgO trends. Heavy black arrows show the direction of each modeled path and the corresponding process modeled to reach each compositional target. R1, R2 etc. = recharge events modeled in the high MgO trend. Each sample composition targeted for modeling by a recharge event is separately color coded for each event (1-4). FC = paths modeled by fractional crystallization. CE = paths modeled by cumulate entrainment.
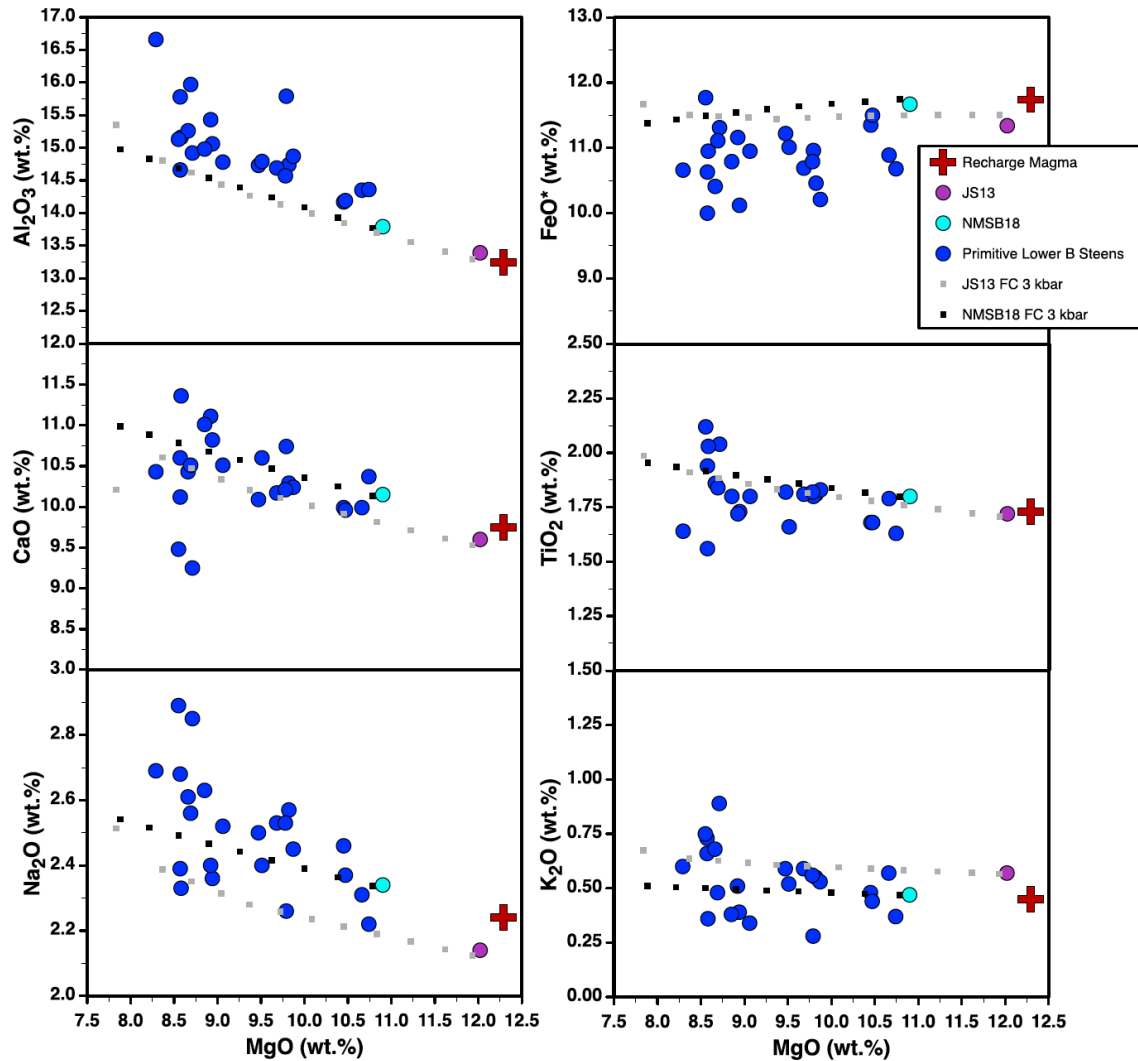
Figure 4.2. Major element compositions for calculated recharge magma in MCS model input. Recharge magma calculated by adding 4% Fo$_{86}$ olivine from the lower B Steens Basalt to sample NMSB18 (light blue circle; whole-rock and mineral composition data from Moore et al. 2018, in press). Fractionation trends from samples NMSB18 and JS13 at 3 kbar are shown. These trends are compositionally similar to the majority of the primitive lower B Steens Basalt samples (blue filled circles, Mg# > 60), and project back towards the calculated recharge magma composition. Though sample JS13 is compositionally similar to the calculated recharge magma at slightly lower MgO, the calculated recharge composition is preferable for use in models because major, trace and isotopic compositions exist for sample NMSB18 (and thus can be included in the calculated recharge magma composition) but not for sample JS13 (analyzed by XRF only; Johnson et al. 1998).
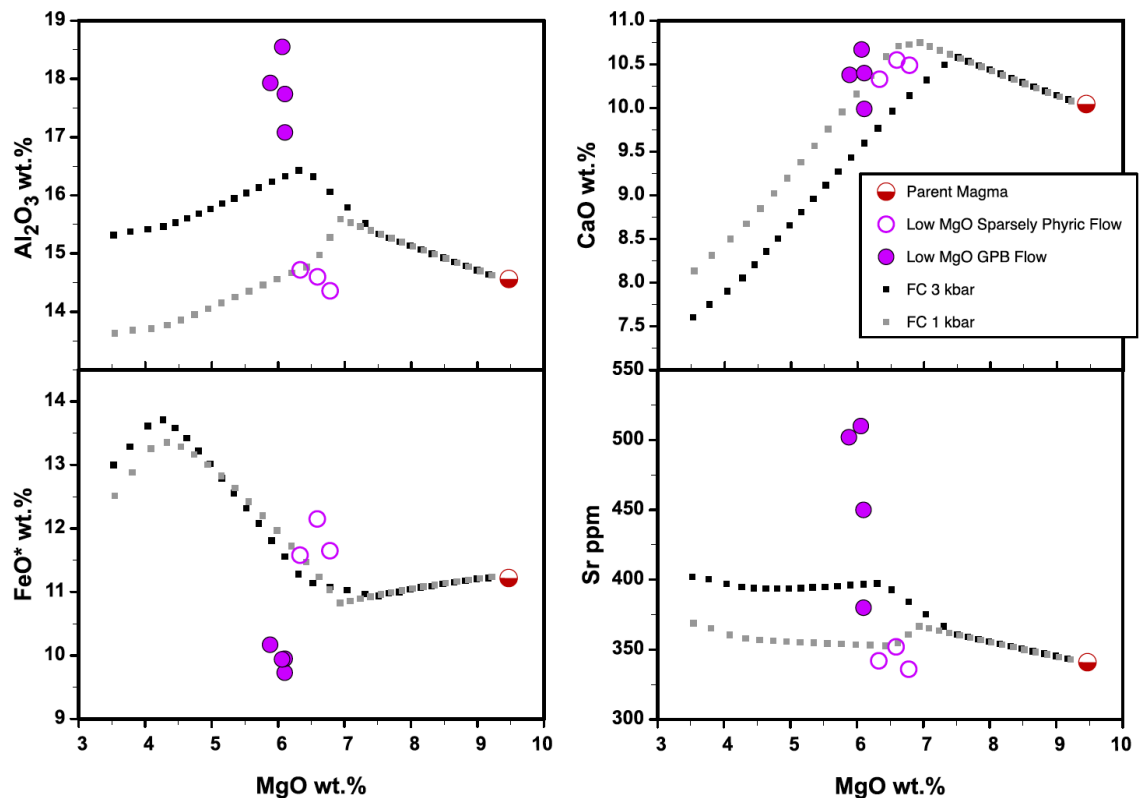
Figure 4.3. Major and trace element compositions of the low MgO trend sample targets and modeled fractional crystallization (FC) paths from the parent magma at 1 and 3 kbar. The 1 kbar FC model is consistent with the compositions of the sparsely phyric target samples in the low MgO trend (open purple circles) but does not fit the GPB target sample compositions for elements, and is a particularly poor fit for Al_2O_3, FeO and Sr. Though the 3 kbar FC model reaches slightly higher Al_2O_3 and Sr, it does not reach compositions similar to the GPB target compositions.
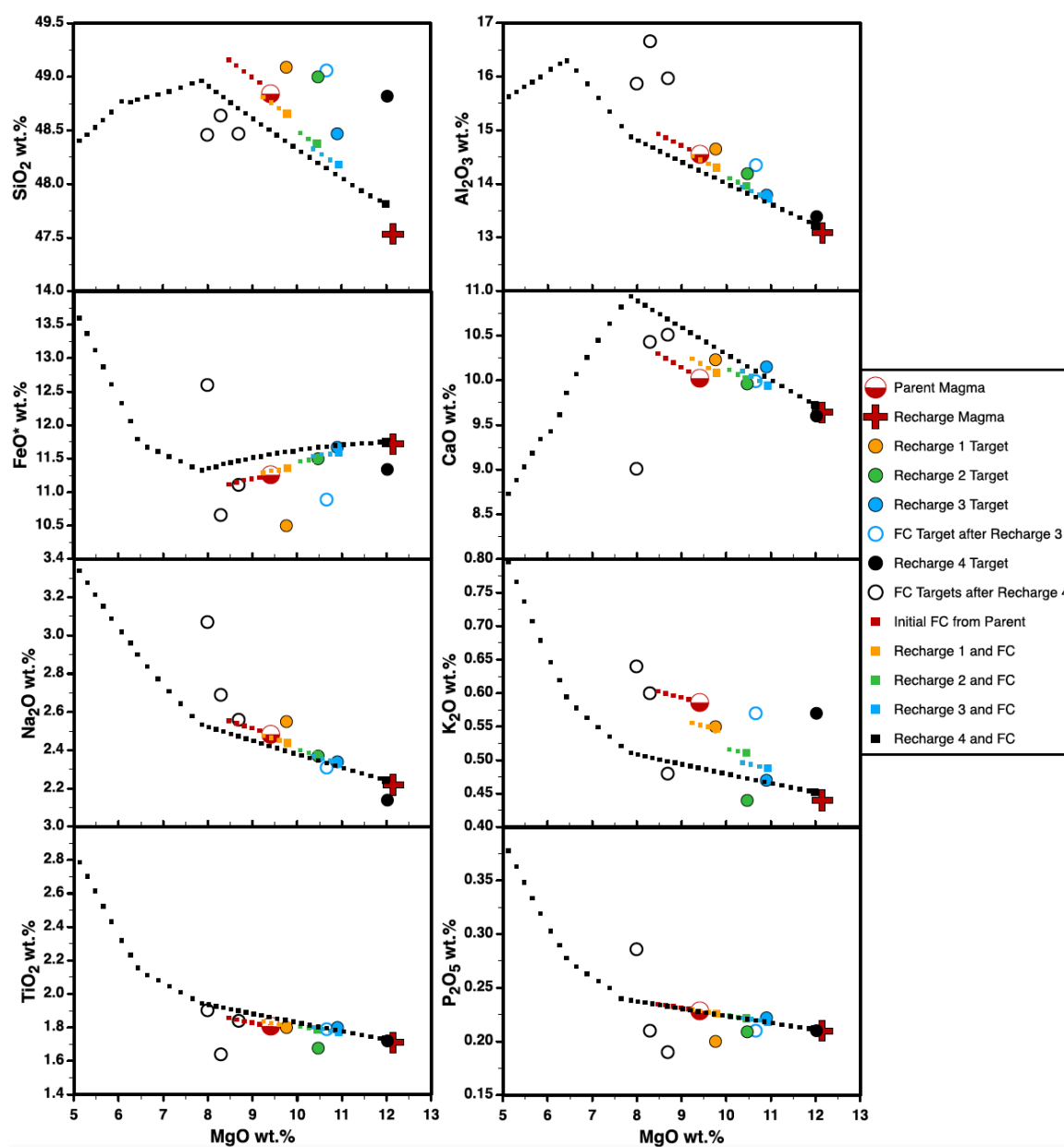
Figure 4.4, Part 1. Whole-rock major, trace and isotopic variation of high MgO trend target samples and 3 kbar RFC model results. Each recharge target sample (filled circles) is color coded to match the modeled recharge event results and subsequent fractional crystallization. Open circles are target samples that are hypothesized to be the result of FC from various recharge events, and are color coded to those events. The high MgO trend model begins with the parent magma, which cools and fractionates over a short interval (small red squares) until recharge event 1 (R1; large orange square). A short interval of cooling and crystallization follows R1 (small orange squares) until R2 occurs (large green square); recharge events continue in this manner until R4 (large black square), after which FC continues through 1050°C (small black squares). See text and Table 4.1 for discussion of calculated recharge and parent magma compositions.
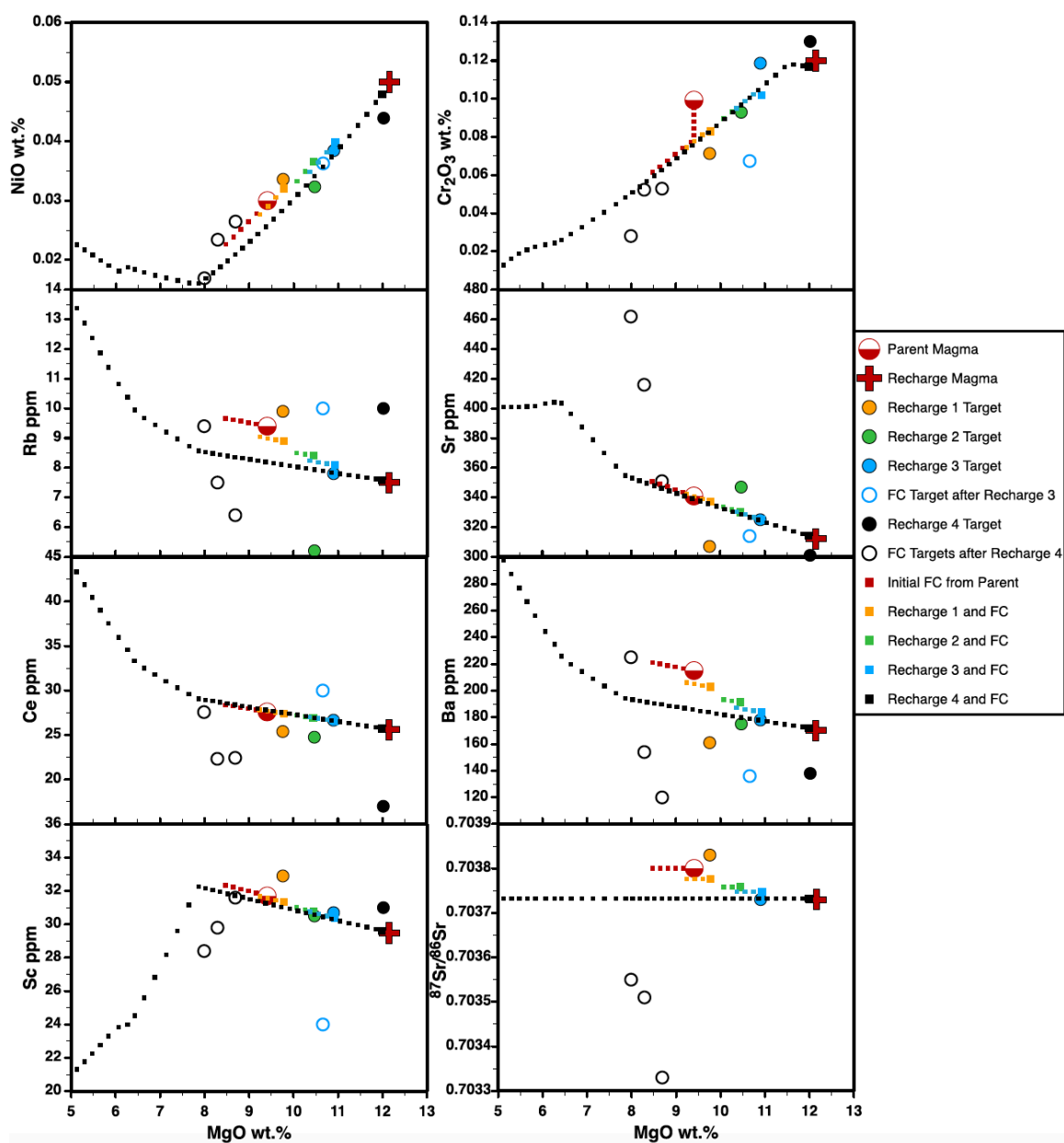
Figure 4.4, Part 2. See caption for Figure 4.4, Part 1.
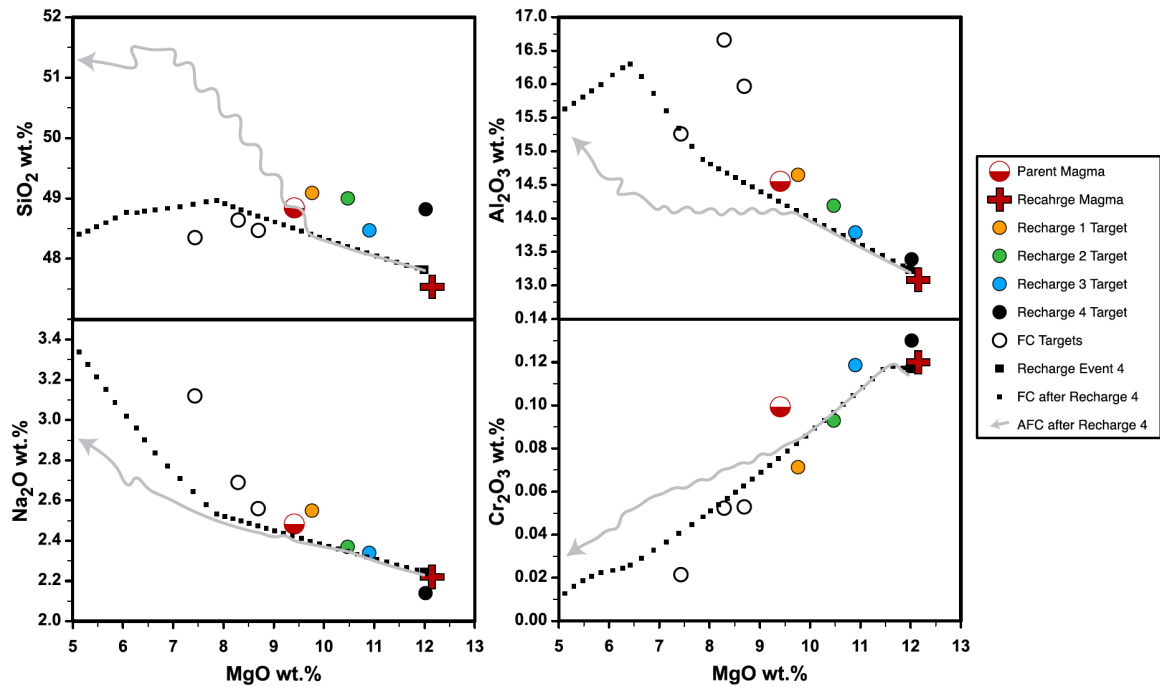
Figure 4.5. Whole-rock major and trace element variation for high MgO path target samples and 3 kbar RAFC model results. The AFC model path initially overlaps the FC model trend after recharge event 4 (large black square). Assimilation of anatectic wallrock melt begins in the simulation after the recharge events cease, and some fractional crystallization has occurred (e.g. the FC trend overlap down to ~10 wt.% MgO). Relative to the FC only model (small black squares), the modeled trend of assimilation (gray arrow) causes a sharp increase in SiO_2 and lesser increase in Cr_2O_3, but a decrease in Al_2O_3 and Na_2O, and thus is a worse fit to explain the compositional trends in the FC target samples than the FC only model. See text and Table 4.1 for discussion of wallrock composition used in modeling.
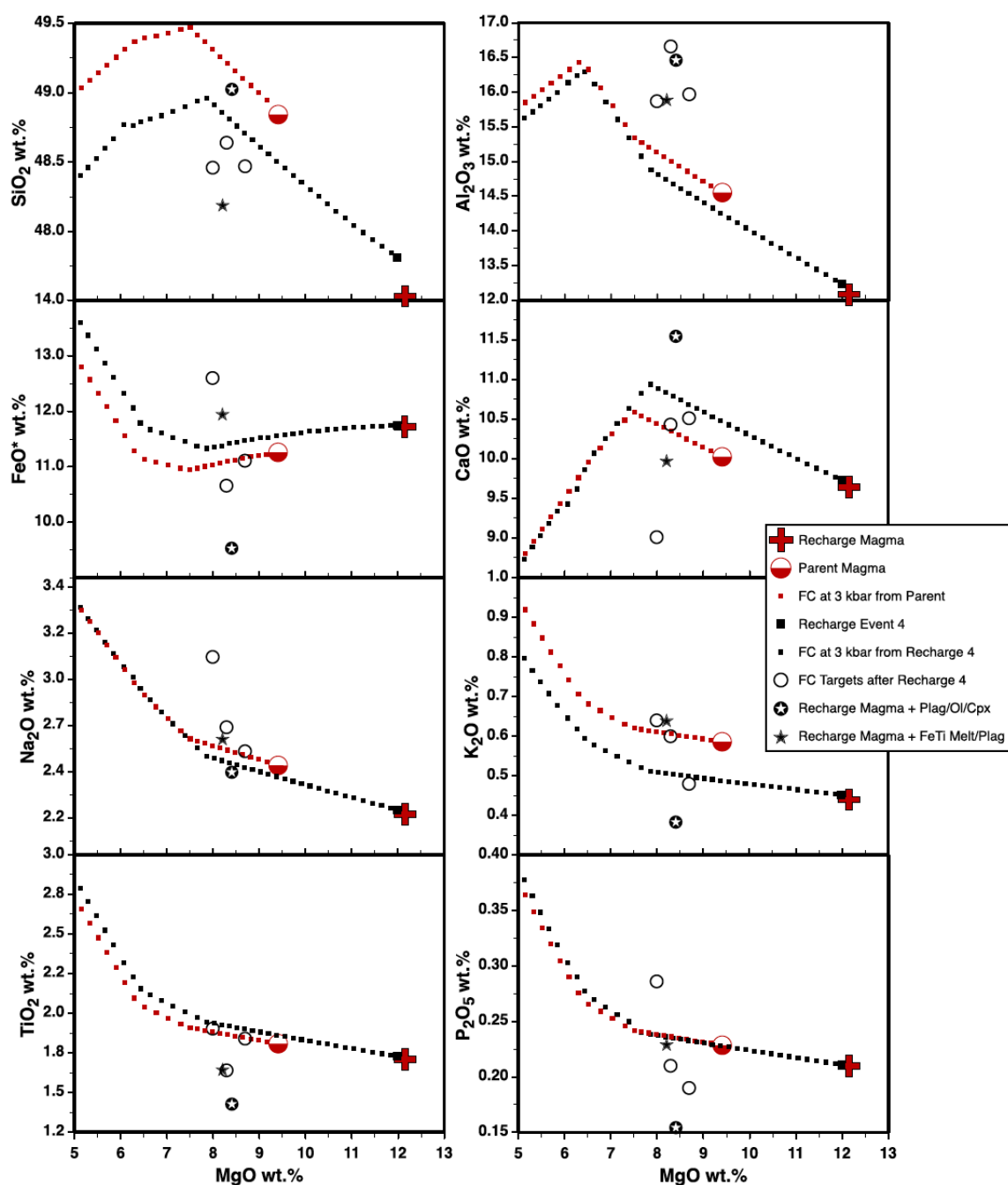
Figure 4.6, Part 1. Whole-rock major, trace and isotopic variation of high MgO trend FC target samples and 3 kbar cumulate entrainment/magma mixing model results. Fractionation from both the model parent magma and after recharge event 4 (small red and black squares, respectively) is consistent with the compositional trends of some of the FC target samples. Two additional processes can account for other trends in the FC targets: entrainment of plagioclase + olivine + clinopyroxene (open star in black circle) and mixing with a FeTi rich melt + plagioclase (black star) into a parent of the recharge magma composition (red cross). (continued next page)
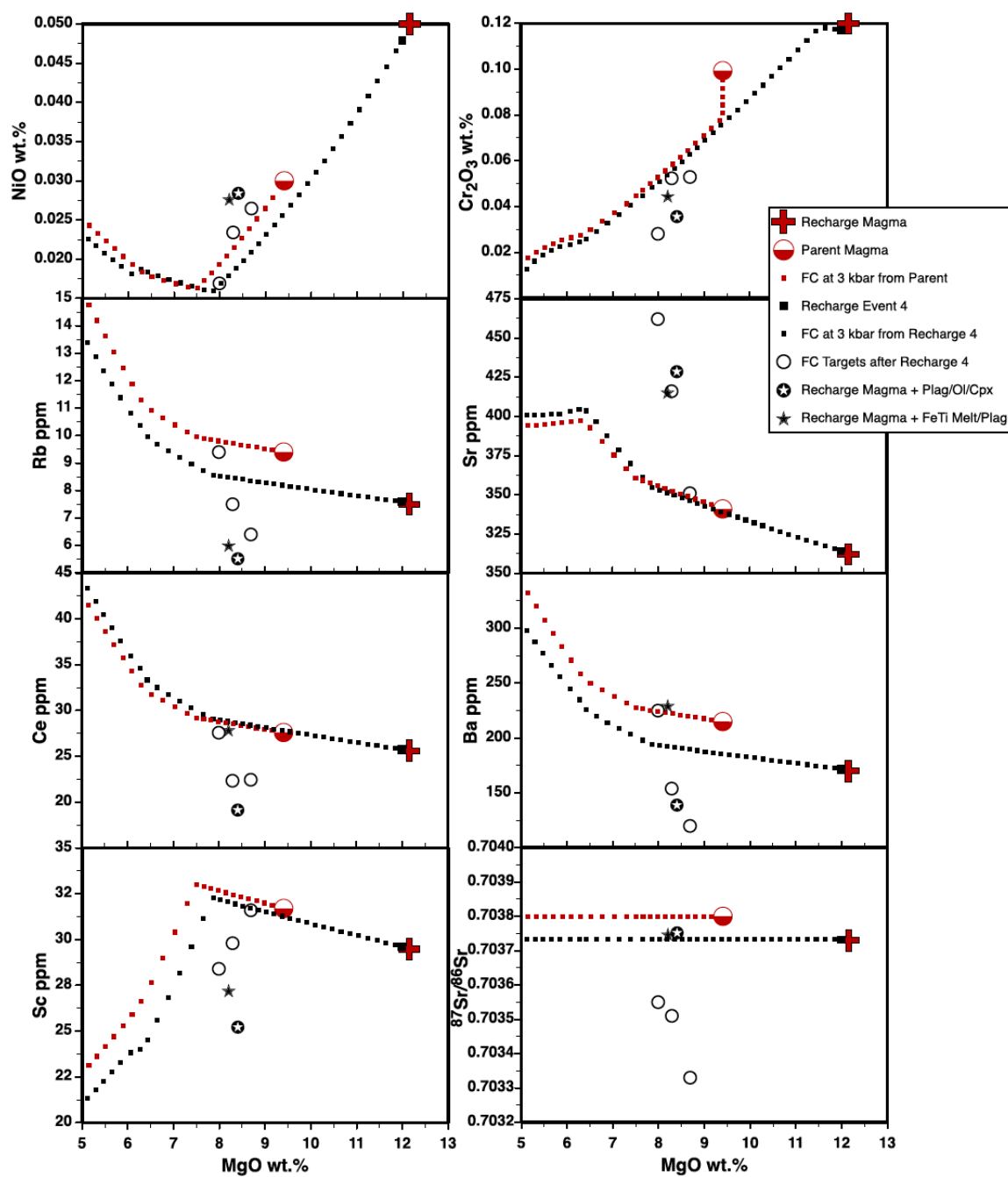
Figure 4.6, Part 2. (continued from Part 1) See text and Table 4.1 for discussion of cumulate and FeTi melt + plagioclase compositions used in the models.
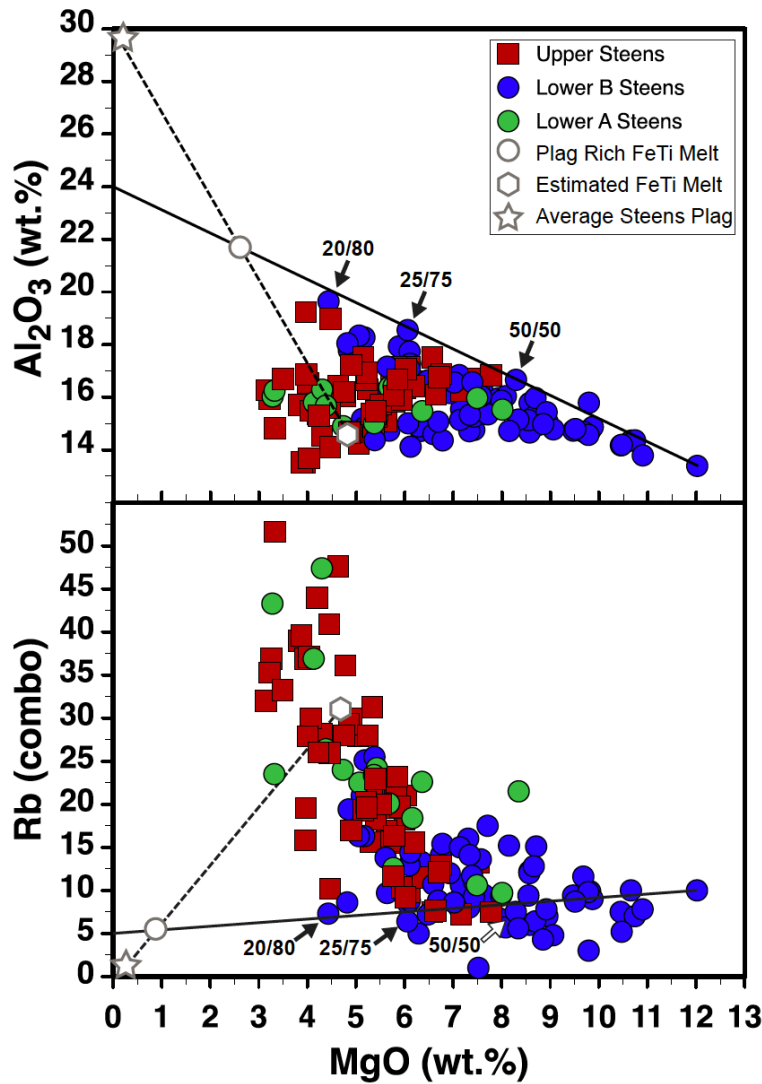
Figure 4.7. Estimation of FeTi melt and plagioclase cumulate component for magma mixing models. Solid black line is a trend in lower B Steens Basalt towards high Al_2O_3 and low Rb that cannot be explained by crystal fractionation (see Fig. 4). Dashed black line represents mixing between an average Steens Basalt plagioclase composition and an estimated FeTi melt. Fractions are the proportion of mixing between a primitive lower B Steens composition and the plagioclase rich FeTi melt (the intersection of the high Al_2O_3 trend and the mixing line) to produce the sample indicated by an arrow. See text for discussion.
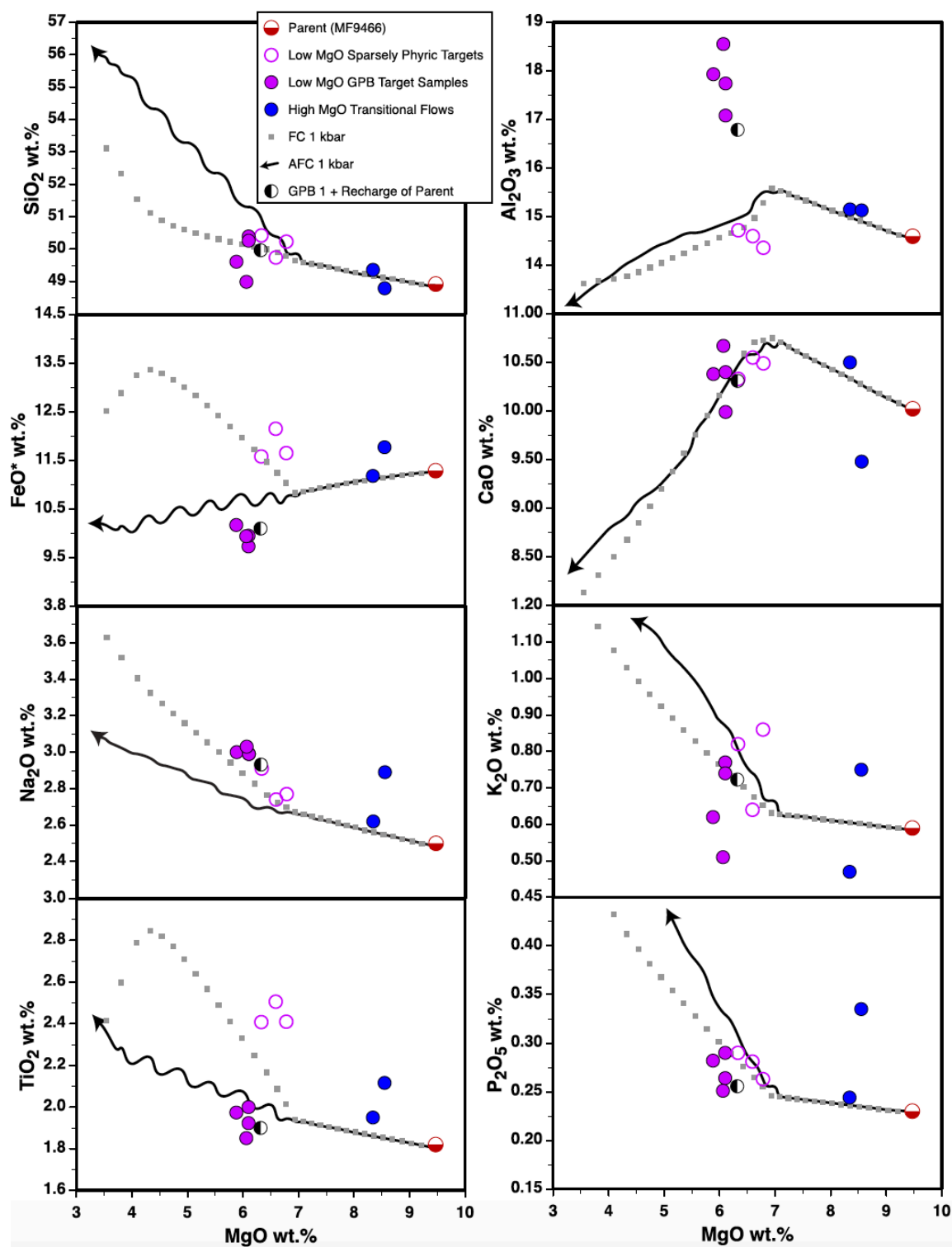
Figure 4.8, Part 1. Whole-rock major, trace and isotopic variation of low MgO trend 1 kbar RAFC model results. The FC model (gray squares) correlates with sparsely phyric target compositions, but not GPB targets. The AFC model (black arrows, not shown for trace elements) is not consistent with all compositions from either group. (cont. next pg.)
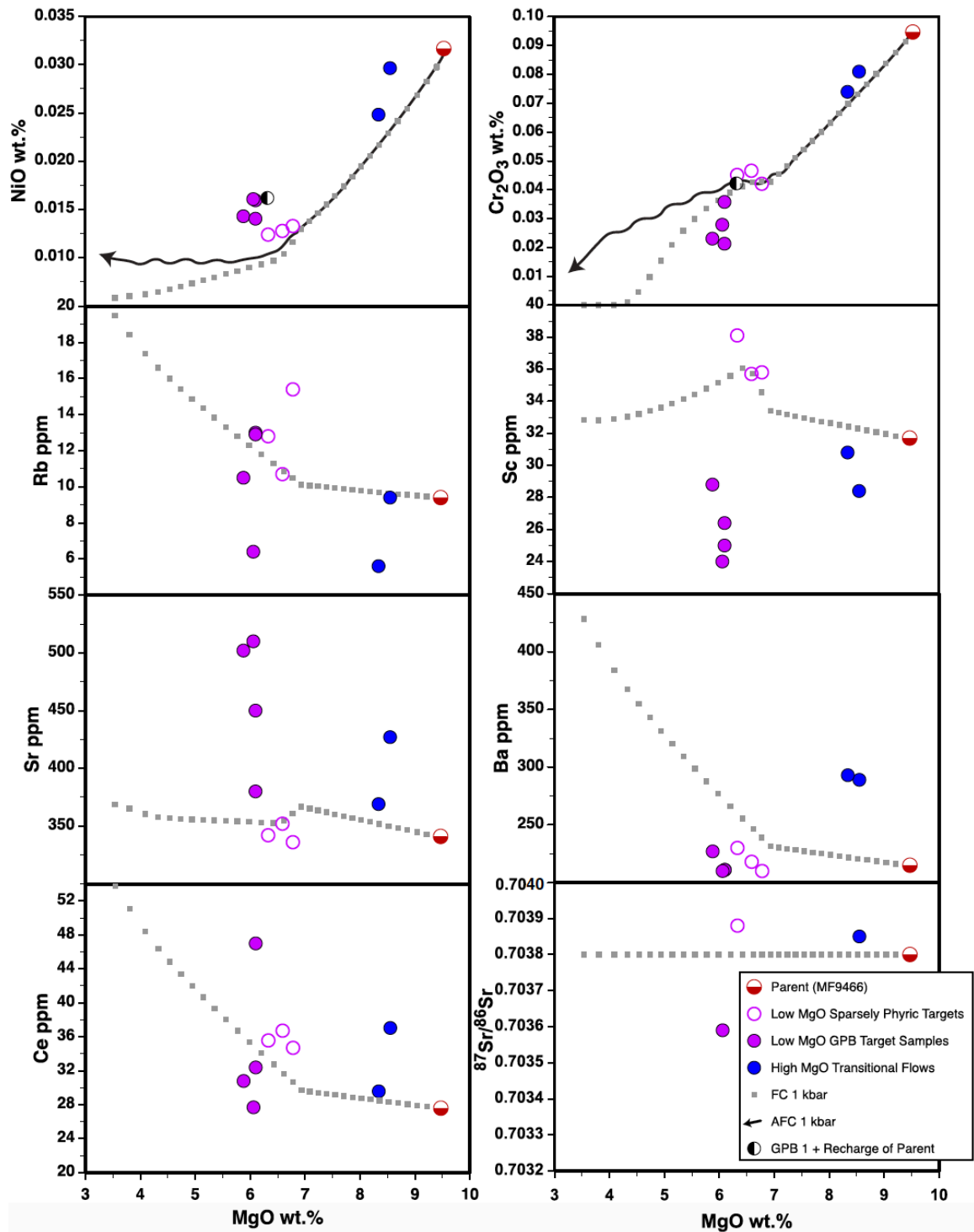
Figure 4.8, Part 2. (continued from Part 1) Recharge of the parent magma to a GPB composition (half-filled black circle, not shown for trace elements) does not reach Al, Fe, or Ti of sparsely phyric samples, so cannot explain the upsection transition from GPB to sparsely phyric flows. See text and Table 4.1 for discussion of parent, recharge, and assimilation compositions used in models.
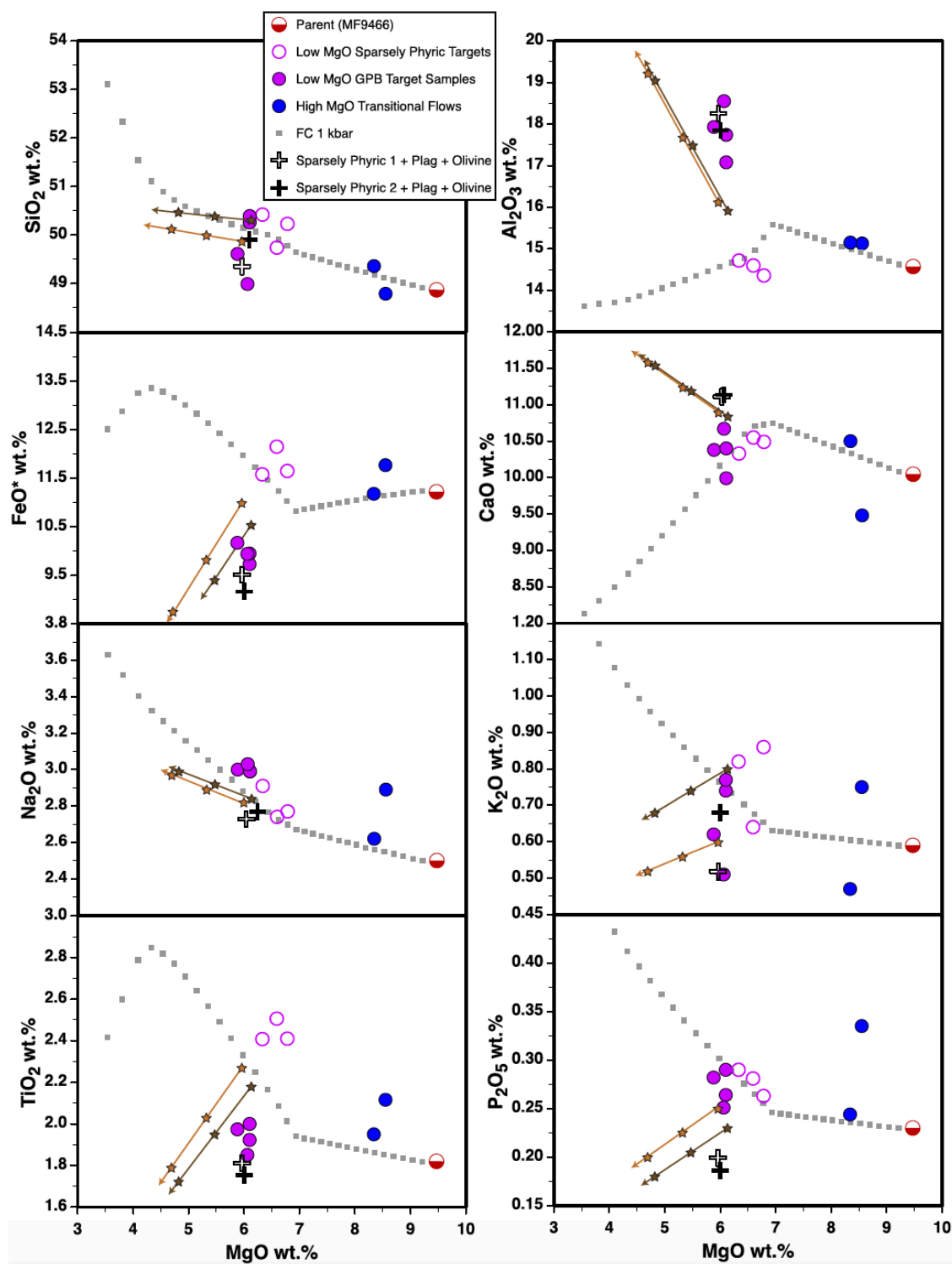
Figure 4.9, Part 1. Whole-rock major, trace and isotopic variation of low MgO trend 1 kbar cumulate entrainment model results. Black and brown arrows show the trajectory of plagioclase only entrainment into sparsely phyric sample 1 (~6.6 wt.% MgO) and sparsely phyric sample 2 (~6 wt.% MgO), respectively. (continued next page)
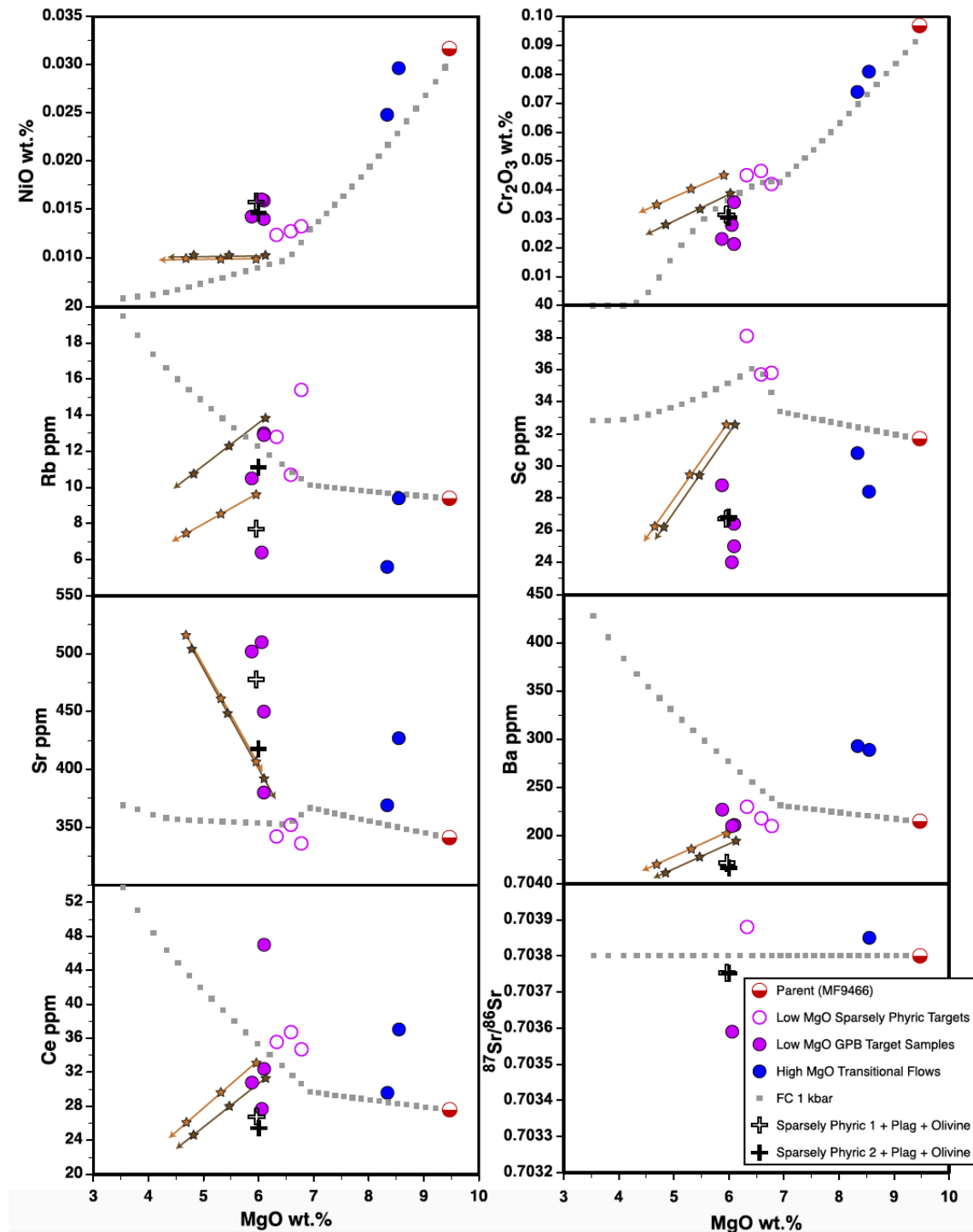
Figure 4.9, Part 2. (continued from Part 1) Each star represents 10% increments of plagioclase addition, up to 30% (near arrow head). Cumulate entrainment of plagioclase + olivine into sparsely phyric samples 1 and 2 (black and open crosses, respectively) matches some elemental trends of the GPB targets. See text and Table 4.1 for discussion of cumulate compositions used in modeling.
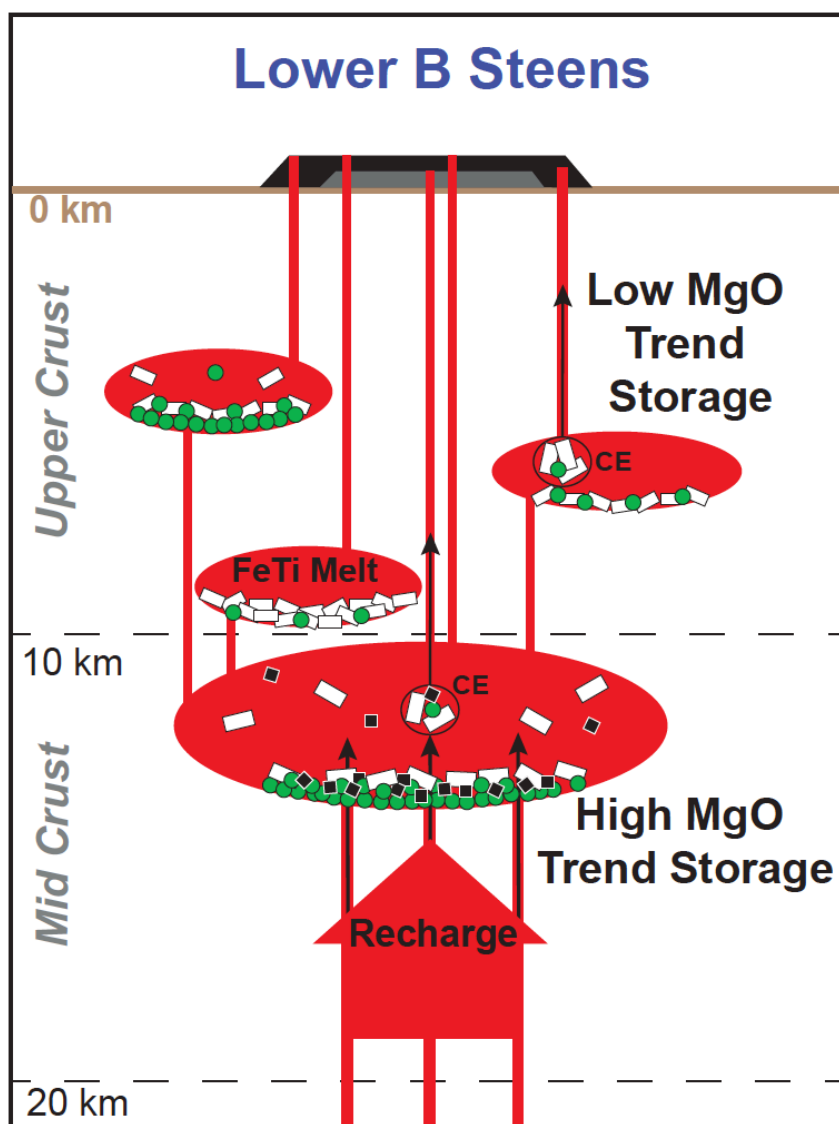
Figure 4.10. Schematic crustal structure and summary of processes for the lower B Steens Basalt stage. The high MgO trend lavas are stored at mid to upper crustal depths and are dominated by recharge that increases with time. Fractionation of olivine (green circles), clinopyroxene (black squares) and plagioclase (white rectangles) occurs in the reservoir between recharge events. Cumulate entrainment (CE) of olivine gabbro that crystallized in an earlier stage of magmatism (i.e. the lower A Steens Basalt stage) and mixing of a differentiated, FeTi rich melt + plagioclase with the recharge magma leads to eruptions of some less magnesian high MgO trend compositions. The recharge reservoir periodically pulses magmas into more shallow storage regions, where magmas cool and fractionate olivine and plagioclase initially, eventually erupting the more differentiated low MgO trend sparsely phyric lavas or entraining cumulates prior to eruption to produce GPB compositions.
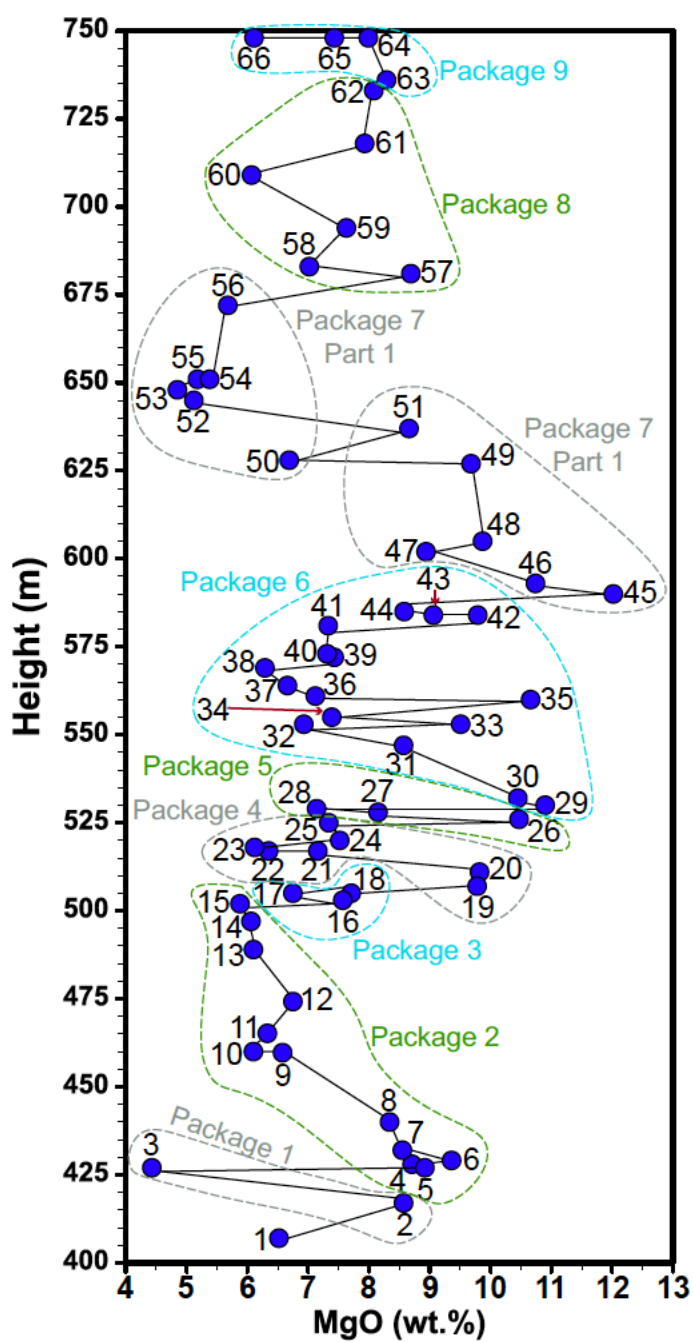
Figure 4.11. Flow numbers and packages defined for the lower B Steens Basalt integrated mass balance calculations. Flow numbers begin at the base of the lower B Steens Basalt section and continue through the informal boundary with the upper Steens Basalt (~750 m). Dashed lines encompass the flows that define individual packages used in each step of the mass balance calculations. See text for discussion.

CHAPTER 5

Conclusions

I present a new suite of stratigraphically controlled whole-rock major and trace element data, Sr, Nd, Pb, Hf, Os and O isotopic data, mineral compositional data, and a new Ar- Ar age for the onset of volcanism of the Steens Basalt in southeast Oregon. A thorough evaluation of petrologic and geochemical characteristics serves as the basis for interpreting the chemostratigraphic changes within the Steens Basalt and provides a means of evaluating the balance of recharge, assimilation, and fractionation (RAFC) through time over the life of this flood basalt event. Study of these characteristics in the Steens Basalt have application for similar studies teasing out the changes in RAFC processes that operate in time at other large mafic systems.

The three-stage petrogenetic evolution defined for the Steens Basalt is evident in stratigraphic compositional changes and records the thermal waxing and waning of a major pulse of basalt into the crust. The lower A stage is initially dominated by low volume magma flux and fractionation, but later becomes more homogenous and heralds the onset of the waxing stage of voluminous magma generation. The lower B stage is dominated by rapid magma input and frequent eruption, which leads to an increasingly mafic magma system where recharge outpaces crystallization and imparts substantial heat to the crust. Towards the end of the lower B stage initiation of the waning period is evident as crystallization begins to outpace recharge. The magmatic system becomes more evolved during the upper Steens Basalt stage, where eruptions become less frequent and less magnesian compositions indicate reduced basaltic recharge. Crustal assimilation in the form of anatectic wallrock melts are introduced in this stage as the crust is sufficiently heated by prior magmatism.

Comparable chemostratigraphic changes are evident in the Imnaha and Grande Ronde Basalts of the Columbia River Basalt Group, the Deccan Traps, Siberian Traps, and in the Bushveld and Stillwater layered mafic intrusions. The compositional evolution with time in these other large mafic systems likely records an early stage of recharge dominance over fractionation, and a later stage of fractionation coupled with crustal melting and assimilation. These comparisons to other continental flood basalts (CFB) and layered mafic intrusions (LMI) are a first step toward identifying similarities in petrogenetic evolution among these large mafic systems.

If total oceanic large igneous province volumes are equivalent to the entire intrusive/extrusive volume of CFB, and LMI roughly represent the intrusive counterparts to CFB that remain in the crust, 50%-85% of the magma input to CFB remains in the crust. Depending on crustal thickness and overall CFB volume, this may effectively remake the crust of these regions into mafic compositions. However, the volumetric differences between oceanic and continental flood basalts could also be due to differences in crustal thickness; the thinner, oceanic crust allowing for melting to continue to shallower levels and thus generating larger volumes of partial melt. In any case, the architecture of the crust changes in time with protracted magmatism. Abundant cumulates are left behind, not only remaking the crust, but leaving behind the equivalent of layered mafic intrusions, containing cryptic and phase layering.

New and existing radiogenic isotopic compositions require at least two distinct mantle sources for the Steens Basalt: an enriched (ES) mantle component and a depleted (DS) mantle. Mixing by other proposed mantle endmembers such as EMI, EMII or HIMU are not evident in the isotopic compositions of the Steens Basalt. Two component partial melt mixing models suggest that roughly equal proportions of the of the DS and ES mantle sources contribute to magma generation during the lower A Stage and into the waxing stage, the lower B Steens Basalt. Input of the DS component increases in time within the lower B stage, contributing up to 70% of the mantle source to lavas erupted towards the end of the stage. Into the upper Steens Basalt stage, the DS and ES mantle endmembers contribute subequal proportions. After prolonged thermal priming of the crust, an additional component contributes to magma generation during the upper stage; significant melts of mafic terrane crust, similar in composition to the Olds Ferry Terrane.

Subsets of data from various stages in the Steens Basalt suggests a role for other processes during magma generation and passage through the crust. Lower B Steens Basalt Os concentrations require a contribution from an Os rich source. This could be either residual sulfide in the DS mantle source, or consumption of sulfides fractionated from earlier magmas upon ascent through the crust. Enriched oxygen isotope compositions in plagioclase phyric flows of Steens Basalt suggest fractionation of significant clinopyroxene occurs in the crust prior to eruption.

Magma Chamber Simulator modeling provides support for the interpretations regarding the change in balance of RAFC processes during the evolution of lower B Steens Basalt. Upsection modeling of distinct high and low MgO trends as separately evolving reservoirs elucidates the range of processes involved in lower B Steens Basalt petrogenesis. Periodic recharge events with small intervals of cooling and crystal fractionation between events is consistent with the initially increasing magnesian character upsection in the high MgO trend. Recharge events become more voluminous in time until the most magnesian flows are erupted. Declining MgO high in the section for the high MgO trend suggests a combination of fractionation, olivine gabbro cumulate entrainment, and magma + cumulate mixing into a range of primitive compositions at mid to upper crustal levels. Sparsely phyric flows in the low MgO trend are consistent with shallower storage and fractionation from a primitive magma parental to the high MgO trend. Low MgO giant plagioclase basalts are the result of entrainment of troctolite cumulates into fractionated melts similar in composition to the sparsely phyric flows. Periodic pulsing by the high MgO recharge trend compositions into the shallower reservoirs provides the parent magmas that store and fractionate into the low MgO trend lavas.

Relative masses of recharge and fractional crystallization from MCS models confirm the dominance of recharge over differentiation during the lower B stage, supporting the conclusion that this stage represents waxing of the magmatic input. A preliminary total mass balance calculation for the entire lower B Steens Basalt package suggests a range of 5-28 km of crustal cumulate addition. Given the thickness of crust in this region, the maximum estimate would require foundering and delamination of crustal roots into the upper mantle. Additional work and refinement of these initial calculations will provide a basis for integrating mass contributions upsection in other CFB.

Though we present the most comprehensive dataset for the Steens Basalt to date, future work can further elucidate the magmatic evolution of the system. The lower A Steens Basalt stage has yet to be analyzed for either Os or Oxygen isotopes, which are an important indicator of the presence and amount of crustal contamination. Given the Sr, Nd, Pb and Hf data for this stage is limited, supplementing these data will also provide

important constraints on the relative contributions of the mantle and crustal sources during this earliest stage of flood basalt magmatism, giving insight into the initial impingement of a CFB that is so often obscured by later magmatism. Some flows with the highest $\delta^{18}O$, and thus potentially the most crustally contaminated, have not been analyzed for the full suite of radiogenic isotope compositions. Adding these data can further elucidate the composition of the crustal contaminant. Similarly, additional Os isotopic data for the upper Steens stage is important to determine the extent of crustal contamination of magmas during this stage and could answer questions regarding the timing of onset of this process. Finally, MCS modeling of the lower A stage needs to be conducted in entirety, and MCS modeling for trace elements and isotopes in the upper Steens has yet to be undertaken. MCS Modeling of both of these stages will assist in quantifying relative mass contributions of recharge, fractionation and assimilation, as well as reveal additional processes that modify the magmas in time, such as cumulate entrainment and magma mixing.

The data, models, and interpretations presented here for the Steens Basalt provide a framework for future studies of chemostratigraphic changes in continental flood basalts and comparison among other large mafic systems. Greater stratigraphic control on the upsection compositional changes through detailed sampling and geochemical analysis in these regimes can further elucidate systematic temporal changes in crustal processes during the evolution of large mafic systems. Comparison across regimes will allow for a broader understanding of similarities and differences among large igneous provinces.